Controlled mechano-chemical synthesis and properties of nanostructured hydrides in the Mg-Al-H and Mg-B-H systems

By

Chun Chiu

A thesis
presented to the University of Waterloo
in fulfilment of the
thesis requirement for the degree of
Doctor of Philosophy
in
Mechanical & Mechatronic Engineering

Waterloo, Ontario, Canada, 2007

© Chun Chiu 2007

I hereby declare that I am the sole author of this thesis. This is a true copy of the thesis, including any required final revisions, as accepted by my examiners.

I understand that my thesis may be made electronically available to the public.

Abstract

The present work reports a study of mechano-chemical synthesis (MCS) and mechano-chemical activation synthesis (MCAS) of nanostructured hydrides in the Mg-H, Mg-Al-H and Mg-B-H systems by controlled reactive mechanical alloying/milling (CRMA/CRMM) in the magneto-mill Uni-Ball-Mill 5. Structural and desorption properties of the milled powders are examined by X-ray diffraction (XRD), scanning electron microscopy (SEM), differential scanning calorimetry (DSC), thermogravimetric analysis (TGA) and desorption test in a Sieverts-type apparatus.

Regardless of the hydride systems, the morphologies of milled Mg-H, Mg-Al-H and Mg-B-H powders after a prolonged milling time can be characterized by dramatic particle size refinement and high tendency to form agglomerates.

The effect of nanograin size and particle size on the DSC desorption temperature of synthesized MgH_2 hydride has been studied. A profound effect of the particle size of synthesized MgH_2 hydride on its hydrogen desorption DSC temperature has been found. The nanograin (crystallite) size of MgH_2 does not seem to have apparent effect on the DSC desorption temperature. The role of both the particle size and the duality of hydride phase in the desorption process is discussed. The nanostructured MgH_2 obtained by CRMM releases hydrogen at ~332^{o}C, which is ~60^{o}C lower as compared to the non-milled commercial MgH_2 (Tego Magnan®) prepared by current manufacturing practices.

In the Mg-Al-H system, no successful synthesis of $Mg(AlH_4)_2$ has been achieved by MCS of the nanostructured $Mg(AlH_4)_2$ complex hydride using four starting stoichiometric Mg-2Al mixtures. It is hypothesized that Al(Mg) solid solution in the

initial stage (~10h) of CRMA and free Al(s) decomposed from solid solution as the milling time increases the initial stage inhibit the reaction to form $Mg(AlH_4)_2$.

After heating the milled Mg-Al-H powder, the MgH_2 hydride in nanometric mixture with Al which does not react with Mg and hydrogen to form $Mg(AlH_4)_2$ in the milled Mg-Al-H exhibits a hydrogen desorption temperature at the same range to those of the nanometric MgH_2 with no Al, produced by CRMM.

In contrast to an unsuccessful synthesis in MCS process, a successful synthesis of the $Mg(AlH_4)_2$ and 2NaCl mixture by MCAS has been achieved. DSC and TGA analysis show that the decomposition of $Mg(AlH_4)_2$ occurs in a two-step reaction at the temperature ranges of 125-180 and 225-340^oC. The MgH_2 in nanometric mixture with Al which is obtained after the decomposition of $Mg(AlH_4)_2$ releases hydrogen at ~270^oC, which is ~80^oC less than that of the nanometric MgH_2 with no Al, produced by CRMM.

In the Mg-B-H system, when the Mg-2B mixture is made with the oxidized amorphous boron containing B_2O_3 then after a prolonged MCS time (200h), only nanometric γ- and β-MgH_2 hydrides are formed. In contrast, oxide-free amorphous boron in the original Mg-2B mixture prompts the formation of a resulting mixture of nanometric MgB_2 and an amorphous phase containing hydrogen. Further annealing of the milled Mg-2B mixtures at ~100-400^oC under ~4-4.3 MPa of hydrogen for 20-100h does not result in the formation of ternary $Mg(BH_4)_2$.

After heating the long-term milled Mg-B-H powder prepared using oxide-free amorphous boron, the MgH_2 in the nanometric mixture with MgB_2 does not exhibit lowered desorption temperature, as compared to nanometric MgH_2 existing without the presence of second phase.

Alternatively, a powder mixture of $2NaBH_4$ and $MgCl_2$ is used as a starting material to synthesize $Mg(BH_4)_2$ hydride. Amorphous $Mg(BH_4)_2$ phase might have been synthesized after MCAS process. However, the formation of $Na(Mg)BH_4$ solid solution might prevent the synthesis of a large amount of $Mg(BH_4)_2$ hydride. Once the solid solution is formed, the amount of Mg will be insufficient to form a large amount of $Mg(BH_4)_2$ hydride.

Acknowledgements

I would like to express my sincere gratitude to my supervisors, Prof. R. A. Varin and Dr. Z. Wronski for their guidance, tireless support and continual encouragement throughout this work. I would also like to thank Dr. J. Huot, Prof. S. Corbin, Prof. X. Li, Prof. T. Leung and Dr. T. Czujko for their constructive criticism.

I wish to express the appreciation for the assistance I received from technical staff members in the materials laboratory, notably N. Wilhelm and Y. Ding for their useful advice and technical assistance.

Dedication

To my lovely parents and brothers

Table of contents

List of Tables

List of Figures

Nomenclature

Solid state hydride

PCI/PCT: pressure-composition isotherm/pressure-composition temperature curve

P_{eq}: plateau pressure

TM/Non-TM: transition metal/non-transition metal

Ball milling techniques

MA: mechanical alloying

MM: mechanical milling

RMA: reactive mechanical alloying

RMM: reactive mechanical milling

CRMA: controlled reactive mechanical alloying

CRMM: controlled reactive mechanical milling

MCS: mechanochemical synthesis

MCAS: mechanochemical activation synthesis

Milling modes and parameters

LES: low energy shearing mode with one magnet

HES: high energy shearing mode with one magnet

IMP1: low energy impact mode with one magnet

IMP2: high energy impact mode with one magnet

IMP710: impact mode with two magnets at 7 and 10 o'clock positions

IMP68: impact mode with two magnets at 6 and 8 o'clock positions

BPWR: ball-to-powder weight ratio

WD: working distance

S: sequential milling

C: continuous milling

Grain size calculation

L: mean dimension of the nanograin (crystallite) composing the powder particle

K: constant (≈1)

e: maximum microstrain

λ: wave length

θ: position of the analyzed peak maximum

$\delta(2\theta)$: instrumental broadening-corrected "pure" XRD peak profile breadth

B: breadth of the Bragg peak from the XRD scans of the experimental powder

b: the breadths of Bragg peak from the XRD scans of the reference powder

FWHM: the full-widths at half maximum

Particle size calculation

ECD: particle equivalent circle diameter

CV(ECD): experimental coefficient of variation

Differential scanning calorimetry (DSC)

LT peak: DSC low-temperature peak in a peak-doublet

HT peak: DSC high-temperature peak in a peak doublet

T_{ON}: DSC peak on-set temperature

T_{end}: DSC peak end temperature

T_{peak}: DSC peak temperature

ΔH^{melt}: enthalpy of melting

Tendency to form amorphous phase

$\Delta V_{AB}/V_A$: atomic volume mismatch factor

C_B^{min}: minimum concentration of the solute element required to form amorphous phase

$r_{A,}$ r_B and r_H: atomic radius

Effect volume of the milling cylinder

$V_{cylinder}$: volume of the milling cylinder

V_{ball}: volume of one ball

V_{sm}: volume of the starting materials

V_{eff} : effective volume during milling with n balls

W: weight (g) of the starting material

ρ:density (g/cm^3) of the starting material

n: number of balls

Hydrogen capacity estimated by the volumetric method

ΔP: the total pressure change of H_2 (Pa) during the test

m: weight of absorbed H_2 (g)

M_H: molar mass of H_2 (g/mol)

T: temperature (K)

R: gas constant ($8.314 J (mol)^{-1}K^{-1}$)

M: initial powder mass (g)

1. Objectives

The objective of present work is to study the mechano-chemical synthesis of hydrogen storage materials based on the Mg-B-H and the Mg-Al-H systems as well as their properties such as microstructure, grain size, hydrogen capacity and thermal hydrogen desorption behavior. To accomplish the objectives, the goal of each topic is given as following.

1.1 Study of the controlled reactive mechanical milling (CRMM) of the reference Mg-H system

MgH_2 is a metal hydride whose properties have been broadly studied. This simple metal hydride might be formed in due course of the processing of the complex metal hydride $Mg(BH_4)_2$ or $Mg(AlH_4)_2$ by CRMA. Hence, CRMM of the reference Mg-H system was chosen to increase the fundamental understanding of the effect of the milling modes and parameters on the structure and properties of materials milled in the Uni-Ball-Mill 5. The morphological and microstructural examination of milled powders was conducted using SEM. Phase formation and nanocrystallization of the powder were studied by X-ray diffraction (XRD) analysis. The thermal hydrogen desorption behavior was studied by differential scanning calorimetry (DSC) and thermogravimetric analysis (TGA). The desorption kinetics were studied using a Sieverts-type apparatus.

1.2 Study of the mechano-chemical synthesis (MCS)/ of nanostructured hydrides and their properties

In the second phase of this study, the goal is to study the synthesis of nanostructured complex metal hydrides, $Mg(BH_4)_2$ and $Mg(AlH_4)_2$ by CRMA of elemental powders, Mg, B (both crystalline and amorphous) and Al, in the magneto-mill Uni-Ball-Mill 5. Research in this phase concentrated on:

(1) Study of mechano-chemical synthesis of complex metal hydrides $Mg(BH_4)_2$ and $Mg(AlH_4)_2$ from elemental powders.

(2) The effect of milling modes and catalyst on the synthesis of hydrides.

(3) The effect of milling time on the microstructural development of the powder mixture.

(4) The properties of synthesized hydrides.

1.3 Study of the mechano-chemical activation synthesis (MCAS) of nanostructured hydrides and their properties

In the third phase of this study, the goal is to study the synthesis of nanostructured complex metal hydrides, $Mg(BH_4)_2$ and $Mg(AlH_4)_2$ by mechano-chemical activation synthesis of compounds in the magneto-mill Uni-Ball-Mill 5. Research in this phase focused on:

(1) Study of mechano-chemical activation synthesis of complex metal hydrides $Mg(BH_4)_2$ and $Mg(AlH_4)_2$ from two chemical compounds or a chemical compound with an elemental powder.

(2) The effect of milling time on the microstructural development of powder mixture.

(3) The properties of synthesized hydrides.

2. Introduction

A stable energy supply has become an essential requirement for the continuous development in both agriculture and industry. Moreover, the supply and using of a clean fuel is important to stop global warming and climate change world-wide.

Emissions of carbon dioxide (CO_2), the main greenhouse gas from human activities, are the most sensitive subject of a world-wide debate about energy sustainability and the stability of global climate in the recent years. The increases of the concentration of CO_2 and the temperature rise consequent upon this increase have been mostly ascribed to the utilisation of fossil fuels. Generally, a sustainable level must absolutely remain below 550 ppm, which is considered as the maximum acceptable value in order to minimise the effects of global climate changes [1]. According to the prediction by the Intergovernmental Panel on Climate Change (IPCC), without a strong policy in respect to the greenhouse gas (GHG) effect, and bearing in mind increased use of energy from fossil fuel, the CO_2 concentration will reach above the 550ppm limit in 2100 [1].

In addition to the environmental concern, people have been consuming natural resources without considering of possible energy supply shortages since the beginning of industrialization. Due to continuous power consumption upon population growth and technological developments, the demand of fossil fuels will soon exceed the available reserves on earth [2,3].

From the above perspective, it is absolutely indispensable for humankind to develop clean and renewable energy sources (e.g., wind, hydraulic/hydro-energy and solar) other than fossil fuels, whose role will become more and more important in the future energy scenarios. Reviewing the historical development of the energy carriers from coal to

natural gas, one can observe that the energy carriers toward more hydrogen rich fuels and the necessity to avoid the emission of CO_2. Continuing from the same path, the hydrogen should be the energy carrier of the future [4]:

C (coal) $\rightarrow$ CH_2 (oil) $\rightarrow$ CH_4 (natural gas) $\rightarrow$ H_2 (hydrogen)

According to many studies in the scientific community we are now at the verge of a new hydrogen age [5,6]. Energy is first produced from renewable sources and stored in the form of hydrogen. Hydrogen is transported and distributed to final applications such as transportation, and electric power generation for industrial and residential use. The process is shown schematically in Fig. 2.1.

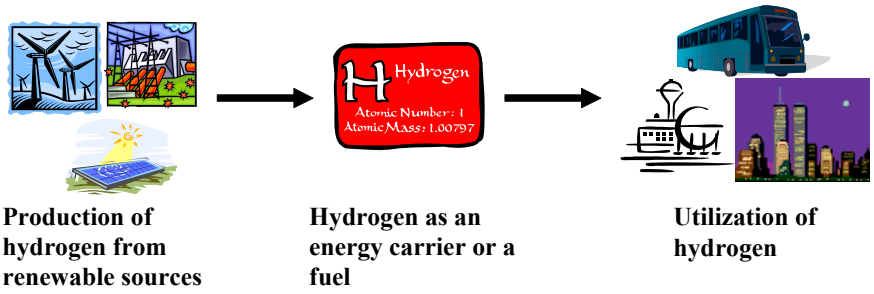

Fig. 2.1 Production and utilization of hydrogen.

Extensive research efforts are laying down the foundation of the next industrial revolution in the application of hydrogen as the fuel of the future. Some focus on contributions that hydrogen can make to sustainable development [7-9]. Others focus on hydrogen's potential to resolving environmental issues [10-12]. Recently, investigations of hydrogen storage systems have become important. As the studies point out, there are still problems in the realization of renewed hydrogen, but the market supply and the cost of hydrogen do not impede the utilization of hydrogen in practical applications. The

biggest and the only roadblock for using hydrogen commercially, especially in vehicular applications, is the storage of hydrogen [4-6,13-17].

The consensus of opinion is setting on hydrogen as a medium to store and supply energy for either supplying fuel cells or internal combustion engines. Modern cars burn about ~24 kg of gasoline for a range of 400 km in a combustion engine. To cover similar range, 4 kg of hydrogen are needed for an electric car with a fuel cell [13,14]. Since 4 kg of hydrogen has a volume of 45 m^3 at room temperature and atmospheric pressure, a tank with considerable storage space would be needed. This volume corresponds to a balloon of 5 m in diameter, which is hardly a practical solution for the mobile applications. One can imagine how difficult it is for the job of hydrogen storage. Hydrogen storage is a major problem, which remains to be solved prior to a wide scale commercialization of hydrogen as a fuel.

3. Hydrogen storage methods for mobile application

Hydrogen storage means the reduction of an enormous volume of hydrogen gas. The aim of hydrogen storage is to pack hydrogen as close as possible, i.e. to reach the highest volumetric density by using as little additional material as possible. For on-board energy storage, vehicles need compact, light, safe and affordable containment. Fig. 3.1 shows a comparison of the volume of 4kg of hydrogen, which is required for ~400km travel range for a modern electric car powered by a fuel cell, compacted in different ways with the size relative to the size of a car. As shown in Fig. 3.1, storage of hydrogen is a critical challenge in mobile application.

Fig. 3.1 Volume of 4kg of hydrogen compacted in different ways, with size relative to the size of a car [13].

There are basically three methods to store hydrogen reversibly including high pressure gas cylinders, liquid hydrogen in cryogenic tanks and absorption of hydrogen in host metals/intermetallics (Table 3.1) [6,13].

Table 3.1 Comparison of the major hydrogen storage methods [6,13].

Storage system	Volumetric density (kg H_2 m^{-3})	Temperature (^oC)	Pressure (bar)	Drawbacks
Compressed hydrogen gas	~40	RT*	800	Safety problems (enormous pressures required)
Liquid hydrogen at cryogenic tank	~71	-252	1	Large thermal losses (boil-off of hydrogen)
Solid metal/intermetallic hydrides	~80-150	RT*	1	None of above two

***RT: room temperature**

Storing hydrogen in gas form is the simplest way. The common high pressure gas cylinders are available at a hydrogen pressure of 20MPa [6]. With the newly developed light weight composite cylinders which support pressure up to 80 MPa, the hydrogen volumetric density can reach ~40 kg m^{-3} [6]. However, the concern in respect to use of the pressurized cylinders is a problem in the regions with high population. The cost of compression together with the low hydrogen density and the safety of high pressure gas cylinder are important drawbacks for this simple storage method [3,6].

Liquid hydrogen is stored in cryogenic tanks at -252^{o}C and ambient pressure. The volumetric density of liquid hydrogen is ~71 kg m^{-3} [6]. There are two major problems needed to be solved for this method: the efficiency of the liquefaction process and the boil-off of hydrogen. The empirical work needed to liquefy hydrogen gas of room temperature is ~15.2kWh/kg, which is almost half of the lower heating value of hydrogen [6]. Due to the low critical temperature of hydrogen (-241^{o}C [6], above this temperature hydrogen is gaseous), liquid hydrogen can only be stored in open systems to prevent strong overpressure. Gasification of liquid hydrogen inside the cryogenic tank is an inevitable loss even with a perfect insulation system. The relatively high energy required

for liquefaction and the continuous boil-off of hydrogen might hinder this method to be accepted commercially [13-15].

Some metals, intermetallic compounds and alloys absorb hydrogen and form solid metal-hydrogen compounds. Hydrides exist as ionic, covalent, metallic and complex hydrides [18,19]. The highest volumetric densities of hydrogen are found in solid hydrides (~80-150 kg m^{-3}) [6]. High gravimetric densities can be achieved by utilizing light-metal compounds based on Li, Na, Mg, B and Al. The detail will be discussed in Chapter 4.

4. Solid state hydrides

An extremely important aspect associated with the synthesis of hydrides by CRMA/CRMM (Ball milling process which will be discussed in Chapter 6) is the entire concept of automotive refueling station. A conventional approach is to replicate exactly the same architecture of refueling as we have known for almost a century for a standard and obviously, well-proven, gasoline station (Fig.4.1). In brief, gaseous hydrogen is supposed to be carried out to the station and for each fuel cell powered vehicle one would directly pump hydrogen gas into a cylinder or recharge on-board some reversible solid state hydrides contained in a canister if such were to be used (Fig.4.1).

Fig. 4.1 A conventional vision of hydrogen refueling station [18].

If reversible solid state hydrides were to be used and recharged on-board by gaseous hydrogen at the station there would be an immense problem to remove the exothermic heat of hydriding at the charging rate of 1.5 kgH_2/min, which is the 2010 target for

FreedomCar program [19]. This would require very substantial and costly heat-exchangers which would seem to practically eliminate any concept of on-board hydride recharging [19].

Instead of gaseous hydrogen, liquid hydrogen can also be used. Distribution of liquid hydrogen in special-tank cars is now well established. However, boil-off is still a major problem, which will amount to huge hydrogen losses if used in mass transportation.

The question however arises if approaches to refueling of fuel cell vehicle would, indeed, make much sense for the implementation of the hydrogen economy. At least the aforementioned major factors have to be solved.

In view of the above problems, an alternative vision of hydrogen refueling station is proposed for fuel cell powered vehicles which in its essence is just a retail station for recyclable hydride containers/cartridges as schematically shown in Fig.4.2 [22]. This concept is directly associated with the commercialization of reactive mechanical alloying/milling. In the ball milling plant the hydrides are being manufactured and simultaneously filled up into containers/canisters and delivered to the retail station. Empty container is removed from the vehicle and exchanged for the full one. The empty containers collected at the station are then delivered to the hydride production plant and the cycle is repeated again and again. A modification of the scheme could be that the synthesized hydride powder could be directly delivered to the retail station and filled up into canister on the spot.

The vision for the future of solid state hydrides [22] is that widespread commercialization of manufacturing hydrides in an external plant (e.g. by reactive mechanical alloying/milling under hydrogen) could essentially eliminate the requirement

of costly hydrogen infrastructure at the refueling stations for automobiles powered by fuel cells or hydrogen internal combustion engines (Fig. 4.2)

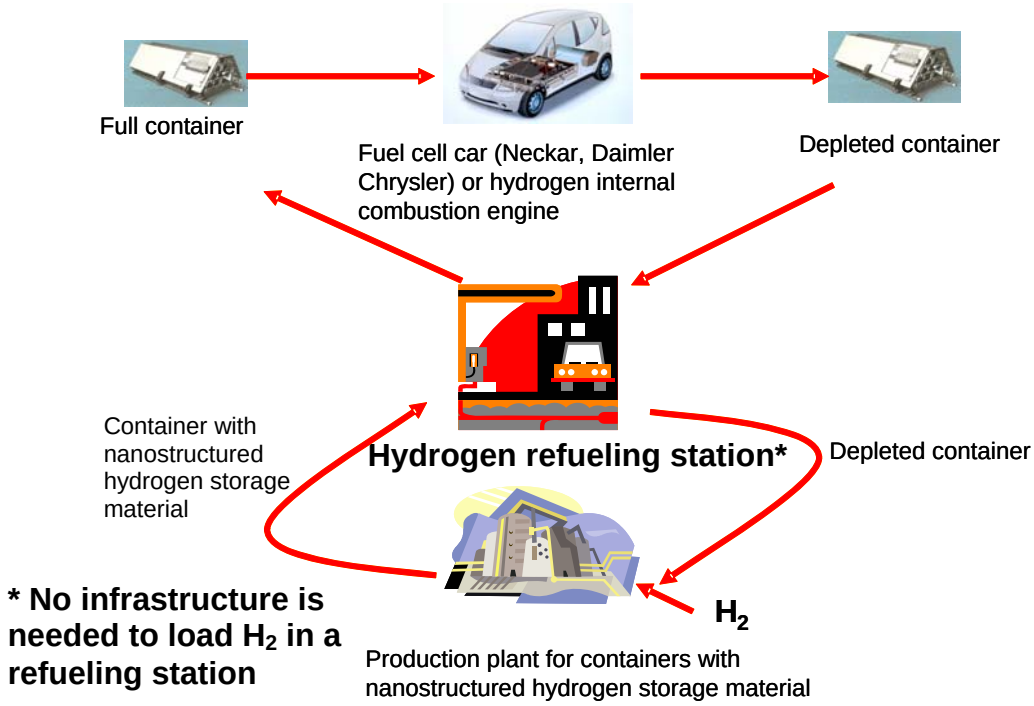

Fig. 4.2 A novel vision of refueling/retail station for fuel cell powered vehicles based on the concept of the synthesis of nanostructured hydrogen storage materials. Adopted from [22].

4.1 Fundamental characteristics of solid state hydrides

Hydrogen-metal system can be generalized to some degree, although numerous deviations and exceptions to those generalizations can be found. Metal hydrides as candidates for storage applications can be formed reversibly by direct interaction of metals or intermetallics with hydrogen at proper temperature and pressure according to the general reaction [23]:

$$M + \frac{x}{2} H_2 \leftrightarrow MH_x + \Delta Q \tag{3.1}$$

The general mechanism of the absorption of hydrogen gas by a metal using a simplified model is shown in Fig. 4.3. As H_2 molecule approaching the surface of a metal, it is first weakly physisorbed on the interface. After this, the molecule is dissociated and then chemisorbed as strongly bounded, individual H-atoms. H-atoms are light and small so that they can quickly diffuse away from the surface into periodic sites (often interstitial) in the crystal lattice. Once in the crystal lattice, H-atoms can take the form of a random solid solution or an ordered hydride phase if the local hydrogen concentration exceeds a certain limit.

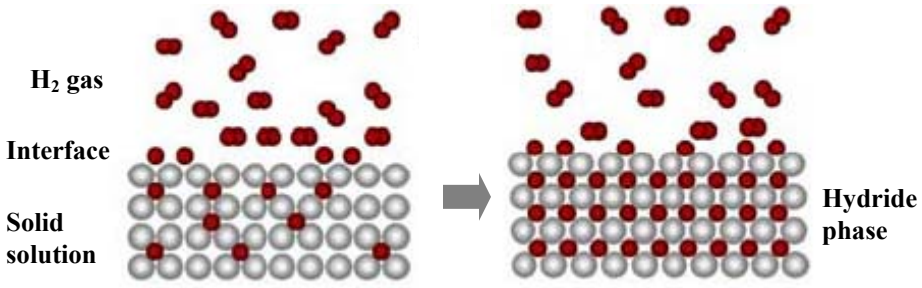

Fig. 4.3 A general mechanism of hydrogen absorption in metals [4].

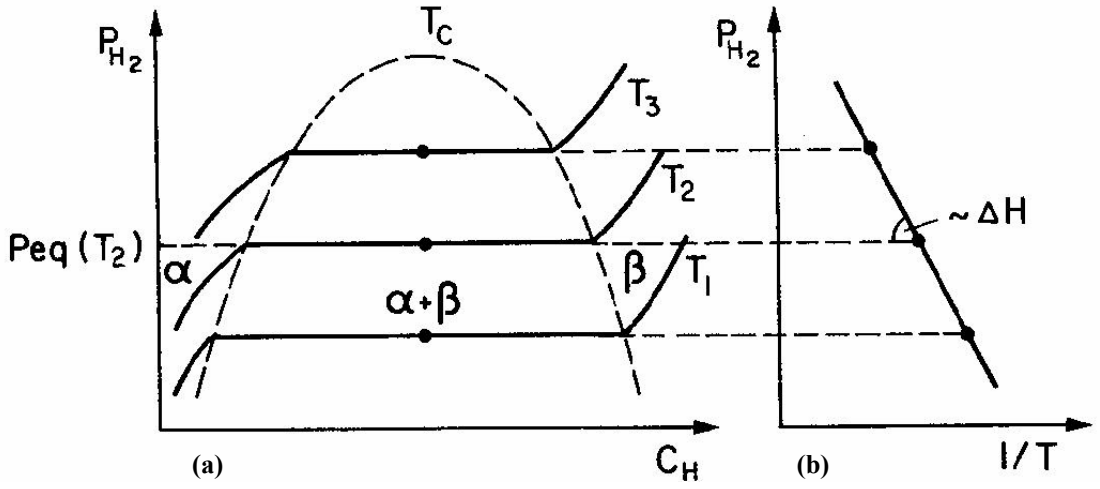

Fig. 4.4 (a) Idealized pressure-composition temperature (PCT) curve and (b) Van't Hoff plot [23].

The thermodynamic aspects of the hydride formation from gaseous hydrogen can be described by pressure-composition temperature (PCT) curves, which is also called pressure-composition isotherm (PCI). An idealized PCT curve is shown in Fig 4.4a. As discussed previously, H_2 molecule will dissociate on the surface of the metal according to the dissociative chemisorption reaction $H_2 \rightarrow 2H$ and then H atoms will diffuse into the metal lattice to form a solid solution (α-phase). As the concentration of dissolved H is increased, at some pressure or composition, nucleation and growth of the ordered hydride phase β start. While the two phases, α and β coexist, the isotherms show a plateau, the length of which determines the amount of hydrogen that can be stored reversibly with small pressure variations. As the plateau is traversed by adding more and more hydrogen, the β phase grows as the expense of the α phase. In the pure β phase, hydrogen pressure rises steeply with the concentration. The two phase region ends in a critical point T_c. The dotted line in Fig 4.4a defines the limit of the two-phase coexistence region on a PCT phase diagram. As temperature increases plateau width decreases and the plateau pressure

increases. In effect, the solubility of hydrogen in the α phase increases and the hydrogen content in β phase decreases.

The plateau pressure P_{eq} strongly depends on temperature. The equilibrium pressure P_{eq} as a function of temperature is related to the changes ΔH and ΔS of enthalpy and entropy, respectively, by the Van't Hoff equation [23]:

$$\ln P_{eq} = \frac{\Delta H}{RT} - \frac{\Delta S}{R} \tag{3.2}$$

As shown in Fig. 4.4b, a plot of ln P_{eq} vs. 1/T tends to be a straight line with the slope equal to ΔH and intercept (1/T=0) equal to ΔS. The knowledge of enthalpy change is important to the heat management required for hydride storage devices and is also a measure of the strength of the M-H chemical bond [4,23]. The entropy term corresponds mostly to the change from molecular hydrogen gas to dissolved solid hydrogen. It is approximately equal to the standard entropy of hydrogen ($-130 Jk^{-1}mol^{-1}$) for all of the metal hydrogen systems [4]. The Van't Hoff plot is a convenient way to graphically represent hydride thermal stability, especially to compare different solid state hydrogen storage systems.

4.2 Requirements for solid state hydrogen storage for fuel cells on vehicles

Fuel cell is an electrochemical energy conversion device. A fuel cell converts the hydrogen and oxygen into water, and in the process it produces electricity. Several kinds of fuel cells with a wide variety of operating temperatures and pressures are available. Among them, the proton exchange membrane (PEM) fuel cell is one of the most promising technologies, which can be use to power vehicles. A single fuel cell consists of

an electrolyte and two electrodes (an anode and a cathode) (Fig. 4.5). Hydrogen gas (H_2) enters the fuel cell on the anode side and it splits into two H^+ ions and two electrons (e^-). The electrons are conducted through the anode, where they make their way through the external circuit (doing useful work such as turning a motor) and return to the cathode side of the fuel cell. The H^+ ions go through the electrolyte and combine with oxygen and the electrons from the external circuit to form a water molecule (H_2O) at the cathode side. Chemistry of a fuel cell can be described as following:

Anode: $2H_2 \rightarrow 4H^+ + 4e^-$ (3.3a)

Cathode: $O_2 + 4H^+ + 4e^- \rightarrow 2H_2O$ (3.3b)

Overall cell reaction: $2H_2 + O_2 \rightarrow 2H_2O$ (3.3c)

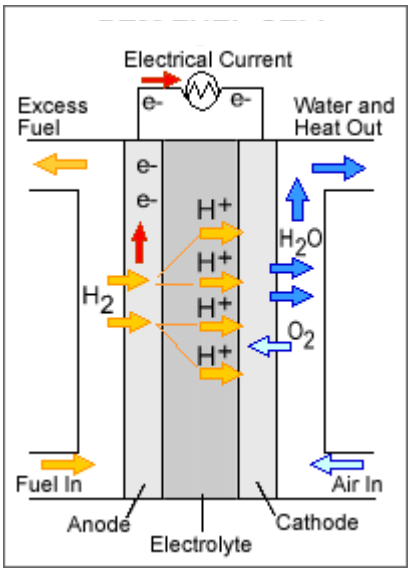

Fig. 4.5 Schematic diagram showing the operation of a fuel cell [24].

A typical coupling of a fuel cell with a hydride bed is shown schematically in Fig 4.6. In order to use the waste heat generated from fuel cell to provide the desorption enthalpy for the hydride and have the proper pressure/flow control to the fuel cell, the operating conditions for hydrides have to match those of the fuel cell. For example, the operating

conditions for hydrides used in the applications of proton exchange membrane fuel cells (PEMs) which catch the highest commercial interest, especially for the mobile applications, are aimed at 0-100°C and 1-10 atm [20,25].

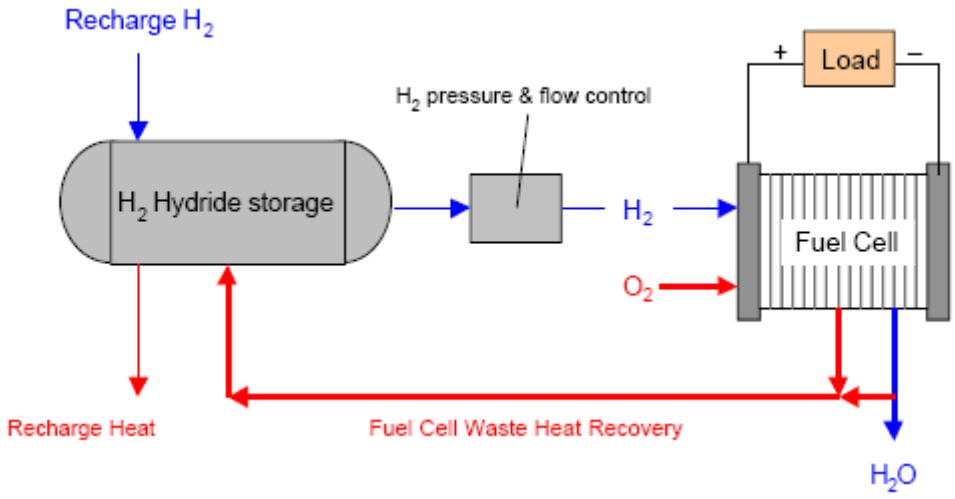

Fig. 4.6 Schematic diagram showing a fuel cell coupled with a solid state hydride device [25].

Important technical targets such as hydrogen capacity (wt.%), desorption temperature, and cycle life proposed for on-board hydrogen storage in various programs from US, Japan and International Energy Agency (IEA) are summarized in Table 4.1. The hydrogen storage gravimetric capacity requirement varies from 3 wt.% (World Energy Network (WE-NET), Japan, 2001 goal) [28] to 9 wt.% (USDOE, 2015 goal) [26].

Table 4.1 Technical targets for on-board hydrogen storage systems in various hydrogen programs [26-28].

Properties	US DOE hydrogen program	Japan WE-NET	IEA hydrogen implementing agreement
Hydrogen capacity (wt%)	9	3	5
Desorption temperature (°C)	N/A	<100	<100
Cycle life	1500	>5000	>1000

In addition to the properties such as storage capacity, operating temperature, kinetics of absorption-desorption, other important properties in respect to applications of metal hydrides to hydrogen storage include [25]: reversibility, cyclic stability, resistance to gaseous impurities, safety and low cost of alloys.

4.3 Solid state hydrides based on elements and alloys

From a hydride "family tree" of the elements, alloys and complexes (Fig. 4.7), it can be seen that besides initial pure elements for hydrogen storage, there are also alloys, intermetallic compounds (on the left side of the tree) and complexes (on the right side of the tree), which are under investigated.

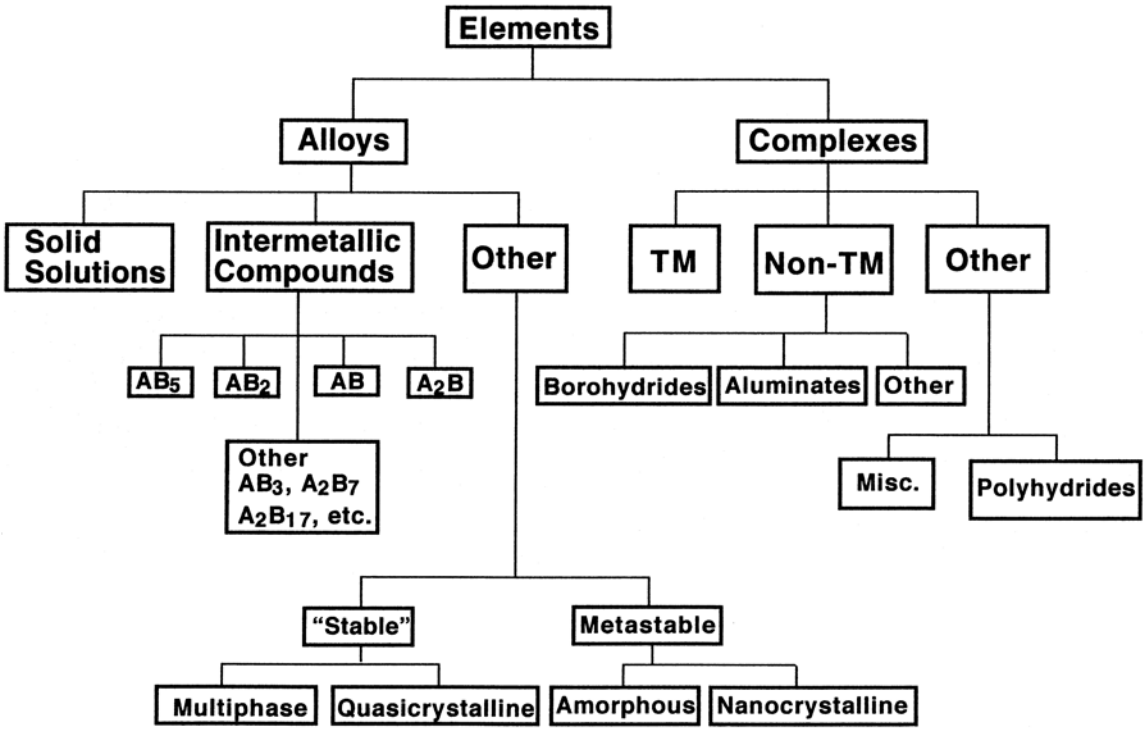

Fig. 4.7 Family tree of hydriding alloys and complexes (TM: transition metals) [20].

Most of the 91 natural elements will absorb hydrogen and form hydride under appropriate pressure and temperature. Properties of selected elemental hydrides are given in Table 4.2. Unfortunately, for elemental hydrides, only vanadium's PCT properties meet the required 1-10atm, 0-100^{o}C range for PEM fuel cell applications [20]. However, it does not store much hydrogen.

Table 4.2 Properties of selected hydrides [20,29].

Type	Metal	Hydride	Capacity (wt%)	Density (g/cm^3)	Enthalpy of formation (ΔH) (kJ/mol)	P_{eq} (atm)/T (^{o}C)
Elemental	Pd	$PdH_{0.6}$	0.7	-	-41.0	1/147
	Mg	MgH_2	7.6	1.5	-74.5	1/279
	V	VH_2	3.8	-	-40.1	2.1/25
	Ti	TiH_2	4.0	-	-164	1/643
	Zr	ZrH_2	2.2	-	-	0.1/727
	La	LaH_2	1.4	-	-208	3×10^{-29}/25
	Ni	NiH	1.7	-	-8.8	3.4×10^{3}/25
AB_5	$LaNi_5$	$LaNi_5H_7$	1.4	8.3	-30.8	1.8/25
AB_2	$TiMn_{1.5}$	$TiMn_{1.5}H_{2.5}$	1.9	6.4	-28.7	8.4/25
AB	FeTi	$FeTiH_2$	1.9	6.5	-28.1	4.1/25
Mg based	Mg_2Ni	Mg_2NiH_4	3.6	2.7	-64.5	1/255

Although not having favorite PCT properties, magnesium remains one of the attractive material for hydrogen storage because of its high hydrogen storage capacity (7.6 wt.%) and the reversible formation of MgH_2 hydride. Magnesium has other advantages such as low cost and abundance in the Earth crust [30]. The practical use of Mg is prevented by its thermodynamic problem, i.e., a high desorption temperature (>350^{o}C) at ambient pressure is required to have a kinetics for practical applications [31]. The other problem for Mg (polycrystalline) is its poor absorption and desorption kinetics. Fortunately, these problems can be largely solved by a structural refinement (nanocrystallization [32,33] or particle size refinement [34]) of hydride powders via high-energy milling in ball mills.

Recently, it has been shown that the mechanical alloying of Mg or MgH_2 with various additives gives rise to much improved hydrogen sorption kinetics [35]. Unfortunately, the operating temperature of nanocrystalline Mg or Mg based nanocomposites is still outside the range of PEM fuel cell [36]. The details of nanocrystalline materials and ball milling will be discussed in Chapter 5 and 6.

From a viewpoint of practical application, the elements allow for little versatility. In order to capitalize on practical application of reversible hydrides, it has been required to combine two or more kinds of elements, a strong hydride forming element A with a weak hydriding element B, to form alloys/intermetallic compounds that have the desired intermediate thermodynamic affinities for hydrogen which includes several prototypes such as AB_5, AB_2, and AB. The variation of the elements allows us to tailor the properties of the hydrides. Table 4.2 summarizes some well-known intermetallic compounds and their properties. Although the intermetallic compounds listed in Table 3.2 have near-ambient PCT properties and can store/release hydrogen reversibly, their rather low hydrogen storage capacity (less than 2 wt.%) hinder the practical application for fuel cell powered vehicles.

Interstitial hydrides (e.g. hydrides based on AB, AB_2, and AB_5 intermetallic compounds) which are easily reversible at the favorite PCT conditions of PEM fuel cells are limited to ~ 2 wt.% hydrogen capacity. On the other hand, hydrides such as MgH_2 and LiH, providing good gravimetric hydrogen capacity (~7-13 wt.%) [37,38], require temperatures greater than 350^oC to release hydrogen, and have slow reaction kinetics [31]. This dilemma (poor thermodynamics/kinetics vs. high storage capacity) has hampered

commercial applications of elemental and intermetallic hydrides and called for research on complex hydrides.

4.4 Complex hydrides

Complex hydrides are generally mixed ionic-covalent compounds. For example, $NaAlH_4$ consists of Na^+ cation and a covalently bonded $[AlH_4]^-$ anion. The hydrogen in the complex hydride is often located in the corners of a tetrahedron with boron or Al in the center. The negative charge of the anion, $[BH_4]^-$ and $[AlH_4]^-$, is compensated by a cation such as Na or Li. New direction in the research on materials for hydrogen storage has focused on complex hydrides because of their high volumetric and gravimetric densities [5,6,20]. So far, there are ~170 complex hydrides listed on the website hydpark.ca.sandia.gov [29].

Complex hydrides were not thought to be suitable for hydrogen storage due to the reason that they release hydrogen irreversibly at conditions outside the temperature and pressure range that is desirable for fuel-cell powered automobiles. Their hydriding and dehydriding kinetics also create significant challenges. This opinion has been changed with the breakthrough work by Bogdanovic and Schwickardi [39], who show that the addition of Ti catalyst to the complex hydride $NaAlH_4$ made it reversibly release and take up 3.7 wt.% of hydrogen under moderate temperature-pressure conditions with an enhanced hydriding kinetics. The hydride complexes of borane, the tetrahydroborates $M(BH_4)_x$ and of alane, the tetrahydroaluminates $M(AlH_4)_x$ are also interesting hydrogen storage materials. Particular interests are found in the group 1-3 light metals (e.g. Li, Mg, B and Al) which build a large variety of complex hydrides because of their light weight

and high hydrogen capacity. Table 4.3 shows the physical properties of some selected complex hydrides.

As shown in Table 4.3, it is clear that Li-B-H, Mg-B-H, Na-B-H, Mg-Al-H and Li-Al-H systems will meet the DOE FreedomCAR goal for 2015. However, all of them have fatal drawbacks: (1) high decomposition (desorption) temperature, which is much higher than ~100^{o}C tolerable by PEM fuel cell [6], and (2) slow kinetics. As a result, it is important to find a way to make these complex hydrides more reversible, especially in the low temperature desorption mode.

Table 4.3 Properties of selected complex hydrides based on light metal hydrogen system [13,21, 40-50]

Metal-hydrogen system	Hydride	Theoretical hydrogen capacity (wt.%)	Density of hydride (g/cm^3)	Enthalpy of formation (ΔH) (kJ/mol)	Decomposition temperature (^{o}C)
Li-B-H	$LiBH_4$	18.4	0.67	-190.8	380
Mg-B-H	$Mg(BH_4)_2$	14.9	0.99	N/A	300-800
Na-B-H	$NaBH_4$	10.6	1.07	-188.6	400
Li-Al-H	$LiAlH_4$	10.6	0.92	-166.3	150-175(1)
Mg-Al-H	$Mg(AlH_4)_2$	9.3	0.98 or 1.30	No unambiguous value is determined (2)	110-170(1)
Na-Al-H	$NaAlH_4$	7.4	1.27	-15.5	210

(1) Temperature range of the first stage desorption
(2) No unambiguous value is established for the enthalpy of formation of $Mg(AlH_4)_2$

4.4.1 M-Al-H (M = Na, Mg, Li and Sr) system

$NaAlH_4$ has been broadly studied to date, serving as a model system to better understand other complex hydrides. Enormous researches followed by the pioneered work by Bogdanovic and Schwickardi have focused on doped $NaAlH_4$ to investigate new methods for the doping of catalysts and to understand the fundamental of the catalyst effects as well as the hydriding mechanisms of doped alanates [37,51-61].

Table 4.4 Decomposition equations of selected complex hydrides [37,64,65,70,74].

Hydride	Equations
$NaAlH_4$	$3NaAlH_4 \rightarrow Na_3AlH_6 + 2Al + 3H_2$ (4.4a) $Na_3AlH_6 \rightarrow 3NaH + Al + 3/2H_2$ (4.4b) $NaH \rightarrow Na + 1/2H_2$ (4.4c)
$LiAlH_4$	$3LiAlH_4 \rightarrow Li_3AlH_6 + 2Al + 3H_2$ (4.5a) $Li_3AlH_6 \rightarrow 3LiH + Al + 3/2H_2$ (4.5b) $3LiH + 3Al \rightarrow 3LiAl + 3/2H_2$ (4.5c)
$SrAlH_7$	$2Sr_2AlH_7 \rightarrow 4SrH_2 + 2Al + 3H_2$ (4.6)
$Mg(AlH_4)_2$	Two-step decomposition. Decomposition reactions will be discussed in Sec. 9.3
$LiBH_4$ (catalyzed with SiO_2)	$LiBH_4 \rightarrow LiBH_{4-\varepsilon} + \varepsilon/2H_2$ (4.7a) $LiBH_{4-\varepsilon} \rightarrow LiBH_2 + (1-\varepsilon/2)H_2$ (4.7b) $LiBH_2 \rightarrow LiH + B + 1/2H_2$ (4.7c)
$Zn(BH_4)_2$	$Zn(BH_4)_2$ (solid) $\rightarrow Zn(BH_4)_2$ (liquid) (4.8a) $Zn(BH_4)_2$ (solid or liquid) $\rightarrow Zn + B_2H_6 + H_2$ (4.8b)
$Mg(BH_4)_2$	$Mg(BH_4)_2 \rightarrow MgH_2 + B + H_2$ (4.9)

The decomposition of $NaAlH_4$ is shown in Eq. 4.4 in Table 4.4. The decomposition of NaH (Eq. 4.4c) occurs at a much higher temperature and is not practical in use [37]. The first two-step reaction of $NaAlH_4$ produces ~5.6 wt.% of hydrogen (~3.7 wt.% for Eq. 4.4a and ~1.9 w.t% for Eq. 4.4b). However, at a temperature below 100^{o}C the maximum reversible capacity has been shown to be about ~3 wt.% only, which is far short for the DOE requirement [36]. As a result, numerous studies have been reported for other complex hydride systems having higher theoretical hydrogen capacities. The main question which remains to be addressed is: Will Ti and other catalysts, which work for $NaAlH_4$ make other complex hydrides reversible?

Lithium alanate, $LiAlH_4$ (theoretical 10.6 wt.% H_2) is desorbed in a three-step decomposition reaction in the range of 150-175^{o}C (Eq. 4.5a), 180-220^{o}C (Eq. 4.5b) and 400^{o}C (Eq. 4.5c) [73]. The last step of decomposition occurs at 400^{o}C and is not practical for the purpose of hydrogen storage. Ball milling of $LiAlH_4$ with Ti- and V- based

addictives reduces decomposition temperature by 50-60^{o}C. However, partial decomposition of $LiAlH_4$ occurs during milling process [43].

Zhang and Akiba [74] reported the synthesis of $SrAlH_7$ hydride by ball milling followed by hydrogenation. Sr_2AlH_7 is synthesized by ball milling of the $SrAl_2$ alloy (induction melting of Sr and Al) under hydrogen (600kPa) at 150rpm for 10h followed by hydrogenation (samples in powder form) or sintering (samples pressed into a pellet) at 260^{o}C for 2 days. The milled product consisting of SrH_2 and Al reacts with hydrogen to form Sr_2AlH_7, which can be expressed as:

$$4SrH_2+2Al+3H_2 \rightarrow 2Sr_2AlH_7 \quad (4.10)$$

The authors also reported that Sr_2AlH_7 prepared by hydrogenation of $SrAl_2$ reversibly dehydrogenated and hydrogenated in a Sieverts type apparatus without a catalyst at 270^{o}C (Eq. 4.6) (theoretically, 1.4 wt.% H_2 is released).

Magnesium alanate, $Mg(AlH_4)_2$, was first synthesized in 1950 by Wiberg and Bauer [75]. It contains 9.3 wt.% of hydrogen and decomposes readily below 200^{o}C. Claudy et al. [44] reported the XRD pattern of $Mg(AlH_4)_2$. However, no crystallographic data was given. Fichtner et al. [76,77] synthesized $Mg(AlH_4)_2$ using a metathesis reaction of magnesium chloride and sodium alanate followed by purification. According to their structural analysis, the structure of $Mg(AlH_4)_2$ resembles that of CdI_2, with the cadmium atoms replaced by Mg and the iodine atoms replaced by AlH_4 groups. Dymova et al. [49,50] reported the mechano-chemical activation synthesis of $Mg(AlH_4)_2$ by ball milling of MgH_2 and AlH_3 as well as MgH_2 and $AlCl_3$. Recently, Bogdanović et al [46], Weidenthaler et al. [47] and Cho et al. [48] reported the preparation of $Mg(AlH_4)_2$ using mechano-chemical activation synthesis by ball milling of $MgCl_2$ with $NaAlH_4$ or $LiAlH_4$.

Kinetic properties were reported by Fichtner et al. [76]. Equilibrium desorption pressure of $Mg(AlH_4)_2$ was in the range between 88 and 130 bar at the temperature range between 75 and 95^oC, which coincides with the working temperature range of a PEM fuel cell. The kinetics of the decomposition of $Mg(AlH_4)_2$ was very slow at these temperatures. Measurements took several days to weeks. $Mg(AlH_4)_2$ decomposes in a two-step reaction [44-50]. The details of decomposition reactions will be discussed in Sec. 9.3.

4.4.2 M-B-H (M = Mg, Li, Na and Zn) system

Many complex metal hydrides contain great amounts of hydrogen, e.g., up to 14.9 wt.% H_2 in $Mg(BH_4)_2$ and 18.2 wt.% H_2 in $LiBH_4$, respectively. These hydrides have the potential to meet the FreedomCAR goals, especially the goal for 2015 (9 wt.% H_2). Goerrig [62] reported direct synthesis of tetrahydroborides from the metal, boron and hydrogen at 350-1000^oC and 30-500atm H_2 using the following reaction:

$$M + B + 2H_2 \rightarrow MBH_4 \quad (4.11)$$

where M = Li, Na, K, Mg and Ba

Stasinevich and Egorenko [63] investigated thermal behaviors of alkali metal and magnesium tetrahydroborides at pressure up to 10 atm. Thermal decomposition of tetrahydroborides can proceed in one of the following directions:

$$MBH_4 \rightarrow M + B + 2H_2 \quad (4.12)$$

$$MBH_4 \rightarrow MH + B + 3/2H_2 \quad (4.13)$$

Recently, Ritter et al. [5] reviewed the research concerning complex metal hydrides and found that only a paucity of the complex hydrides are currently being studied, essentially those that are commercially available (e.g., $LiBH_4$ and $NaAlH_4$). $LiBH_4$ and $NaBH_4$ are well-known reducing agents [64,65]. Recently they have attracted more attention as a

hydrogen storage material due to their high hydrogen storage capacity. Züttel et al. [66,67] reported a structural transition at 108°C (Eq. 4.7a) and a two-step hydrogen desorption (13.5 wt.% H_2) starting at approximately 200°C when SiO_2 powder was added to the $LiBH_4$ (Eq. 4.7b and 4.7c). It was also found that the hydrogen desorption temperature is lowered by about 50°C by the partial cation substitution of Li by Mg in $LiBH_4$ [68]. However, the reversibility is still a problem to be solved.

Li et al. [69] reported the synthesis of $NaBH_4$ by a mechano-chemical activation of MgH_2 with NaB_4O_7 through ball milling at room temperature. Hydrogen generation from hydrolysis of $NaBH_4$ solution with a catalyst (e.g., Ni_xB, x = 1.5-5 and Pt-TiO_2) are being studied widely [70,71].

Jeon and Cho [72] synthesized $Zn(BH_4)_2$ (theoretical 8.5 wt.% H_2) by a mechano-chemical activation, which is a dry milling process of a mixture of $NaBH_4$ and $ZnCl_2$ powders. The thermal stability of $Zn(BH_4)_2$ with the presence of inert by-product NaCl studied by DSC shows two endothermic peaks in the 85-140°C range. $Zn(BH_4)_2$ melts at ~85°C and starts to decompose almost at the same time producing diborane B_2H_6 and hydrogen gas (Eq.4.8). It has to be pointed out that a considerable amount of free Zn was observed in the XRD pattern of the stored powder which was sealed in a vial inside a glove box for one week at room temperature. This indicates that $Zn(BH_4)_2$ is unstable even at room temperature and might not be suitable for hydrogen storage for on-board applications.

Although having a great capacity for hydrogen storage (theoretical 14.9 wt.% H_2) and low density (0.99 g/cm^3) [41], which are excellent for the on-board storage, little is known about the complex hydride, $Mg(BH_4)_2$. Magnesium boron hydride exists in two

crystalline forms: low-temperature α-$Mg(BH_4)_2$ (ICDD PDF file 26-1212) has a tetragonal lattice (a = 1.359nm, c = 1.651nm), while high-temperature β-$Mg(BH_4)_2$ (ICDD PDF file 26-1213) has a face-centered cubic lattice (a = 1.55nm). The tetragonal-to-cubic transformation temperature is ~186^oC [41]. PDF files for α- and β-$Mg(BH_4)_2$ are given in Table B.9 and B.10. Konoplev and Bakulina [41] synthesized $Mg(BH_4)_2$ using a metathesis reaction of anhydrous magnesium chloride and sodium borohydride in diethyl ether, in which cations and anions exchange partners. The authors also studied the thermal behavior of $Mg(BH_4)_2$. Four endothermic events in the intervals 182-186, 304-314, 375 and 402-406^oC were recorded while heating to 800^oC. The first event, not associated with gas evolution, relates to the tetragonal-to-cubic transformation. The event at 304-314^oC was due to melting with simultaneous decomposition and the formation of magnesium hydride. The decomposition of magnesium hydride is observed at 402-406^oC. The nature of the event at 375 ^oC is not clear. About 75% of the theoretical amount of hydrogen, contained in $Mg(BH_4)_2$, is evolved when heating up to 800^oC.

5. Nanocrystalline materials

Nanocrystalline materials are single-phase or multi-phase polycrystals with the grain sizes from a few nanometers to ~100 nm in at least one dimension [78-81]. Nanocrystalline materials can be classified into four categories according to the nanostructure dimensionality [81]. They can be basically zero-dimensional atom clusters and cluster assemblies, one- and two-dimensionally modulated multilayers, and three-dimensional equiaxed nanostructure crystallites (Fig. 5.1). Recently, researches have concentrated on the three-dimensional nanocrystalline materials, which are expected to find applications based on their improved mechanical, magnetic, and other properties. In a powder form, nanostructured/nanocomposite means that each phase present in the individual powder particle is in the form of grains with nanometer size. One particle is one nano-polycrystal.

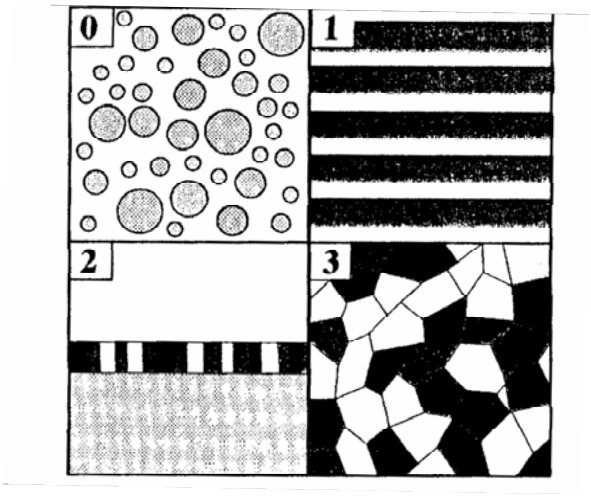

Fig. 5.1 Schematic classification of the four types (zero, one, two and three dimension) of nanocrystalline materials [81].

A schematic representation of a hard sphere model of an equiaxed nanostructured material formed by only one kind of atoms is showed in Fig. 5.2. Two types of atoms can be distinguished: the crystallites (atoms represented by open circles) and the boundary regions/intercrystalline regions (dark circles). The atomic structure of all crystallites is identical. The only difference between them is their crystallographic orientation. In the boundaries regions, the average atomic density, interatomic spacing and the coordination between nearest neighbour atoms deviates from the ones in the crystallites and differs from region to region. The presence of these two structural constituents (crystallites and boundaries) of comparable volume fractions and with typical crystal sizes of a few nanometers is crucial for the properties of nanocrystalline materials [78-81].

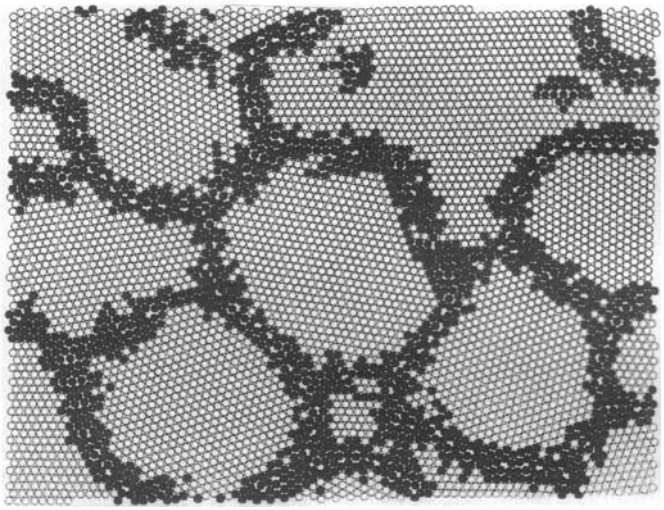

Fig. 5.2 Schematic representation of an equiaxed nanocrystalline material distinguishing between crystallite (open circles) and inter-crystalline regions (dark circles) [80].

Many of the physical and mechanical properties of nanocrystalline solids such as thermal expansion, elastic constants, fracture stress and ductility are widely different from those of the same material with conventional grain sizes. This is a direct consequence of the fraction of atoms in intercrystalline positions being significant.

Consequently, interface structures in these materials are bound to play a major role in material properties. Once the crystal size and boundary dimensions become comparable with certain length scales new physical effects are to be expected. Interesting question to ask is: Will nanocrystallization affect properties of solid state hydrides?

Nanostructure addresses one of the key issues of hydrogen sorption kinetics: the diffusion of hydrogen within the metal leading to the formation of the hydride. Numerous experiments indicate that in practically all metal hydrides, the kinetics of both absorption and desorption can be improved by reducing the grain size of the compound [53,54]. An example for the improvement of absorption is shown in Fig. 5.3a for Mg_2Ni. It can be seen that the polycrystalline sample does not exhibit any significant hydrogen absorption at 200^{o}C, whereas the nanocrystalline sample absorbs hydrogen relatively quickly. Fig. 5.3b shows an example of the enhancement in hydrogen desorption for Mg_2NiH_4. A reduction in desorption temperature is found as the grain size of the hydride is brought to nanoscale.

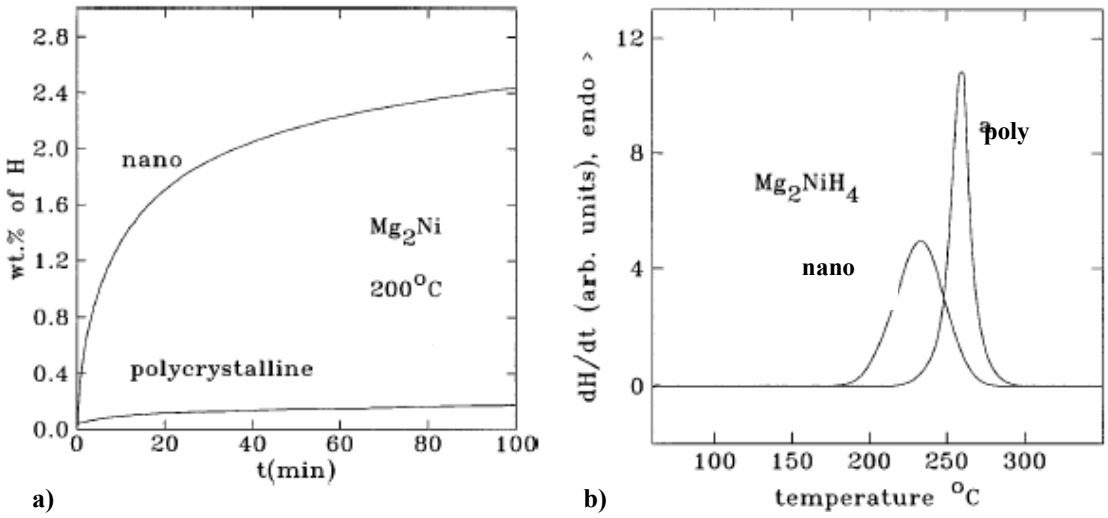

Fig. 5.3 Effect of nanocrystallization of (a) hydrogen absorption and (b) desorption temperature of hydrogen [32].

It must, however, be made clear that what is usually meant in the literature by formation of nanostructure is essentially a development of nanosized grains (crystallites) within individual hydride powder particles which otherwise could have micrometric sizes. The development of nanograins occurs during hydride powder processing by mechanical (ball) milling which is the principal mechanical process used to induce nanostructure. The effects of particle size are usually either totally neglected or treated very marginally in the considerations regarding improvement of hydrogen storage properties. However, in the mechanical (ball) milling process there is always a concomitant reduction of the powder particle size which accompanies the reduction of grain size of the phases residing within the particles. Therefore, a very fundamental question arises as to what factor is primarily responsible for the improvement of hydrogen storage properties and in particular for the reduction of hydrogen desorption temperature: the size of nanograins or the mean size of hydride particle? So far, this problem has never been tackled in a quantitative manner in which the influence of both parameters (nanograin and nanoparticle size) could be formally separated to show a relative importance of each of them. Only very recently, it has been reported that the mean particle size of MgH_2 hydride either commercial processed by mechanical milling or synthesized by reactive mechanical milling of pure Mg under hydrogen has profound effect on its hydrogen desorption temperature as measured by differential scanning calorimetry (DSC) [82,83]. It has been found that up to a certain critical (threshold) size range of the MgH_2 powder particle the DSC desorption temperature decreases only slightly with decreasing particle size. However, below this critical threshold size the DSC desorption temperature starts decreasing quite rapidly with decreasing of the mean hydride powder particle size. In

addition, a quantitative evidence shows that two factors such as refined powder particle size and the γ-MgH_2 phase residing within the powder particles, acting additively, are responsible for a substantial reduction of hydrogen desorption temperature of MgH_2 hydride. In contrast, the nanograin (crystallite) size of MgH_2 did not seem to have apparent effect on DSC desorption temperature strongly suggesting that for desorption temperature the hydride grain size seems to be of secondary importance. These two factors should be carefully assessed against other hydrides. In conclusion, it is apparent that nanostructured materials have properties markedly different from their conventional crystalline counterparts and are promising candidates for hydrogen storage in solid state hydrides.

6. Ball milling techniques for manufacturing nanohydrides

Ball milling is a solid state powder processing technique. Starting materials, usually powder mixtures, are placed in a ball mill and subjected to intense mechanical deformation by collision of balls. During milling the powder particles are repeatedly flattened, cold welded, fractured and rewelded. The technique was originally developed to produce oxide-dispersion strengthened nickel- and iron-base alloys for applications in the aerospace industry in 1966 [84]. It has been shown that ball milling is capable of synthesizing a variety of equilibrium and non-equilibrium alloy phases starting from blended elemental or prealloyed powders [84-86]. Recent advances in several ball milling processes including mechanical alloying (MA), mechanical milling (MM), reactive mechanical alloying (RMA)/mechanochemical synthesis (MCS) and mechanochemical activation synthesis (MCAS) have been widely reviewed [84-88]. The details of these major milling processes, which differ from each other for starting materials and milling atmospheres, will be discussed in section 6.2.

6.1 The process and process variables of ball milling

A ball mill apparatus usually consists of a container placed in a rotating or vibrating frame. For example, in mechanical alloying (MA), the process starts with loading mixture of powders inside the mill along with the grinding medium (e.g. steel balls). The mixture is then milled for certain length of time until the composition of every powder particle is the same (a steady state is reached), an alloy is formed or certain property of the material

is obtained. The important components of the ball milling process are the ball mill, and process variables.

Different types of ball mills are used to produce mechanically alloyed powders. They differ in their capacity, efficiency of milling and arrangements of heating and cooling [84-86]. In conventional ball mills (planetary or shakers), the trajectories of grinding balls are rather chaotic (Fig. 6.1). This creates a continuous and erratic change of various mechanical modes of milling from shearing to impact during the same milling cycle. However, in the magneto-mill, Uni-Ball-Mill Model 5, the trajectories of the balls are controlled by the magnetic field created by strong FeNdB permanent magnets (Fig. 6.2). The milling mode can be then adjusted from shearing to impact by changing the angular position of the external magnets, as it is shown in Fig. 6.2.

Ball milling is a complex process which involves optimization of milling parameters to achieve the desired product microstructure and properties. The important parameters are:

(1) Milling mode

(2) Number of balls used for milling

(3) Milling speed

(4) Milling time

(5) Milling atmosphere

(6) Ball-to-powder-ratio

(7) Working distance (WD)

The above process variables are not completely independent. For example, in Uni-Ball-Mill, the milling mode depends on milling speed and working distance. Also, milling time depends on milling mode and ball-to-powder-ratio.

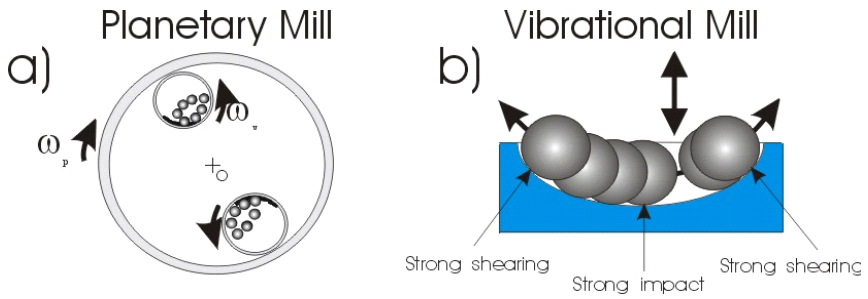

Fig. 6.1 Schematic of (a) planetary and (b) vibrational mill [89].

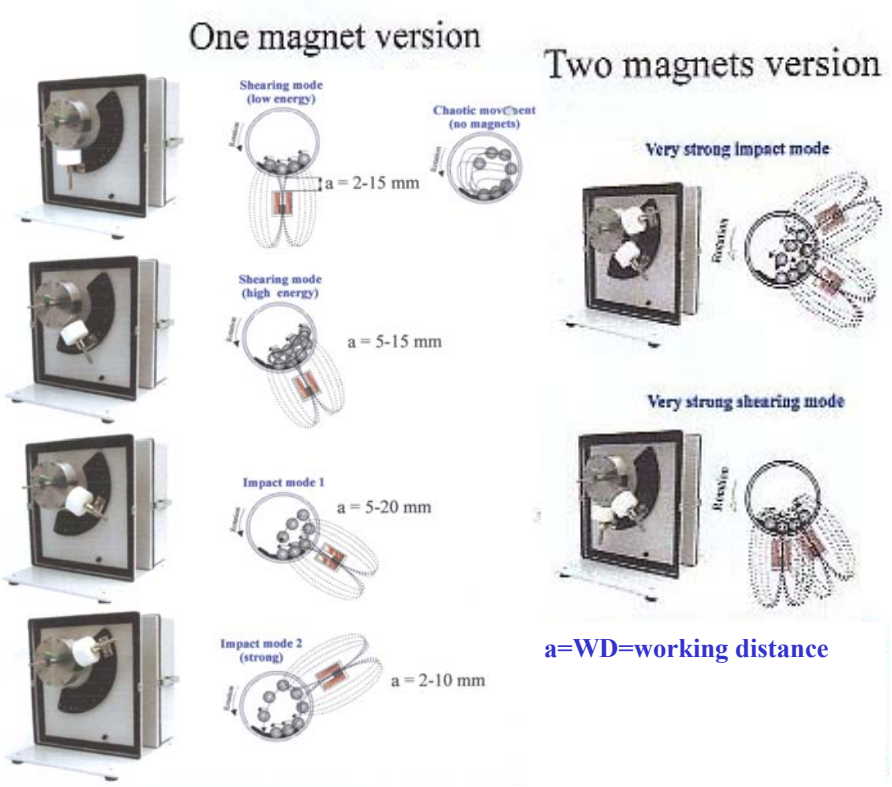

Fig. 6.2 Various controlled modes of milling available in the Uni-Ball-Mill 5 [90].

6.2 Ball milling on nanostructured hydrides

Processes of manufacturing of nanostructured hydrides by ball milling are shown in Fig. 6.3. Conventionally, materials for hydrogen storage have been prepared by arc melting and annealing and subsequent pulverization. Suitable nanostructured hydrides can be fabricated by non-equilibrium processing techniques such as ball milling from at least two types of elemental powders in a process called mechanical alloying (MA).

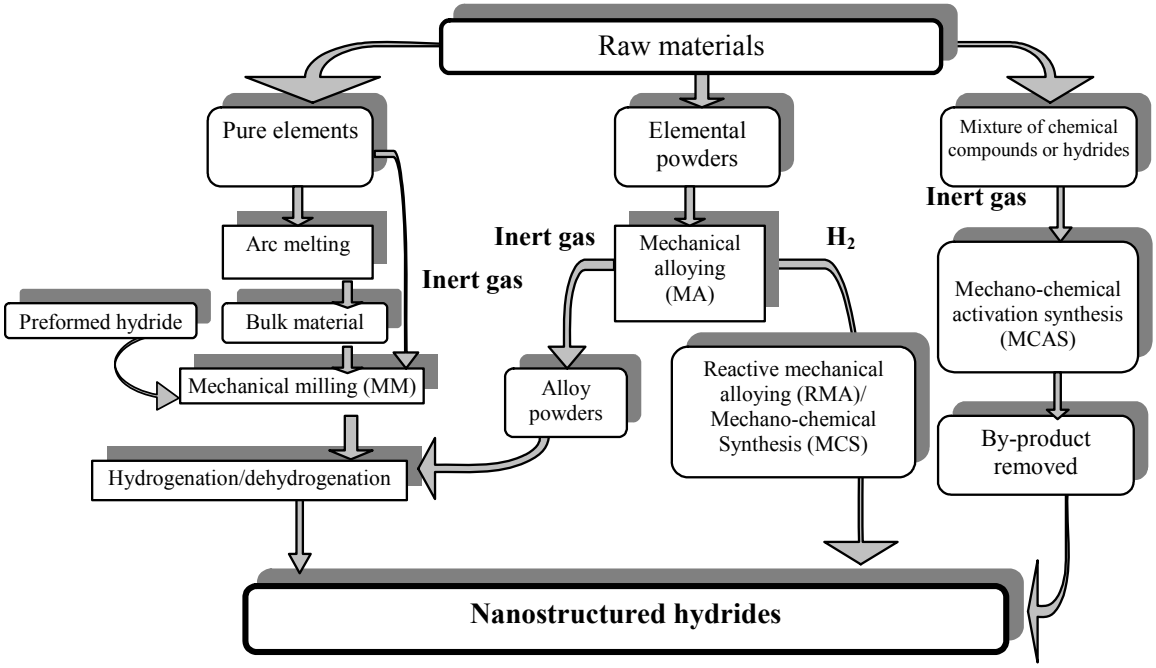

Fig. 6.3 Flow chart showing the possible routes of manufacturing of nanostructured hydrides. Adopted from Ref. [91].

Alternatively, they can be obtained from pre-alloyed polycrystalline bulk alloys in a mechanical milling (MM) process. The MA and MM are conducted under a protective atmosphere (Ar or He). The manufactured nanostructured alloy powders undergo subsequent hydrogenation by exposure to gaseous hydrogen at elevated temperatures. Mechano-chemical activation synthesis (MCAS) of a mixture of compounds has been used to produce oxides and oxide compounds [85, 86]. Recently, it has been found that

MCAS can also be used to synthesize nanostructured hydrides by milling a mixture of chemical compounds (e.g. $MgCl_2$) and hydrides (e.g. $NaAlH_4$) [44-48], which would normally be produced in wet metathesis reactions. However, unlike the processes in MM or MA, the synthesized hydrides have to be separated from the reaction by-products after MCAS.

For sake of cost reduction, and for ease of the hydride formation, a more attractive process is such in which nanostructured hydrides can be formed in a single step. This process involves milling of elemental powders directly under hydrogen and is referred to as reactive mechanical alloying (RMA)/mechanochemical synthesis (MCS) or reactive mechanical milling (RMM).

In the specially designed Uni-Ball Mill 5, if hydrogen atmosphere is used, RMA is referred to as controlled reactive mechanical alloying (CRMA) which is based on a mechano-chemical synthesis of the metallic elements and hydrogen into a hydride phase. Through CRMA, it is possible to study the effect of milling mode on the hydride structure and properties.

7. Experimental

7.1 Milling procedure

Syntheses of nanostructured hydrides were implemented by controlled reactive mechanical alloying (CRMA) of the mixtures of pure elemental powders as well as compounds in the magneto-mill, Uni-Ball-Mill 5 apparatus (Fig. 6.2). The milling modes in the Uni-Ball-Mill 5 can be adjusted from shearing to impact by changing the angular position of strong NdFeB external magnets. The magnitude of the magnetic pulling force exerted on the balls can be adjusted by changing the distance (working distance, WD) between the magnets and the milling vial (Fig. A.1e).

In the present work, milling modes from high-energy shearing (HES) to impact with 2 magnets (IMP710 and IMP68) as well as milling variables such as the ball-to-powder weight ratio (BPWR), number of balls, working distance (WD), milling time, rotation speed and hydrogen pressure were adjusted. The positions of magnets for different milling modes are shown in Fig. A.1a-1d and A.2. The composition of powders and the processing parameters applied during controlled milling are summarized in Table 7.1-7.3.

Milling vial was always evacuated and purged several times with argon gas before the final fill up with either argon or hydrogen. The procedure of loading hydrogen into milling vials is given in Appendix A.2. The purity of the helium, argon and hydrogen gases is 99.999% (H.P. 5.0). During milling under hydrogen atmosphere, the vials were systematically refilled with hydrogen in order to keep the constant hydrogen pressure. Pressure drops during milling were recorded to estimate the amount of absorbed hydrogen. A volumetric method was used to calculate the amount of hydrogen absorbed

during milling. The details of calculation are given in Appendix A.3 and A.4. The accuracy of hydrogen capacity measured by the volumetric method is about ±0.4wt.% H_2.

Small amount of samples of the milled powder were collected at various stages during the milling for XRD analysis, thermal analysis and microstructural examination. This kind of sample will be referred to as subjected to sequential milling. On the other hand, samples milled continuously without extraction during milling will be referred to as subjected to continuous milling. All of the powder handlings were performed in a purged glove bag under argon.

The compositions of powder mixtures milled in the present work and the details of milling parameters are summarized in Table 7.1-7.3. In Mg-H system, elemental powder of Mg (-325mesh, 99.8% purity) was milled under hydrogen atmosphere. The composition of powder and ball milling details are shown in Table 7.1. In the Mg-Al-H system, the following combinations of starting materials were used (Table 7.2):

(1) Starting materials in the stoichiometric composition Mg-2Al
   (a) Mixture of elemental Mg (-325mesh, 99.8% purity) and Al (-325mesh, purified) powders
   (b) Mixture of elemental Al powder and commercial AZ91 alloy (9.1 wt% Al, 0.69 wt% Zn, 0.33 wt% Mn and Mg-bal), the latter filed into fine chips
   (c) As-cast and powdered Mg-2Al alloy (manufactured by CANMET Material Technology Laboratory, Ottawa)
   (d) Mixture of elemental Al powder (-325mesh, purified) and commercial MgH_2 powder (98% purity)

(e) Mixture of as-cast Mg-2Al alloy and 10 wt% of elemental Fe powder after milling for 1h under argon atmosphere in SPEX ball-mill.

(2) Starting materials using a mixture of $NaAlH_4$ (90%, Sigmal-Aldrich) and $MgCl_2$ (99%, Alfa-Aesar) in a 2:1 stoichiometric ratio

In the Mg-B-H system, the following combinations of starting materials were used (Table 7.3):

(1) Starting materials in the stoichiometric composition Mg-2B

(a) Mixture of elemental Mg (-325mesh, 99.8% purity) and crystalline boron powders (purity is not given by the supplier)

(b) Mixture of elemental Mg (-325mesh, 99.8% purity) and as-received amorphous boron powders (purity is not given by the supplier)

(c) Mixture of elemental Mg (-325mesh, 99.8% purity) and oxide-free amorphous boron powders (amorphous boron annealed at 370^{o}C for 20h to remove B_2O_3)

(2) Starting materials using commercial MgB_2 powders (-325mesh, purity is not given by the supplier)

(3) Starting materials using a mixture of $NaBH_4$ (98% purity) and $MgCl_2$ (anhydrous, 99.9% purity) in a 2:1 stoichiometric ratio

Table 7.1 Composition of powders and processing parameters for controlled reactive mechanical alloying of Mg-H powders.

Powder description	Powder composition	Gas	RPM	Speed (%)	Ball to powder ratio	# of balls	WD (mm)	Mode	Milling	CRMA Time (h)
Mg1H	Mg	Hydrogen (750kPa)	100	30	40:1	2	2	HES	S	5,20,50,100,150
Mg7H	Mg	Hydrogen (880kPa)	100	30	40:1	4	2	HES	S	5,20,50,100,150
Mg6H	Mg	Hydrogen (880kPa)	100	30	40:1	4	2	HES	C	150
Mg2H	Mg	Hydrogen (700kPa)	170	55	40:1	2	2	IMP2	S	100
Mg4H	Mg	Hydrogen (880kPa)	200	60	40:1	4	2	IMP2	C	150
Mg5H	Mg	Hydrogen (880kPa)	200	60	80:1	4	2	IMP2	C	150
Mg9H	Mg	Hydrogen (880kPa)	225	70	40:1	4	2	IMP710	C	60
Mg10H	Mg	Hydrogen (880kPa)	225	70	40:1	5	2	IMP710	C	60
Mg11H	Mg	Hydrogen (880kPa)	225	70	20:1	4	2	IMP710	C	100
Mg12H	Mg	Hydrogen (880kPa)	230	75	40:1	5	2/10	IMP68	C	30
Mg13H	Mg	Hydrogen (880kPa)	230	75	100:1	5	2/10	IMP68	C	30
Mg14H	Mg	Hydrogen (880kPa)	230	75	20:1	5	2/10	IMP68	C	30

HES: high energy shearing with one magnet

IMP2: strong impact mode with one magnet

IMP710: impact mode with 2 magnets at 7 and 10 o'clock position; IMP68: milling mode with 2 magnets at 6 and 8 o'clock position

S: sequential milling

C: continuous milling

Table 7.2 Composition of powders and processing parameters for controlled reactive mechanical alloying of Mg-Al-H powders.

Powder description	Powder composition	Gas	RPM	Speed (%)	Ball to powder ratio	# of balls	WD (mm)	Mode	Milling	CRMA Time (h)
A1H	Mg-2Al	Hydrogen (870 kPa)	150	50	~40:1	4	2	IMP2	S	1,10,200, 270
A1Ar	Mg-2Al	Argon (880 kPa)	150	50	~40:1	4	2	IMP2	C	1
A2H	AZ91+Al (Mg-2Al)	Hydrogen (880 kPa)	170	55	~40:1	4	2	IMP2	S	10,50,100, 200
A3H	Cast ingot (Mg-2Al)	Hydrogen (880 kPa)	170	55	~40:1	4	2	IMP2	S	10,50,100, 200
A4H	Poly-MgH_2+Al (Mg-2Al)	Hydrogen (880 kPa)	170	55	~40:1	4	2	IMP710	S	10,50,100
A5H	Mg-2Al Cast ingot +10wt.%Fe	Hydrogen (880 kPa)	225	70	~40:1	4	2	IMP710	C	50
A10H	Mg-2Al	Argon (880 kPa)	225	70	~40:1	4	2/10	IMP68	C	30
A11Cl	$2NaAlH_4$+$MgCl_2$	Argon (600kPa)	225	70	~40:1	4	2/10	IMP68	C	5,10 and 40

IMP2: strong impact mode with one magnet

IMP710: impact mode with 2 magnets at 7 and 10 o'clock position; IMP68: milling mode with 2 magnets at 6 and 8 o'clock position

S: sequential milling

C: continuous milling

Table 7.3 Composition of powders and processing parameters for controlled reactive mechanical alloying of Mg-B-H powders.

Powder description	Powder composition	Gas	RPM	Speed (%)	Ball to powder ratio	# of balls	WD (mm)	Mode	Milling	CRMA Time (h)
B6H	Mg-2B (crystalline B)	Hydrogen (520 kPa)	75	25	~40:1	2	3	LES	S	100, 200
B8H	Mg-2B (crystalline B)	Hydrogen (700 kPa)	170	55	~40:1	3	5	IMP2	C	100
B7H	Mg-2B (oxidized amorphous B)	Hydrogen (520 kPa)	75	25	~40:1	2	3	LES	S	100, 200
B9H	Mg-2B (oxidized amorphous B)	Hydrogen (700 kPa)	170	55	~40:1	3	5	IMP2	C	100
B10H	Mg-2B (oxide free amorphous B*)	Hydrogen (880 kPa)	170	55	~40:1	3	2	IMP2	S	200, 300
B14H	Mg-2B (oxide free amorphous B*)	Hydrogen (880 kPa)	225	70	~40:1	4	2	IMP710	C	50, 200
B15H	Mg-2B (oxidized amorphous B)	Hydrogen (880 kPa)	225	70	~40:1	4	2	IMP710	C	200
B11H	MgB_2 (as-received)	Hydrogen (880 kPa)	225	70	~40:1	4	2	IMP710	C	50, 200
B17H	$2NaBH_4+MgCl_2$	Argon (600kPa)	225	70	~40:1	4	2/10	IMP68	C	1,3,10,20,50 and 100

***Amorphous boron annealed at 370^{o}C for 20h to remove B_2O_3**

LES: low energy shearing with one magnet; IMP2: strong impact mode with one magnet

IMP710: impact mode with 2 magnets at 7 and 10 o'clock position; IMP68: milling mode with 2 magnets at 6 and 8 o'clock position

S: sequential milling; C: continuous milling

7.2 Characterization of as-milled powders

7.2.1 XRD phase identification and nanograin size calculation

X-ray powder diffraction (XRD) analysis was performed on a Rigaku Rotaflex D/Max B rotating anode powder diffractometer in the CANMET laboratories, Ottawa. Monochromated Cu $K\alpha_1$ radiation (λ =0.15406 nm) was used in this study produced at an accelerating voltage of 55 kV and a current of 18 mA. The scan range was from 2θ = 10 to 90° and the scan rate was 2° min^{-1} at the step size of 0.02°.

For milled powder mixtures of $NaAlH_4$ and $MgCl_2$ as well as powder mixtures of $NaBH_4$ and $MgCl_2$ (A11Cl and B17H powders), XRD analysis was performed on a Bruker D8 powder diffractometer using CuKα (λ =0.15418 nm) radiation with an accelerating voltage of 40 kV and a current of 30 mA. The scan range was from 2θ = 10 to 90° and the scan rate was 3° min^{-1} at the step size of 0.05°.

The microconstituent phases in the milled samples were identified by comparing the peak positions and intensities listed in ICDD-PDF [92] using the software TRACES™ v.6.5.1. The ICDD-PDF files used in the present work are listed in Appendix B. The nanograin (crystallite) size of phases residing in the milled powders was calculated from the broadening of their respective XRD peaks. Since the Bragg peak broadening in an XRD pattern is due to a combination of grain refinement (nanograin/crystallite) and lattice strains, it is customary to use computing techniques by means of which one can separate these two contributions [93]. The separation of crystallite size and strain was obtained from Cauchy/Gaussian approximation by the linear regression plot according to the following equation [93]:

$$\frac{\delta^2(2\theta)}{\tan^2\theta} = \frac{K\lambda}{L}\left[\frac{\delta(2\theta)}{\tan\theta\ \sin\theta}\right] + 16e^2 \qquad (7.1)$$

where the term $K\lambda/L$ is the slope, the parameter L is the mean dimension of the nanograin (crystallite) composing the powder particle, K is constant (≈1) and e is the so-called "maximum" microstrain (calculated from the intercept), λ is the wave length, θ is the position of the analyzed peak maximum. The term $\delta(2\theta) = B[1 - (b^2/B^2)]$(rad) is the instrumental broadening-corrected "pure" XRD peak profile breadth where B and b are the breadths in radians of the same Bragg peak from the XRD scans of the experimental and reference powder, respectively. They were calculated by the software TRACES™ v.6.5.1 as the full-widths at half maximum, FWHM. A compound LaB_6, the National Institute of Standards and Technology (NIST) standard reference material (SRM) 660, was used as a reference for calculating FWHM. It must be noted that when FWHM of the instrumental line profiles were obtained in this manner, the Bragg peaks for the LaB_6 SRM were at different 2θ angles than those of the analyzed hydride in the milled powders. While the interpolated FWHM values between angles for the SRM peak scan could be found using a calibration curve, satisfactory results were obtained by simply using FWHM values for a nearby peak of the SRM. Reference FWHMs used in XRD analysis of data from Rigaku Rotaflex D/Max B and Bruker D8 powder diffractomer are summarized in Table C.1-C.5 and C.6-C.9, respectively. As an example the calculation of nanograin size and strain using MgH_2 phase is given in Appendix C.2. Lattice parameters of the phases formed in the milled powders were determined using germanium as a standard with the software TRACES™ v.6.5.1.

7.2.2 Microstructure and morphology characteristics

Morphological and microstructural examination was conducted using high resolution, field emission scanning electron microscope (FE SEM) LEO 1530 with an option of backscattered electron (BSE) contrast. Chemical composition of the particles in the milled powders was analyzed using quantitative energy dispersive x-ray spectroscopy (EDS) (EDAX Pegasus 1200 EDS system).

The measurement of the powder particle size was carried out by attaching loose powder to sticky carbon tape and taking pictures under SEM mode in FE SEM, The images were analyzed by the Image Tool v3.00 software. The size of the powders was calculated as the particle equivalent circle diameter, $ECD = (4A/\pi)^{1/2}$, where A represents the projected particle area. Experimental coefficient of variation CV(ECD) = S.D. (EVD)/M(ECD), where S.D. is standard deviation and M is mean value. The coefficient of variation indicates whether the entire population of particle sizes is uniform or not in a milled powder.

7.2.3 Thermal analysis

Thermal hydrogen desorption behaviour of the milled powders was studied by differential scanning calorimetry (DSC), thermogravimetric analysis (TGA) and desorption test in a Sieverts-type apparatus. DSC analysis was performed in a Netzsch Model 404 system at a heating rate of $4^{o}C$/min and an argon flow rate of 16 or 50ml/min. For the milled powder mixture of $2NaAlH_4$ and $MgCl_2$, a heating rate of $20\ ^{o}C$/min was also used. Approximately 20mg of sample was loaded into an alumina crucible having a lid with a pinhole in a glove bag and transferred in an argon filled vial to DSC apparatus to minimize the exposure of samples to air. Peak areas were first calibrated on the basis

of average heats of melting of In, Bi Al, Ag and Au as standards. After the first calibration, peak areas were calibrated again using a commercial MgH_2 powder as a standard (95 wt.%; Tego Magnan®). Correction factor for DSC was 1.19, which was calculated by dividing an average hydrogen capacity measured using a Sieverts-type apparatus (~7.3 wt.%, which is correct with description given by the supplier) by an average hydrogen capacity estimated using DSC method (~6.1 wt.%).

In DSC measurements, the weight percent of a phase was calculated using the peak area of the DSC curve and its reported heat of formation. An example of calculating the weight percent of β-MgH_2 in a milled powder was given in Appendix A.5.

TGA measurement was carried out in TA INSTRUMENT Q600 system at a heating rate of 4^{o}C/min and a 100ml/min nitrogen flow rate. Approximately 10mg of sample was loaded into an alumina crucible in TGA tests. The hydrogen desorption kinetics and the hydrogen capacity of the milled powders were evaluated using a Sieverts-type apparatus custom-built by A.O.C. Scientific Engineering Pty Ltd., Australia (Fig. 7.1).

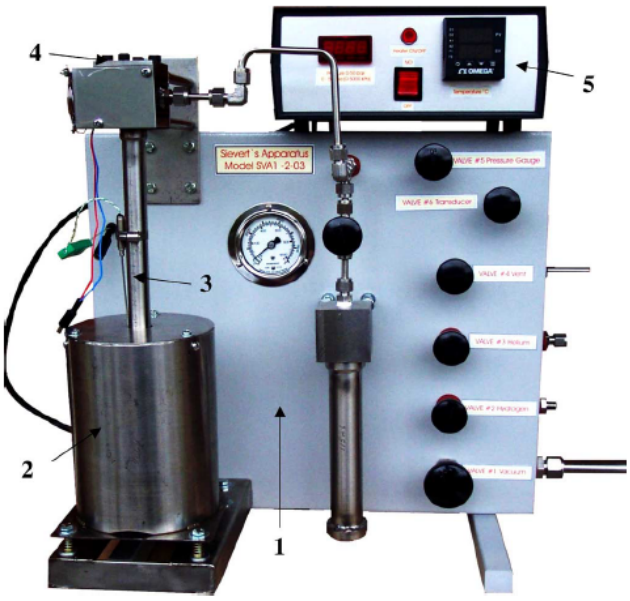

Fig. 7.1 A Sieverts-type apparatus custom-built by A.O.C. Scientific Engineering Pty Ltd., Australia, for evaluating hydrogen storage properties. (1) Gas pressure unit up to 5MPa; (2) furnace up to ~ 500°C; (3) tubular specimen chamber; (4) specimen chamber lid; (5) electronic control unit (pressure transducer and thermocouple).

Approximately 100-200 mg of sample was used in a desorption test. The calibrated accuracy of desorbed hydrogen capacity is about ±0.2wt.% H_2 (calibrated for the commercial MgH_2) and that of temperature reading is ±5°C. Before starting the desorption test, the inner tubing of the apparatus was also evacuated and purged four times with argon and then two times with hydrogen. Subsequently, hydrogen of ~4MPa pressure was admitted into the airtight cylindrical desorption chamber containing the hydride powder and the temperature of the chamber was gradually increased up to the desired desorption temperature. The ~4MPa pressure barrier was applied to prevent any desorption during the period of temperature stabilization (15-20min.) within the desorption chamber. Once the temperature stabilized the hydrogen pressure was quickly reduced to 0.1MPa and the hydrogen desorption process had begun. No elaborate activation procedure was applied to the powders.

8. Mg-H system

Different types of ball mills are used to produce mechanically alloyed powders. They differ in their capacity, efficiency of milling and arrangements of heating and cooling, etc [84,86]. Optimization of milling parameters is crucial to achieve the desired product microstructure and properties. Synthesis of MgH_2 by reactive mechanical milling (RMM) of elemental Mg powder under hydrogen has been widely studied [30,82, 94-100]. As a result, controlled reactive mechanical milling (CRMM) of Mg-H system is chosen to optimize the process parameters for preparation of chemical hydrides with AOC Uni-Ball Mill 5 based on the results of CRMM of elemental Mg powder.

8.1 Microstructure

Fig. 8.1 shows representative BSE micrographs of morphology of Mg powder milled under hydrogen atmosphere after a short and a long milling time. Regardless of milling conditions, it is quite clear that a fraction of the particles has their size refined to ~100-200nm range after a prolonged milling time although some particles become cold-welded forming larger aggregates (Fig. 8.1b).

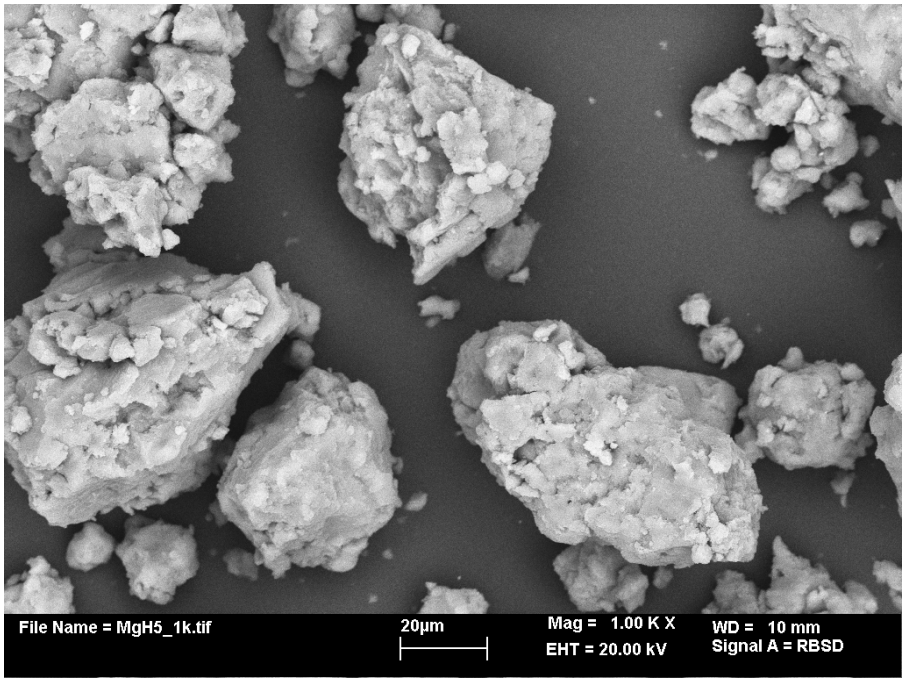

(a)

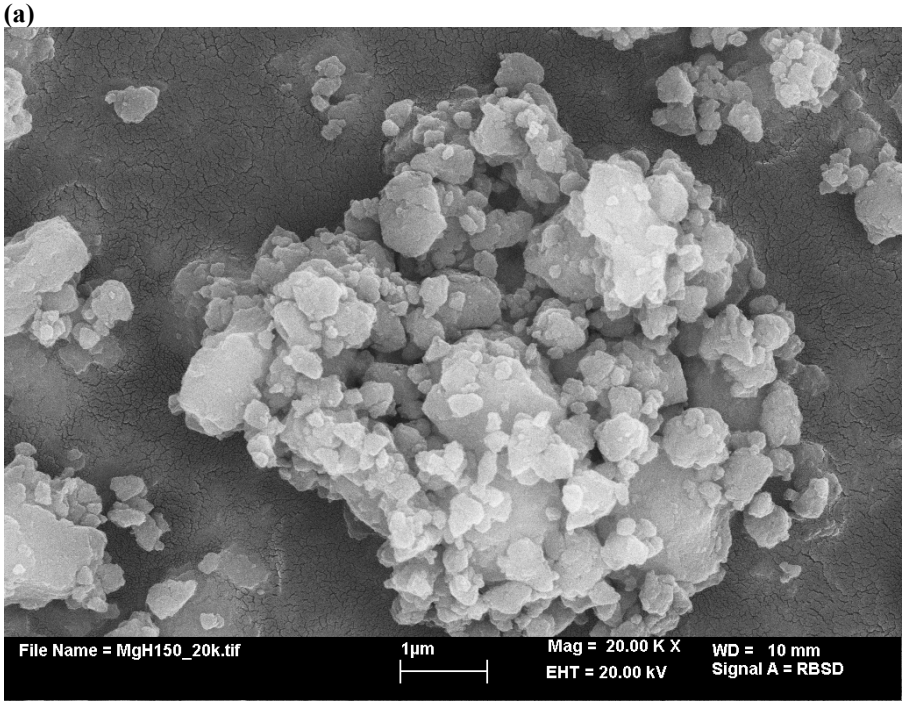

(b)

Fig. 8.1 BSE micrographs showing representative morphology of powder after (a) a short and (b) a long milling time.

8.2 Phase evolution and thermal behavior of the milled powders as a function of milling time

Selected results from XRD and DSC analysis of the milled powders are summarized in Table 8.1. Details of the results from XRD and DSC analysis are given in Table F.1 and G.1, respectively. The phase evolution of Mg powders milled in hydrogen atmosphere can be represented by XRD patterns as a function of milling time under HES mode (Fig. 8.2). Tetragonal β-MgH_2 (ICDD PDF file12-0697 in Table B.12 [92]) is formed in the initial period of milling (5h). The presence of this phase is more evident after 20h. Retained crystalline Mg (ICDD PDF file 35-0821 in Table B.5 [92]) is still detected after milling up to 50h. An interesting result is the formation of orthorhombic γ-MgH_2 (ICDD PDF file35-1184 in Table B.13 [92]), which is a metastable phase transformed from β-MgH_2 at 2.5GPa of hydrogen pressure [96,97], after milling for 50h. Fig. 8.3 shows a representative XRD pattern indicating the formation of β- and γ-MgH_2 after milling of Mg powders longer than 20h in hydrogen atmosphere under HES, IMP2, IMP710, and IMP68 mode (Table 7.1). The only exception is the powder milled under HES mode with only two balls (Mg1H powder), which only contains β-MgH_2 after milling more than 20h (Fig. F.1). The appearance of MgO (ICDD PDF file 45-0946 in Table B.14 [92]) is most probably due to the reaction of highly reactive milled Mg with air during XRD tests [98-100]. No further changes are observed between 100h and 150h of milling. The corresponding DSC curves of Mg powders milled in hydrogen atmosphere after various milling times under HES mode are shown in Fig. 8.4. The 5h milled sample has only one small peak at 410.5^{o}C, but the others show contiguous peaks (doublet). Desorption peak temperatures of peak doublet first decrease as the milling time increases and then

Table 8.1 Selected Results of XRD analysis and DSC analysis of the milled powders in Mg-H system.

Sample description	Mode	CRMA time (h)	Phases in the as-milled powder (β: β-MgH_2; γ: γ-MgH_2)	Nanograin size (nm) of β-MgH_2	Mean particle size (ECD)±STD* of hydride powders (nm)	CV (ECD) for size distribution	DSC peak (^oC)			Yield of MgH_2 (wt.%)
							T_{ON}	LT	HT	
Commercial MgH_2 (Tego Magnan®)	-	-	Mg, β	67	35878±16370	0.46	399.0	-	410.1	95.0
Mg1H	HES	5	Mg, β, MgO	38	-	-	311.8	-	375.7	5.8
		20	Mg, β, MgO	13	1789±1432	0.80	372.1	380.8	406.8	35.3
		50	Mg, β, MgO	9	712±570	0.80	361.2	369.5	408.4	53.2
		100	β, MgO	7	-	-	341.1	352.8	392.4	54.9
		150	β, MgO	6	-	-	339.5	354.2	382.1	56.0
Mg7H	HES	5	Mg, β, MgO	33	39671±33930	0.86	398.8	-	410.5	9.8
		20	Mg, β, MgO	15	2123±1783	0.84	375.3	387.3	398.1	48.5
		50	Mg, β, γ, MgO	9	444±363	0.82	350.8	372.9	389.3	67.1
		100	β, γ, MgO	8	384±281	0.73	349.0	365.5	397.7	73.0
		150	β, γ, MgO	7	374±263	0.70	351.8	370.5	392.7	74.6
Mg6H	HES	150	β, γ, MgO	8	393±255	0.65	351.7	371.3	391.3	78.1
Mg2H	IMP2	100	β, γ, MgO	8	374±162	0.43	335.4	349.7	376.3	84.3
Mg4H	IMP2	150	β, γ, MgO	8	374±233	0.62	347.0	361.6	380.3	81.2
Mg5H	IMP2	150	β, γ, MgO	8	338±201	0.59	326.0	348.3	369.0	74.9
Mg9H	IMP710	60	β, γ, MgO	8	-	-	351.8	375.2	394.6	75.0
Mg10H	IMP710	60	β, γ, MgO	7	-	-	351.0	367.8	388.6	71.4
Mg11H	IMP710	100	β, γ, MgO	8	-	-	350.5	365.5	392.0	70.1
Mg12H	IMP68	30	β, γ, MgO	9	728±456	0.63	346.2	365.9	392.1	84.7
Mg13H	IMP68	30	β, γ, MgO	9	643±399	0.62	348.7	367.5	379.7	86.0
Mg14H	IMP68	30	Mg, β, γ, MgO	9	563±347	0.62	347.9	363.8	383.8	88.3

***STD: standard deviation**

stabilize after 100h. Regardless of the microstructure present in the milled powder, the DSC curve of a powder milled less than 20h shows a single peak (e.g., 5h milled Mg7H powder in Fig. 8.4) while those milled longer than 20h show either a peak hidden in the shoulder and a well-developed peak, or a peak doublet (Fig. 8.5). XRD analysis performed on the samples after DSC desorption only shows Mg and MgO phases (Fig. 8.6). This indicates that the decomposition of β- and γ-MgH_2 is completed after DSC heating.

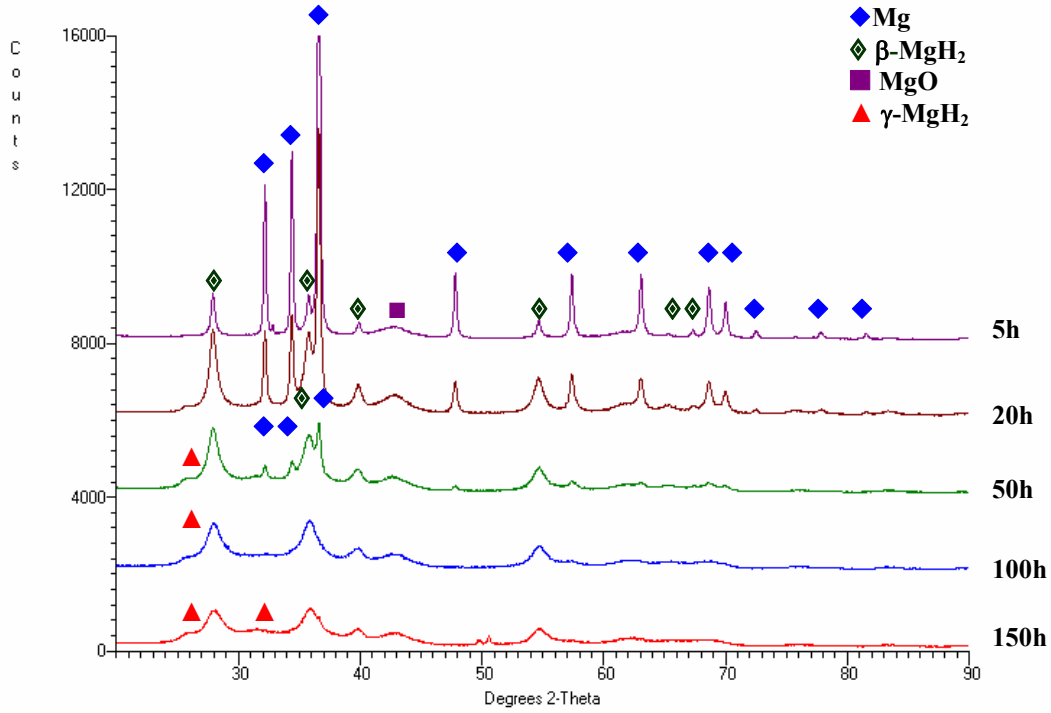

Fig. 8.2 Evolution of representative XRD patterns as a function of milling time in HES mode.

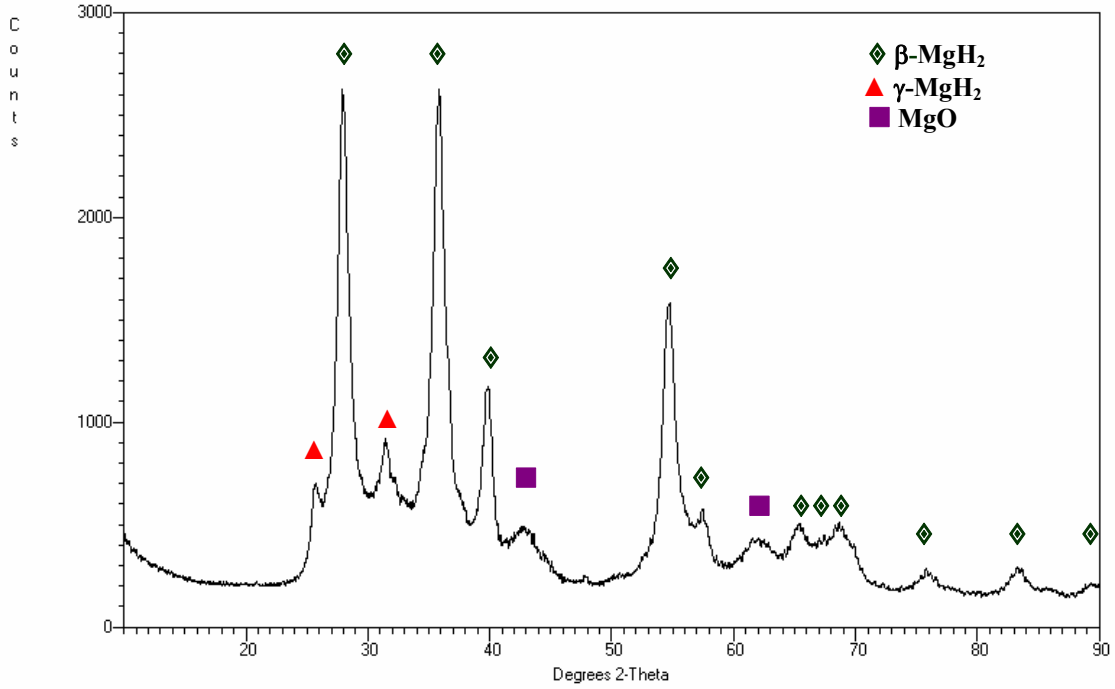

Fig. 8.3 Representative XRD pattern of as-milled powders which contain both β- and γ-MgH_2 (this XRD is for a powder milled for 10h under IMP710 mode).

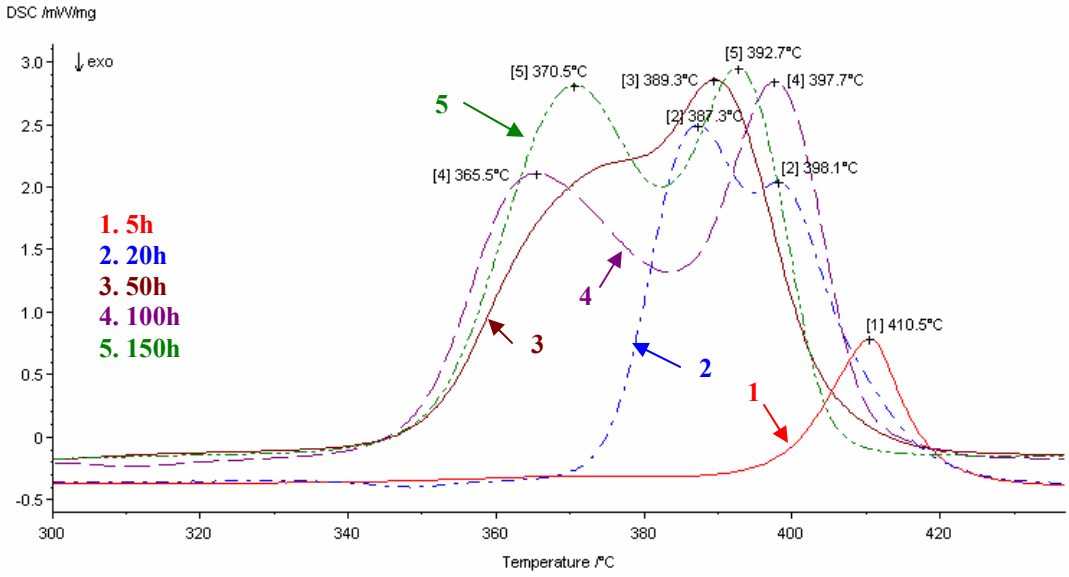

Fig. 8.4 Evolution of representative DSC curves as a function of milling time in HES mode.

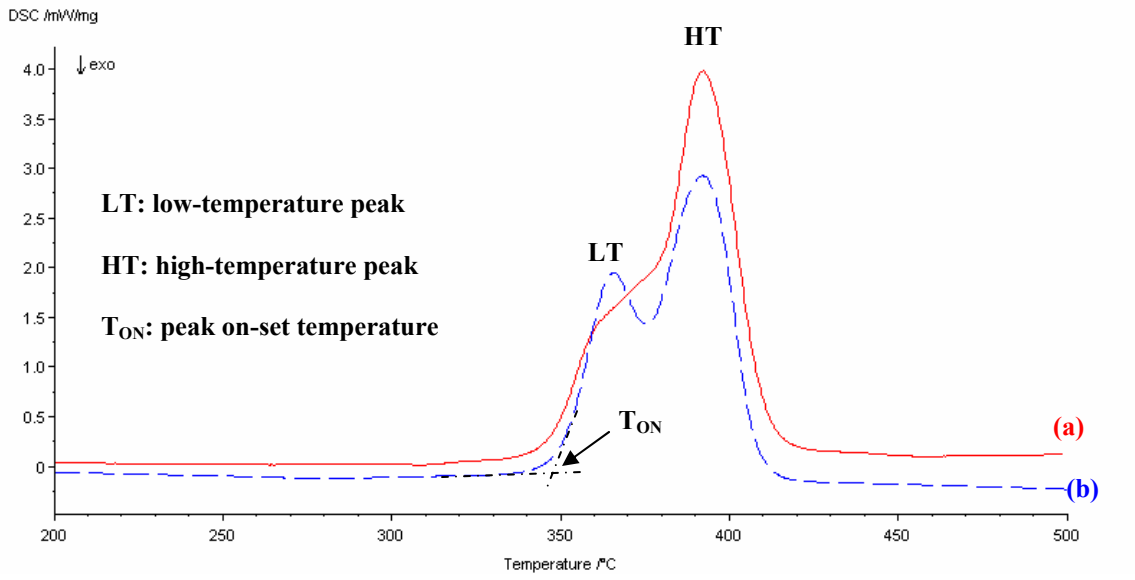

Fig. 8.5 Representative DSC curves of powders milled more than 20h showing (a) peak with a shoulder (hidden peak) and a well-developed peak or (b) double peaks.

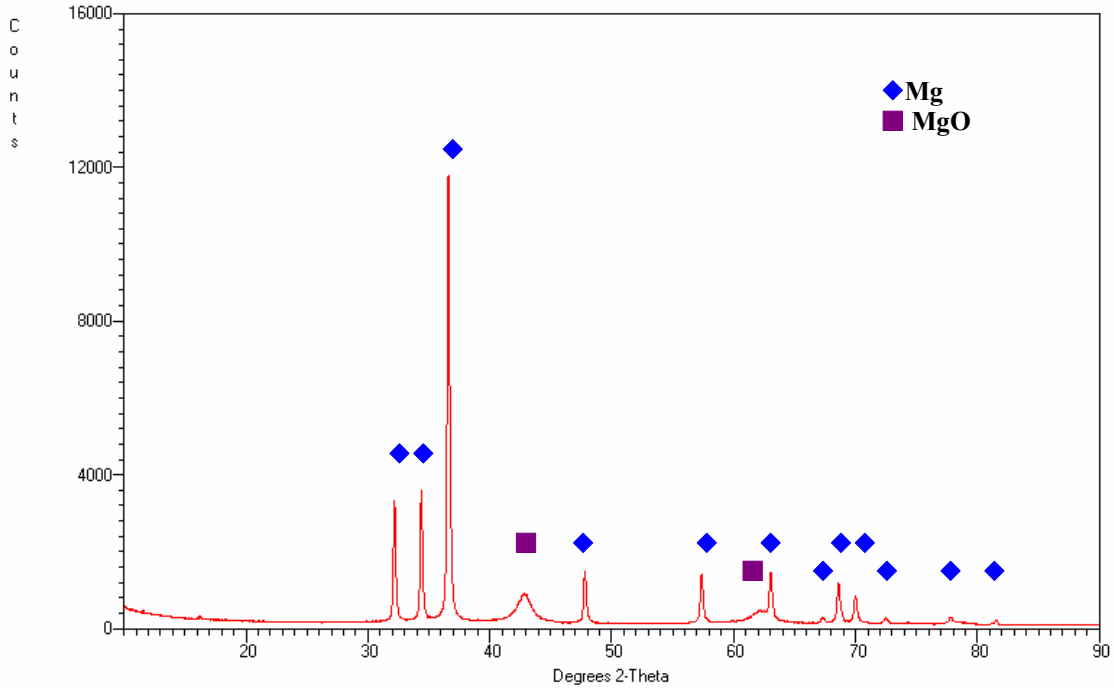

Fig. 8.6 XRD pattern of powder milled for 100h under HES mode after DSC test up to 500°C showing a complete decomposition of MgH_2.

In order to analyze the nature of the double peaks in the DSC curve of milled Mg-H powders (Fig. 8.5), the milled powders containing only β-MgH_2 as well as both of β- and γ-MgH_2 were analyzed by running small samples of those powders in DSC first to the temperature (375^oC) after the end temperature of the low-temperature peak (LT) and then to the temperature (450^oC) after the end temperature of the high-temperature peak (HT) (Fig. 8.5). By monitoring the phase evolution before and after the thermal reaction, the nature of the thermal reaction can be revealed. The XRD patterns corresponding to the powders containing only β-MgH_2 and both of β- and γ-MgH_2 analyzed in DSC to selected temperatures are shown in Fig. 8.7a and Fig. 8.7b, respectively.

As shown in Fig. 8.7a, after heating up to 375^oC, Mg peaks appear and the intensities of β-MgH_2 peaks decrease profoundly. A weak peak belonging to β-MgH_2 can still be detected. However, after heating up to 450^oC, no β-MgH_2 peaks are observed. The intensities of Mg peaks increase with respect to those at 375^oC. The above results indicate that both of the endothermic double (contiguous) peaks arise from the decomposition of β-MgH_2 in the milled powder which contains only β-MgH_2.

For the milled powder containing both of β- and γ-MgH_2 phases, it can be seen that after heating to 300^oC (Fig. 8.7b), which is lower than the onset temperature (T_{ON}) of the LT peak (Fig. 8.5), the powder still contains β- and γ-MgH_2 phases. At 375^oC, γ-MgH_2 no longer exists. The Mg peaks appear and intensities of β-MgH_2 peaks decrease with respect to those at 375^oC. At 450^oC, the only phases existing in the microstructure are Mg and MgO, the latter formed from the exposure of the newly formed Mg to air. As a result, the LT peak is attributed to a full decomposition γ-MgH_2 and a partial decomposition of β-MgH_2 while the remnant β-MgH_2 decomposes completely after the HT peak of the

peak doublet in the DSC curve [98]. The reason why decomposition of β-MgH_2 yields double peaks will be discussed in detail in Sec. 8.3.3.

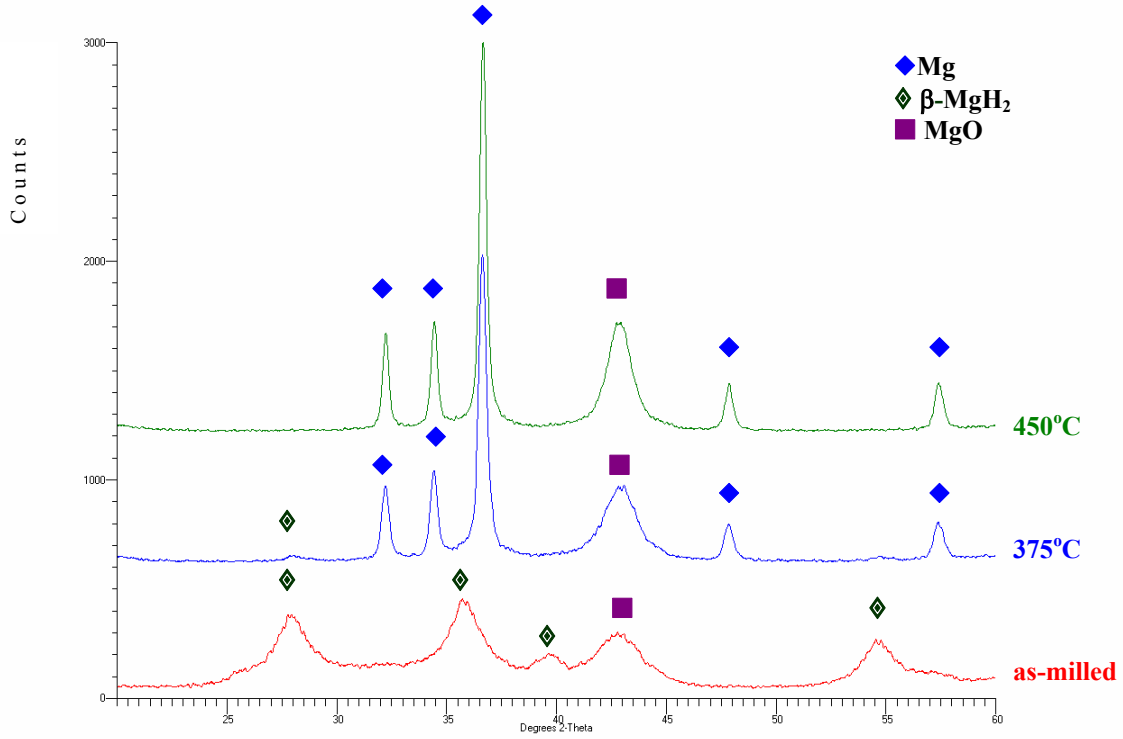

(a)

Fig. 8.7 XRD patterns of (a) the milled powder containing only β-MgH_2 phase after heating to 375 and 450°C, and (b) the milled powder containing both β- and γ-MgH_2 phases after heating to 300, 375 and 450°C.

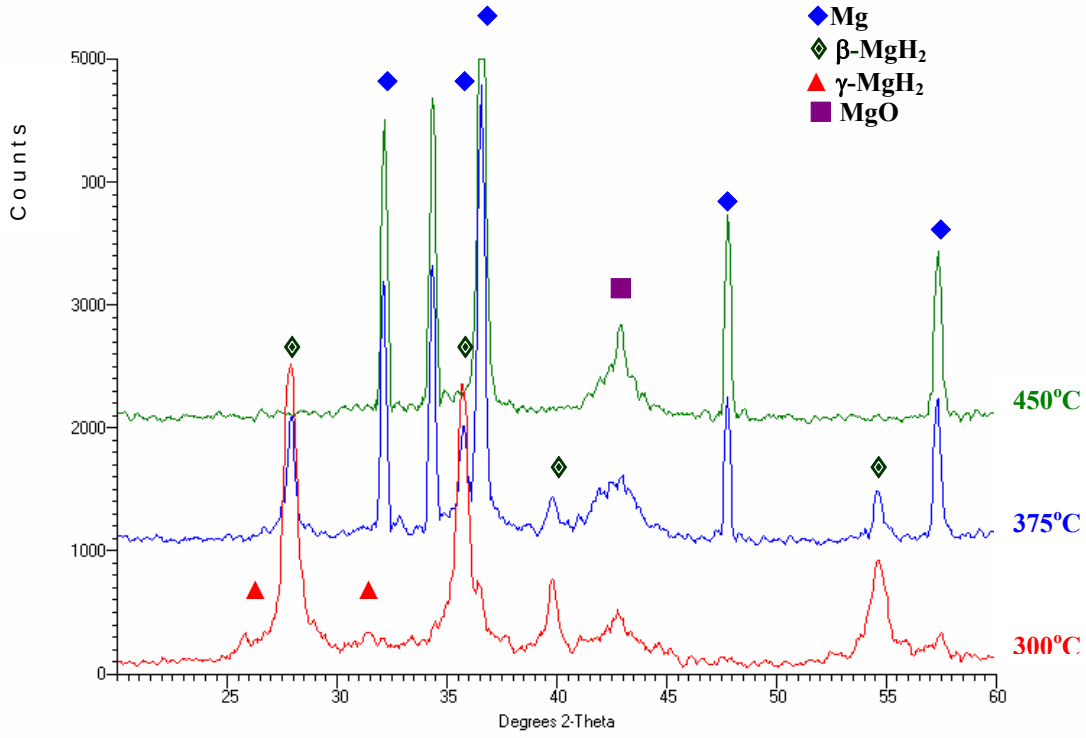

(b)

Fig. 8.7 cont'd

Fig. 8.8 shows nanograin (crystalline) size of β-MgH_2 in the Mg-H powders milled under different milling modes. It can be seen that for all of the milled powders, β-MgH_2 phase undergoes a very fine nanostructurization and becomes saturated (crystallite size ~6-9nm) after ~30-50h of milling time with or without a very small associated lattice strain (Table F.1). Further refinement proceeds slowly, and the nanograin size finally reaches a steady-state value of ~6-9nm rather than decreasing indefinitely [101].

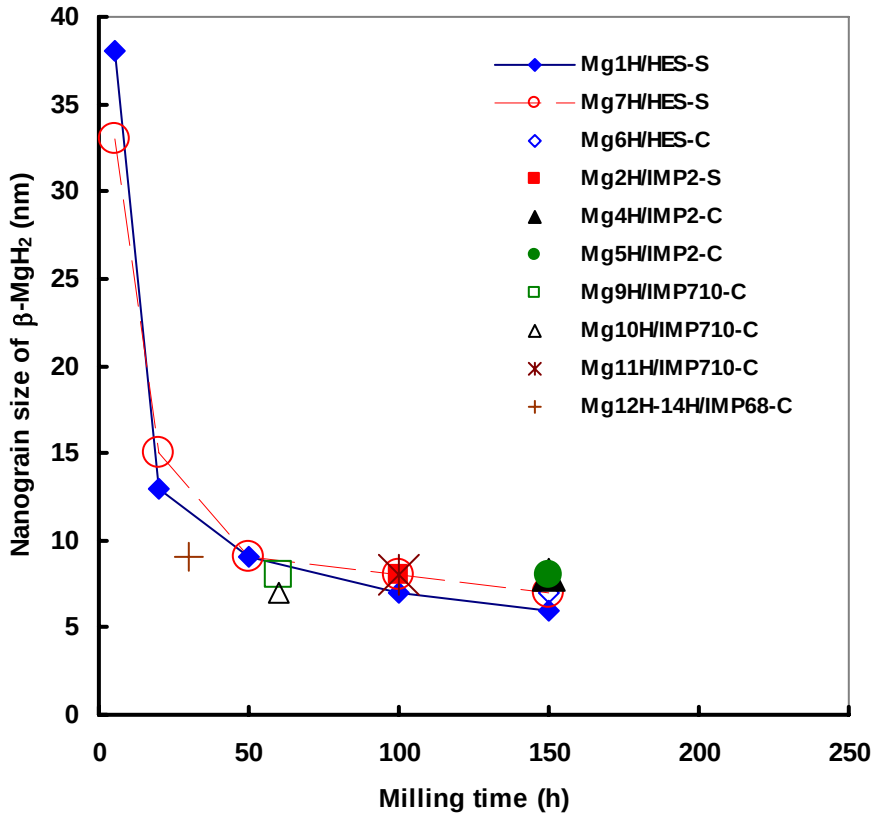

Fig. 8.8 Nanograin (crystalline) size of β-MgH_2 phase in the Mg-H powders milled under different milling modes. S-sequential milling; C-continuous milling.

Fig. 8.9 shows the yield of MgH_2 phase, which is estimated by DSC analysis as a function of milling time, in Mg-H powders milled under various milling modes. The dependence of the yield of MgH_2 on the milling time can be best represented using

Mg1H and Mg7H powders milled under HES mode as examples. Yield of MgH_2 first increases dramatically in the early stage of milling and attains a saturation level after milling for 100h. The lowest yield of MgH_2 (56.0 wt%) at saturation level is found in Mg1H powder after milling for 150h under HES mode, while the highest value is ~88 wt.% in the Mg14H powder after milling for 30h under IMP68 mode.

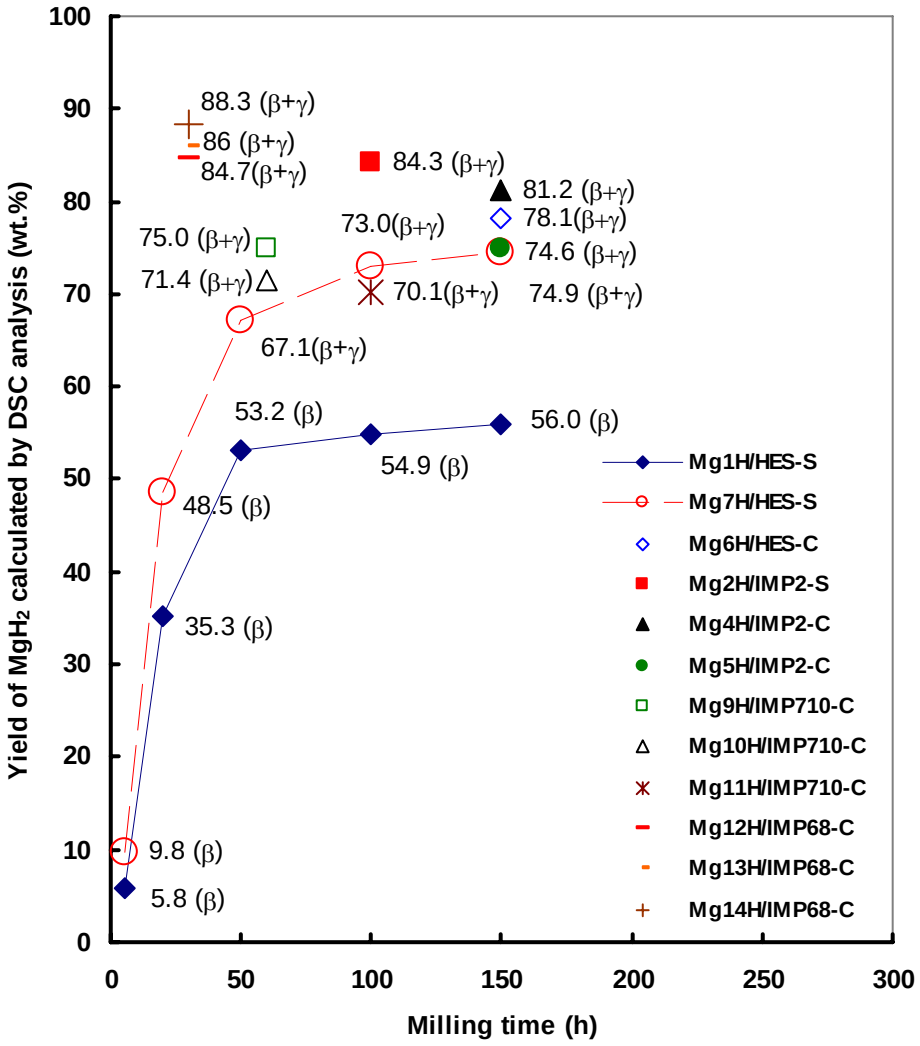

Fig. 8.9 DSC yield of MgH_2 phase in the milled powders as a function of milling time. Numbers beside data points indicate DSC yield of MgH_2 (wt.%). β or β+γ indicates milled powders contain only β-MgH_2 or both of β and γ-MgH_2 phase, respectively. S-sequential milling; C-continuous milling.

A volumetric method was also used to estimate the hydrogen capacities of milled powders by monitoring the pressure change during the milling processes. Fig. 8.10 and Fig. 8.11 show hydrogen capacities of the powders (ball-to-powder ratios = 20:1 and 40:1) as a function of milling time in the IMP710 and IMP68 mode, respectively. Hydrogen capacity first increases as the milling time increases at the initial milling stage and then it reaches the saturation level. The saturation time depends on milling parameters, which will be discussed later in Sec. 8.3.1.

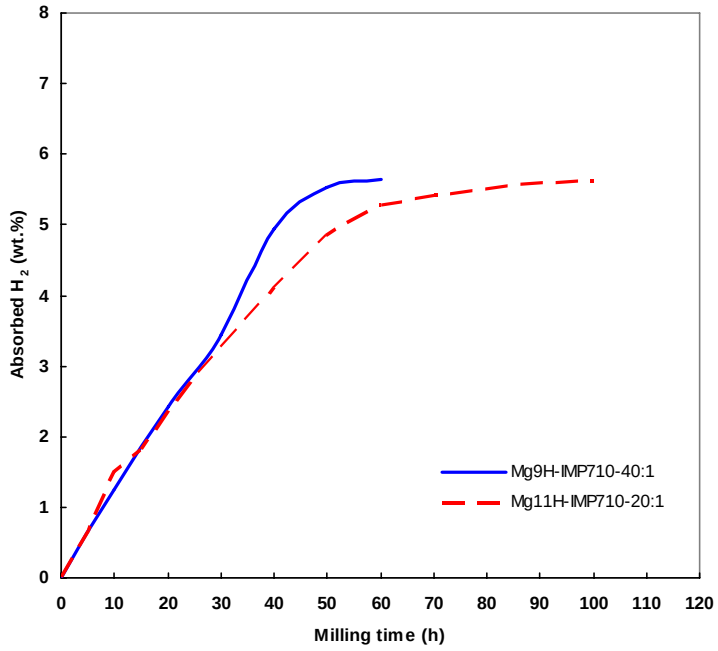

Fig. 8.10 Absorbed hydrogen (wt.%) during milling as a function of milling time for powders milled under IMP710 mode with the ball-to-powder ratio of 20:1 and 40:1.

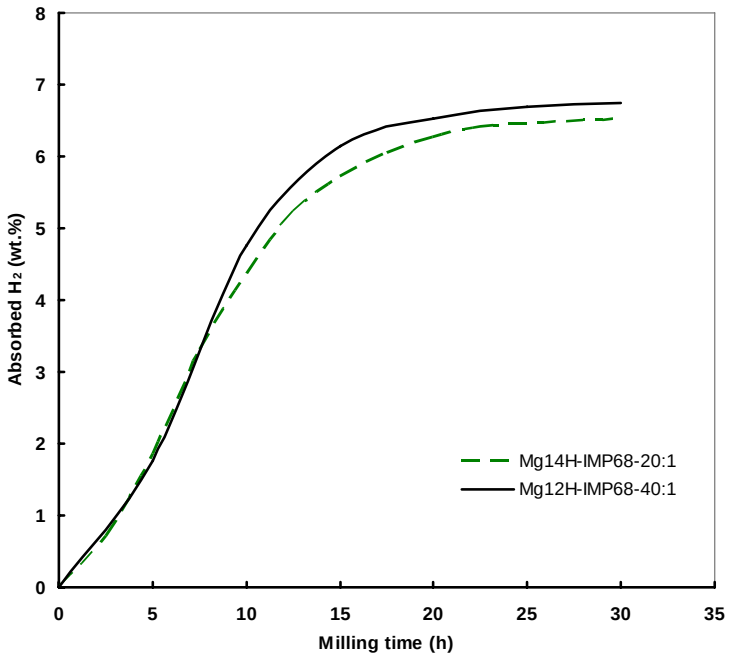

Fig. 8.11 Absorbed hydrogen (wt.%) during milling as a function of milling time for powders milled under IMP68 mode with the ball-to-power ratio of 20:1 and 40:1.

8.3 Discussion

8.3.1Effect of milling parameters on the yield of MgH_2 hydride

8.3.1.1 Effect of milling mode

The yield of MgH_2 in the Mg4H powder milled under IMP2 mode for 150h (81.2 wt.%) is slightly higher than that in the Mg6H powder milled under HES with the same duration (78.0 wt.%) (Fig. 8.9). However, there is a noticeable increase in the yield from 67.1 wt.% in Mg7H powder after milling under HES mode for 50h to 75.0 wt.% in the Mg9H powder after milling under IMP710 mode for 60h. The yield of MgH_2 further increases to ~85-88wt.% while milling under IMP68 mode. Not only the yield is increased but the milling duration is shortened while milling under more energetic mode. Using yield of MgH_2 and milling time as rough estimation of the efficiency of milling modes applied in

the present work in Uni Ball Mill, the weakest to the strongest mode is: HES < IMP2 < IMP710 < IMP68.

8.3.1.2 Effect of number of balls

In Mg1H, Mg7H, Mg9H and Mg10H powders, ball to powder ratio is kept at 40:1 while the number of balls is increased from 2 balls in Mg1H to 4 balls in Mg7H powder, and from 4 balls in Mg9H to 5 balls in Mg10H powder. Yield of MgH_2 in Mg7H powder (74.6 wt.%) after milling for 150h is much higher than that in Mg1H powder (56.0 wt.%) after 150h under the same milling mode (Fig. 8.9). When number of balls increases from 2 to 4 balls under HES mode with the same ball-to-powder ratio, the yield of β-MgH_2 increases. This might be the result of increased contacts between balls and powders when the number of balls increases. Energy applied to powder particles increases as the number of collisions (contacts) increases. As a result, the yield of the product increases.

However, the dramatic increase of the yield of β-MgH_2 is not observed while milling under IMP710 mode as the number of balls changes from 4 balls in Mg9H (~75 wt.%) to 5 balls in Mg10H (~71 wt.%) (Fig. 8.9). It seems that 4 balls are required to produce sufficient numbers of contacts between balls and powders in Uni-Ball Mill which results in a very efficient milling.

8.3.1.3 Effect of ball-to-powder ratio

As shown in Fig. 8.10, longer time is required to reach the saturation level of the yield when ball-to-powder ratio is reduced from 40:1 in Mg9H to 20:1 in Mg11H powder under IMP710 mode. This indicates that milling time is dependent on the ball-to-powder

ratio. The higher the ball to powder ratio, the shorter is the milling time, which is also reported by Suryanaraya [78] and Lü et. al [86] for general mechanical alloying processes.

However, it has to be pointed out that under IMP68 mode the time to reach the saturation level of the yield in Mg12H powders with a 40:1 ball-to-powder ratio is very close to that in Mg14H with a 20:1 ball-to-powder ratio (Fig. 8.11). The dependence of saturation time on the ball-to-powder ratio in powders milled under IMP68 mode is not as noticeable as that in the powders milled under IMP710 mode.

In conclusion, when the number of balls is fixed, the milling time is a function of the ball-to-powder ratio and milling mode, while the latter has the stronger effect.

8.3.2 Correlation between structural characteristics and the amount of hydrogen absorbed in the milling process

Nanocrystalline MgH_2 hydride has been synthesized successfully by controlled reactive mechanical milling (CRMM) of elemental Mg powder under hydrogen atmosphere in Uni-Ball Mill 5. The correlation between structural characteristics and the amount of hydrogen absorption in the CRMA process can be exemplified by the change of the particle size, the grain (crystalline) size and the amount of absorbed hydrogen of the Mg7H powder as a function of milling time.

At the early stage of CRMA (5h), large cold-welded aggregates are formed. The particle size ± standard deviation of the 5h-milled Mg7H powder which contains primarily Mg and a small amount of MgH_2 (Fig. D.5a; 39671±33930nm) is much larger than that of the elemental Mg powder (Fig. D.1; 9500±5500nm). Hydrogen capacity of the 5h-milled Mg7H powder is low (only 0.8 wt.%). At the transitional state (20h and 50h), rapid decrease of the particle size and nanograin size of the milled powder leads to a dramatic

increase of hydrogen absorption (3.7 wt.% after 20h and 5.1 wt.% after 50h). At the final stage (100h and 150h), the particulate aggregates are formed (Fig. D.5d). Both the particle size and grain size reach saturation, which does not give a better hydrogen capacity (~5.7 wt.% after saturation) in the milled powder.

8.3.3 Effect of particle size and nanograin size on DSC decomposition temperature

During a milling process, there is always inevitable reduction of the powder particle size which accompanies the reduction of grain size of the phases residing within the particles (Table 8.1). It is very interesting to investigate whether the size of nanograin or the mean size of particle is the primary factor responsible for the improved hydrogen storage.

The results of particle size distribution analysis are given in Table 8.1 for selected powders by a mean particle size and a coefficient of variation, CV(ECD), indicating whether the entire population of particle sizes is uniform or not in a milled powder.

A particle size of ~36μm having CV(ECD) ~0.46 characterizes the commercial MgH_2 powder with a rather uniform population of coarse particles. The Mg1H20 and Mg1H50 powders have much smaller mean particle size than that of commercial MgH_2 powder, but with a much larger coefficient of variation CV(ECD) = 0.80, which suggests a rather non-uniform particle size distribution. A particle size of ~39μm having CV(ECD) ~0.86 in Mg7H5 powder indicates the formation of large aggregates and nonuniform particle size distribution, which is commonly observed in the powders containing primarily Mg and a small amount of MgH_2 in the early stage of milling of reactive milling of elemental Mg under hydrogen atmosphere. Mg7H20 and Mg7H50 powders have smaller mean particle size but still larger coefficients of variation CV(ECD) = ~0.82-0.84, suggesting a

rather non-uniform particle size distribution. As milling time exceeds 100h for the Mg7H powders, the mean particle size decreases below ~384nm and the value of CV(ECD) decreases to ~0.70, which indicates a more uniform particle size distribution.

The value of CV(ECD) starts to decrease to a 0.62-0.67 range for the Mg4H, Mg6H and Mg12H-Mg14H powders whose mean particle size is reduced below ~730nm. The Mg5H powder has the smallest mean particle size ~338nm with a CV(ECD) ~0.6. A CV(ECD) of 0.43 for the Mg2H100 powder indicates the highest uniformity. However, the reduction of CV(ECD) which may indeed indicate more uniformity of the particle size is associated with the appearance of the γ-MgH_2 hydride phase (Table 8.1).

In general, there is no noticeable difference between the nanograin sizes of β-MgH_2 phases in the milled powder which are slightly less than 10nm, except for the powders milled for less than 20h in which the β-MgH_2 phase has a nanograin size in a range of ~13-38nm (Table 8.1). Peaks of γ-MgH_2 are less intense and overlapped with the peaks of β-MgH_2. As a result, one can not make any meaningful estimate of γ-MgH_2 grain size using Eq. 6.1. Nevertheless, based on the heavy peak broadening, it can be reasonably concluded that the grain size of γ-MgH_2 is not much larger than that of β-MgH_2, i.e., most likely, within the 10nm range [82].

As shown in Fig.G.1, a single endothermic DSC peak at ~410^{o}C characterizes the commercial MgH_2 powder (Tego Magnan®) which has a coarse particle size with a rather uniform distribution of particle sizes. Most of the synthesized MgH_2 hydrides in the present work show a double hydrogen desorption peak on the hydrogen desorption DSC curves, except those formed after a short milling time (5h). The peak onset temperature

(T_{ON}) and the peak maximum temperature for low temperature (LT) and high temperature (HT) peaks in the peak doublet, as shown in Fig. 8.5, are listed in Table 8.1.

For the Mg1H20, Mg1H50, and Mg7H20 powders, which contain a β-MgH_2 hydride, the low temperature DSC peak slightly decreases from ~381^oC (~387^oC) for the Mg1H20 (Mg7H20) powder to ~370^oC for the Mg1H50 powder. However, the high temperature DSC peak for both powders remains approximately at the temperature range of ~400-408^oC, which is very close to that for the commercial MgH_2 powder. As mentioned earlier, the Mg1H20, Mg1H50 and Mg7H20 powders are characterized by a large CV(ECD) value ~0.80-0.84, meaning the presence of fine and coarse particle fractions in these powders. As a result, it is postulated that low and high temperature DSC peaks in a doublet correspond to the hydrogen desorption from the finer and coarser particle fractions in powders containing only a single-phase β-MgH_2 hydride.

For the Mg6H, Mg2H, Mg4H, Mg5H, and Mg7H powders (milled time > 50h) and the Mg12H-Mg14H powders milled under a very strong impact mode for 30h, containing both β- and γ-MgH_2 hydrides, the mean particle size is less than ~700nm. These powders are still characterized by DSC doublet although LT peak in some of them is hidden in a shoulder rather than being a well-developed peak. Since these powders have CV(ECD) smaller than ~0.8, their particulate population seems to be more uniform than that of the Mg1H20, Mg1H50, and Mg7H20 powders. Therefore, the appearance of peak doublet in DSC curve cannot be solely attributed to the presence of finer and coarser fractions of particles. It might be explained by the presence of both β- and γ-MgH_2 hydrides with the possibility that the latter preferentially occupies the finer particle population and has a lower desorption temperature than β-MgH_2 as shown in Fig. 8.5b, which is also

suggested by Gennari et al. [98]. Finally, as can be seen in Table 8.1, Fig. 8.12 and Fig. 8.13, the reduction of grain size of β-MgH_2 from ~67nm to ~9nm does not seem to affect the DSC peak temperature.

A dependence of desorption temperature on the particle size of the milled AlH_3 powder was reported by Sandrock et al. [19]. It was found that particle size reduction effectively lowered the hydrogen desorption temperature. It has been shown very recently that the reduction of the DSC desorption temperature of mechanically milled commercial MgH_2 (Tego Magnan®) is the result of additive effect of two factors: the presence of γ-MgH_2 and the particle size reduction [83].

In conclusion, peak doublets observed in the DSC curves of Mg-H powders in the present work are suspected to be the combination results of the coexistence of both γ-and β-MgH_2 phase and the inhomogeneous particle size distribution of MgH_2.

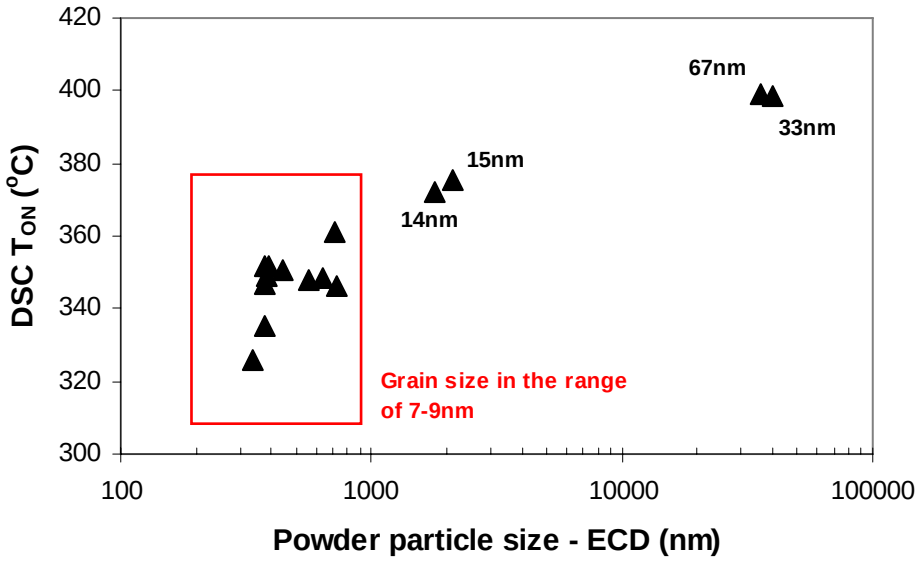

Fig. 8.12 Onset temperature (T_{ON}) DSC peak vs. particle size. Numbers beside data points indicates the grain size of the MgH_2 phases.

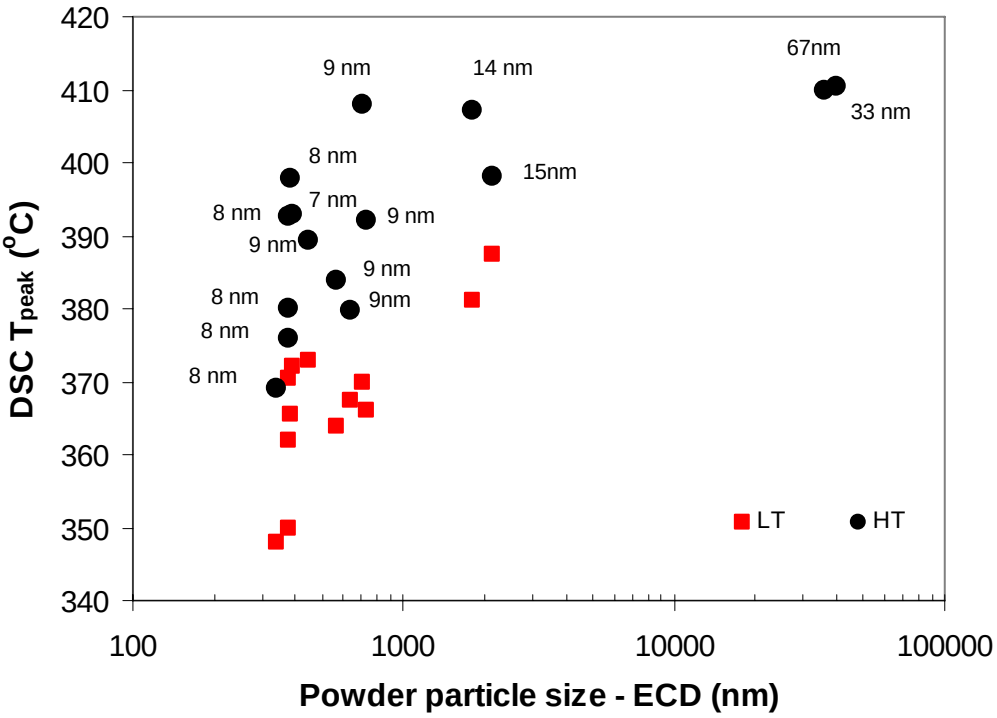

Fig. 8.13 Low temperature (LT) and high temperature (HT) DSC peaks vs. particle size. Numbers beside data points indicates the grain size of the MgH_2 phase.

9. Mg-Al-H

9.1 Nanohydride formation by using stoichiometric Mg-2Al powder mixture

9.1.1 As-milled powders

9.1.1.1 Evolution of microstructure of as-milled powders

Fig. 9.1 shows the microstructure of as-cast Mg-2Al alloy, which is used as the starting material for the A3H powders, observed under BSE contrast in SEM. The composition of the matrix measured by EDS analysis (Al=61.7±0.1at.%, Mg=38.3±0.1at.%) corresponds well to the stoichiometry of the intermetallic compound Al_3Mg_2 which exists in the Al-Mg binary system [104]. Within the matrix in Fig. 9.1, a typical dendritic structure of the Al(Mg) solid solution (Al=80.1±1.1at.%, Mg=19.9±1.1at.% as obtained from EDS analysis) is clearly seen. The average composition of the ingot is Al=63.7±0.2at.% and Mg=36.2±0.2at.%. It corresponds well to the intended stoichiometric composition of Mg-2Al.

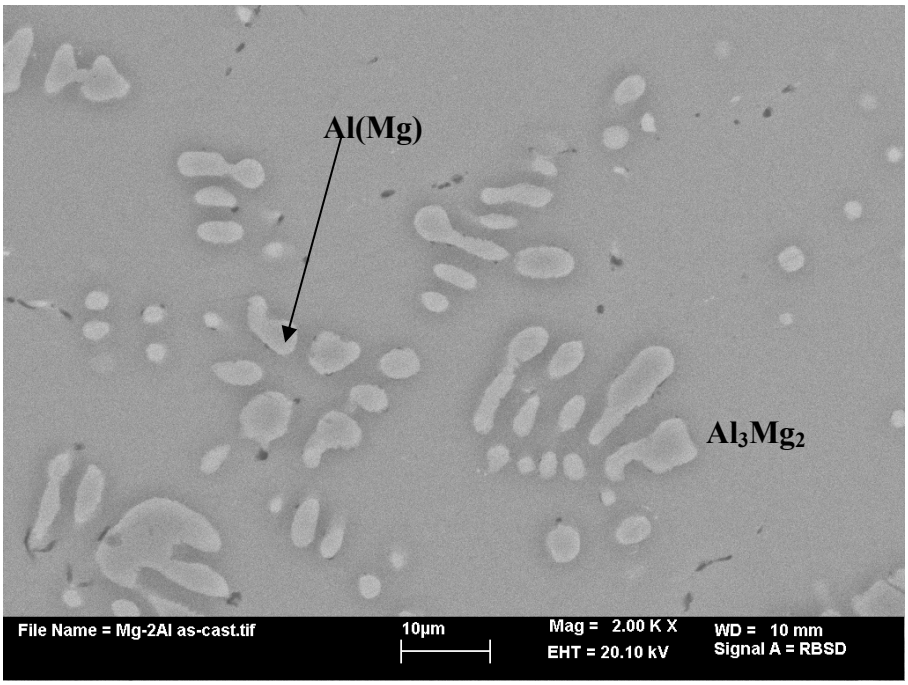

Fig. 9.1 BSE micrograph showing the microstructure of cast Mg-2Al alloy.

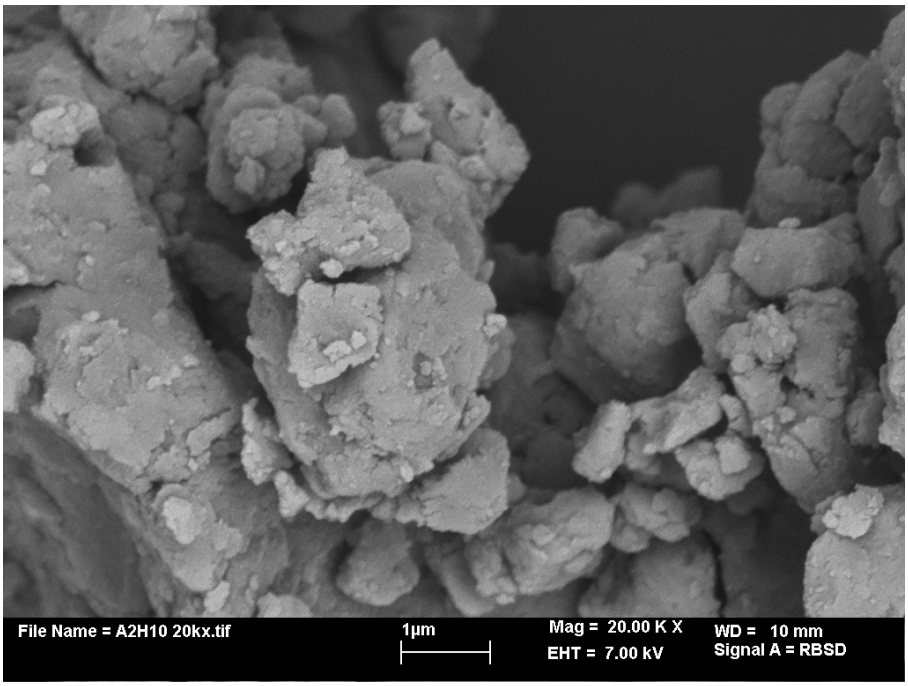

(a)

Fig. 9.2 BSE micrographs showing morphology of (a) A1H powder milled for 10h, (b) A2H powder milled for 10h, (c) A3H powder milled for 10h, (d) A4H powder milled for 10h, (e) A1H powder milled for 200h, (f) A2H powder milled for 200h, (g) A3H powder milled for 200h and (h) A4H powder milled for 100h.

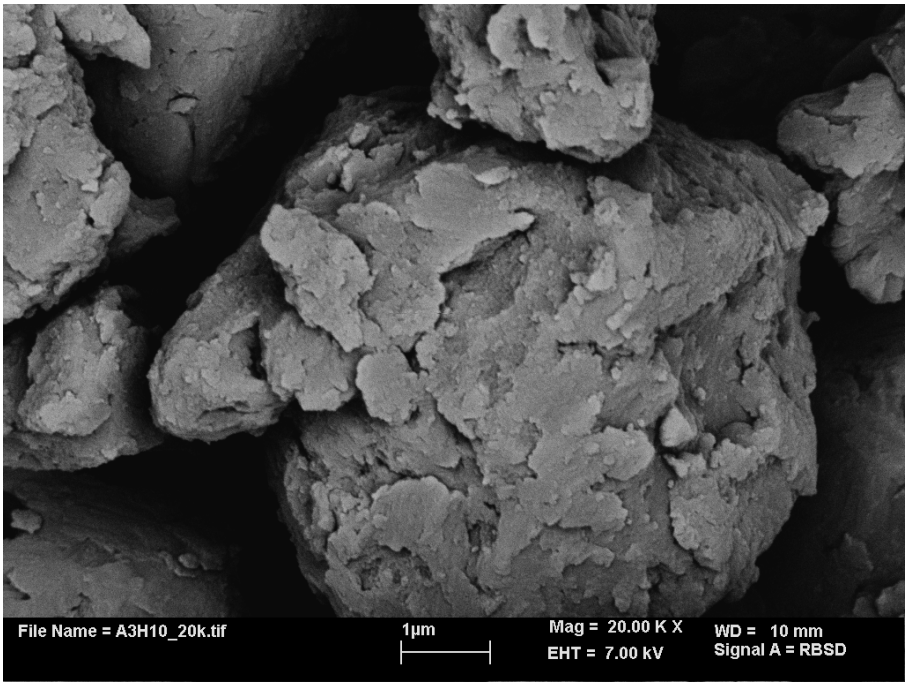

(b)

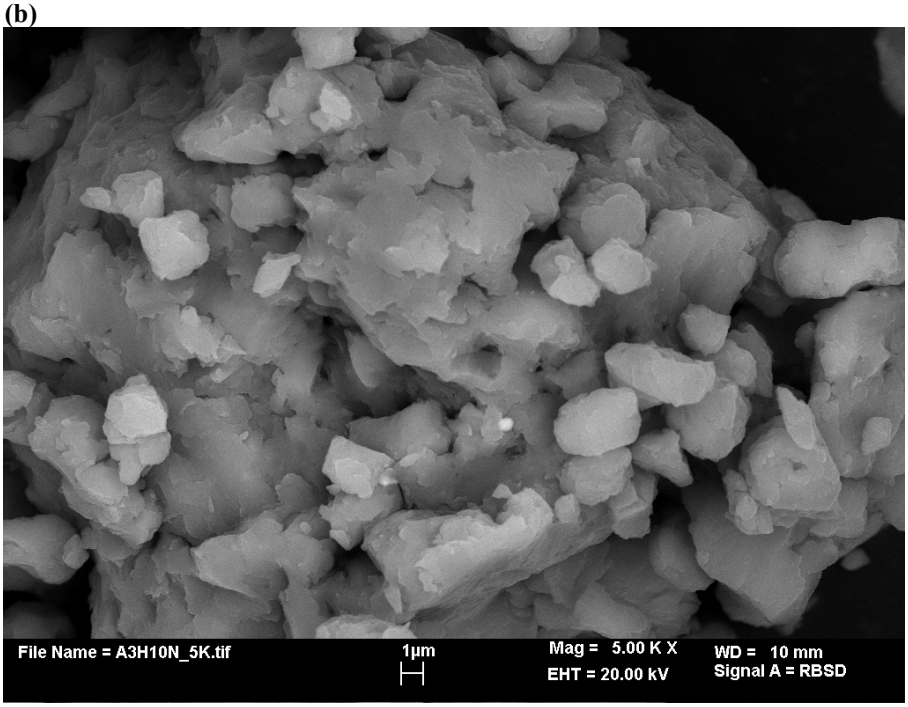

(c)

Fig. 9.2 cont'd

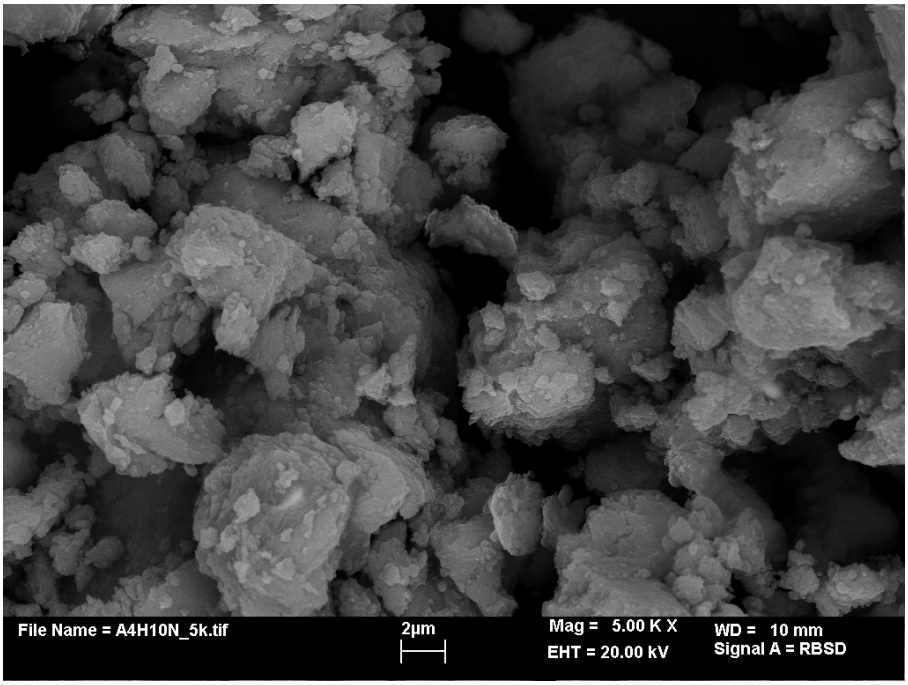

(d)

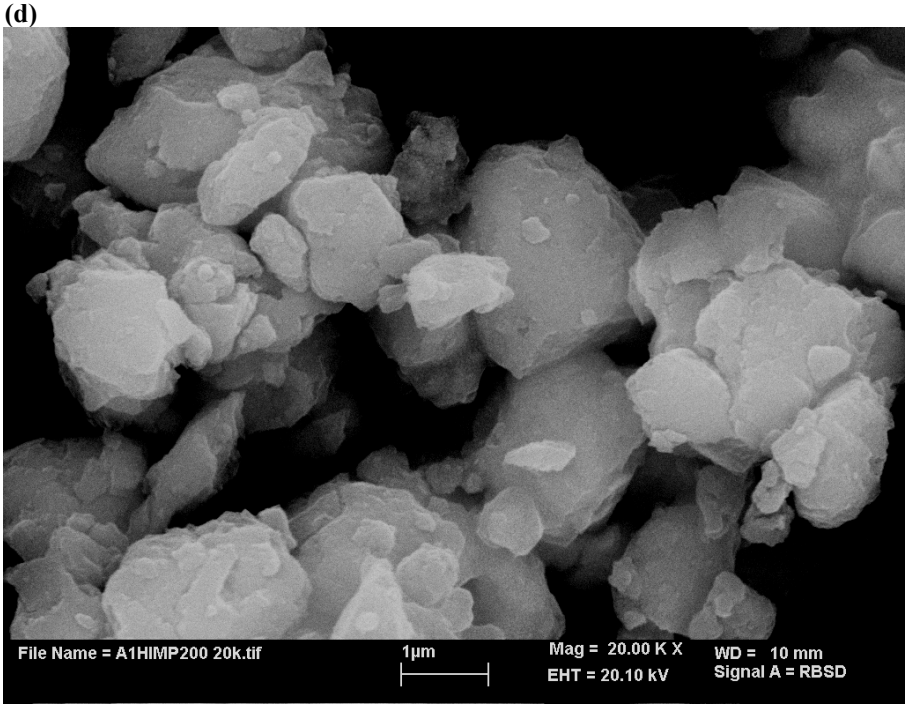

(e)

Fig.9.2 cont'd

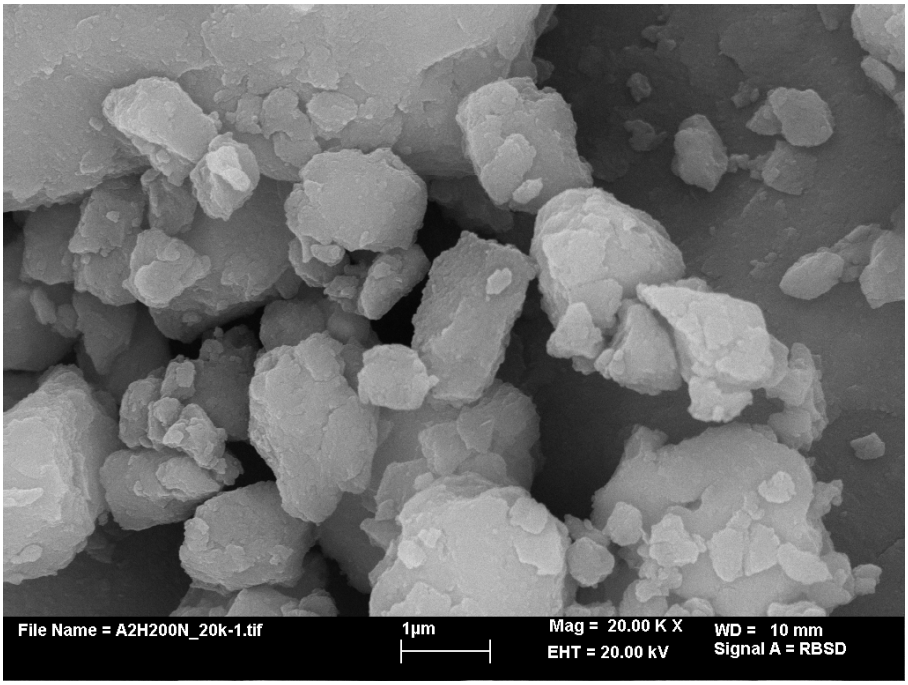

(f)

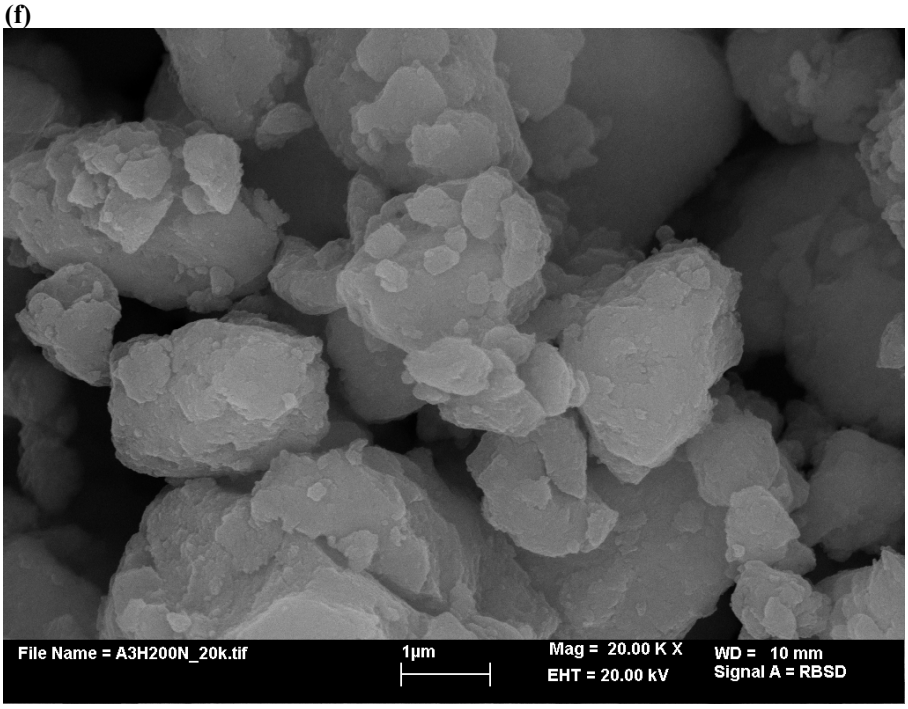

(g)

Fig.9.2 cont'd

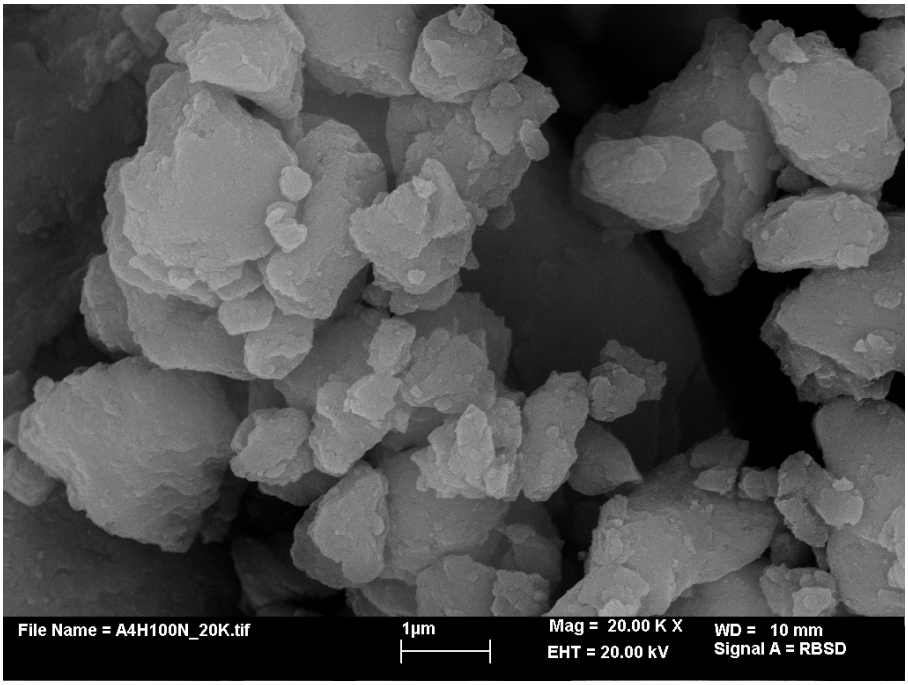

(h)

Fig.9.2 cont'd

Fig. 9.2 shows the BSE micrographs of the morphology of A1H, A2H, A3H and A4H powders (Table 7.2) after milling for 10h (Fig. 9.2a-d) and 100h/200h (Fig. 9.2e-h). The powders are well refined after 200h of CRMA regardless of what combination of starting materials was used for milling (Fig. 9.2e-h). The measurements of particle size have been carried out and Fig. 9.3 shows the dependence of the particle equivalent circle diameter (ECD) for A1H-A3H powders after milling for 10 and 200h. The results show that the ECD of A1H10 is almost six fold smaller than the other two and the milling for 200h refines very substantially the particle size for each powder batch.

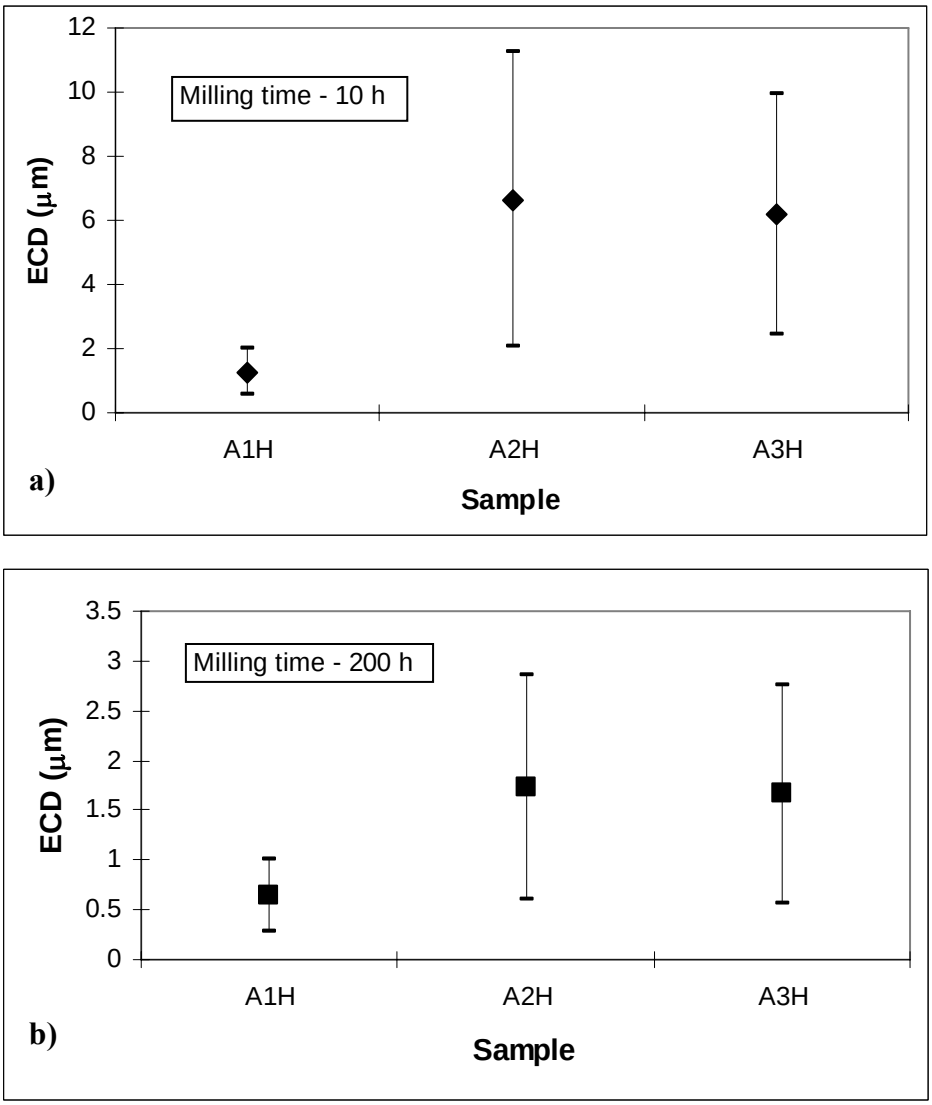

Fig. 9.3 The equivalent circle diameter (ECD) of powder particles after milling for (a) 10h and (b) 200h for A1H, A2H and A3H powders.

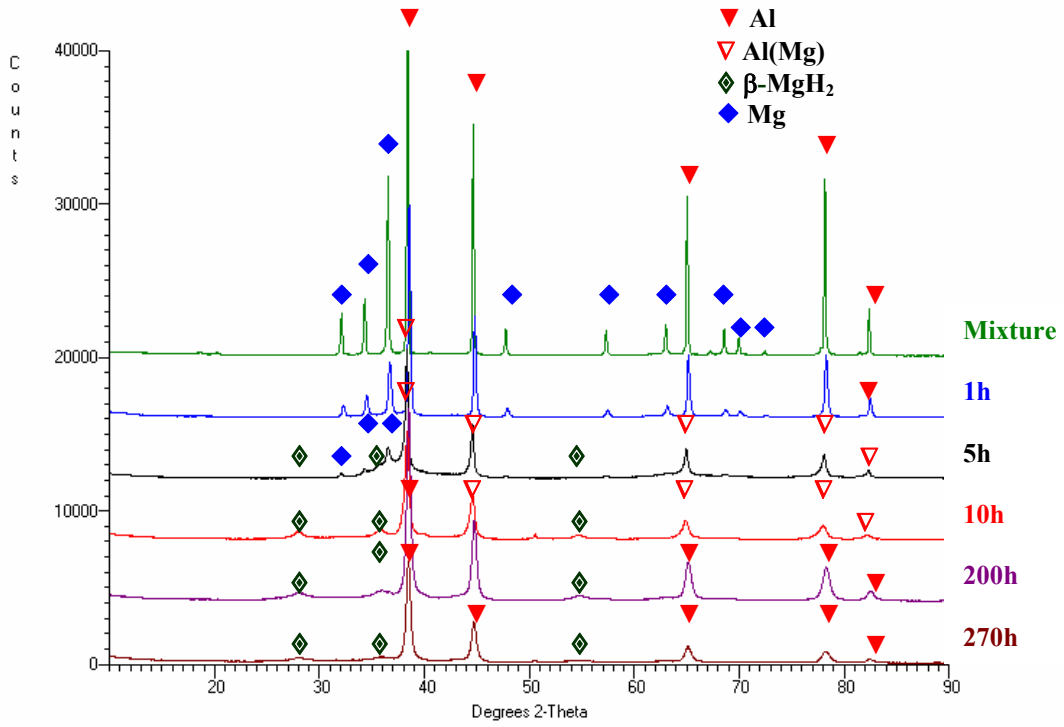

Fig. 9.4 XRD patterns of A1H powders milled using elemental Mg and Al powders as starting materials.

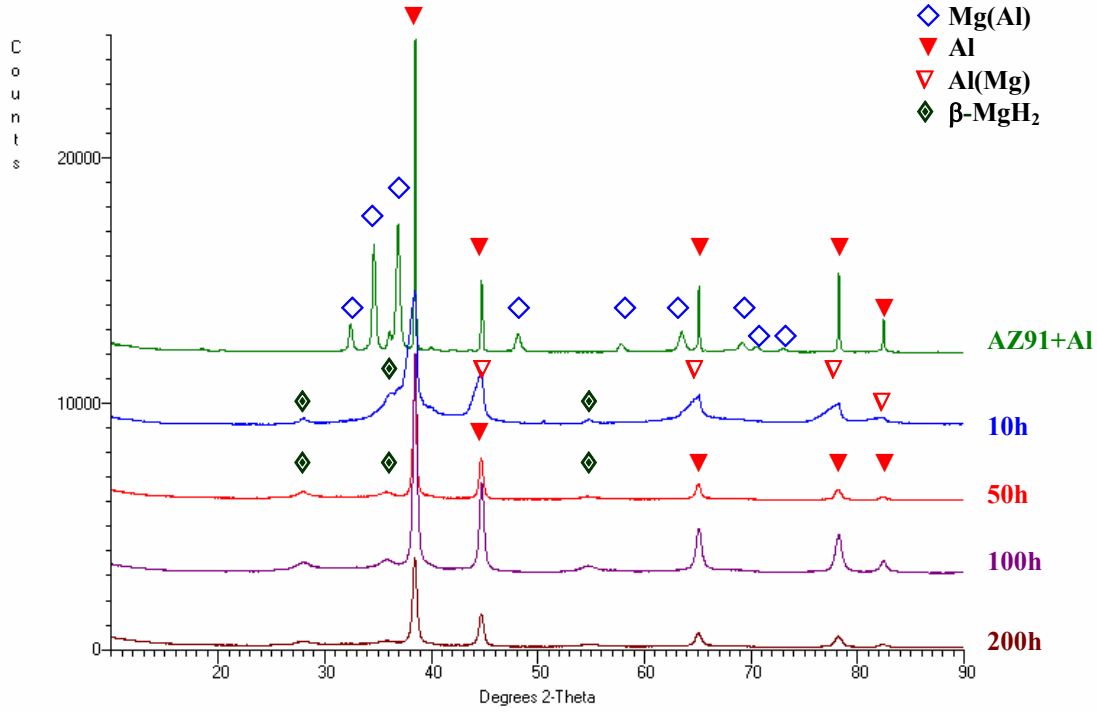

Fig. 9.5 XRD patterns of A2H powders milled using commercial AZ91 and the elemental Al powder as starting materials.

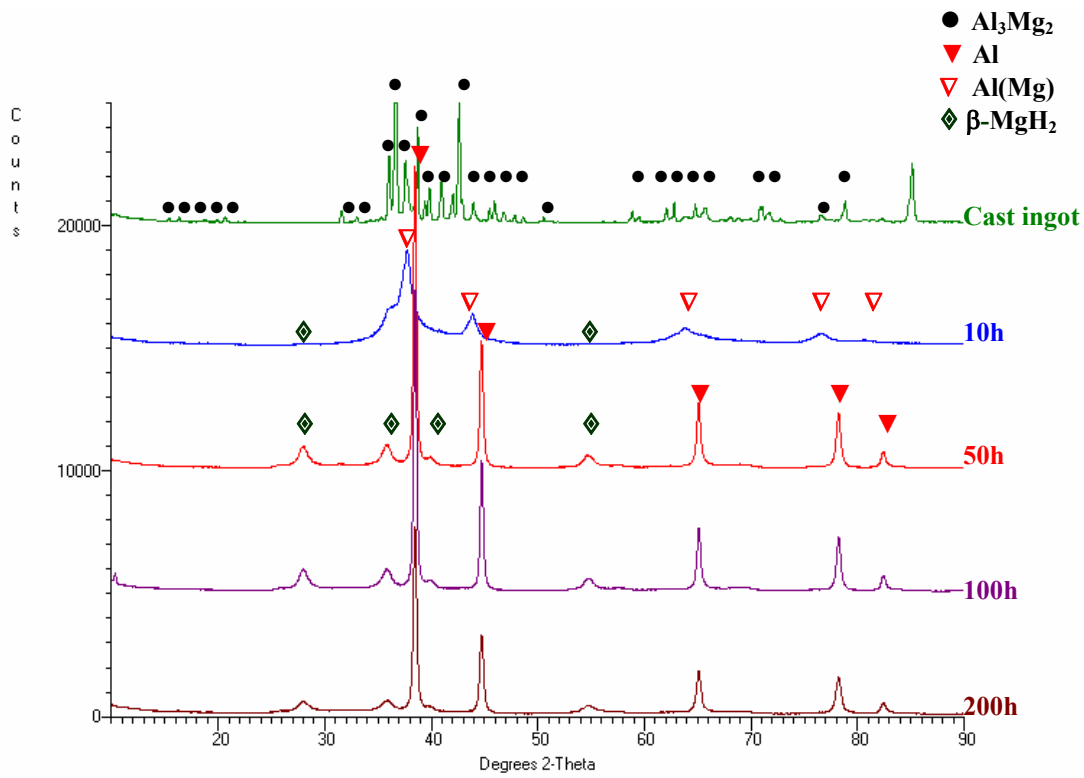

Fig. 9.6 XRD patterns of milled A3H powders milled using cast and powdered Mg-2Al ingot as starting material.

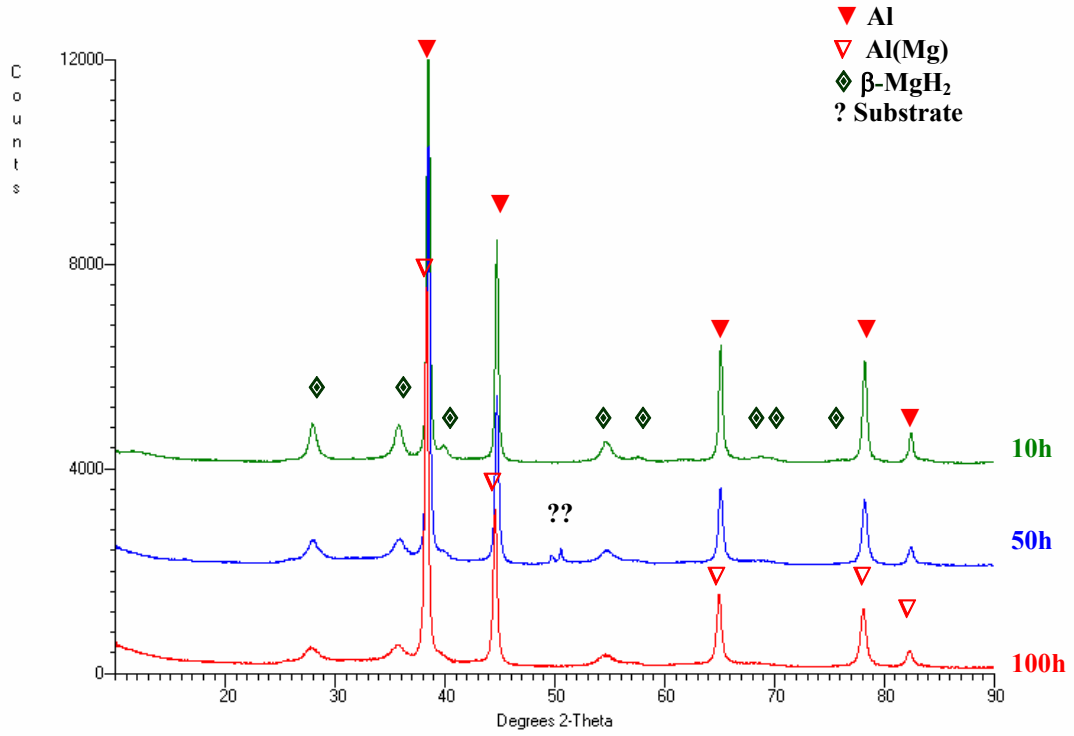

Fig. 9.7 XRD patterns of A4H powders milled using mixture of commercial MgH_2 and 2Al as starting material.

Table 9.1 Lattice parameter of primary Al powder and Al(Mg) solid solution present in the starting materials and as-milled powders.

Powder	Milling time (h)	Lattice parameter (nm) (FCC)	
		Average	Error[2]
Pure Al	0	0.4031	0.0013
	0	0.4038	0.0016
A1H	1	0.4031	0.0013
	5	0.4043[1]	0.0017
	10	0.4048[1]	0.0014
	200	0.4032	0.0015
	270	0.4032	0.0015
A2H	0	0.4035	0.0014
	10	0.4043[1]	0.0022
	50	0.4038	0.0015
	100	0.4035	0.0014
	200	0.4036	0.0015
A3H	10	0.4114[1]	0.0014
	50	0.4036	0.0015
	100	0.4035	0.0014
	200	0.4034	0.0015
A4H	10	0.4036	0.0014
	50	0.4036	0.0014
	100	0.4042[1]	0.0017

[1] Al(Mg) solid solution
[2] Average lattice parameter and error are calculated by software TRACES™ V.6.5.1

Table 9.2 Lattice parameter of pure Mg and Mg(Al) solid solution present in the starting material and as-milled powders.

Powder	Milling time (h)	Lattice parameter (nm) (Hexagonal)			
		a		c	
		Average	Error[2]	Average	Error[2]
Pure Mg	0	0.3206	0.0004	0.5208	0.0289
A1H	0	0.3215	0.0002	0.5214	0.0003
	1	0.3208	0.0003	0.5204	0.0006
	5	0.3214	0.0004	0.5216	0.0005
A2H	0	0.3191[1]	0.0004	0.5178[1]	0.0005

[1] Mg(Al) solid solution in commercial AZ91 alloy
[2] Average lattice parameter and error are calculated by software TRACES™ V.6.5.1

Microstructural evolution of batches A1H-A4H as a function of milling time can be seen by XRD patterns in Fig. 9.4- Fig. 9.7. Table 9.1 and Table 9.2 show the estimate of lattice parameters of Al, Mg and their solid solutions. In the A1H powder, in which the

elemental Mg and Al powders were used as starting materials, the peaks of β-MgH_2 phase which co-exist with the peaks of Al, are clearly observed after 10h of milling (Fig. 9.4). However, a striking finding is that the lattice parameter of Al in Table 9.1 increases for the powder A1H5 milled for 5h (0.4043±0.0017nm) and reaches the maximum after 10h (0.4048±0.0014nm). It means that a measurable lattice expansion occurred due to formation of a solid solution of Mg in Al, i.e. Al(Mg). The lattice expansion due to solid solution is very consistent with the magnitude of the atomic radius of Al and Mg which is 0.1432 and 0.1604 nm, respectively [103]. As milling time increases over 10h, the lattice parameter of Al decreases to the value characteristic of pure Al (Table 9.1). Since the changes in the lattice parameter of Al occur simultaneously with the formation and growth of β-MgH_2, it appears that up to approximately 10h of milling a large fraction of Mg dissolves in Al forming the Al(Mg) solid solution and the remaining Mg reacts with hydrogen to form β-MgH_2 whose diffraction peaks are clearly discernible after 10h of milling (Fig. 9.4). When the milling duration increases the Mg atoms in the solid solution start reacting with hydrogen to form more β-MgH_2. As a result, the solid solution is gradually depleted with Mg until it practically becomes nearly a pure Al. It can be deduced that the formation of Al(Mg) solid solution and β-MgH_2 hydride are strongly competitive processes up to approximately the first 10h of reactive milling. It leads to the conclusion that in the first 10h of milling the rate of formation of the Al(Mg) solid solution is higher than the rate of formation of β-MgH_2. The XRD Al peaks for the A1H powder are still observed after milling for 270h, which indicates that the Al phase has not reacted with either β-MgH_2 or hydrogen to form $Mg(AlH_4)_2$. As a result, no peaks of complex hydride $Mg(AlH_4)_2$ are observed in the XRD pattern of the milled A1H powder

even after 270h of milling duration. As milling time increases, the β-MgH_2 peaks become gradually broadened and weaker due to the reduction of its crystallite (nanograin) size to the nanometric level.

The A2H powder was prepared by mixing a commercial AZ91 alloy and the elemental Al powder. The majority phase in AZ91 is essentially a Mg(Al) solid solution whose XRD peaks are clearly designated in Fig. 9.5. The lattice parameter of Mg(Al) solid solution is smaller than that of pure Mg (Table 9.2) which indicates a lattice contraction and is consistent with the fact that the atomic radius of Al is smaller than Mg [103] as shown earlier. After milling for 10h, the XRD peaks of Mg(Al) disappear and the peaks of β-MgH_2 appear (Fig. 9.5). This means that the Mg(Al) solid solution quickly decomposes. Simultaneously, the Al peaks become asymmetrical (Fig. 9.5) and the lattice parameter of Al in this powder becomes the largest one after 10h of milling (Table 9.1). This is a result of a lattice expansion due to formation of Al(Mg) solid solution similar to that in the A1H10 powder. With increasing milling time the lattice parameter of Al in A2H starts decreasing (Table 9.1) which indicates that Mg in the solid solution starts reacting intensively with hydrogen to form more β-MgH_2. As mentioned earlier, the formation of Al(Mg) solid solution and β-MgH_2 hydride are competitive processes and formation of the former prevails up to approximately the first 10h of milling. The Al peaks are still observed after milling for 200h, which indicates that the Al phase has not reacted with either β-MgH_2 or hydrogen to form $Mg(AlH_4)_2$. As such, no peaks of complex hydride $Mg(AlH_4)_2$ are observed in the XRD pattern of milled A2H powder even after 200h of milling duration. With increasing milling time the β-MgH_2 peaks

become broadened and weaker (Fig. 9.5) due to the reduction of its crystallite (nanograin) size to the nanometric level.

The XRD pattern of A3H powder, (Fig. 9.6) shows that the starting material, which is the as-cast Mg-2Al alloy, consists of majority Al_3Mg_2 intermetallic phase. A short milling time of 10h results in the complete decomposition of Al_3Mg_2 and the creation of solid solution Al(Mg). An important finding is that the lattice parameter of Al(Mg) in the A3H10 powder after 10h of milling is actually the largest one as compared to the Al(Mg) parameter in A1H10 and A2H10 (Table 9.1). That indicates the most extensive solutionizing effect as a result of the decomposition of Al_3Mg_2. The XRD peaks of β-MgH_2 are weak but recognizable after 10h (Fig. 9.6) which shows that a limited amount of hydride has been formed. Such a behavior again confirms a competition between formation of Al(Mg) solid solution and β-MgH_2. The rate of formation of Al(Mg) seems to be much faster than that of β-MgH_2 up to 10h of reactive milling. The lattice parameter of Al(Mg) in the A3H powder profoundly decreases with increasing milling time such that after 50h it is nearly equal to that of pure Al (Table 9.1). In addition, longer milling produces larger amount of β-MgH_2 although there is no discernible difference between its peak intensities from 50 to 200h (Fig. 9.6). No peaks of complex hydride $Mg(AlH_4)_2$ are observed in the XRD pattern of milled A3H powder even after 200h of milling duration. With increasing milling time the β-MgH_2 peaks become broadened and weaker (Fig. 9.6) due to the reduction of its crystallite (nanograin) size to the nanometric level.

Finally, XRD patterns of A4H powder, which uses a mixture of commercial MgH_2 powder and elemental Al powder as starting materials, are shown in Fig. 9.7. The competition between formation of Al(Mg) solid solution and β-MgH_2 observed in A1H-

A3H powders is weak in the A4H powders because free Mg has not been available until a 100h of milling. Increase of the lattice parameter of Al in A4H powders after milling for 100h (Table 9.1) indicates a formation of Al(Mg) solid solution. The origin of free Mg is not clear but it may be due to the partial decomposition of β-MgH_2 in the presence of Al after a prolonged milling time (100h). No peaks of complex hydride $Mg(AlH_4)_2$ are observed in the XRD pattern of milled A4H powder after milling for 100h. With increasing milling time the β-MgH_2 peaks become broadened and weaker (Fig. 9.7) due to the reduction of its crystallite (nanograin) size to the nanometric level. The two unidentified peaks (marked as "?") in the XRD pattern of 50h milled sample are most likely from the substrate.

Table 9.3 and Table 9.4 show nanograin (crystallite) size and lattice strain of the β-MgH_2 and Al phase present in the as-milled A1H-A4H powders, respectively. It can be seen in Table 9.4 that for all of the A1H-A4H batches the β-MgH_2 phase undergoes a very fine nanostructurization and its crystallite (nanograin) size becomes saturated (~6-11nm), without associated lattice strain, after reactive milling for 50h and longer. However, as can be seen in Table 9.4, the crystallite (nanograin) size of Al and Al(Mg) is still in the ~30-60 nm range exhibiting lattice strain.

The hydrogen pressure changes inside the milling vial were monitored throughout the entire milling duration to calculate the amount of absorbed hydrogen. Fig. 9.8 shows an example of the absorbed hydrogen (wt.%) as a function of milling time calculated by the sum of hydrogen pressure drop ($\Sigma\Delta P$) inside the milling vial as a function of milling time for the A3H powder. The amount of absorbed hydrogen increases with increasing reactive milling time up to 50h after which the absorbed hydrogen saturates for longer

milling times (maximum amount is ~2.8 wt.%). This means that the process of the formation of β-MgH_2 hydride phase which absorbs hydrogen was essentially completed up to 50h of milling and afterwards the formation of β-MgH_2 stopped despite longer milling duration. This is accompanied by the saturation of its crystallite (nanograin) size with prolonged milling (Table 9.3).

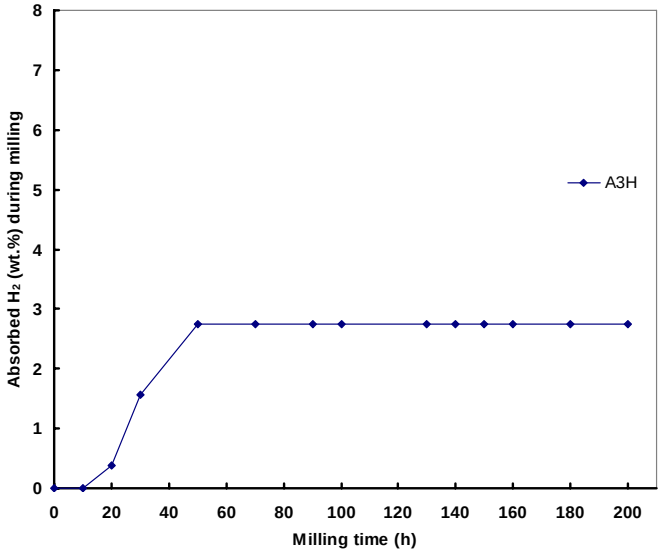

Fig. 9.8 Absorbed hydrogen (wt.%) for the A3H powder as a function of milling time.

Table 9.3 Nanograin size L, strain e, numbers of XRD peaks used for calculation and linear regression coefficient R^2 from Eq. 6.1 of β-MgH_2 in the A1H-A4H powders.

Powder	β-MgH_2 Nanograin size, L and strain, e				
	Milling time (h)	L (nm)	e	R^2	No. of XRD peaks
A1H	5	25	2.1×10^{-3}	0.999	3
	10	12	0	0.998	3
	200	6	0	0.999	3
	270	6	0	0.994	3
A2H	10	16	0	0.999	3
	50	13	0	0.865	4
	100	6	0	0.989	3
	200	6	0	0.992	4
A3H	10	12*	-	-	1
	50	9	0	0.999	4
	100	10	0	0.995	4
	200	11	0	0.981	4
A4H	10	14	1.1×10^{-3}	0.932	5
	50	8	0	0.994	4
	100	6	0	0.987	4

***Calculated using Scherrer equation**

Table 9.4 Nanograin size L, strain e, numbers of XRD peaks used for calculation and linear regression coefficient R^2 from Eq. 6.1 of Al in the A1H-A4H powders.

Powder	Al nanograin size, L and strain, e				
	Milling time (h)	L (nm)	e	R^2	No. of XRD peaks
A1H	1	119	5.6×10^{-5}	0.999	4
	5	77*	7.5×10^{-4}	0.595	5
	10	25*	1.4×10^{-3}	0.946	5
	200	45	2.5×10^{-3}	0.766	5
	270	34	2.5×10^{-3}	0.944	5
A2H	10	13*	4.3×10^{-3}	0.978	5
	50	59	1.9×10^{-3}	0.724	5
	100	32	1.6×10^{-3}	0.919	5
	200	34	2.2×10^{-3}	0.966	5
A3H	10	7*	0	0.906	5
	50	73	1.1×10^{-3}	0.672	5
	100	77	1.1×10^{-3}	0.684	5
	200	50	1.4×10^{-3}	0.884	5
A4H	10	119	1.4×10^{-3}	0.333	5
	50	62	1.4×10^{-3}	0.738	5
	100	59*	1.8×10^{-3}	0.734	5

***Al(Mg) solid solution**

9.1.1.2 Thermal behavior

Hydrogen desorption was investigated by DSC analysis. Fig. 9.9 shows DSC curves obtained upon heating up to 500°C for the A1H-A4H powders. Almost all DSC curves show two endothermic peaks. Peak #1 occurs at lower temperature (LT) and peak #2 at higher temperature (HT). The only exception is the A1H1 powder (milled for 1h) whose DSC curve shows only a single HT endothermic peak (Fig. 9.9a). DSC data for LT and HT peak such as the temperature of peak maximum (T_{peak}), onset (T_{on}) and end (T_{end}), enthalpy of the peak (ΔH), yield of β-MgH_2, hydrogen capacity and percentage of Mg reacted are summarized in Table 9.5.

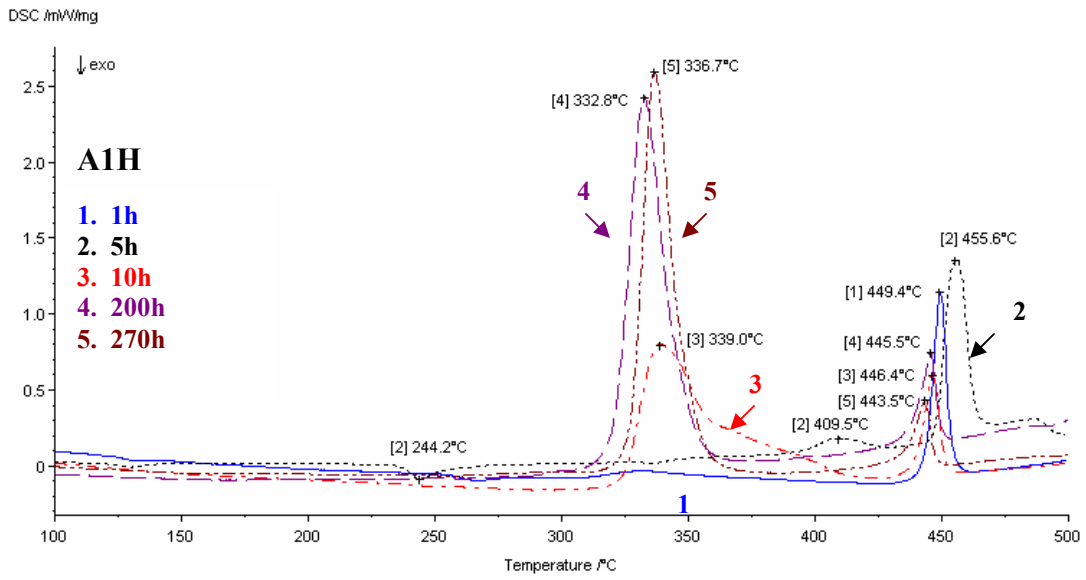

(a)

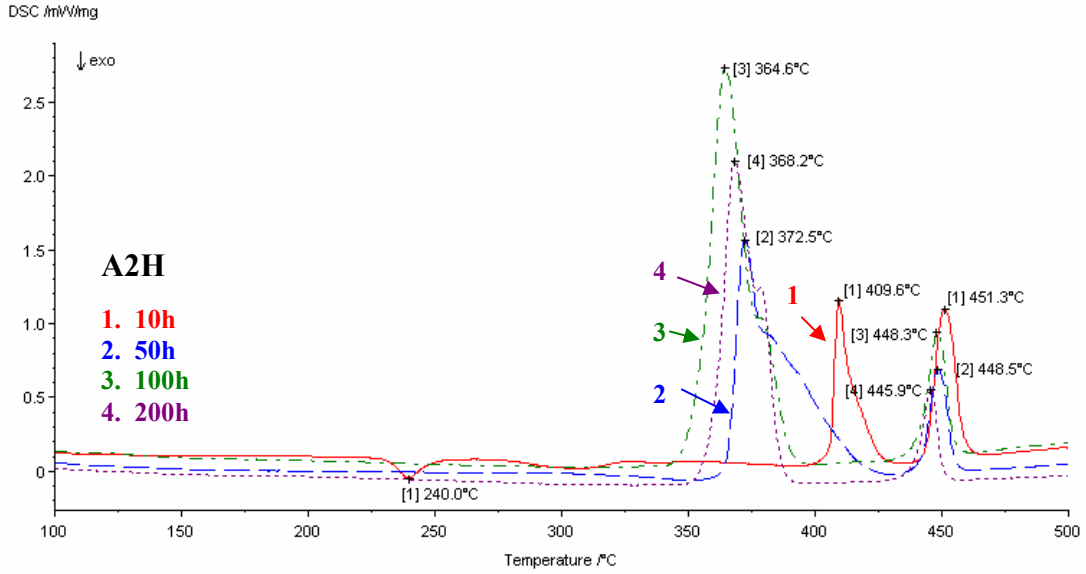

(b)

Fig. 9.9 DSC curves obtained upon heating for (a) A1H, (b) A2H, (c) A3H and (d) A4H powders.

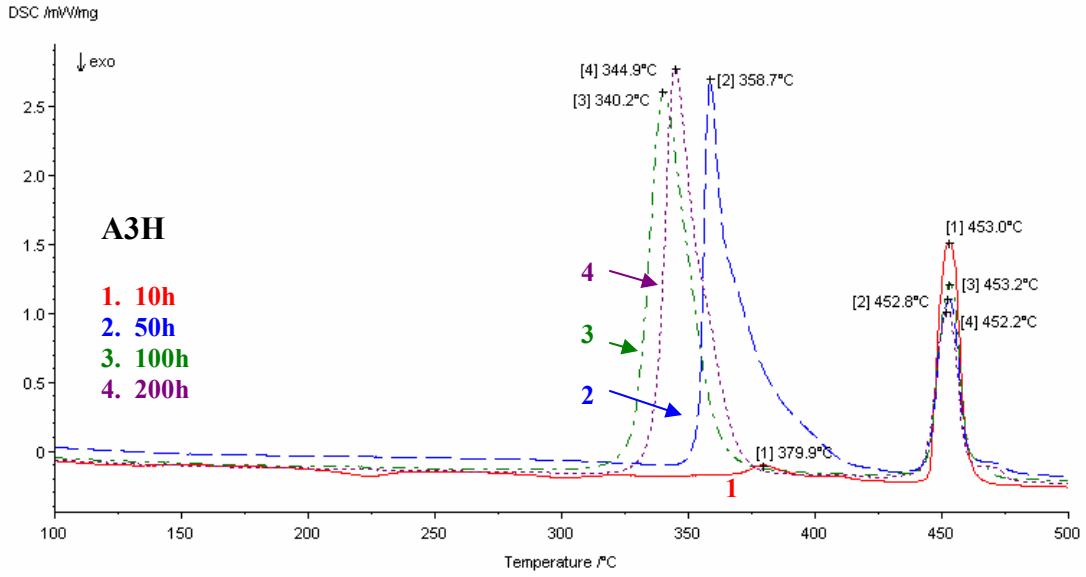

(c)

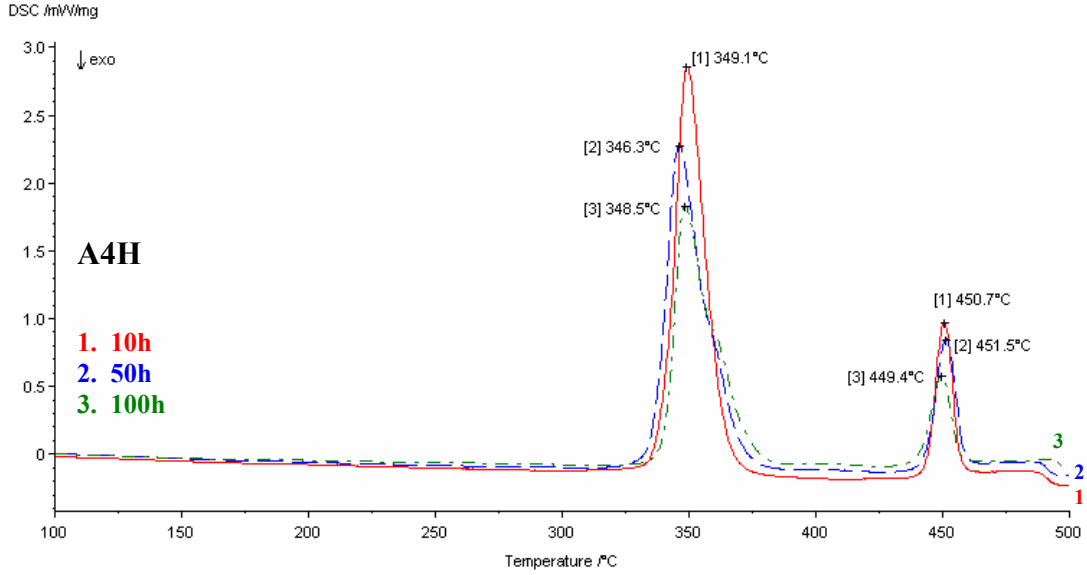

(d)

Fig. 9.9 cont'd

Table 9.5 Summary of DSC data for A1H-A4H powders upon heating.

	Endothermic-Peak #1 (LT)				Endothermic-Peak #2 (HT)						
	T_{on} (^oC)	T_{peak} (^oC)	T_{end} (^oC)	ΔH (J/g)	T_{on} (^oC)	T_{peak} (^oC)	T_{end} (^oC)	ΔH^{melt} (J/g)	Yield of MgH_2 (wt.%)	Desorbed Hydrogen from MgH_2 (wt.%)	Mg reaction rate (%)
A1H1	-	-	-	-	443.3	449.4	453.8	149	-	-	-
A1H5	395.6	409.5	425.2	29	447.9	455.6	462.9	218	1.0	0.1	3.0
A1H10	325.3	339.0	410.6	423	440.0	446.4	451.3	93	14.9	1.2	45.9
A1H200	321.0	332.8	346.7	761	438.7	445.5	450.2	79	26.8	2.1	81.5
A1H270	326.5	336.7	349.3	706	436.4	443.5	446.7	61	24.8	1.9	75.6
A2H10	406.1	409.6	426.4	185	444.2	451.3	458.7	179	6.4	0.5	19.2
A2H50	358.9	372.5	396.4	719	442.5	448.3	456.3	120	25.3	2.0	75.0
A2H100	353.4	364.6	389.9	939	440.8	448.3	454.5	143	33.0	2.5	97.9
A2H200	359.4	368.2	385.8	673	439.5	445.9	450.3	86	23.7	1.9	70.3
A3H10	370.4	379.9	388.7	20	445.4	453.0	459.7	312	0.7	0.1	2.1
A3H50	354.2	358.7	406.5	854	445.3	452.8	459.4	212	30.0	2.4	89.2
A3H100	329.1	340.2	360.7	954	444.8	453.2	459.6	278	33.5	2.6	99.5
A3H200	336.9	344.9	360.3	918	444.4	452.2	459.2	255	32.2	2.5	95.7
A4H10	340.2	349.1	362.6	784	444.3	450.7	456.7	166	27.5	2.1	82.1
A4H50	336.5	346.3	361.6	766	443.9	451.5	458.2	159	26.9	2.1	79.9
A4H100	340.8	348.5	372.4	622	441.7	449.4	456.6	114	21.8	1.6	64.9

There is a weak exothermic peak at ~240-244^{o}C in A1H5 and A2H10 powder during heating process.
The enthalpy, ΔH and ΔH^{melt}, was calculated from the endothermic peak area by DSC software using linear protocol.
Yield of β-MgH_2 was estimated assuming that the enthalpy formation of β-MgH_2 is ΔH_f = 74kJ/mol [34].
Mg reaction rate is equal to the amount of Mg in the β-MgH_2 divided by the amount of Mg in the starting material.

Furthermore, if one compares DSC curves (Fig. 9.9) and XRD patterns of the investigated powders (Fig. 9.4-Fig. 9.7), it can be seen that the LT peak is observed in the DSC curves for all powders for which the β-MgH_2 phase is observed in the corresponding XRD pattern. Since the A1H1 powder does not contain β-MgH_2 after 1h of reactive milling (Fig. 9.4) its DSC curve has only a singular HT peak (Fig. 9.9a). The temperature range of LT peak in Table 9.5 falls in the temperature range of the reported decomposition temperatures of β-MgH_2 synthesized by reactive mechanical alloying in

[98]. This confirms that the LT peak is due to the decomposition of β-MgH_2. In order to investigate the nature of the HT peak, an extra batch of elemental powder mixture Mg-2Al was milled for 1h under argon. Fig. 9.10 shows its DSC curve obtained upon heating. Only one HT peak with the maximum at 451.1°C is observed on DSC curve. This temperature is very close to the temperature of 449.4°C of HT peak for the A1H1 powder which does not contain β-MgH_2 (Table 9.5). This result indicates that the HT peak on DSC curves for the A1H-A4H powders in Fig. 9.9 is definitely not due to hydrogen desorption. Most likely, it is due to the melting of milled Mg-2Al powder mixture. The stoichiometric composition of Mg-2Al mixture (33at% Mg-67at% Al) falls exactly within the compositional range of Al(Mg)-Al_3Mg_2 eutectic in the binary Al-Mg system (Fig. G.11) whose melting temperature is reported as 450°C [104]. This is very close to the temperature observed for the HT peak on DSC curves in Fig. 9.9 and Fig. 9.10. Therefore, it is quite clear now that the Mg-2Al mixture hydrogenated upon reactive milling into β-MgH_2 and free Al (or Al(Mg)) when subjected to DSC test, in the first stage releases hydrogen by decomposition of β-MgH_2 giving rise to the first LT peak. After this, the mixture is converted back to the elemental Mg-2Al composition and starts melting eutectically, giving rise to the second HT peak on a DSC curve (Fig. 9.9).

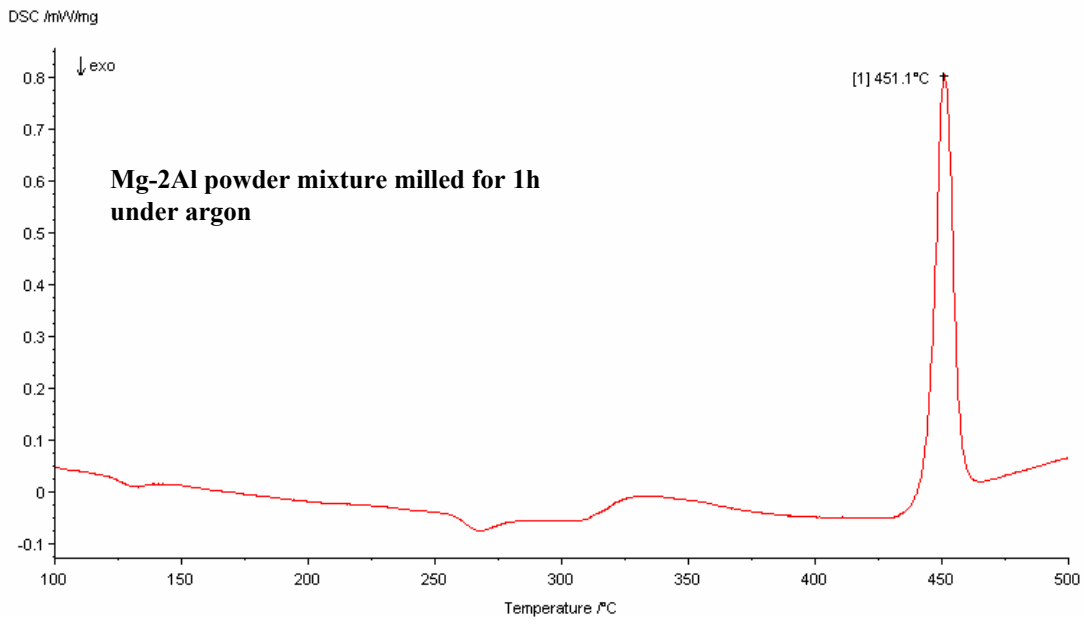

Fig. 9.10 DSC curve for the mixture of elemental Mg-2Al powder milled under argon for 1h.

However, a striking feature is observed in Table 9.5 with regard to the enthalpies of melting, ΔH^{melt}, calculated from the area under the HT peak. First, the enthalpy of melting of elemental mixture Mg-2Al calculated from the peak in Fig. 9.10, 130 J/g, is very close to the enthalpy of melting (149J/g) for A1H1 powder (1h milling) which does not contain β-MgH_2. Apparently, the 130-149 J/g range is the characteristic range of the enthalpy of melting of the elemental Mg and Al powders in the stoichiometric ratio Mg-2Al.

Second, the enthalpy of melting, ΔH^{melt}, for the powders milled for 5h or 10h, comprising the Al(Mg) solid solution and β-MgH_2 (with possibly some free elemental Al), is always the largest one for each A1H, A2H and A3H batch. When milling time increases beyond 10h and the Al(Mg) solid solution becomes depleted with Mg which

forms more β-MgH_2, the microstructure evolves into a phase mixture of Al + β-MgH_2 and the enthalpy of melting, ΔH^{melt}, starts decreasing with increasing milling time.

Third, the range of ΔH^{melt} for powders after 10h of milling is the smallest one for A1H (a mixture of elemental Mg + Al powders), larger for A2H (a mixture of AZ91 alloy + elemental Al powder) and the largest one for A3H (Mg-2Al cast alloy).

However, trends of ΔH^{melt} observed in A1H-A3H powders do not apply in A4H powders, which use a mixture of commercial MgH_2 powder and elemental Al powder as starting materials. ΔH^{melt} is the lowest in the A4H powder after milling for 100h containing Al(Mg) solid solution. This might be due to the fact that commercial MgH_2 powder rather than elemental Mg or Mg alloy is used as a starting material.

Table 9.6 Summary of DSC data for A1H-A4H powders upon cooling.

	Exothermic peak			
	T_{on} (^oC)	T_{peak}(^oC)	T_{end}(^oC)	ΔH (J/g)
A1H1	444.1	430.5	418.3	-120
A1H5	438.9	427.9	410.2	-185
A1H10	435.2	426.0	414.6	-88
A1H200	436.5	428.7	419.8	-93
A1H270	438.4	428.2	416.2	-72
A2H10	435.2	423.5	408.5	-140
A2H50	433.3	422.9	410.2	-112
A2H100	436.1	424.5	413.8	-136
A2H200	435.8	426.9	413.2	-81
A3H10	440.5	427.5	414.4	-253
A3H50	440.2	425.4	410.7	-182
A3H100	439.1	427.0	414.4	-213
A3H200	438.1	424.9	414.2	-190
A4H10	436.5	423.1	409.9	-108
A4H50	436.7	429.5	415.9	-148
A4H100	414.0	424.9	436.4	-109

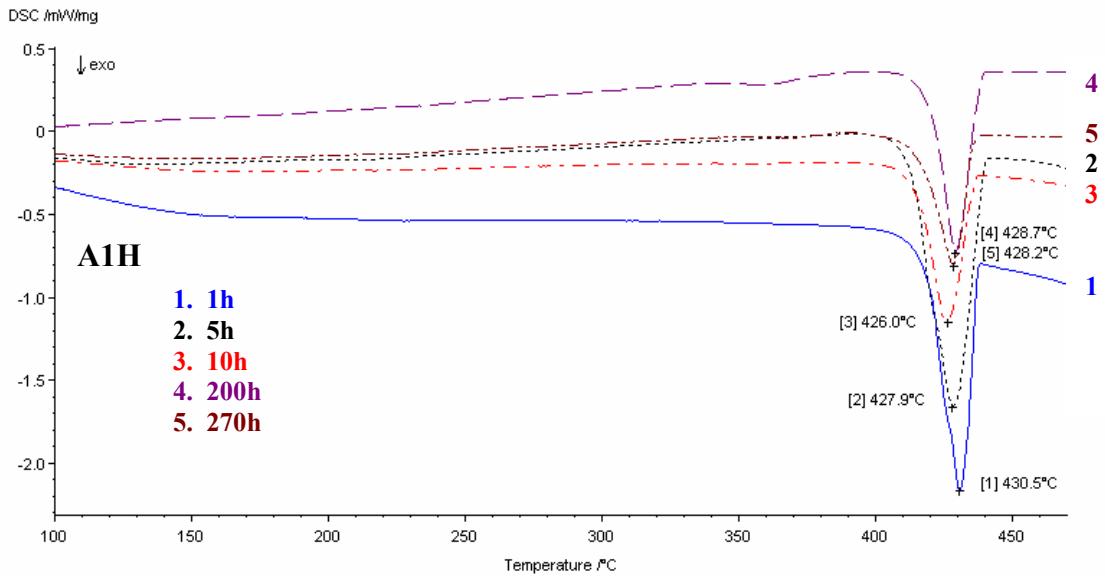

(a)

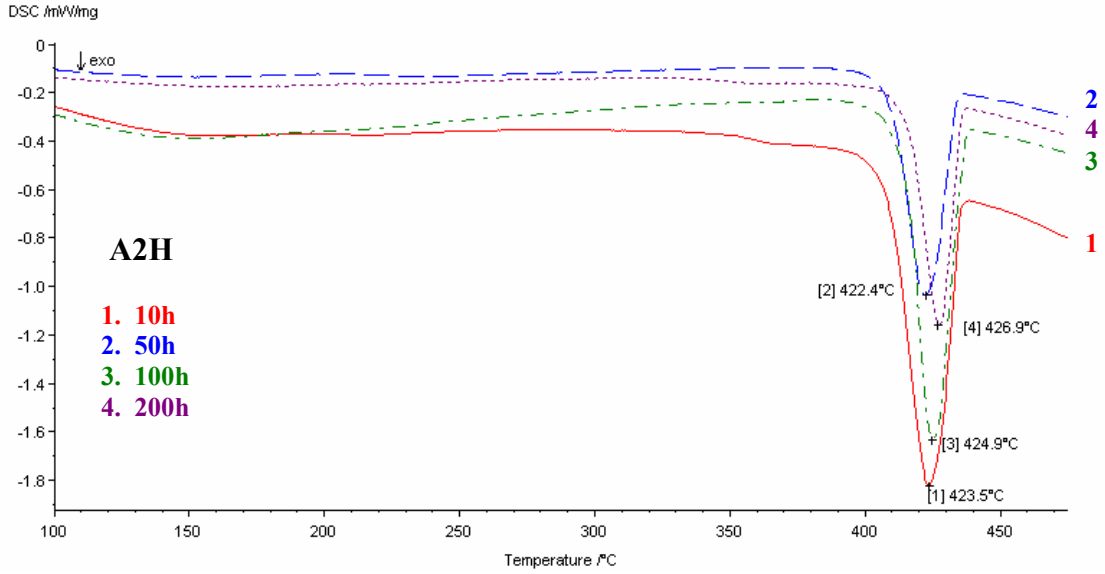

(b)

Fig. 9.11 DSC curves obtained upon cooling from 500°C for (a) A1H, (b) A2H, (c) A3H and (d) A4H powders.

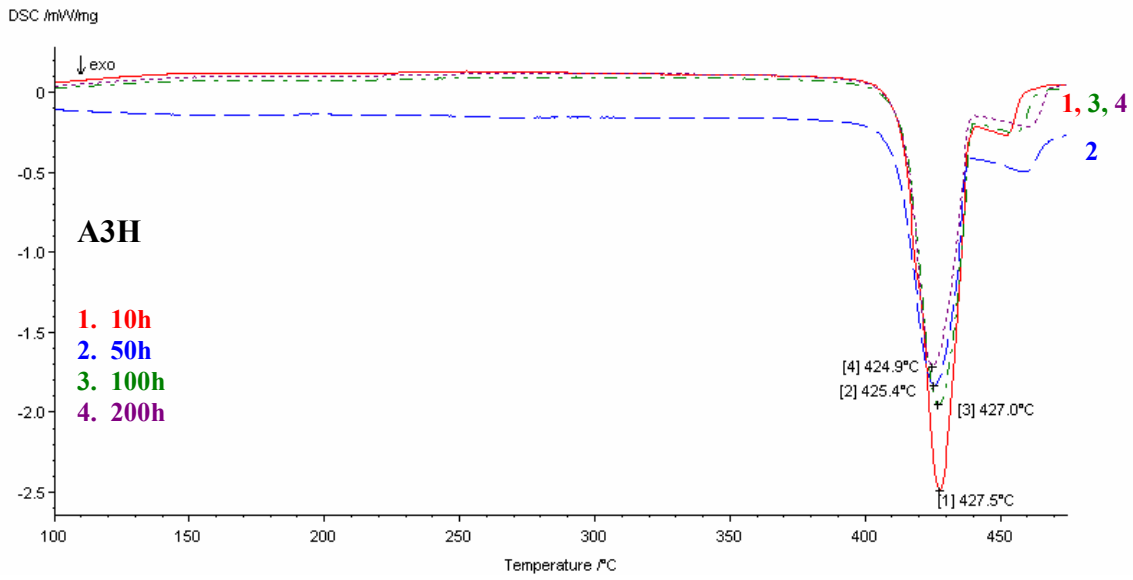

(c)

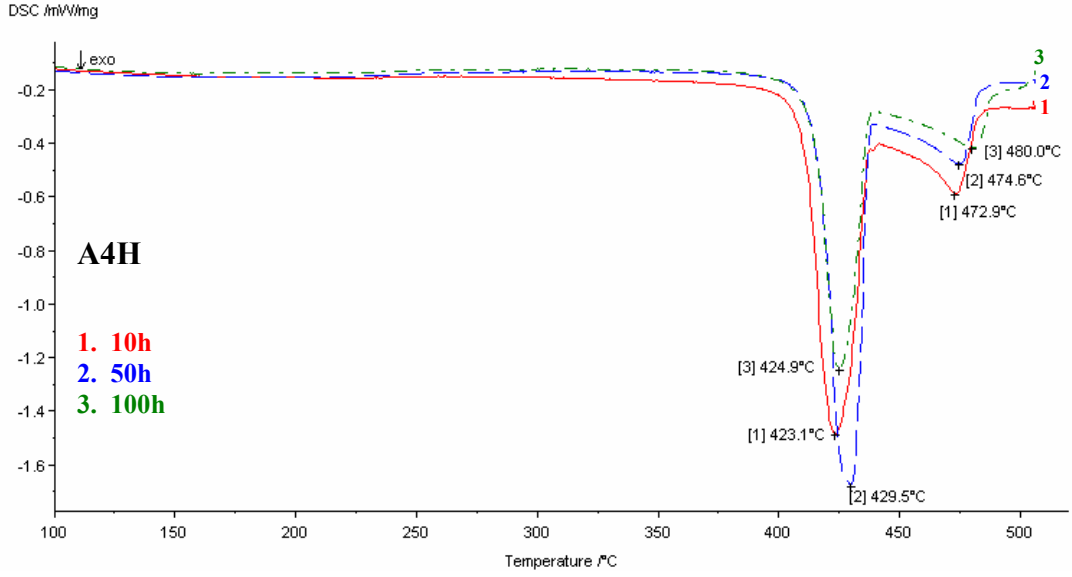

(d)

Fig. 9.11 cont'd

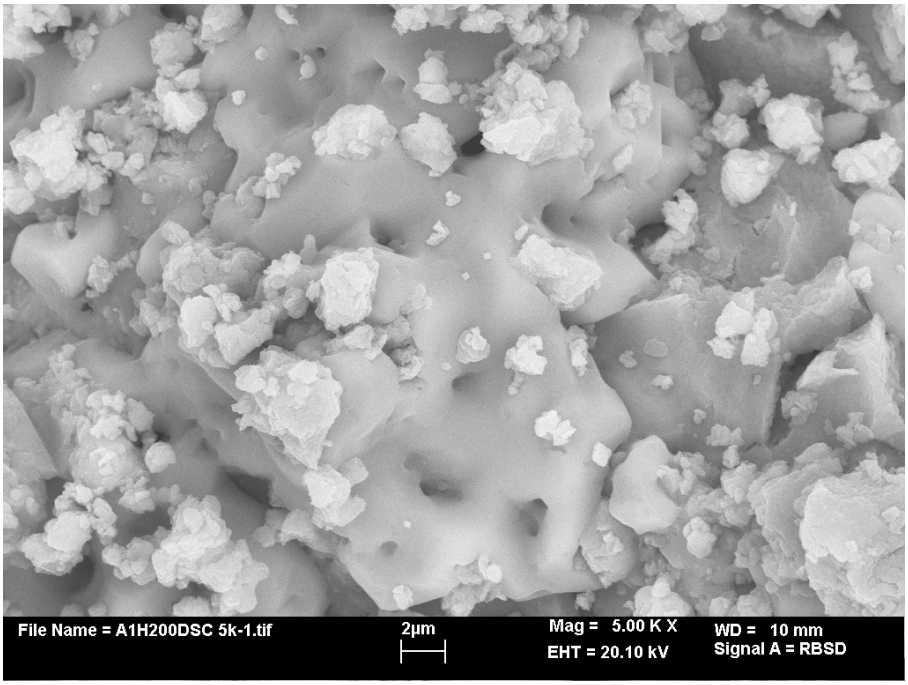

Fig. 9.12 BSE micrograph of the microstructure of A2H200 (milled for 200h) powder after cooling from 500°C to room temperature at 10°C/min in a DSC test.

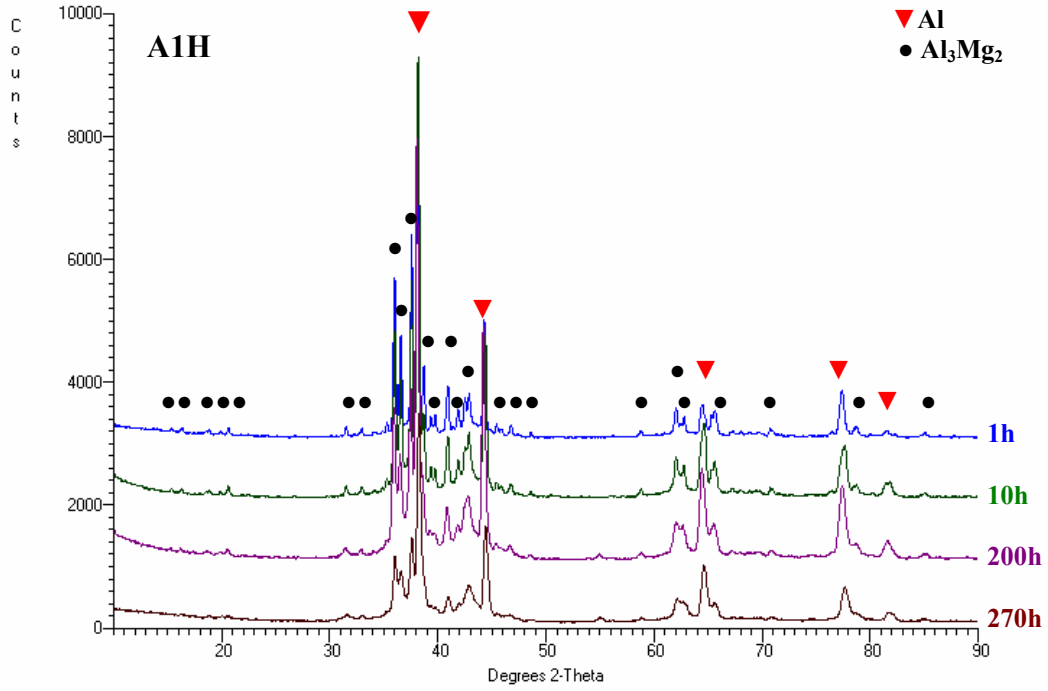

Fig. 9.13 XRD patterns of A1H powders after cooling from 500°C to room temperature at 10°C/min in a DSC test.

Some interesting information is also provided by DSC curves obtained on cooling, which are shown in Fig. 9.11. Without exception all four batches show a strong exothermic peak on cooling from 500°C. DSC data for the peak such as the temperature of peak maximum, onset and end, and enthalpy of the peak (ΔH) are summarized in Table 9.6 for all four powder mixtures. The range of the temperature of peak maximum is within a narrow 420-430°C interval. As a striking example, Fig. 9.12 shows BSE-SEM micrograph of the A2H200 (milled 200h) sample after cooling down to room temperature in DSC test. It is observed that the majority of powder particles underwent melting upon heating and solidification upon cooling. All the powders after cooling to room temperature were also investigated by XRD. Fig. 9.13 shows an example of XRD pattern for the A1H powders after cooling from 500°C in DSC. The majority phase in XRD pattern is the intermetallic phase Al_3Mg_2 coexisting with some excess Al. The XRD patterns obtained after cooling for the A2H-A4H powder mixtures are very similar to that in Fig. 9.13. Hence, it is quite clear that in DSC test up to 500°C, regardless of the combination of starting constituents and the duration of reactive milling time, the powders undergo eutectic melting at ~450°C and upon subsequent cooling they solidify at the 420-430°C range into the phase mixture of Al_3Mg_2 plus some excess Al. This is exactly an equilibrium structure corresponding to the stoichiometric composition of Mg-2Al in the binary Al-Mg system [104]. The solidification enthalpy for the powders milled for 5h or 10h is always the largest one for A1H, A2H and A3H. The magnitude of the solidification enthalpy for powders after a 10h of milling is the smallest one for A1H, larger for A2H and the largest one for A3H.

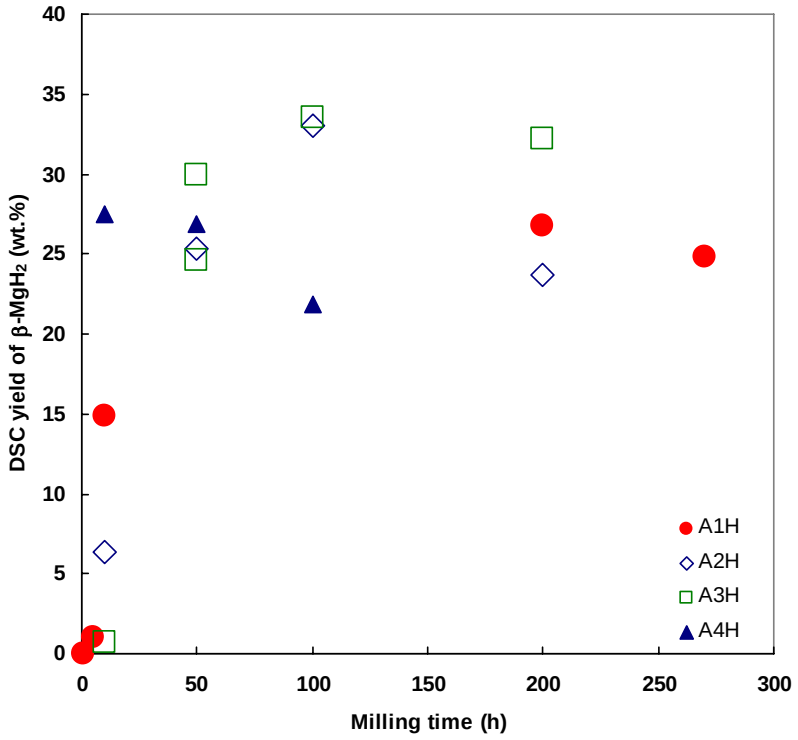

Fig. 9.14 DSC yield of β-MgH_2 as a function of milling time in A1H-A4H powders.

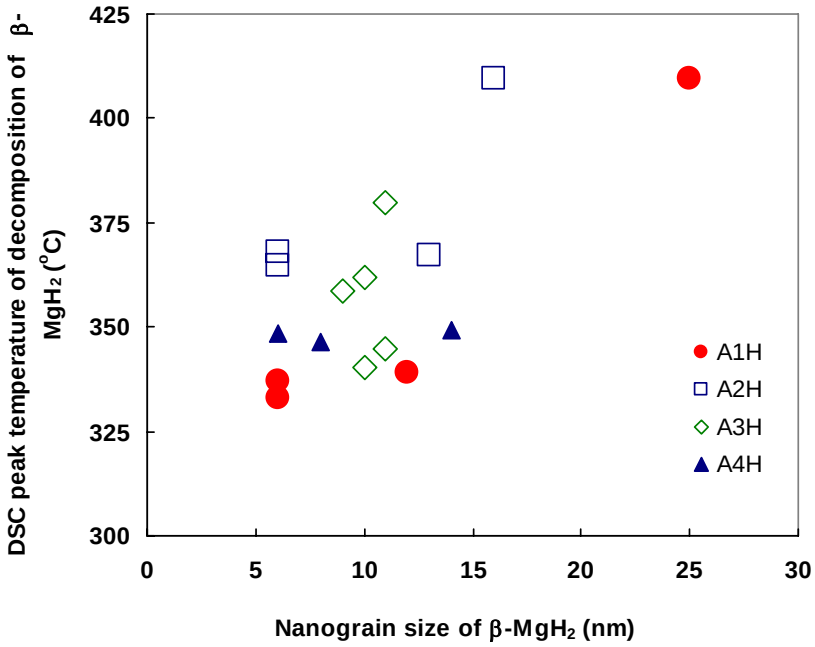

Fig. 9.15 DSC peak temperature of decomposition of β-MgH_2 (T_{peak}) versus nanograin size of β-MgH_2 present in A1H-A4H powders.

Fig. 9.14 shows the DSC yield of β-MgH_2 as listed in Table 9.5 as a function of milling time. In the A1H-A3H powders, the yield first increases dramatically in the early stage of milling and then attains a maximum (~34 wt.%) after milling for 100h and slightly decreases after further milling especially for the A1H200 and A2H200 powders. In A4H powders, the yield first keeps at ~ 27 wt.% after 50h of milling and then drops to ~22 wt.% after milling for 100h. This implies a decomposition of β-MgH_2 in the presence of Al, in which free Mg is available to form Al(Mg) solid solution after 100h.

Fig. 9.15 shows the DSC hydrogen desorption temperature (T_{peak} in Table 9.5) versus nanograin size of β-MgH_2. It seems that there is no systematic correlation between the DSC hydrogen desorption temperature and the nanograin size of β-MgH_2 formed in the mechanically alloyed Mg-Al-H system.

9.1.2 Annealed powders

In order to investigate the effect of annealing and the effect of property of Al on the phase transformation in the as-milled powders, A1H powders containing different types of Al were annealed in a Sieverts-type apparatus at various conditions (Table 9.7). Among them, A1H1 (milled for 1h) contains primary Al, A1H5 (milled for 5h) contains Al(Mg) solid solution, and A1H270 (milled for 270h) contains secondary Al. There are no substantial changes in morphologies of annealed A1H powders. In general, the particle size of annealed powders still governed by the milling time of as-milled powders which are used for annealing.

Table 9.7 Annealing parameters for A1H powders in a Sieverts-type apparatus.

Powder description	Powder used for annealing	Gas	Pressure (MPa)	Temperature (^{o}C)	Time (h)
A1H1-350-40-20	A1H1	Hydrogen	4.0	350	20
A1H1-100-40-100	A1H1	Hydrogen	4.0	100	100
A1H5-350-40-20	A1H5	Hydrogen	4.0	350	20
A1H5-100-40-100	A1H5	Hydrogen	4.0	100	100
A1H270-100-45-100	A1H270	Hydrogen	4.5	100	100

XRD patterns and DSC curves of the annealed A1H powders at various annealing conditions are given in Appendix F.2.1 and G.2.1, respectively. β-MgH_2, Al_3Mg_2 and Al(Mg) exist in the A1H1 and A1H5 powder after annealing at 350^{o}C under 4.0 MPa of hydrogen for 20h. Mg, Al and $Al_{12}Mg_{17}$ phases are present in the A1H1 and A1H5 powder after annealing at 100^{o}C under 4.0 or 4.5MPa of hydrogen for 100h powder. The phase constitution in the annealed A1H270 powder does not change with respect to those (β-MgH_2 and Al) in the as-milled A1H270 powder.

Except the DSC curve for A1H1-100-40-100 powder, which shows only an endothermic peak at the high temperature (HT), the rest of DSC curves for annealed A1H powders show two endothermic peaks at similar temperature ranges to those in as-milled A1H powders. As mentioned earlier, the low temperature (LT) peak and the high temperature (HT) peak in the annealed A1H powders are due to the decomposition of β-MgH_2 and the melting of milled Mg-2Al powder mixture, respectively. No ternary hydride is formed after annealing A1H powders at conditions given in Table 9.7.

9.2 Nanohydride formation under stronger milling mode

9.2.1 Milling mode

Mg-2Al powder mixture (A10H powder) was first milled for 30h under a more energetic mode (IMP68 mode in Table 7.2) and followed by annealing at 350^{o}C under 4MPa of hydrogen for 20h. β-MgH_2 and Al phase are observed in the as-milled and annealed powder mixture (Appendix F.2.2).

Similar to the DSC curves of the counterparts in A1H powders, two endothermic peaks corresponding to the decomposition of β-MgH_2 and the eutectically melting of the Mg-2Al mixture are observed (Appendix G.2.2). The broadened and diffused low-temperature peak in DSC curve upon heating for the annealed powder mixture might due to an inhomogeneous particle size distribution after annealing.

The above results indicate Al phase does not reacted with either β-MgH_2 or hydrogen to form $Mg(AlH_4)_2$ in the powder mixture even after the milling mode has been changed to a more energetic one and after the following annealing under hydrogen.

9.2.2 Iron as a catalyst

Bobet et al. [105] studied the reactive mechanical alloying (RMA) of Mg under hydrogen and found that the formation ratio of MgH_2 in the milled powder mixture of MgH_2 and Mg can be improved by adding iron as a catalyst. Here, iron was added to the Mg-2Al cast ingot to study the effect of iron on the formation of ternary $Mg(AlH_4)_2$ hydride. A mixture of a Mg-2Al cast ingot and 10wt.% of iron was first pre-milled for 10h in a SPEX ball mill under argon and then milled in the Uni-Ball Mill for 50h under

hydrogen. The milled powder mixture was then annealed at 260^{o}C under 4.3MPa of hydrogen for 144h.

β-MgH_2, Al and Fe phase exist in the powder mixture after milling for 50h (Appendix F.2.2). This indicates Al or Fe phase has not reacted with either β-MgH_2 or hydrogen to form $Mg(AlH_4)_2$ in A5H powders even after the milling mode has changed to a more energetic one. The followed annealing of A5H50 powder results in the formation of Al_6Fe, which coexists with β-MgH_2, Al and Fe phase in the as-milled A5H50 powder. It seems that 10wt.% of iron does not act as a catalyst for the formation of $Mg(AlH_4)_2$.

DSC patterns (Appendix G.2.2) of the powder mixture are similar to those of the powder of Mg-2Al cast alloy (A3H powder). The low-temperature (LT) and high-temperature (HT) endothermic peaks must correspond to the decomposition of β-MgH_2 and the eutectically melting of the Mg-2Al mixture.

9.3 Synthesis of $Mg(AlH_4)_2$ hydride by mechano-chemical activation synthesis (MCAS)

9.3.1 Evolution of microstructure as a function of milling time

Fig. 9.16 shows the morphology and particle size distribution of the mixture of $NaAlH_4$ and $MgCl_2$ in a 2 to 1 stoichiometric ratio after milling for 5h, 10h and 40h (A11Cl powders in Table 7.2). Mean ECD particle sizes ± standard deviations of the powder after milling for 5, 10 and 40h are 2.7±2.3μm, 2.4±2.2μm and 2.3±2.2μm, respectively. Standard deviation is at the same level of the particle size. A prolonged milling time beyond 5h does not seem to change the mean value of particle size. Nonuniform particle size distribution is established after a 5h of milling and is still kept after 40h.

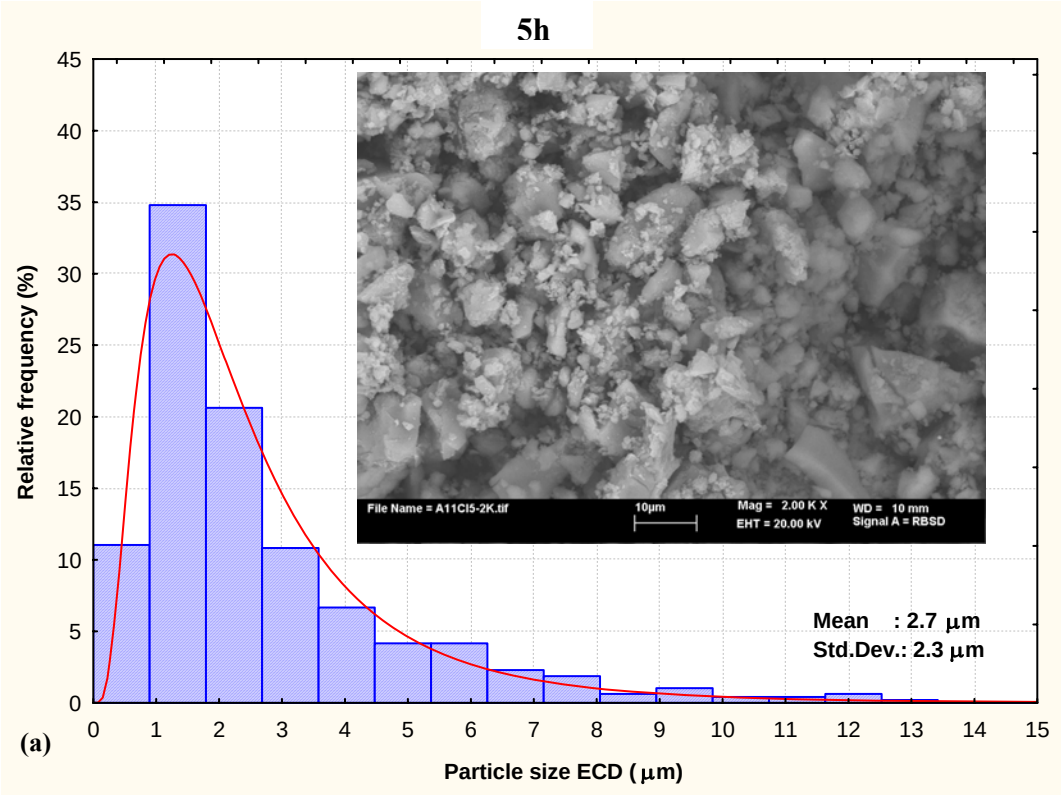

Fig. 9.16 Morphology and particle size distribution of the powder mixture of $NaBH_4$ and $MgCl_2$ in a 2 to 1 stoichiometric ratio (A11Cl powder) after milling for (a) 5h, (b) 10h and (c) 40h.

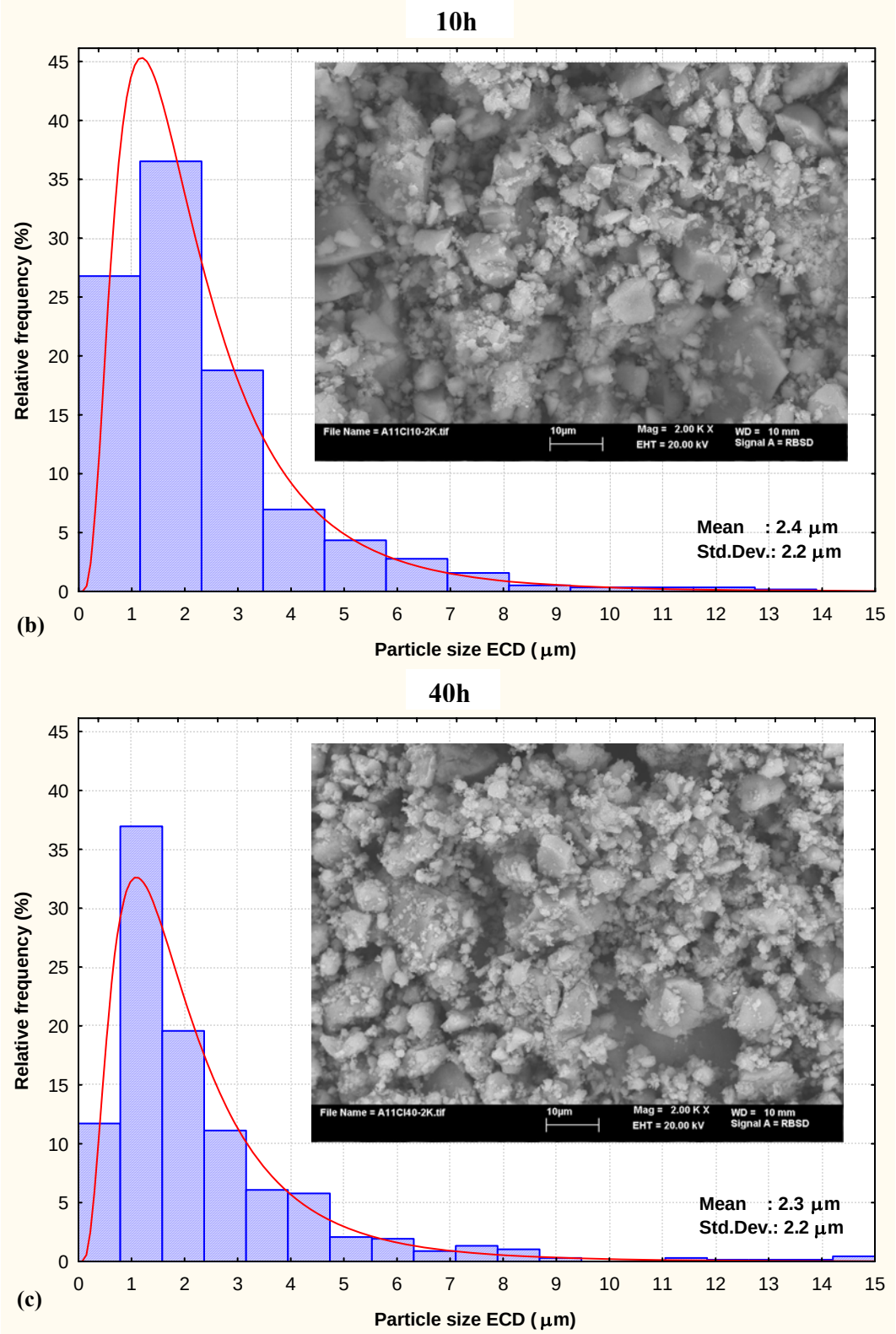

Fig. 9.16 cont'd

Fig. 9.17 shows XRD patterns of the mixture of $NaAlH_4$ and $MgCl_2$ in a 2 to 1 stoichiometric ratio (A11Cl powders) after milling for 5, 10 and 40h. The powder after milling for 5h consists of $Mg(AlH_4)_2$ (identified from JCPDS # 47-0980) and NaCl (identified from JCPDS # 05-0628). No peaks of starting compounds are observed. As a result, it can be assumed that after 5h of controlled mechano-chemical activation synthesis (MCAS) in the Uni-Ball Mill 5, the synthesis of $Mg(AlH_4)_2$ is completed according to the following reaction:

$$2NaAlH_4 + MgCl_2 \rightarrow Mg(AlH_4)_2 + 2NaCl \quad (9.1)$$

Mamatha et al. [46,47] and Kim et al. [48] also reported a synthesis of $Mg(AlH_4)_2$ by MCAS after a short milling time (1-3h). In the present work, it confirms that indeed only a relatively short time of milling is required for completion of the reaction (9.1).

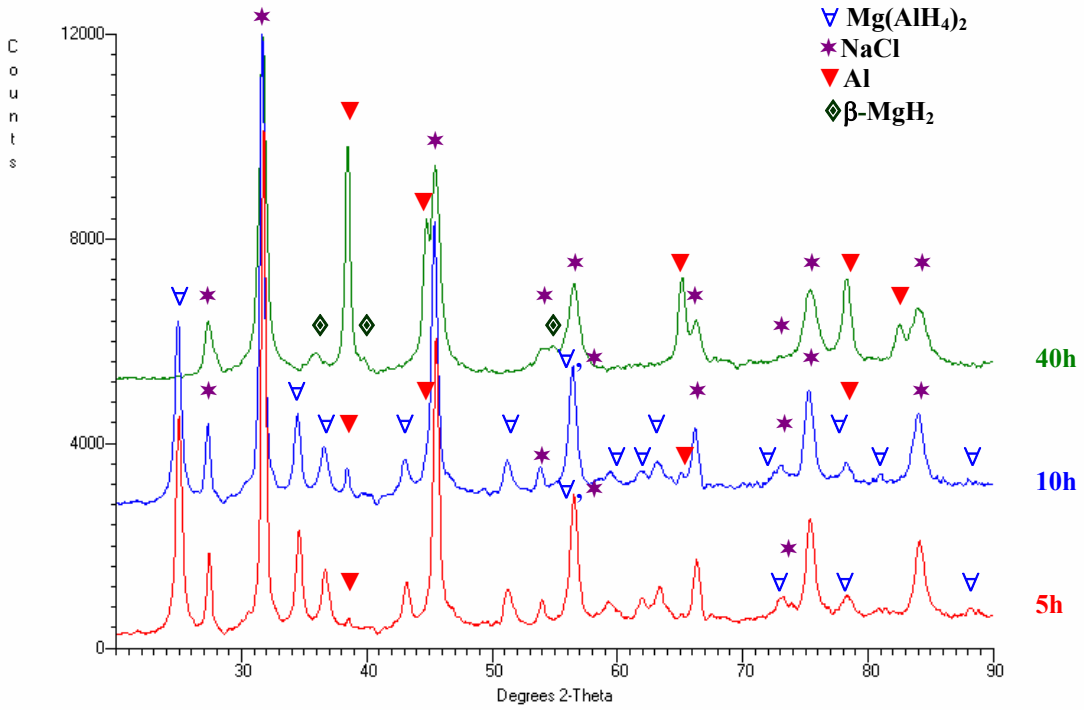

Fig. 9.17 XRD patterns of the powder mixture of $NaBH_4$ and $MgCl_2$ in a 2 to 1 stoichiometric ratio (A11Cl powder) after milling for 5, 10 and 40h.

The effect of prolonged milling duration on the reaction can be seen in Fig. 9.17. Only a very weak XRD peak of Al phase is observed in the XRD pattern of the 5h-milled powder (Fig. 9.17, a very weak peak of Al at $2\theta \sim 38^{o}$), which indicates a very small amount of Al exists in the powder after milling for 5h. As the milling time increases, intensities of Al peaks also increase. After 40h, the peaks of $Mg(AlH_4)_2$ are not observed and the MgH_2 peaks appear. In the mean time, pressure insides the milling cylinder increases by ~465 kPa, which equals to ~2.5wt.% of desorbed hydrogen assuming that hydrogen is the only gas released after milling for 40h. It can be concluded that after a short milling time, maximum a few hours, a mixture of $Mg(AlH_4)_2$ and NaCl is being

formed but further prolonged milling of the mixture results in a gradual decomposition of the magnesium alanate $Mg(AlH_4)_2$ in the mixture according to the following reaction:

$$Mg(AlH_4)_2\ (+2NaCl) \rightarrow \beta\text{-}MgH_2 + 2Al + 3H_2\ (+2NaCl) \quad (9.2)$$

It has to be pointed out that this decomposition occurs without the addition of Ti metal catalyst which was used by Mamatha et al. [46]. As opposed to the reaction (9.1) which occurs during short milling, the reaction (9.2) is not a metathesis reaction. Instead, a long milling triggers a reduction-oxidation (redox) reaction. The H and Al are mutually oxidized and reduced as shown below

$$Mg + 2\left(Al^{+3}H_4^{-1}\right)^{-1} \rightarrow MgH_2^{-1} + 3H_2^0 + 2Al^0 \quad (9.3)$$

and the partial reactions are as follows

$$2H^- - 2e \rightarrow H_2{}^0 \ \mid \times 3 \quad (9.4a)$$

$$Al^{+3} + 3e \rightarrow Al^0 \ \mid \times 2 \quad (9.4b)$$

As shown in Table 9.8, the hydrides and metal phase resulting from either the synthesis or decomposition reaction during milling are nanocrystalline. A grain size of ~18nm indicates that nanocrystalline $Mg(AlH_4)_2$ is produced after MCAS for 5h and 10h (Table 9.8). Grain sizes of Al (~20-26nm) and MgH_2 (~11nm) after decomposition of $Mg(AlH_4)_2$ during a prolonged milling are still in a nanometric range (Table 9.8). However, it must be noticed that with cycling, the complex hydrides generally may not maintain a small grain (crystallite) size.

Table 9.8 Nanograin (crystallite) size, D and strain, e of phases in the powders after milling for 5, 10 and 40h.

Powder	Nanograin size, D and strain, e of phases in the powders after milling					
	Phase	Milling time (h)	D (nm)	e	R^2	No of XRD peaks
A11Cl5	$Mg(AlH_4)_2$	5	18	0	0.973	11
A11Cl10	$Mg(AlH_4)_2$	10	18	6.6×10^{-4}	0.975	9
A11Cl10	Al	10	26	0	0.995	4
A11Cl40	Al	40	20	0	0.945	4
A11Cl40	β-MgH_2	40	11	-	0.983	3

9.3.2 Thermal behaviors

9.3.2.1 DSC and TGA thermal analysis up to 500°C

Thermal behavior of the milled powders after milling for 5, 10 and 40h was investigated by DSC and TGA. The by-product NaCl was not removed from the milled powders because it does not react with $Mg(AlH_4)_2$ during heating and removing salt using chemical methods might bring impurities which may affect the thermal behavior of $Mg(AlH_4)_2$ [48].

Fig. 9.18 shows the evolution of DSC curves of the milled powders upon heating to 500°C at the scan rate of 4 and 20°C/min. DSC curves registered at the scan rate of 4 and 20°C/min for powders after milling for 5 and 10h show some small heat flow fluctuations at the low temperature range of 120-180°C (Fig. 9.18a and b) while the DSC trace for the 40h milled powder is rather flat at this low temperature range. Thermal events at the low temperature range of 120-180°C will be discussed in more detail in Sec.9.3.2.2. DSC curves obtained at the scan rate of 4°C show two endothermic peaks for the 5h and 10h milled powder at the 225-340°C range and one endothermic event at a 450-460°C range (Fig. 9.18a). Increase of the scan rate to 20°C/min shifts the medium-temperature range

peak maxima to higher temperatures (~250-375°C) but does not change the shape of the peaks (Fig. 9.18b).

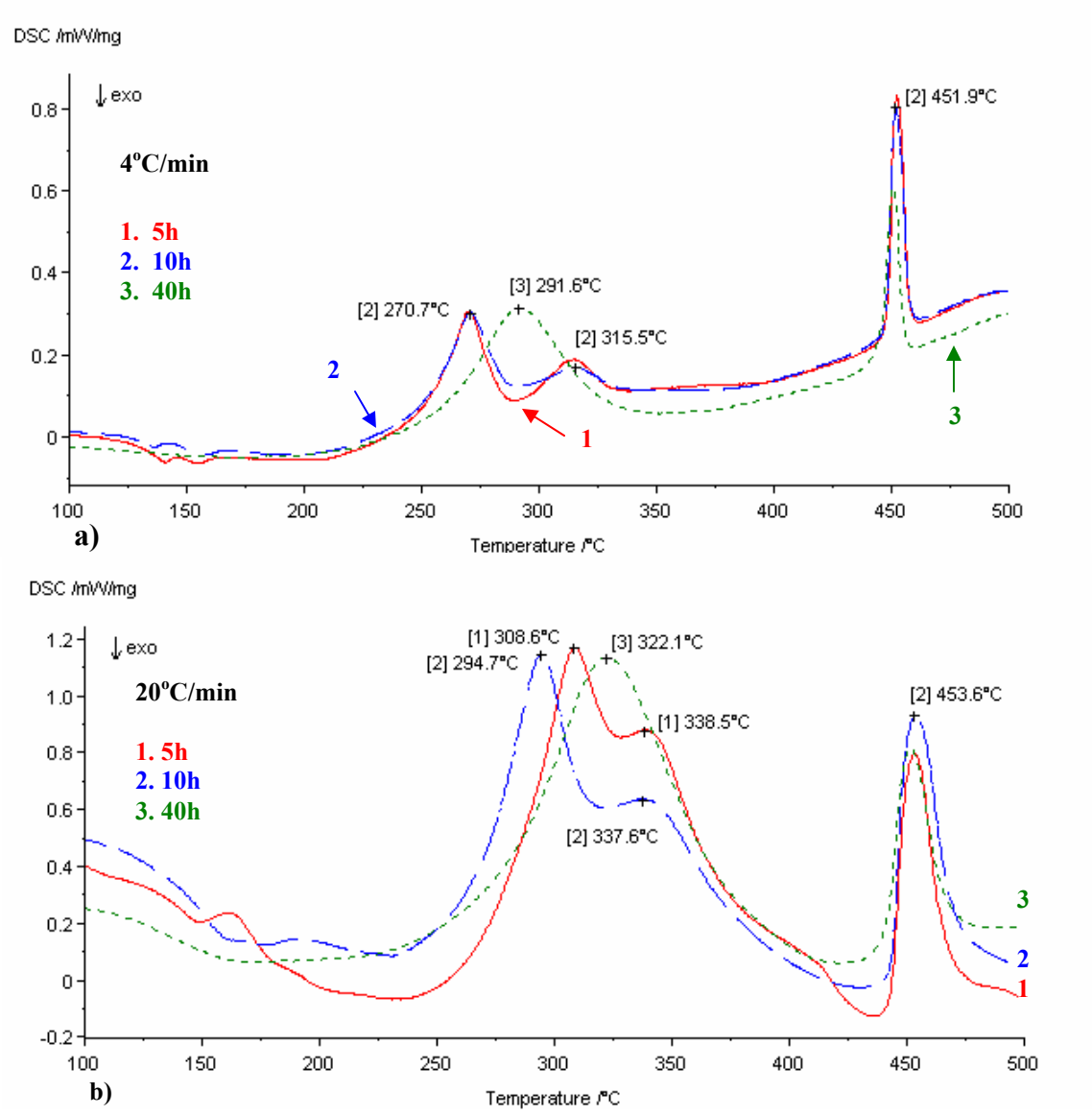

Fig. 9.18 DSC curves of the milled powders after milling for 5, 10 and 40h upon heating to 500°C at the scan rate of (a) 4°C/min and (b) 20°C/min.

For powders after milling for 40h, a single endothermic peak at ~292°C is observed at the scan rate of 4°C, which is in contrast to double peaks at the 225-340°C range for powder after milling for 5 and 10h. An endothermic peak at ~450°C upon heating (Fig.

9.18) and an exothermic peak at ~406-414°C upon cooling from 500°C to room temperature (Fig. 9.19) are observed in all of the DSC curves of milled powders. Results of DSC analysis at the scan rate at 4°C, which were used to study the phase transformation upon heating from 180 to 500°C, are summarized in Table 9.9.

From results of XRD (Fig. 9.17) and DSC analysis (scan rate: 4°C/min) (Fig. 9.18a), it can be seen that thermal events at the 120-180°C range in the DSC curves of the powders after milling for 5 and 10h must be attributed to the decomposition of $Mg(AlH_4)_2$ because the DSC curve of the 40h-milled powder, which does not contain $Mg(AlH_4)_2$, shows no peaks (very flat trace) in the low temperature range of 120-180°C. The endothermic peak at ~292°C in the DSC curve of the powder after milling for 40h is due to the desorption of hydrogen from β-MgH_2 since β-MgH_2 is the only hydride observed in the XRD pattern of the 40h-milled powder. The nature of the double peaks at the 225-340°C range for powder after milling for 5 and 10h will be discussed in more detail later in this section.

The nature of the endothermic reaction at ~450°C upon heating (Fig. 9.18), which was investigated at our previous study [106], is due to the eutectic melting of the mixture of Al_3Mg_2 and Al(Mg) solid solution which essentially occurs according to the equilibrium phase diagram of Al-Mg (Fig.G.11) [104]. Upon cooling from 500°C to room temperature (Fig. 9.20), Al(Mg) solid solution and Al_3Mg_2 phase are formed, which was also observed at our previous study [106]. As a result, the exothermic reaction at ~406-414°C upon cooling (Fig. 9.19) is the result of powders undergoing eutectic melting at ~450°C and subsequently solidifying into the mixture of Al_3Mg_2 and Al(Mg) from the liquid zone.

Table 9.9 Summary of DSC data for 5h, 10h and 40h milled powders upon heating from 180 to 500°C at the scan rate of 4°C/min as well as the data for the milled powders upon cooling from 500°C to room temperature.

Milling time (h)	5				10				40			
Temperature range (°C)	T_{on} (°C)	T_{peak} (°C)	T_{end} (°C)	ΔH (J/g)	T_{on} (°C)	T_{peak} (°C)	T_{end} (°C)	ΔH (J/g)	T_{on} (°C)	T_{peak} (°C)	T_{end} (°C)	ΔH (J/g)
225-340 (heating)	257.2 295.4	270.0 314.8	282.2 330.0	60.1 26.0	259.3 294.5	270.7 315.5	287.6 331.4	45.8 14.2	258.4	291.6	324.0	194.1
445-460 (heating)	448.1	452.2	457.3	55.4	447.8	451.9	457.6	52.8	445.5	451.0	455.4	43.5
440-405 (cooling)	414.8	406.1	396.1	-47.0	415.8	407.1	396.1	-45.0	437.0	414.1	406.9	-43.3

[1]Thermal events at the temperature range of 120-180°C for DSC curves of 5h and 10h milled powders (Fig. 9.18a) are inconclusive due to the very low enthalpy of decomposition of $Mg(AlH_4)_2$ and corresponding small size of the DSC peaks.
[2] There are no thermal events in the DSC curve of 40h milled powder (Fig. 9.18a).

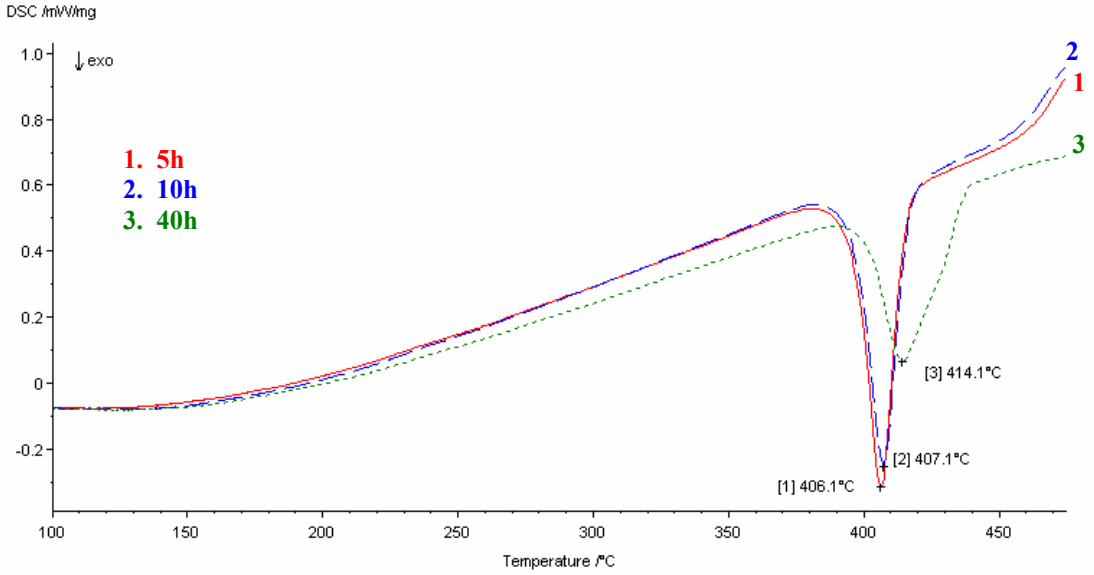

Fig. 9.19 DSC curves of the milled powders after milling for 5, 10 and 40h upon cooling from 500°C to room temperature.

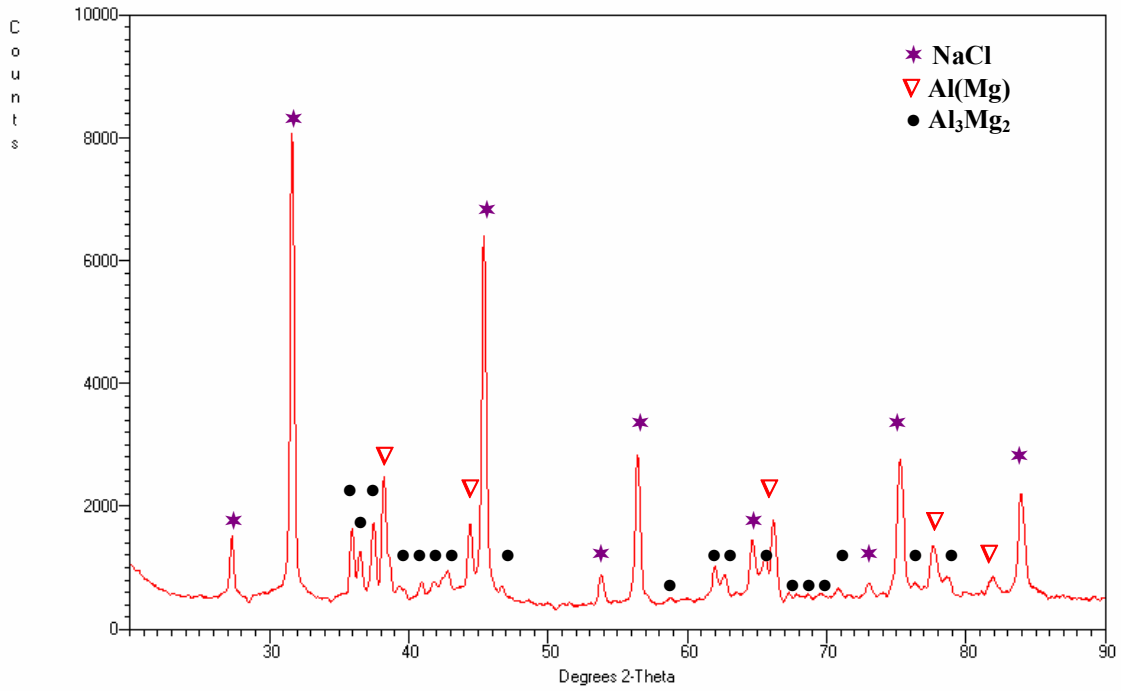

Fig. 9.20 XRD pattern of the 10h milled powder (A11Cl10) after cooling from 500°C to room temperature in a DSC test.

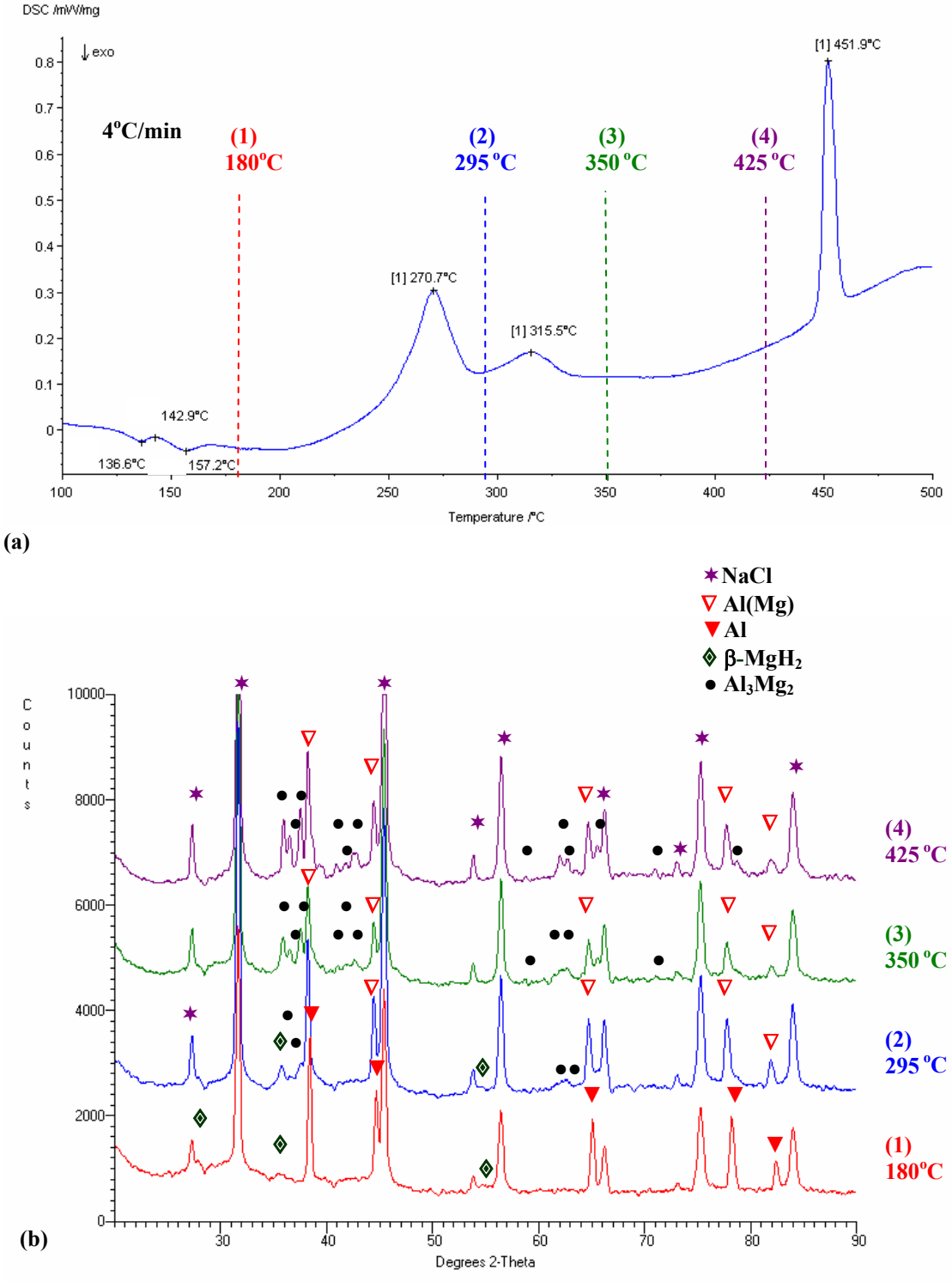

Fig. 9.21 (a) DSC curves of powders after milling for 10h showing a separation into the four segments corresponding to thermal events registered on the curve (scan rate: 4°C/min) and (b) corresponding XRD patterns of powders heated to 180, 295, 350 and 425°C in a DSC test shown in Fig. 9.21a.

In order to analyze the nature of the thermal events above 180°C observed in milled powders, small samples of the 10h-milled powder containing $Mg(AlH_4)_2$ were heated to DSC temperatures marked by the vertical lines at the rate of 4°C/min in Fig. 9.21a. By monitoring the phase evolution before and after the thermal reaction, the nature of the thermal reaction can be revealed. The XRD patterns corresponding to the powders heated in DSC to the selected temperatures are shown in Fig. 9.21b.

After heating to 180°C the only phases existing in the powder are β-MgH_2, Al and residual NaCl. This confirms that peaks at the lower temperature range are due to the complete decomposition of $Mg(AlH_4)_2$ phase into β-MgH_2 and Al. From results of low temperature DSC test (up to 180°C) and prolonged milling (40h), it shows that $Mg(AlH_4)_2$ can decompose either by heating at a low temperature (~180°C) or milling for a prolonged time according to the reaction (9.2). Peak intensities of β-MgH_2 are weak in Fig. 9.21b because the amount of β-MgH_2 is small due to the nature of the MCAS reaction (9.2) that two moles of NaCl are formed when one mole of $Mg(AlH_4)_2$ is synthesized.

Two endothermic peaks at ~271 and ~316°C are observed in Fig. 9.21a. As shown in Fig. 9.21b, after heated to 295°C, which is higher than the end temperature of the first DSC thermal event having the peak maxima at ~271°C, the powder contains a negligible amount of β-MgH_2, a small amount of Al_3Mg_2 intermetallics (very low peak intensities in Fig. 9.21b), a large amount of Al(Mg) solid solution (high peak intensities in Fig. 9.21b) and residual NaCl. After the first endothermic reaction (peak maxima at ~271°C), the majority of β-MgH_2 decomposes into free Mg and H_2. Simultaneously, reaction of Mg

and Al to form Al_3Mg_2 and Al(Mg) solid solution occurs. The above reactions can be written as the following:

β-MgH_2+2Al (+2NaCl)$\rightarrow$Mg+H_2+2Al (+2NaCl) (225-340^{o}C at 4^{o}C/min) (9.5a)

Mg+2Al$\rightarrow$0.5Al_3Mg_2+0.5Al(Mg) (225-340^{o}C at 4^{o}C/min) (9.5b)

After DSC run up to the temperature of 350^{o}C, which is higher than the end temperature of the second DSC thermal event having the peak maxima at ~316^{o}C, the decomposition of the remnant MgH_2 is completed and the microstructure consists of residual NaCl, large amount of Al_3Mg_2 intermetallic compound (high intensity XRD peaks in Fig. 9.21b) and large amount of Al(Mg) solid solution (high intensity XRD peaks in Fig. 9.21b).

However, there is now some problem with the interpretation of two endothermic peaks at ~271 and ~316^{o}C. Supposing that the first peak at ~271^{o}C is due to decomposition of β-MgH_2 then the second peak at ~316^{o}C would have to be due to the formation of the Al_3Mg_2 intermetallic compound. At this point, however, the problem is that the formation of Al_3Mg_2 should be an exothermic reaction [48] and there is none observed in DSC curve upon heating. One explanation might be that it overlaps with the endothermic peaks at 250-340^{o}C range. In addition, the formation enthalpy of Al_3Mg_2 might be small compared to the decomposition enthalpy of MgH_2 and the formation of Al_3Mg_2 gives rise to a very small exothermic DSC peak size. It is also feasible that the peak at ~316^{o}C could be due to the final decomposition of the remnant β-MgH_2 but then the question arises why would β-MgH_2 decompose in two stages.

Morphologies of the 10h milled powders and the same powder after heating to 180, 295, 350 and 425^{o}C in a DSC test are shown in Fig. 9.22. It can be seen that morphologies of the powders after heating do not have a visible change with respect to those of the as-

milled powder (Fig. 9.16). In addition, the morphology of the powder does not change as the temperature increases. The nonuniform distribution of the particle size in the as-milled powder is still kept after heating to 425^{o}C (Fig. 9.22d). As a result, one explanation to the presence of double peaks at the ~250-340^{o}C range might be that the nonuniform particle size distribution in milled powders after MCAS using Uni-Ball Mill 5 (Fig. 9.16). Although not showing double peaks at ~250-340^{o}C range in the DSC curve, the powder after milling for 40h still shows a broad single peak at ~292^{o}C, which can also be attributed to a nonuniform distribution of particle size. At the temperature range of 250-340^{o}C, Mamatha et al. [46,47] and Kim et al. [48] reported only a single endothermic peak with the maximum around 280-290^{o}C for the mixture $Mg(AlH_4)$+2NaCl. The nature of the two endothermic peaks observed in the present work still need more clarification.

It must be pointed out that the formation of Al(Mg) solid solution in due course and after complete decomposition of MgH_2 observed by XRD in Fig. 9.21 was first identified by visible shifting of Al peaks to lower angles, with respect to their position for a pure Al, in XRD patterns of 295, 350 and 425°C (Fig. 9.21b). Subsequently, the lattice parameters of Al(Mg) were calculated by the software Traces v. 6.5.1 and are listed in Table 9.10. It is clear that the lattice parameter of Al is much larger in samples after annealing in DSC at 295, 350 and 425°C than that in the samples after milling and annealing at 180°C. This means that a measurable lattice expansion occurred due to formation of the solid solution of Mg in Al, i.e. Al(Mg). The lattice expansion is consistent with the magnitude of the atomic radius of Al and Mg which is 0.1432 and 0.1604nm, respectively [103]. Similar effect of the Al(Mg) solid solution formation during milling of the elemental powders

with Mg-2Al ratio, pre-alloyed Mg-2Al ingot and AZ91 alloy was reported in [106]. Fossdal et al. [45] claimed the formation of the Al(Mg) solid solution during low-temperature desorption of $Mg(AlH_4)_2$ below 180°C. However, lattice parameter changes do not confirm this behavior in the present work (Fig. 9.21b and Table 9.10). Mamatha et al. [46,47] never reported the formation of the Al(Mg) solid solution in their studies of the thermal analysis of the mechano-chemically synthesized $Mg(AlH_4)_2$ although Kim et al. [48] mentioned about increase in the lattice parameter of Al most probably due to formation of the Al(Mg) solid solution.

In contrast, the powder after milling for 40h shows only a broad single peak at ~292^{o}C (Fig. 9.18), which is attributed to the decomposition of β-MgH_2 and probably overlapping with the peak of the formation of Al_3Mg_2. The DSC annealing (the scan rate: 4°C/min) of the 40h milled powder at 350°C, which is above the peak maximum at ~292^{o}C in Fig. 9.18a, resulted in the formation of the mixture of Al_3Mg_2 and Al(Mg) solid solution (Fig. 9.23) whose lattice parameter is also listed in Table 9.10. This clearly confirms that the formation of Al_3Mg_2 and Al(Mg) in the present work occurs with the assistance of temperature rather than during ball milling as observed in [106]. This can be related to different methods of synthesis used in the present work (MCAS) and in [106] (reactive mechanical milling of elemental powders).

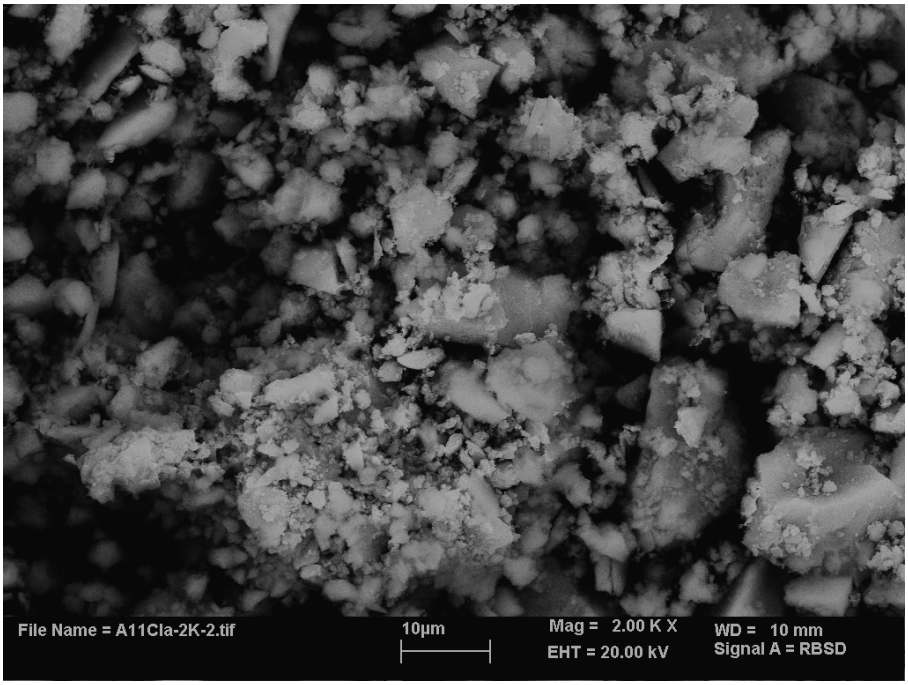

(a)

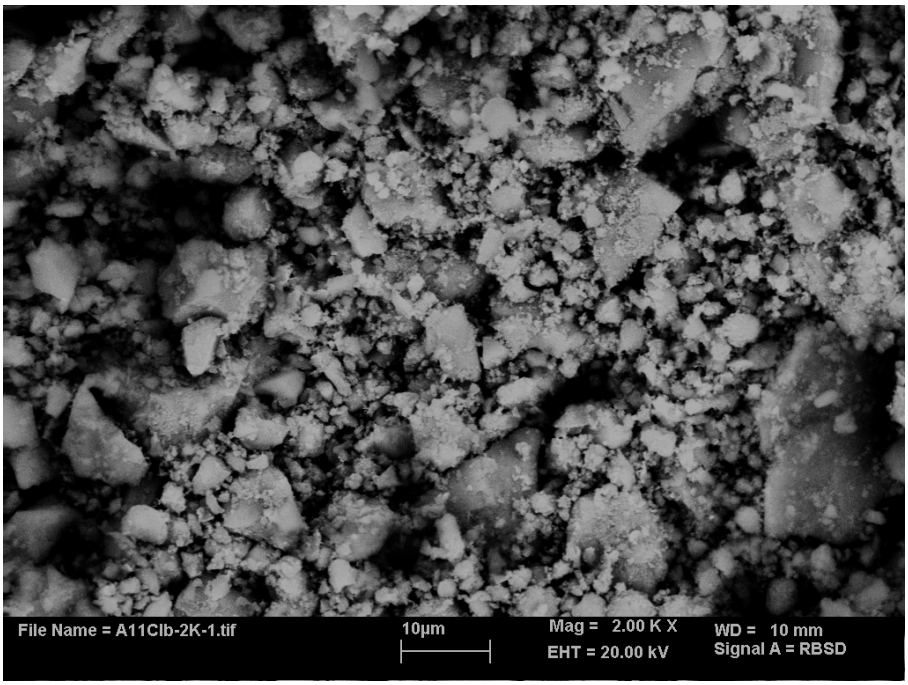

(b)

Fig. 9.22 Morphologies of the 10h milled powders after heating to (a) 180, (b) 295, (c) 350 and 425^{o}C at a scan rate of 4^{o}C/min in a DSC test.

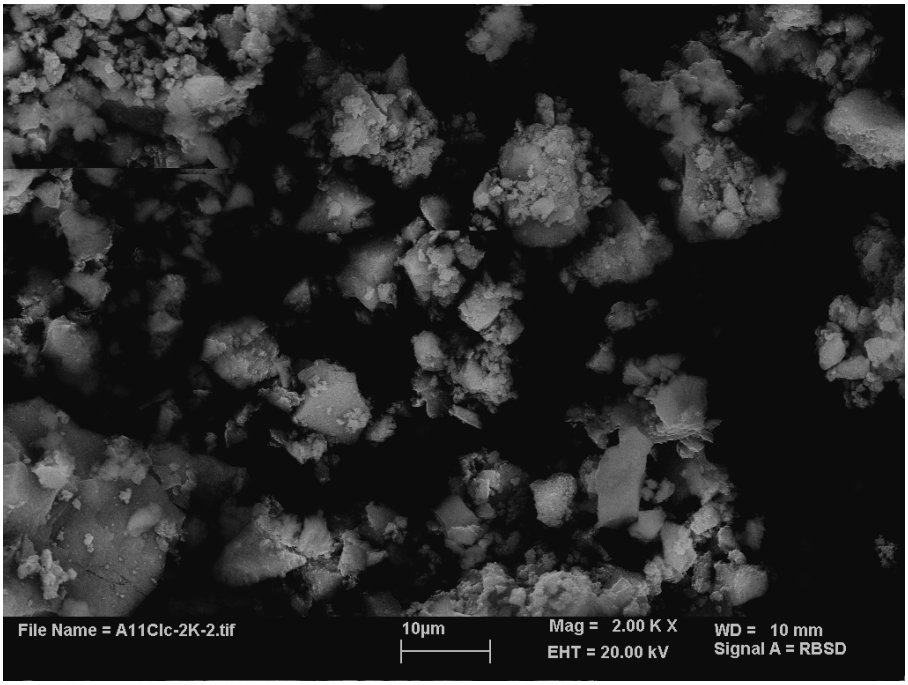

(c)

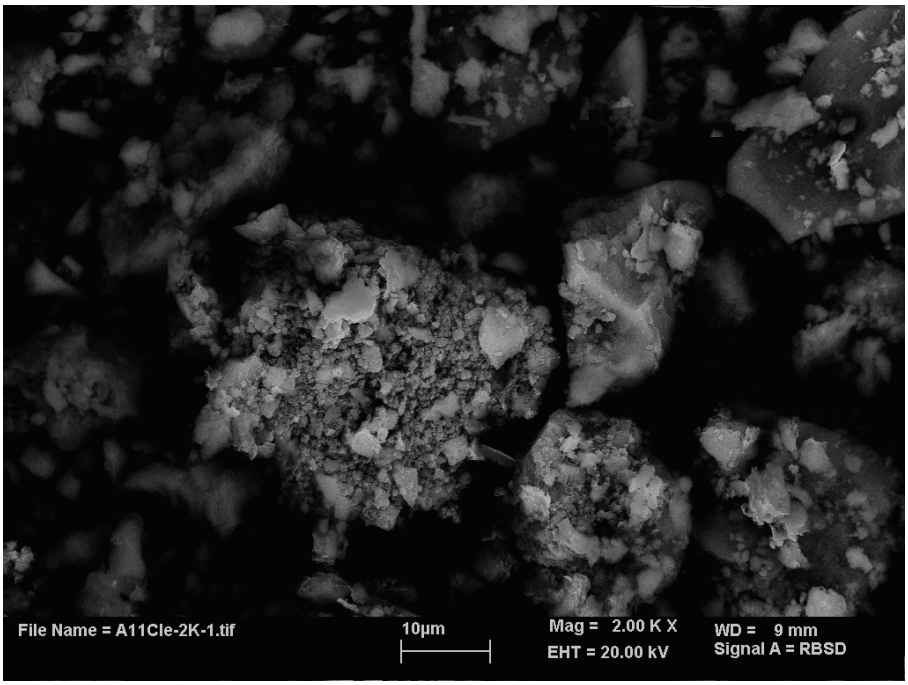

(d)

Fig. 9.22 cont'd

Table 9.10 Lattice parameters of Al and Al(Mg) solid solution in the as-milled and DSC tested samples (scan rate: 4°C/min).

Powder	Temperature of DSC test (°C)	Lattice parameter of Al (FCC) (nm)	
		Average	Error[2]
	As-milled (before DSC heating)	0.4037	0.0015
	180	0.4039	0.0015
10h milled	295	0.4059[1]	0.0018
	350	0.4062[1]	0.0016
	425	0.4063[1]	0.0013
40h milled	350	0.4065[1]	0.0012

[1]) Al(Mg) solid solution
[2] Average lattice parameter and error are calculated by software TRACES™ V.6.5.1

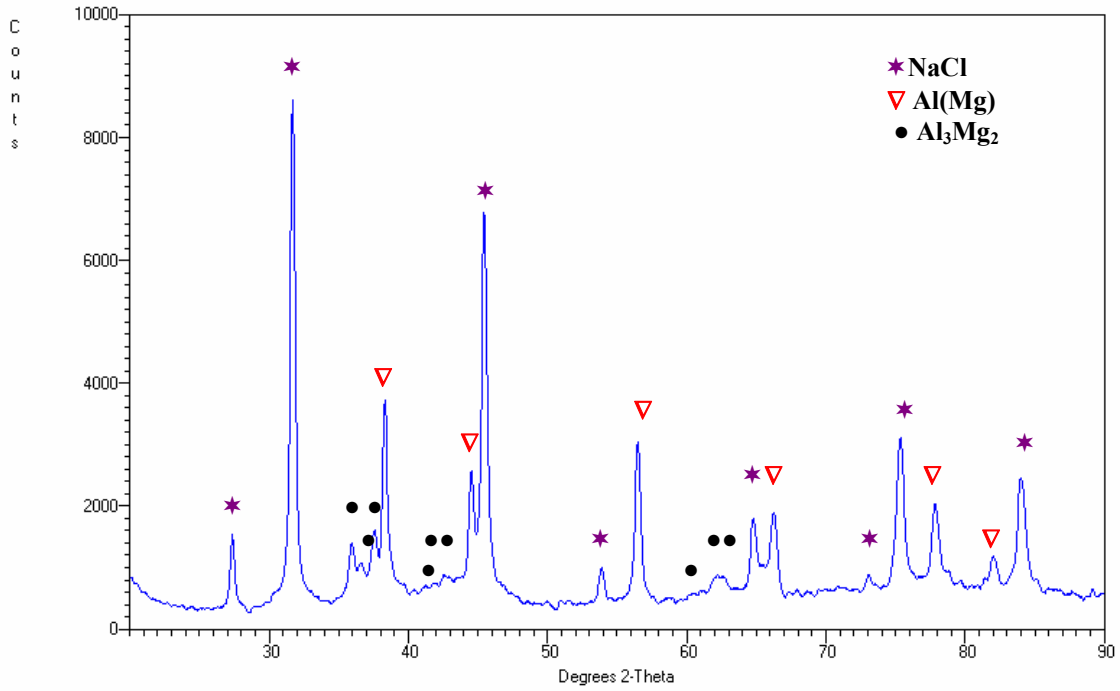

Fig. 9.23 XRD pattern of the 40h milled powder after heating to 350°C at the rate of 4°C in a DSC test.

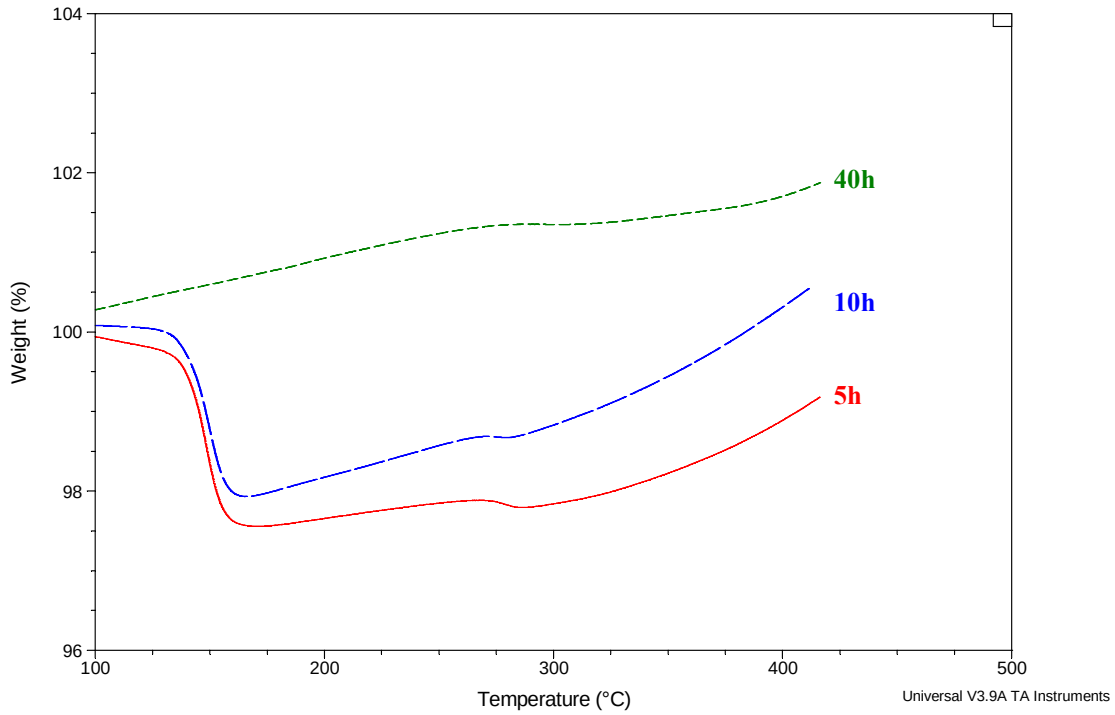

Fig. 9.24 TGA curves of the milled powders after milling for 5, 10 and 40h upon heating to 420°C.

TGA curves of powders after milling for 5, 10 and 40h are shown in Fig. 9.24. The temperature ranges of two weight losses at ~120-180°C range and ~270-300°C, which were observed in TGA tests for the powders containing $Mg(AlH_4)_2$ (5h and 10h), match well with those at DSC curves (~120-180°C and ~225-340°C ranges in Fig. 9.18a). The TGA weight losses in the first and second step decomposition in the powder after milling for 5h are 2.37 wt.% and 0.08wt.%. Corresponding weight losses for the powder after milling for 10h are 2.14wt.% and 0.02wt.%. Assuming the MCAS is completed (i.e., products have a 1 mol of $Mg(AlH_4)_2$ and 2 mol of NaCl), which is very likely because there are no peaks from reactants ($NaAlH_4$ and $MgCl_2$) in the XRD pattern of the milled powder (Fig. 9.17), the theoretical hydrogen capacity in the mixture of $Mg(AlH_4)_2$+2NaCl is ~3.97 wt.% rather than ~9.3 wt.% as in a pure $Mg(AlH_4)_2$. From TGA analysis, the largest total weight loss ~2.45 wt.%, which is observed in the powder

after milling for 5h, is less than the theoretical value ~3.97 wt.%. A shortage of ~1.5 wt.% might be a combined effect of the partial decomposition of $Mg(AlH_4)_2$ during milling for 5h and the underestimation of the weight loss in the second step (~270-300^oC) due to the oxidation of Mg during TGA run under flowing nitrogen. The total hydrogen desorption of ~2.16wt.% in TGA for the 10h milled powder is most probably due to the prior partial decomposition of $Mg(AlH_4)_2$ during milling. No weight loss in the ~120-180^oC range for the 40h milled powder further confirms that $Mg(AlH_4)_2$ decomposes after a prolonged milling time.

9.3.2.2 The nature of phase transformations up to 180^{o}C in DSC

The heat flow effects due to the decomposition of $Mg(AlH_4)_2$ in DSC are difficult to monitor due to its very low enthalpy of decomposition [47] and corresponding small size of the DSC peaks. Fig. 9.25a shows the enlargement of the low temperature region up to 180°C observed on the full DSC curve in Fig. 9.18a (scan rate 4°C/min) of the powder synthesized for 10h. Taking the flat DSC portion for the 40h sample as a baseline, one can invoke the existence of either two exothermic or one endothermic peaks due to the decomposition of $Mg(AlH_4)_2$. In order to shed more light on these low-temperature heat flow events, a few 5h and 10h milled powder samples were also tested at the scan rate of 20°C/min in DSC. DSC curves at the scan rate of 20^{o}C/min are plotted in Fig. 9.25b together with the flat trace for the 40h sample which can be considered as a baseline. With respect to this baseline, one 5h and one 10h milled samples show the DSC humps which could be considered as endothermic. In contrast, other 5 and 10h samples show a diffuse trough that could be classified as due to an exothermic reaction.

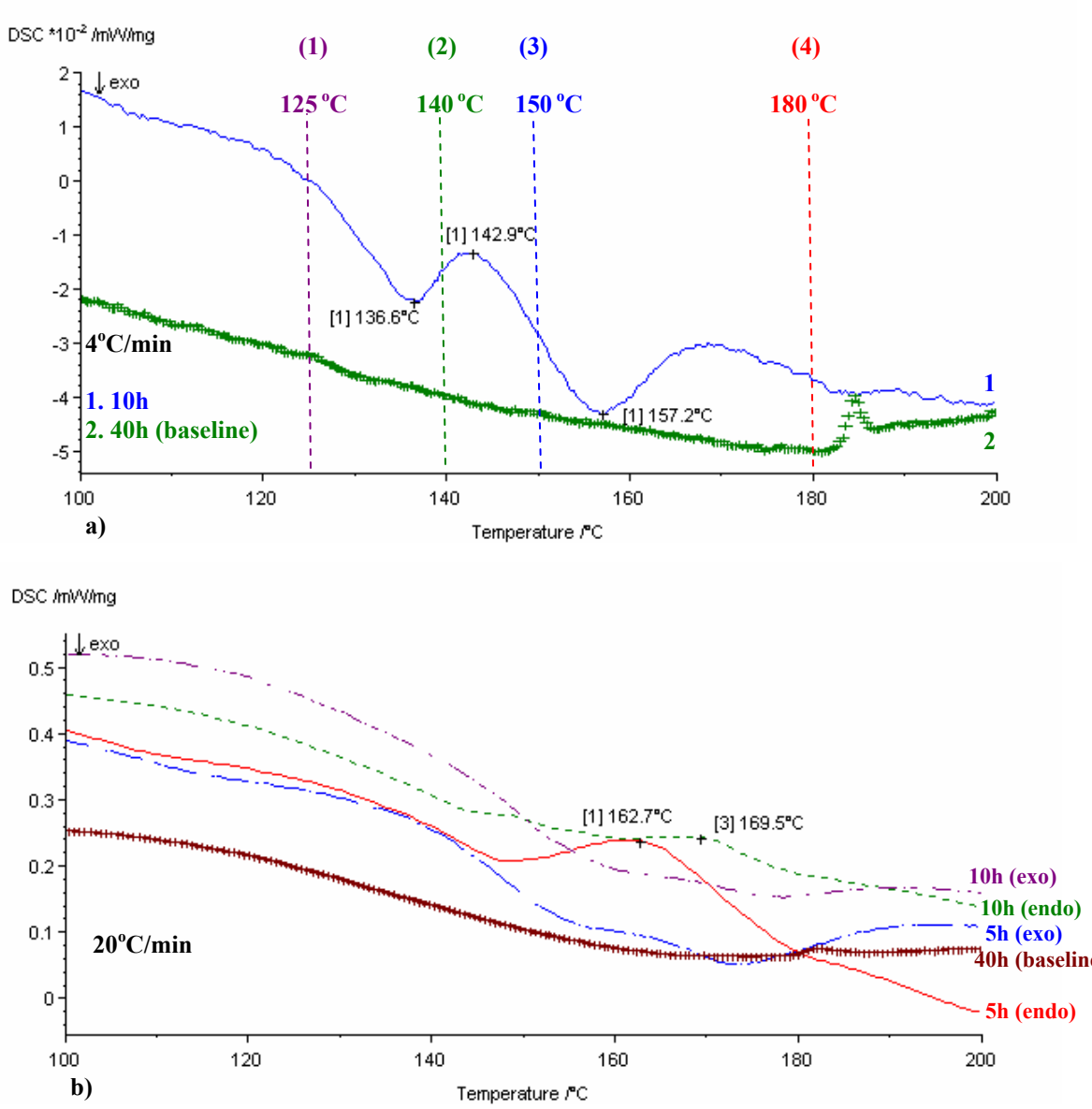

Fig. 9.25 An enlargement of the low temperature section of DSC curve of the 10h milled powder registered at the scan rate of (a) 4°C/min and (b) 20°C/min. (c) Corresponding XRD patterns of powders heated to 125, 140, 150 and 180°C at the scan rate of 4°C/min in a DSC test.

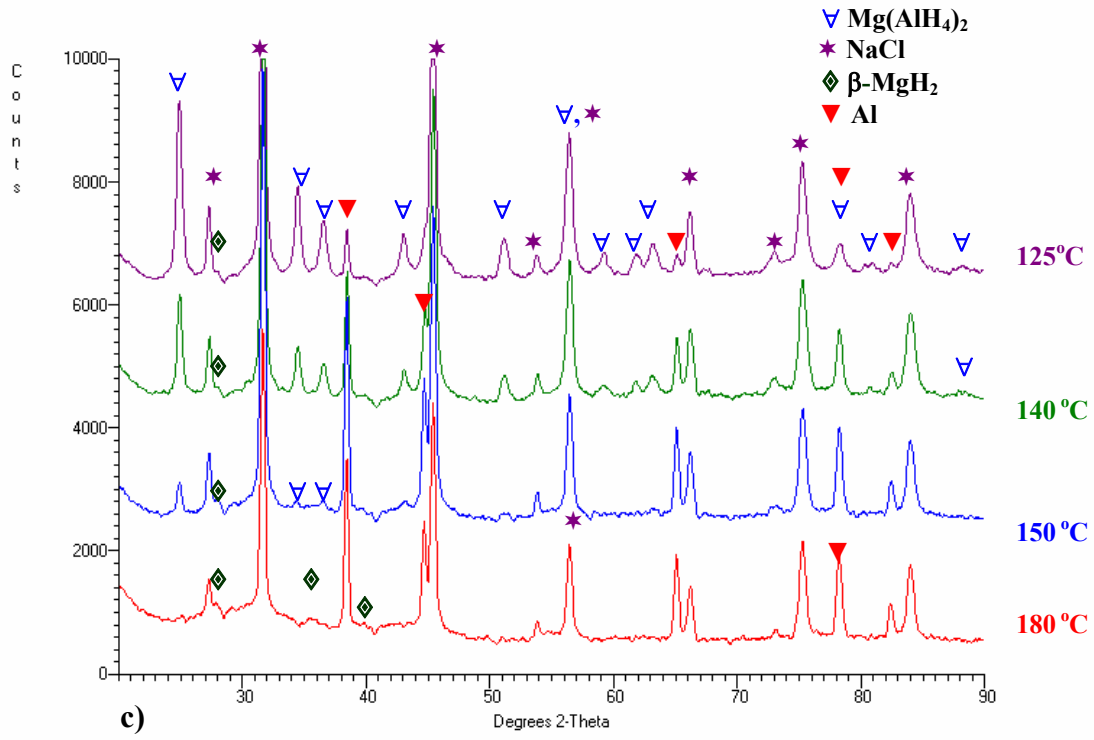

Fig. 9.25 cont'd

In order to investigate the microstructural nature of the reactions taking place up to 180°C (Fig. 9.25a), a few samples of the 10h milled powder containing $Mg(AlH_4)_2$ were run in a DSC test up to the temperatures marked by the vertical lines in Fig. 9.25a. Subsequently, XRD phase analysis was performed for each sample after DSC test and the XRD patterns corresponding to the powders analyzed in DSC to selected temperatures are shown in Fig. 9.25c. Samples annealed to 125°C and 140°C still contain $Mg(AlH_4)_2$, residual NaCl, traces of β-MgH_2 and Al rather than the Al(Mg) solid solution as mentioned earlier. This is in essence is almost the same microstructure as that after ball milling for 10h (Fig. 9.17) except the trace amount of β-MgH_2. The presence of the latter indicates that the beginning of the decomposition of $Mg(AlH_4)_2$ starts occurring around 125°C (4°C/min). After a DSC run up to 150°C the microstructure contains only a very

small amount of $Mg(AlH_4)_2$ as can be deduced from a greatly reduced intensity of the strongest $Mg(AlH_4)_2$ peak at 2θ~25° (100% intensity) and almost complete disappearance of two other strong peaks at 2θ~34.5° (80% intensity) and 2θ~36.6° (75% intensity) (JCPDS#47-0980) in Fig. 9.25c (150°C). After DSC run to 180°C the microstructure does not contain $Mg(AlH_4)_2$ any longer which is an indication of its complete decomposition.

This analysis clearly shows that approximately up to 180°C, $Mg(AlH_4)_2$ is already decomposed. However, the nature of this transformation being either endothermic [46,47] or exothermic [48] can not be unambiguously established. Most probably, this situation arises owing to a very small enthalpy of decomposition of $Mg(AlH_4)_2$ which is cited in the literature as being equal to ~1.7 kJ/molH [47]. It is quite possible that at this value of the enthalpy of decomposition even small microstructural fluctuations always present in the powders synthesized by mechanochemical reactions may lead to stabilization or destabilization of the powder resulting in either endothermic [46,47] or exothermic [48] heat flow.

9.3.2.3 Desorption Kinetics

Hydrogen desorption kinetics of the powder after milling for 5h, which contains a mixture of $Mg(AlH_4)_2$ and 2NaCl, were studied in a Sieverts-type apparatus at 150 and 350°C. A hydrogen pressure of 4.1 MPa was used to prevent desorption before the system temperature was stabilized at the desired test temperature. After the system was stabilized, high hydrogen pressure was released and the amount of desorbed hydrogen was recorded at 0.1 MPa of hydrogen pressure. The kinetics curves obtained at 150°C and 350°C are shown in Fig. 9.26. The desorbed amounts of hydrogen at 150 and 350°C are 0.45 wt.% and 0.75 wt.%, respectively. XRD pattern of the powder after desorption at 150°C

indicates a completed first step decomposition (reaction 9.2) of $Mg(AlH_4)_2$ (Fig. 9.27a). However, the value 0.45 wt.% is much smaller than ~2.37wt.% of the first step decomposition estimated by TGA and the theoretical value for the first step decomposition (~2.98wt.%) calculated from reaction (9.2) (the theoretical hydrogen capacity is ~3.97wt.% in the mixture of $Mg(AlH_4)_2$+2NaCl, which is equal to the amount stored within four H_2 in $Mg(AlH_4)_2$; as a result, one H_2 should store ~0.99 wt.% (= 3.97/4) in the mixture; taking into account that three H_2 are desorbed in the reaction (9.2) and one H_2 is released in reaction (9.5a), the theoretical amount of hydrogen desorbed in the reaction (9.2) and (9.5a) are ~2.98wt.% and ~0.99wt.%, respectively).

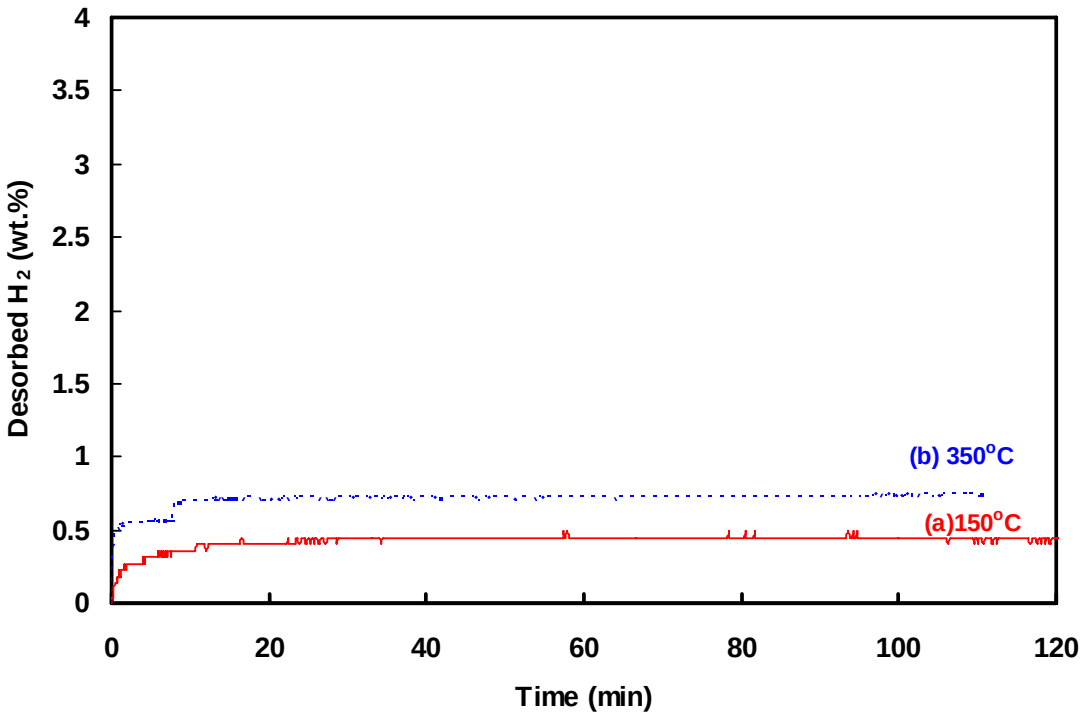

Fig. 9.26 Hydrogen desorption kinetic curves obtained at (a) 150°C and (b) 350°C for the powder after milling for 5h.

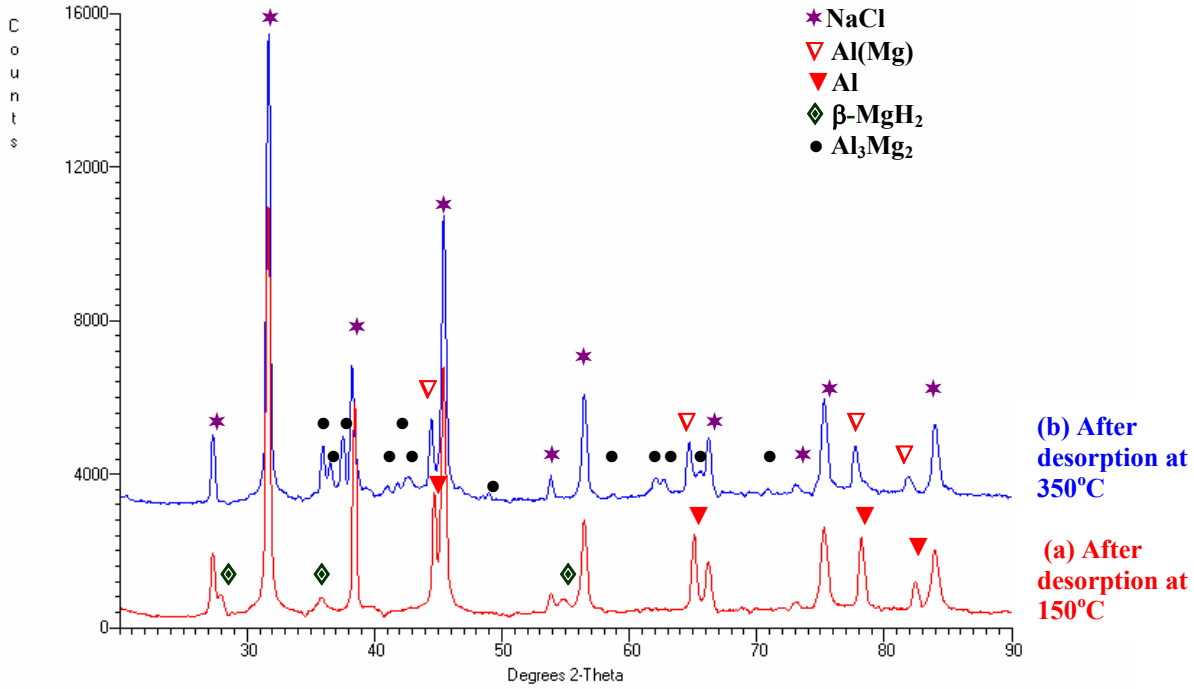

Fig. 9.27 XRD patterns of the 5h milled powder after desorbing at (a) 150 and (b) 350°C in a Sieverts-type apparatus.

As for the desorption at 350°C, microstructure of the powder after desorption at 350°C contains Al_3Mg_2, Al(Mg) and retained NaCl. This phase make up indicates a complete decomposition of $Mg(AlH_4)_2$ (both of the first and the second step have finished) (Fig. 9.27b). However, the desorbed value 0.75 wt.% is still much smaller than the total desorbed amount (~2.45wt.%) estimated by TGA and the theoretic amount of the full decomposition (~3.97wt.%).

The question which has to be answered is the possible cause of incomplete desorption in a Sieverts-type apparatus. Fichtner et al. [76] reported the equilibrium pressure of pure $Mg(AlH_4)_2$ in the 75-95°C range to be between 8.8 and 13MPa. As a result, a hydrogen pressure barrier of 4.1MPa which were used in the present work during temperature stabilization period in a Sieverts-type apparatus seems to be insufficient to prevent the

reaction (9.2) to occur at 150 and 350^{o}C. In other words, during heating to 150 and 350^{o}C in the temperature stabilization period, the first step desorption according to the reaction (9.2) had already occurred, i.e. even before the temperature was fully stabilized. This explanation is supported by the pressure increase monitored during temperature stabilization period at 150°C. Since the pressure increase is due to two factors such as temperature and hydrogen release then its increment due to just hydrogen release can be estimated by subtracting the pressure increase due to temperature estimated from the heating of empty crucible from the pressure registered while heating crucible containing a 5h milled powder sample. This estimate gives ~1.79 wt.%H_2 already released during temperature stabilization period at 150°C. Therefore, the total amount of hydrogen desorbed will be the sum of the hydrogen desorbed during temperature stabilization period (~1.79 wt.%) and the hydrogen desorbed in the isothermal desorption period of the test at 150 ^{o}C, i.e. 0.45wt.%. This summation gives the total of 2.24 wt.%H_2 desorbed at 150^{o}C, which is slightly smaller than the theoretical 2.98wt.%H_2.

Similar estimate taking into account the pressure increase calculated from the heating of empty crucible up to 350°C gives ~2.5wt.% H_2 desorbed during temperature stabilization period up to 350°C. Adding this up to the amount of ~0.75 wt.% desorbed during the isothermal desorption period of the test at 350^{o}C (as discussed above) gives ~3.25wt.% of the total desorbed hydrogen, which is still smaller than the total theoretical of ~3.97wt.%H_2 stored in the $Mg(AlH_4)_2$+2NaCl mixture. The total amount of hydrogen desorbed at both of 150 and 350^{o}C in a Sieverts-type apparatus is short of ~0.7 wt.% with respect to the theoretical hydrogen capacity values. Since the calibrated accuracy of desorbed hydrogen capacity is about ±0.2wt.% H_2 in the Sieverts-type apparatus

(calibrated on a commercial MgH_2) used in the present work, the experimental deficiency of ~0.7wt.% is not due to the experimental error and as such must be related to some other factor. One possibility could be that the 5h milled powder has already lost about ~0.7wt.% of hydrogen due to partial decomposition of $Mg(AlH_4)_2$ during milling. However, this hypothesis needs further study.

9.4 Discussion

9.4.1 The effect of starting materials (as-milled A1H-A4H powders)

The ternary magnesium alanate $Mg(AlH_4)_2$ has not been synthesized in the present work by mechano-chemical synthesis (MCS) using CRMA of four stoichiometric Mg-2Al batches: (a) elemental Mg and Al powders, (b) elemental Al powder and AZ91 alloy, (c) powder of as-cast Mg-2Al alloy and (d) commercial MgH_2 powder and Al powder. This is in striking contrast to a successful mechano-chemical synthesis of nanostructured ternary complex hydride Mg_2FeH_6 [107,108]. It was reported that the presence of MgO in the milled powder could be an important factor inhibiting the formation of hydrides for other systems [98-100]. MgO might have blocked the nucleation sites for the complex hydrides. However, as can be seen in Fig. 9.4-Fig. 9.7 the diffraction peaks of MgO are not observed in XRD patterns of the four stoichiometric Mg-2Al powders. Apparently, this is not the reason that $Mg(AlH_4)_2$ has not been synthesized.

Therefore, it is imperative to seek for another explanation as to why $Mg(AlH_4)_2$ has not been synthesized. An important discovery is the competition between formation of Al(Mg) solid solution and the β-MgH_2 hydride occurring to a various extent up to ~10h of CRMA in all three batches: A1H, A2H and A3H, as discussed earlier. The most extensive solutionizing effect occurs in the A3H10 powder due to decomposition of the

initial Al_3Mg_2 intermetallic compound which results in the largest lattice expansion (Table 9.1) and the least MgH_2 formed after 10h of reactive milling (Table 9.5). Now, this situation can be contrasted with the elemental 2Mg-Fe powder system in which we achieved a very successful mechano-chemical synthesis by CRMA of the nanostructured ternary complex hydride Mg_2FeH_6 [109,110] as a result of the reaction $2MgH_2+Fe+H_2 \leftrightarrow Mg_2FeH_6$ (or alternatively $3MgH_2+Fe \leftrightarrow Mg_2FeH_6+Mg$ where Mg is amorphized) [94]. In due course of reactive milling of the 2Mg-Fe system no formation of solid solutions have been observed [109,110]. Therefore, it is hypothesized here that the presence of Al(Mg) solid solution in the initial stage of the synthesis process (up to 10h) inhibits the following reaction

$$MgH_2+2Al(Mg)+3H_2 \rightarrow Mg(AlH_4)_2 \quad (9.6)$$

or $$MgH_2+Al(Mg)+Al(free)+3H_2 \rightarrow Mg(AlH_4)_2 \quad (9.7)$$

Furthermore, the initial presence of Al(Mg) solid solution has a long-term adverse effect on the synthesis of $Mg(AlH_4)_2$ as the reactive milling duration increases beyond the initial 10h. It has been discussed earlier that in due course of prolonged reactive milling the Al(Mg) solid solution eventually decomposes into Mg and Al(s), where the latter is the secondary Al from solid solution, as evidenced by the lattice shrinkage of Al (Table 9.1). However, despite that after decomposition a free Al(s) is available for the reaction below

$$MgH_2+2Al(s)+3H_2 \rightarrow Mg(AlH_4)_2 \quad (9.8)$$

the reaction does not occur. Another hypothesis is put forward, namely, that Al(s) still retains its physico-chemical characteristics from the former solid solution which strongly inhibits the reaction (9.6). In other words, the nature of Al(s) is not exactly the same as

that of free elemental Al powder. One may say that Al(s) is already "poisoned" after being a host for dissolved Mg.

There is strong experimental evidence supporting this notion. As discussed earlier in the text, the range of the enthalpy of melting, ΔH^{melt} (peak #2-HT in Table 9.5) between 10h to 200h of milling time increases drastically from 93-79 J/g for A1H, to 179-86J/g for A2H and eventually to 312-255 J/g for A3H. Therefore, the question arises why would the range of the enthalpy of melting be so different for different powder mixtures. Quite obvious answer would be a difference in the average powder particle size, i.e. the finer the powder, the smaller the range of the enthalpy of melting. As can be seen from Fig. 9.3 the A1H powder after 10 and 200h of milling has the finest particle size (ECD) and the smallest range of ΔH^{melt}. However, the other two powder batches A2H and A3H have a very similar ECD size range but A3H has the range of ΔH^{melt} much greater (almost twofold) than that of A2H. In conclusion, such drastic differences in the range of ΔH^{melt} as seen in Table 9.5 cannot be explained by simple differences in the average powder particle size.

However, the increase in the range of ΔH^{melt} directly correlates with the increase of the fraction of Al(Mg) solid solution in the microstructure of the powders. In the A1H and A2H batches there exists some amount of free elemental Al powder alongside with Al(Mg) after 10h of milling and subsequently Al(s) after longer milling duration but in the A3H batch there is exclusively Al(Mg) from the decomposition of Al_3Mg_2 after 10h of milling and correspondingly Al(s) is exclusively formed after longer reactive milling. Correspondingly, the A3H has the greatest range of ΔH^{melt}. Apparently, more energy must be supplied as reflected in the enthalpy of melting to allow melting of a eutectic

mixture of Mg and Al(Mg) or Al(s) (Mg-2Al(Mg) or Mg-2Al(s)). This is the most convincing evidence that the nature of Al(s) is altered although there is no clear explanation at the moment what physico-chemical characteristics have indeed been altered. Also, it is not surprising now that the order of the enthalpies of solidification in Table 9.6 must exactly mimic the order of the enthalpies of melting discussed above.

It is also observed in Table 9.6 that ΔH^{melt} decreases with increasing milling time beyond 10h for powder batches A1H-A3H within each corresponding range of ΔH^{melt}. This is directly related to the refinement of average particle size (ECD) with increasing milling time as shown in Fig. 9.3. It is, therefore, obvious that the decrease of ΔH^{melt} within its characteristic range with increasing milling time observed in Table 9.5 for each powder batch is the result of a substantial reduction of the average powder particle size upon milling. Furthermore, the observation that the ΔH^{melt} for the A1H1 powder (milled for 1h) is about 149J/g and that for A1H10 (milled for 10h) is much smaller being equal to 93J/g (Table 9.5) can be explained by a very small average particle size of A1H10 which has ECD~1μm (Fig. 9.3a).

In A4H powders, which use commercial MgH_2 and elemental Al powders as starting materials, a partial decomposition of MgH_2 after a 100h of milling time can be deduced from the decrease of DSC yield of MgH_2 (Table 9.5). Unlike the cases in A1H-A3H powders, free Mg is not available until the milling time reaches 100h in A4H powders. As a result, no competition between MgH_2 and Al(Mg) solid solution has occurred until the milling time reaches 100h. The substantial decrease of ΔH^{melt} after 100h of milling is most likely due to the reduction of the average particle size upon milling. Although there is no solid solution before 100h of milling time in A4H powders, ternary $Mg(AlH_4)_2$ is

not synthesized. This can be explained by a low energy input during milling. After 100h, energy input might be enough. However, at this moment Al(Mg) solid solution is formed and impedes the formation of $Mg(AlH_4)_2$ hydride.

So far there has not been any quantitative analysis reported on the relationship between nanograin size and hydrogen desorption temperature. As seen in Fig. 9.15 there is no correlation between both quantities for β-MgH_2 as also reported for the β-MgH_2 and Mg_2FeH_6 hydrides in [107-108]. In the Mg-Al-H powders made by milling of elemental Mg and Al powders, β-MgH_2 desorbs in the range of ~340 to 410^oC, which falls in the range of that of β-MgH_2 in the Mg-H system. This indicates that Al does not act as a catalyst for the decomposition of β-MgH_2 in the Mg-Al-H powders made by milling of elemental Mg and Al powders.

9.4.2 The effect of annealing on the phase transformations of nanohydrides

A1H powder containing three different types of Al were selected to study the effect of the property of Al on the hydrogenation of as-milled powders: (a) A1H1 (milled for 1h) containing primary Al, (b) A1H5 (milled for 5h) containing Al(Mg) solid solution, and (c) A1H270 (milled for 270h) containing secondary Al. Hydrogenation was performed by annealing the as-milled powders at two different combinations of temperature and hydrogen pressure in a Sieverts-type apparatus: a high annealing temperature with a short annealing time, and a low annealing temperature with a long annealing time (Table 9.7).

$Mg(AlH_4)_2$ has not been synthesized by annealing the as-milled A1H powders at various temperatures and pressures under hydrogen. This contrasts with a successful synthesis of ternary complex hydride Sr_2AlH_7 by hydrogenation of the as-milled Sr_2H_2 and Al

powders at 260°C under 7MPa of hydrogen for 2 days [74]. The differences in a bond strength between Sr, H and Al on the one hand and Mg, H and Al on the other hand cannot explain such diametrically different behavior during processing by a combination of ball milling and annealing. The enthalpy of formation of SrH_2 (-180 kJ/mol [40]) is larger than that of MgH_2 (-74 kJ/mol [94]), which indicates that the bonding between Sr and hydrogen is stronger than that between Mg and hydrogen. The annealing of Sr_2H_2 and Al powders was carried out at 260°C under 7MPa of hydrogen for 2 days. The annealing of MgH_2 and Al was carried out under 4MPa only. Besides the hypothesis that the formation of solid solution and intermetallics deplete Al required for reaction, the hydrogen pressure used in the present work might also not be sufficient for the absorption to occur. Fichtner et al. reported the equilibrium pressure of pure $Mg(AlH_4)_2$ in a 75-95°C range is between 8.8 and 13MPa [76]. As a result, the equilibrium hydrogen pressures at annealing temperatures in the present work (100°C and 350°C) must be higher than 13MPa. A hydrogen pressure of 4.5MPa, which is the maximum allowed in a Sieverts-type apparatus used in the present work, might be too low to start the absorption of hydrogen.

Akiba and Zhang [74] also reported that once a Al(Fe) solid solution is formed (Fe impurity from balls and milling vial), the amount of Al will not be enough to form Sr_2AlH_7 hydride. A prolonging milling time and a further hydrogenation cannot results in a formation of Sr_2AlH_7 after the formation of the solid solution [74]. In annealed A1H1 and A1H5 powders, which form solid solution and intermetallic phases, the reasons that ternary $Mg(AlH_4)_2$ hydride has not been synthesized by hydrogenation of the as-milled powder are most likely due to the formation of a Al(Mg) solid solution and intermetallic

compounds, which deplete the amount of Al. As for annealed A1H270 powder, which does not contains solid solution or intermetallics, the lack of $Mg(AlH_4)_2$ might be the reason that secondary Al still holds its properties as those in a Al(Mg) solid solution. In other words, secondary Al(s) phase is positioned (i.e., Al(s) still retains its physico-chemical characteristics from the previous solid solution which strongly inhibits the reaction to form $Mg(AlH_4)_2$ and cannot react with MgH_2 to form ternary hydride). As for the annealed A5H powders, Al-Fe intermetallic phase is formed but there is no evidence that Mg-Al-H ternary hydrides are synthesized. Again, formation of intermetallics might deplete the amount of Al which is necessary for synthesis.

Milling under energetic mode only reduces the milling time but the problem with the solid solution still exists and hampers the formation of ternary hydride in A10H powders. Iron does not work as a catalyst in Mg-Al-H system.

9.4.3 $Mg(AlH_4)_2$ hydride synthesized by MCAS

$Mg(AlH_4)_2$ has been synthesized in the present work by mechano-chemical activation synthesis (MCAS) of mixture of $2NaAlH_4$ and $MgCl_2$. It is prudent to discuss briefly the importance of the present results and those reported earlier by Mamatha et al. [46,47] and Kim et al.[48] for the feasibility of $Mg(AlH_4)_2$ synthesized by MACS as a solid state hydrogen storage medium. The major problem in the MCAS technology is the formation of a large amount of waste by product NaCl. With 2 moles of NaCl per only 1 mol of $Mg(AlH_4)_2$ (reaction 9.1), the excellent theoretical hydrogen capacity ~9.3wt.% of pure $Mg(AlH_4)_2$ is reduced to the very inferior ~3.97wt.% in the mixture of $Mg(AlH_4)_2$+2NaCl. As reported by Mamatha et al. [47] it is possible to separate $Mg(AlH_4)_2$ from NaCl by the Soxhlet extraction method which is based on the suspension of the $Mg(AlH_4)_2$+2NaCl

mixture in the diethyl ether (Et_2O) solvent. However, there are a couple of disadvantages of this extraction method. First, the extracted $Mg(AlH_4)_2$ is usually contaminated with the solvent adduct [48]. Second, the extraction process needs several days to be completed and then the product requires some additional long-time annealing in vacuum [47]. Such a long production time is definitely not suited for industrial environment. Therefore, if ball milling is to be used than the most suitable method of synthesizing a relatively pure $Mg(AlH_4)_2$ is still a direct reactive synthesis from the elemental metals under hydrogen [106]. In this case, however, an effective catalyst must be found which would accelerate the reaction between MgH_2 and Al [106]. Such a catalyst is still unknown.

It should also be noted that the decomposition temperature of β-MgH_2 occurring in the 250-340^oC range (reaction 9.5) as shown in Fig. 9.18 is much lower than ~380^oC range for the MgH_2 reactively synthesized using elemental Mg powder under the same milling condition (Sec. 8.2). This might be due to a catalytic effect of a special active Al which is produced after decomposition of $Mg(AlH_4)_2$. In our previous study [106], the decomposition temperature of MgH_2 (~320-340^oC) produced by milling of the elemental Mg and Al powders under hydrogen is still higher than that of MgH_2 in the present powders. Therefore, the special active Al in the present powders might have a different property than the Al in the mixture of MgH_2+Al produced by milling of elemental Mg and Al under hydrogen [106].

As mentioned in Sec. 3.4, $NaAlH_4$ and $LiAlH_4$ first decompose into an intermediate M_3AlH_6 (M=Na or Li) (Eq. 3.4a and Eq. 3.5a) and then into a binary hydride MH (M= Na or Li) (Eq. 3.4b and Eq. 3.5b). Dymova et al. [49] synthesized $Mg(AlH_4)_2$ by MCAS of a mixture of MgH_2+2$AlCl_3$. $Mg(AlH_4)_2$ was identified by IR spectrum because no

diffraction peaks of $Mg(AlH_4)_2$ were observed in the XRD pattern. The authors claimed that an intermediate hydride $MgAlH_5$ exists in the decomposition of $Mg(AlH_4)_2$ into MgH_2. However, from the XRD and DSC analysis in the present work, $Mg(AlH_4)_2$ decomposes into MgH_2 directly. No intermediate hydride is observed. This is in an agreement with the decomposition procedure reported by Claudy et al. [44], Fossdal et al. [45], Fichtner et al. [76,77], Mamatha et al. [46,47] and Kim et al. [48] who observed crystalline $Mg(AlH_4)_2$. A similar direct-decomposition of alanate into a binary hydride SrH_2 was observed for Sr_2AlH_7 hydride [74]. Besides the direct decomposition of complex hydride into a binary hydride for $Mg(AlH_4)_2$, the formation of an intermetallic phase Al_3Mg_2 also differs from the decomposition of $NaAlH_4$ and $LiAlH_4$.

As shown in Fig. 9.25, the enthalpy of decomposition for the first step decomposition of $Mg(AlH_4)_2$ into MgH_2, Al and H_2 is much smaller than those for the dissociation of β-MgH_2 in Mg-H, Mg-Al-H and Mg-B-H systems (20-1850J/g). Results of desorption test indicate the equilibrium (plateau) pressure is much higher than 4.1Mpa at 150^{o}C (probably the pressure will go above ~13MPa as reported by Fichtner et al. [76]), which is too high for a PEM fuel cell application. Although the first-step decomposition temperature is relatively low (<180^{o}C), the second-step decomposition starts at ~225^{o}C, which is still higher than the working temperature for PEM fuel cell.

Besides the working temperature and pressure, reversibility of the hydride has to be taken into account. Even though an intermetallic compound Al_3Mg_2 is formed after the full decomposition of $Mg(AlH_4)_2$, reaction (9.5) is proofed to be reversible either by milling (A3H powder in Sec.09.1) or by hydrogenation under hydrogen pressure which is very sluggish [111]. However, reaction (9.2) (i.e., synthesis of $Mg(AlH_4)_2$ by a mixture of

Mg + Al or MgH_2 + Al either by milling or hydrogenation under hydrogen pressure) has still not been reported to be reversible [106]. These problems have to be solved before $Mg(AlH_4)_2$ can be used as a hydrogen storage material for PEM fuel cell.

10. Mg-B-H

10.1 Nanohydride formation by using crystalline boron as the starting material

A representative morphology of the powder mixture of elemental Mg and crystalline boron powder in a stoichiometric Mg-2B ratio (B6H and B8H powders in Table 7.3) after a prolonged reactive mechanical alloying is shown in Fig.10.1. A dramatic particle size refinement and a high tendency to form agglomerates are observed after a prolonged milling time (>100h).

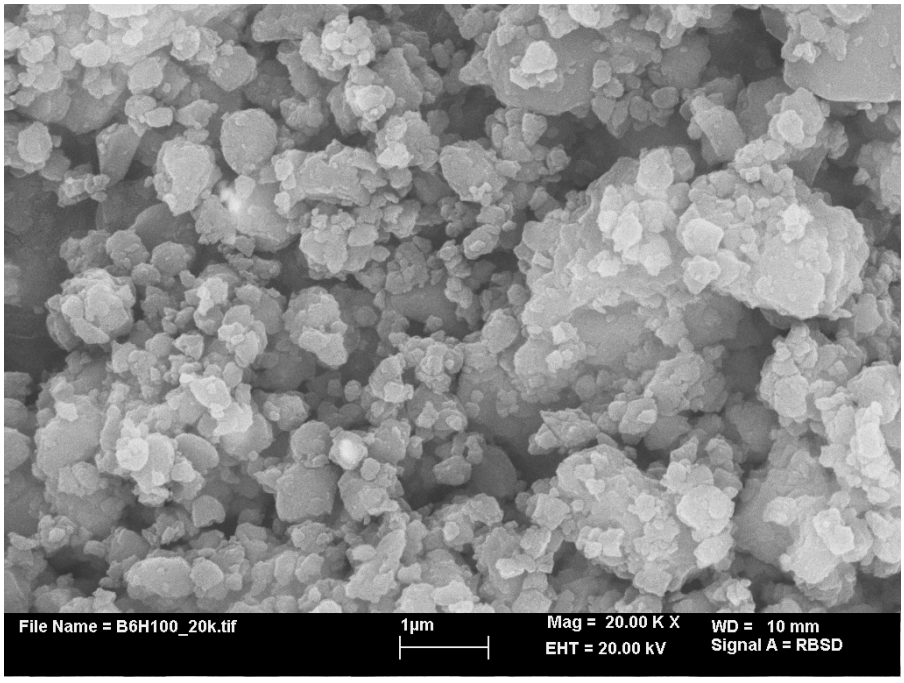

Fig.10.1 BSE micrograph showing a representative morphology of a stoichiometric Mg-2B powder mixture with crystalline boron (B6H and B8H) after a prolonged reactive mechanical milling for 100h.

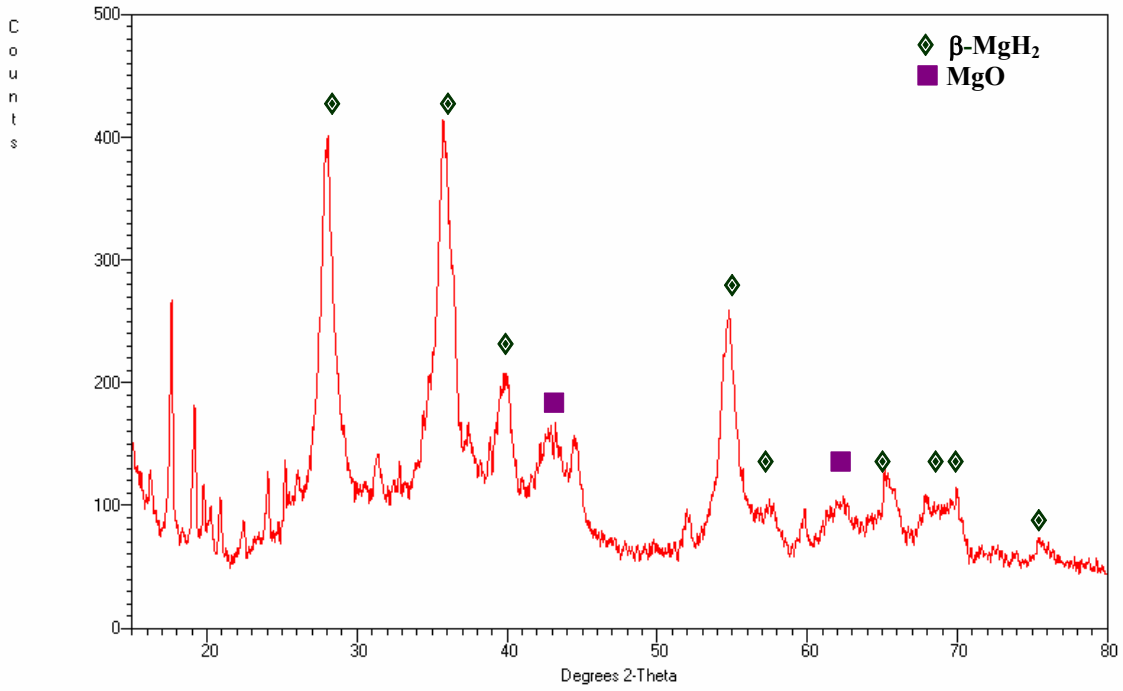

Fig.10.2 The representative XRD pattern of a stoichiometric Mg-2B powder mixture with crystalline boron (B6H and B8H) after a prolonged reactive mechanical milling for 100h. Unmarked peaks belong to crystalline boron phase.

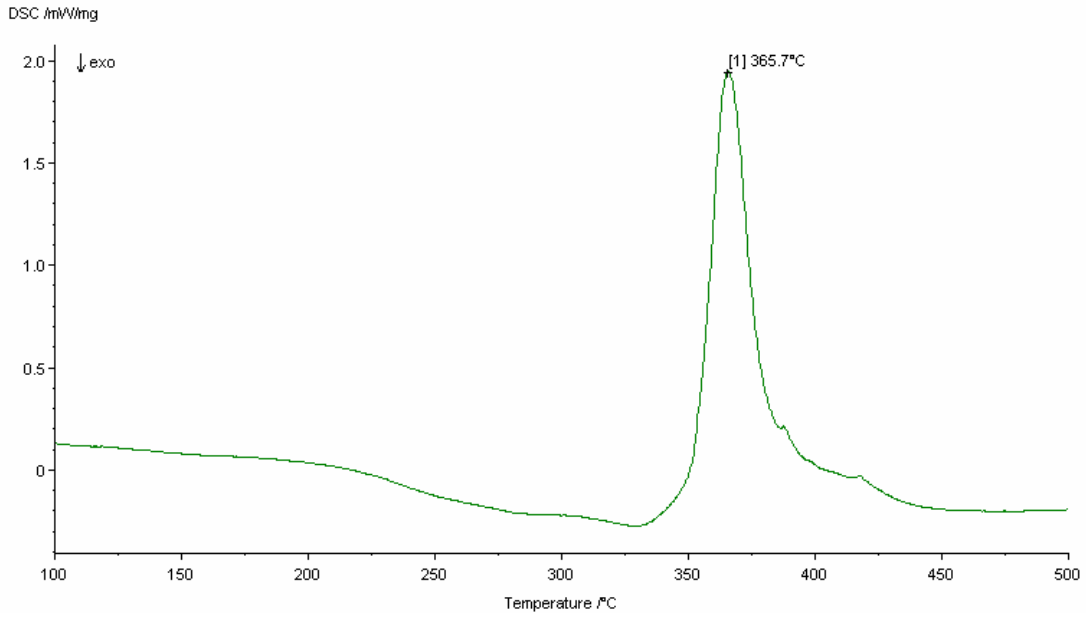

Fig.10.3 The representative DSC curve of a stoichiometric Mg-2B powder mixture with crystalline boron (B6H and B8H) after a prolonged reactive mechanical milling for 100h.

Fig.10.2 and Fig.10.3 show the representative XRD pattern and the DSC curve of milled powders using a mixture of crystalline boron and Mg in a stoichiometric Mg-2B ratio as starting materials under LES and HES mode. XRD patterns, DSC curves, nanograin size of phases present in the milled powders and the summary of DSC tests of B6H and B8H powders after various milling time are given in Appendix F.3.1 and G.3.1.

After a prolonged milling time, Mg reacts with hydrogen and forms nanometric β-MgH_2 (grain size 5-10nm) (Fig.10.2). However, crystalline boron (unmarked peaks in XRD patterns shown in Fig.10.2) (ICCD PDF# 31-0207 [92]) does not react with hydrogen or Mg to form $Mg(BH_4)_2$ phase. The presence of MgO after milling indicates incomplete reaction of Mg, which after milling forms an oxide upon exposure to air. A single endothermic peak observed in the DSC curves (Fig.10.3) must be attributed to the decomposition of β-MgH_2 phase because it is the only hydride observed in the XRD pattern.

Changing the milling mode from low energy shearing mode (LES) with WD = 3 mm in B6H powder to high energy impact mode 2 (IMP2) with WD = 5 mm in B8H powder (Table 7.3) does not increase the yield of β-MgH_2 dramatically (36.0wt.% in B6H100 powder; 34.6wt.% in B8H100 powder) (Table G.6) in the milled powder mixture of Mg and crystalline boron in a stoichiometric Mg-2B ratio.

10.2 Nanohydride formation by using oxidized and non-oxidized amorphous boron as the starting material

In B7H and B9H powders, powder mixtures of Mg and oxidized amorphous boron in a stoichiometric Mg-2B ratio were milled under LES and IMP2 mode for a prolonged milling time (100-300h) while in the B10H powder non-oxidized amorphous boron powder was used. No $Mg(BH_4)_2$ hydride is formed in the as-milled B7H, B9H and B10H powder. The only synthesized phases are β-MgH_2 and/or γ-MgH_2. Further annealing of the as-milled powder at 126 and 212^{o}C under 4.6MPa of hydrogen for 24h does not result in the formation of $Mg(BH_4)_2$ hydride (Fig. F.21). Results of XRD and DSC analysis for B7H, B9H and B10H powders are summarized in appendix F.3.2 and G.3.2.

Unlike changing both the milling mode and types of amorphous boron (oxidized or non-oxidized) in B7H-B10H powders, the milling mode is fixed at IMP710 mode in B15H and B14H powders to study the effect of oxidized and non-oxidized amorphous boron on the phase transformations of nanohydrides in the Mg-B-H system.

10.2.1 B15H (stoichiometric mixture Mg-2B with oxidized amorphous boron milled under IMP710 mode)

Fig.10.4 shows the morphology of powder mixture of Mg and oxidized amorphous boron in a stoichiometric ratio Mg-2B after reactive mechanical alloying under IMP710 mode for 200h (B15H powder). After milling for 200h, a large amount of number of the powders is refined within 200nm. On the other hand, a large size of aggregates in the 1-2 μm range shows the high tendency of aggregation after a prolonged milling time.

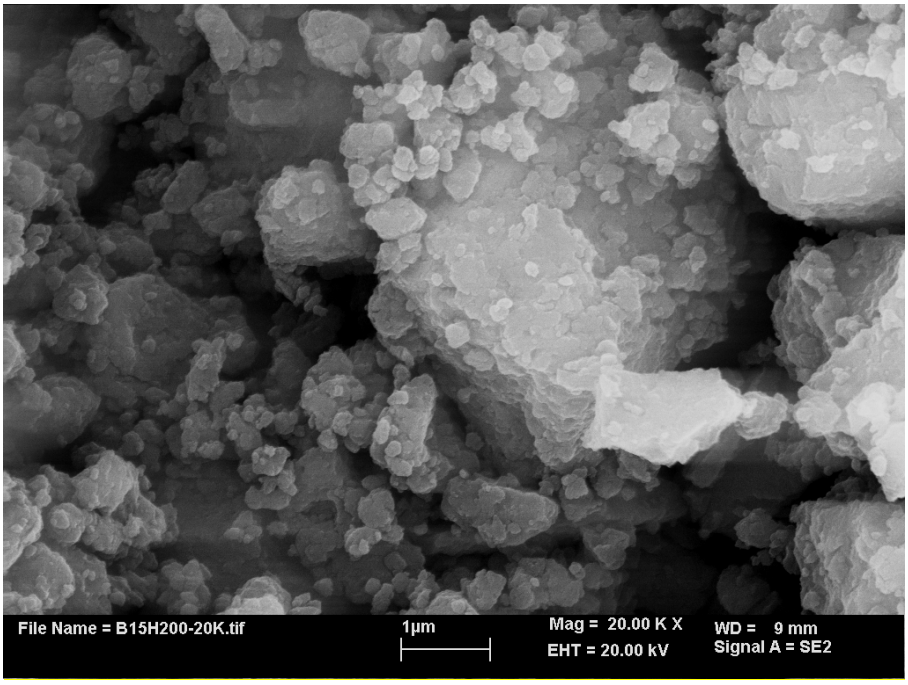

Fig.10.4 Secondary electron micrograph showing morphology of a stoichiometric Mg-2B powder mixture with oxidized amorphous (B15H) after milling for 200h under IMP710 mode.

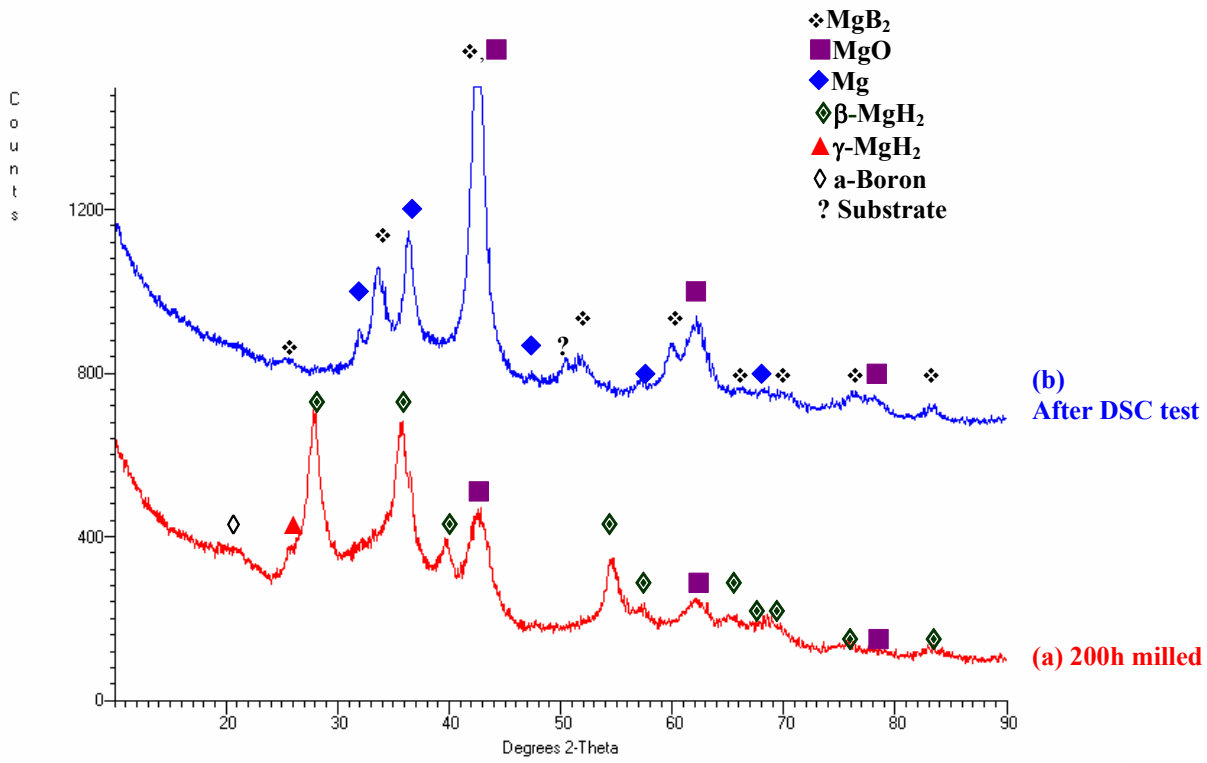

Fig.10.5 XRD patterns of (a) a stoichiometric Mg-2B powder mixture with oxidized amorphous boron (B15H) after milling for 200h under IMP710 mode and (b) the same powder after DSC test.

Fig.10.5a shows the XRD pattern of the Mg-2B powder mixture with oxidized amorphous boron (B15H powder) after reactive mechanical alloying under IMP710 mode for 200h. Only γ- and β-MgH_2 hydrides are synthesized after a 200h of milling time. No ternary $Mg(BH_4)_2$ hydride or MgB_2 is formed.

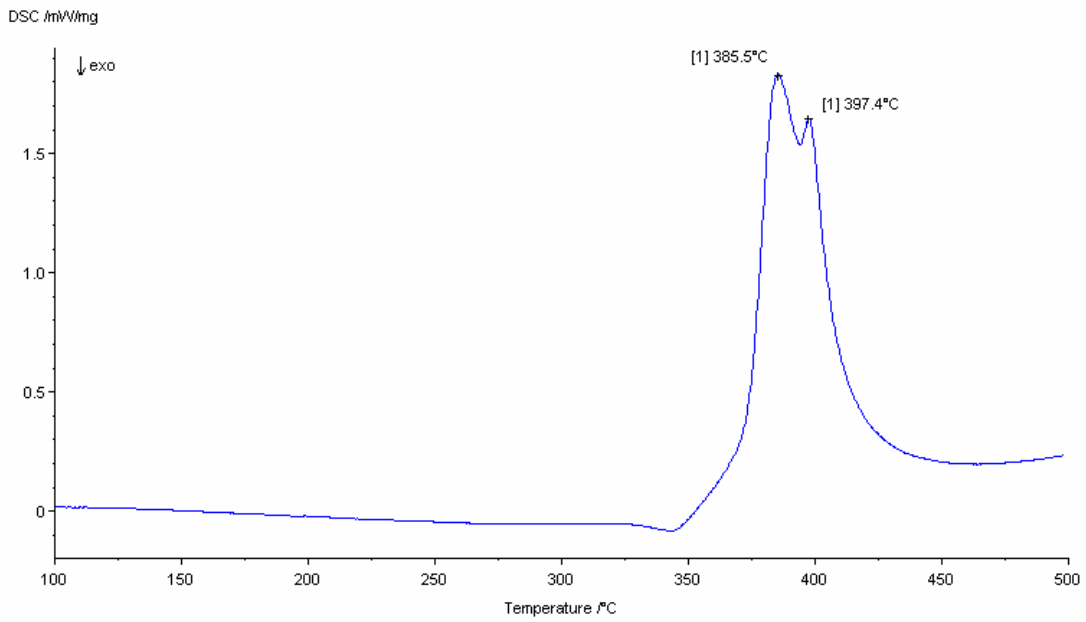

Fig.10.6 DSC curve of a stoichiometric Mg-2B powder mixture with oxidized amorphous boron (B15H powder) after milling for 200h under IMP710 mode.

Hydrogen desorption behavior was investigated by DSC analysis up to 500°C and desorption test at 350°C in a Sieverts-type apparatus. The structural changes after desorption process were investigated by XRD analysis. Table G.8 (Appendix G.3.3) summarizes DSC data upon heating. The peak doublet in the DSC curve (Fig.10.6) must be attributed to the desorbed hydrogen from MgH_2 phases because there are no other hydride phases. The peak doublet might be the result of different particle size distribution or the coexistence of both γ- and β-MgH_2. A nanograin size of 6nm shows a very fine grain size refinement of β-MgH_2 after a prolonged milling time (Table F.10). After the decomposition of β-MgH_2, free-active Mg reacts with retained amorphous boron (might be partially free of oxides after heating to 500°C) and forms MgB_2 (Fig.10.5b) with a nanograin size of 13nm (Table F.11). Hydrogen capacity of the B15H200 powder estimated by DSC test (~2.7 wt.%) correlates well with that calculated by desorption test (~2.6 wt.%) (Fig. G.21).

10.2.2 B14H (stoichiometric mixture Mg-2B with oxide-free amorphous boron milled under IMP710 mode)

10.2.2.1 As-milled powders

10.2.2.1.1 Microstructure and XRD analysis

The B14H powders were prepared by milling a mixture of elemental Mg and oxide-free amorphous boron powder (amorphous boron powder annealed at 370^{o}C for 20h to remove oxide impurities) (Fig. F.18) under IMP710 mode. There is no substantial difference between morphologies of B14H powders after milling for 50h and 200h. Morphologies of the B14H powders are similar to that of the B15H200 powder (Fig.10.4).

The phases present in B14H powder after milling for 50h are γ- and β-MgH_2, retained Mg, retained amorphous boron and MgO (Fig.10.7a). MgO in the XRD pattern of B14H50 powder is most probably from the oxidation of retained Mg upon the air exposure during the XRD test. Nanograin size of β-MgH_2 is reduced to ~ 6 nm after 50h of milling, which shows a grain size refinement (Table F.10). As milling time increases over 50h and reaches 200h, the XRD pattern shows the complete disappearance of crystalline MgH_2 phases and the formation of MgB_2 (Fig.10.7b).

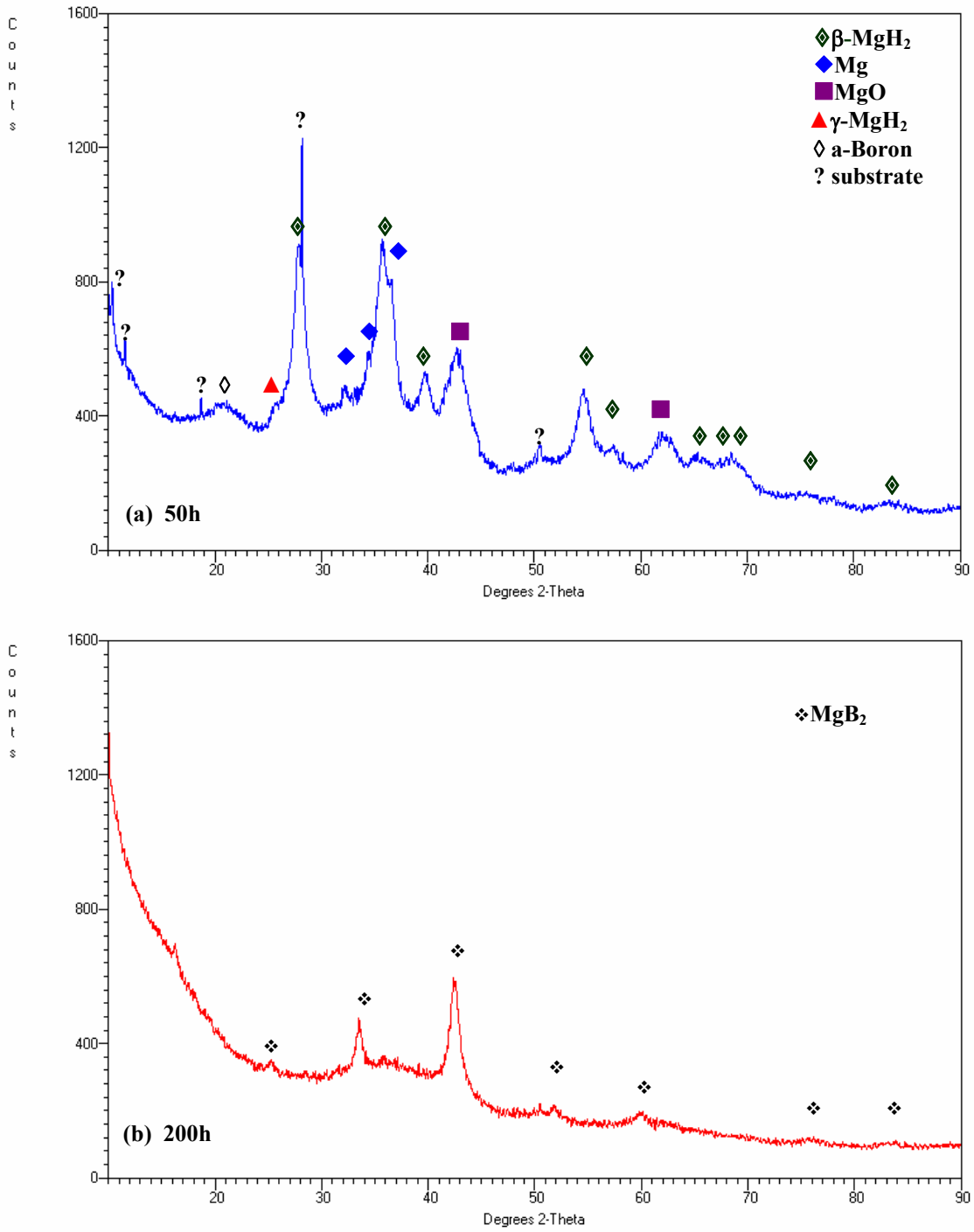

Fig.10.7 X RD patterns of a stoichiometric Mg-2B powder mixture with oxide-free amorphous boron powder (B14H) after milling under IMP710 mode for (a) 50h, and (b) 200h.

10.2.2.1.2 Thermal behavior

DSC curves of Mg-2B powder mixture with oxide-free amorphous boron (B14H) after milling for 50h and 200h under IMP710 mode are shown in Fig.10. 8. DSC test data are summarized in Table 10.1. A single endothermic peak at ~383^{o}C characterizes hydrogen desorption from γ- and β- MgH_2 phases in the 50h milled powder (Fig.10. 8a). After the decomposition of MgH_2 phases, free-active Mg reacts with retained amorphous boron (non-oxidized) and forms MgB_2 (Fig.10.9a) with a nanograin size of 14nm (Table F.11). A striking result is that the DSC curve of the B14H powder after milling for 200h shows an endothermic peak at ~358^{o}C (Fig.10. 8b) although there is no crystalline hydrides in the 200h milled powder (Fig.10.7b). Since it is unlikely the hydrogen is released from crystalline MgB_2, the only explanation is that hydrogen is desorbed from an amorphous phase containing hydrogen, which gives broad backgrounds in the XRD pattern (Fig.10.7b). XRD pattern of the 200h milled B14H powder (made with oxide-free boron) after DSC in Fig.10.9b shows the presence of free Mg, MgB_2 and MgO. The latter is most likely due to the fast oxidation of free-active Mg after exposure to air during XRD test because it is absent after milling for 200h (Fig.10.7b). The XRD pattern of the 200h milled powder after DSC test in Fig.10.9b indicates that the decomposition of amorphous phase occurred during a DSC test as also observed by the appearance of an endothermic peak in Fig.10. 8b.

From results of XRD (Fig.10.7) and DSC analysis (Fig.10. 8), it can be proposed that as milling time passes 50h and reaches 200h, the γ- and β-MgH_2 hydrides transform into amorphous phase containing hydrogen and free-active Mg. Free-active Mg reacts with oxide-free amorphous boron to from MgB_2. The phase transformation during milling in

milled B14H powder (Mg-2B mixture made with oxide-free boron) as milling time increases over 50h and reaches 200h can be postulated by the following reactions (not balanced):

γ- and β-MgH_2 → amorphous phase containing hydrogen + Mg (free-active) +H_2 (10.1a)

Mg (free-active) + 2 a-B (non-oxidized) → MgB_2 ("a-": amorphous) (10.1b)

Hydrogen capacities of B14H powders measured by desorption tests (Fig. G.22 and Fig. G.23) in a Sieverts-type apparatus are summarized in Table 10.2. The result that hydrogen capacity of the B14H powder after milling for 200h (~1.4wt.%) is lower than that of the B14H powder after milling for 50h (~2.9wt.%) and that of the B15H powder (Mg-2B mixture with oxidized amorphous boron) after milling for 200h (~2.6wt.%) supports the notion that the release of hydrogen indeed occurred during the phase transformation from γ- and β-MgH_2 to amorphous MgH_x (reaction 10.1a).

Table 10.1 Summary of DSC data for the milled and the annealed B14H powders (Mg-2B mixture with oxide-free amorphous boron) upon heating.

Powder	Endothermic peak					
	T_{on} (^oC)	T_{peak} (^oC)	T_{end} (^oC)	ΔH (J/g)	Yield of MgH_2 (wt.%)	Desorbed Hydrogen from MgH_2 (wt.%)
B14H50	367.4	383.3	398.2	983	35.0	2.7
B14H50-350-40-20	295.7	308.5	374.7	489	17.4	1.4
B14H200	347.6	357.7	373.8	822	-	-
B14H200-100-43-100	372.6	381.7/423.6	436.5	707	-	-
B14H200-220-43-100	314.1	329.9/367.4	396.0	616	-	-
B14H200-400-40-20	334.3	389.6	429.9	47	-	-

Table 10.2 Hydrogen capacity (wt.%) of the milled and the annealed B14H powders (Mg-2B mixture with oxide-free amorphous boron) measured by desorption test in a Sieverts-type apparatus.

Sample	Hydrogen capacity (wt.%)
B14H50	2.9
B14H200	1.4
B14H200-100-43-100	1.7
B14H200-220-43-100	0.9
B14H200-400-40-20	0.6

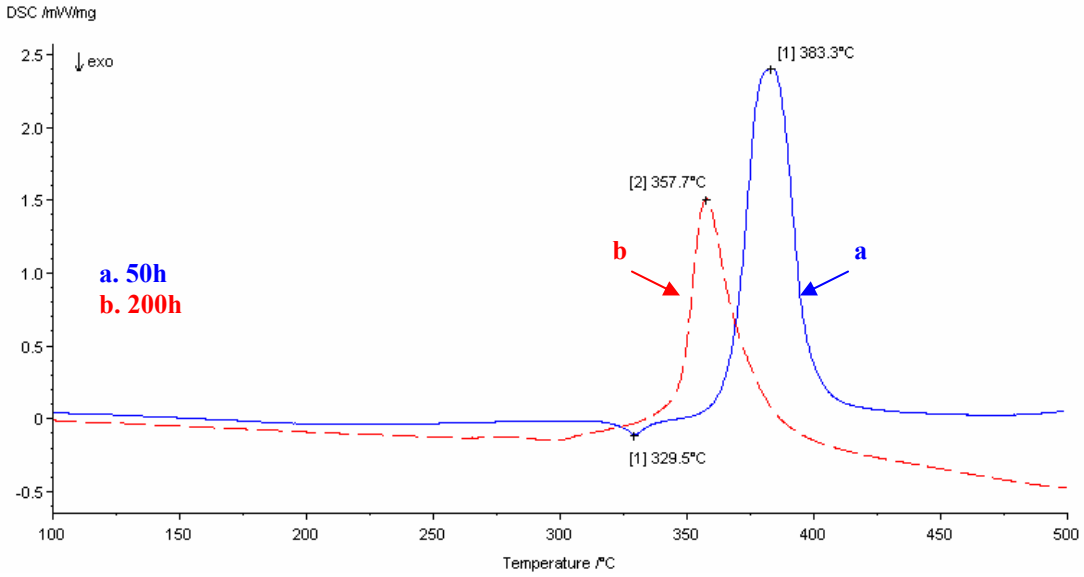

Fig.10. 8 DSC curves of B14H powder made by milling of Mg-2B powder mixture with oxide-free amorphous boron powder for (a) 50h and (b) 200h under IMP710 mode.

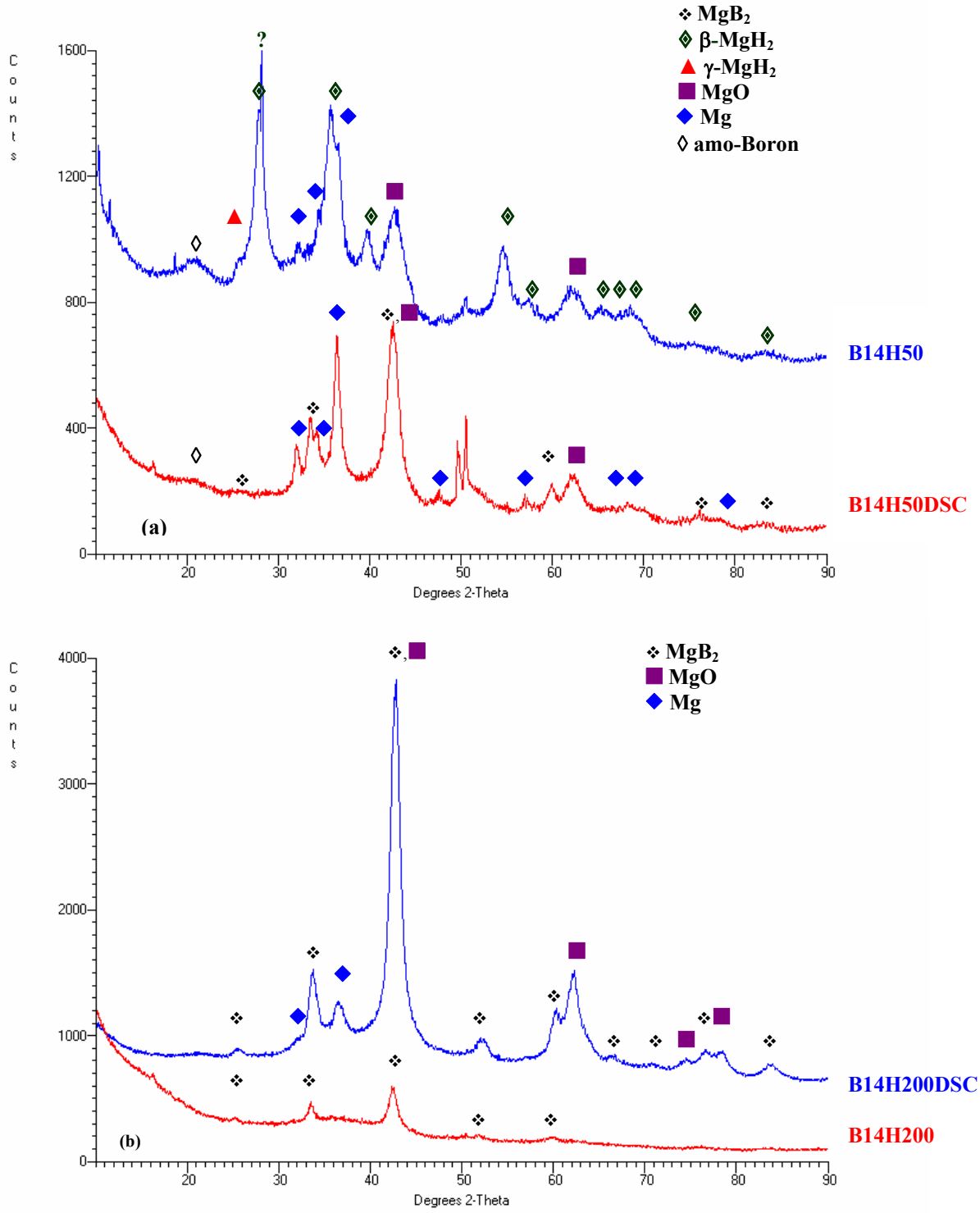

Fig.10.9 XRD patterns of (a) 50h milled and (b) 200h milled Mg-2B powder mixture with oxide-free amorphous boron (B14H) after DSC test (B14H50DSC and B14H200DSC). For comparison, the XRD pattern after milling for 50h and 200h (B14H50 and B14H200) are replotted from Fig.10.7.

10.2.2.2 Annealed powders

As-milled Mg-2B powder mixture made with oxide-free amorphous boron (B14H) was further annealed in a Sieverts-type apparatus under various temperatures and for varying time periods (Table 10.3) to study the effect of annealing on the phase transformation.

Table 10.3 Annealing parameters of Mg-2B powder mixture made with oxide-free amorphous boron (B14H) in a Sieverts-type apparatus.

Powder description	Gas	Pressure (MPa)	Temperature (^{o}C)	Time (h)
B14H50-350-40-20	Hydrogen	4.0	350	20
B14H200-100-43-100	Hydrogen	4.3	100	100
B14H-220-43-100	Hydrogen	4.3	220	100
B14H200-400-40-20	Hydrogen	4.0	400	20

***The annealing temperatures 100 and 220^{o}C are selected based on the transformation temperature (186^{o}C) of the $Mg(BH_4)_2$ [41].**

Hydrogen pressure is fixed at ~4-4.3 MPa, which is the maximum pressure allowed in the apparatus. Since the plateau pressure of $Mg(BH_4)_2$ hydride is unknown, both low and high annealing temperatures (100 to 400^{o}C) coupled with a long and a short annealing time (100h and 20h) were used. The annealed powders have similar morphologies to those of as-milled powders. Morphology of the annealed powders can still be characterized with particles with a ~200 nm particle size and large aggregates. Unfortunately, as shown in Fig.10.10a and Fig.10.11 for XRD patterns of the annealed powders, no $Mg(BH_4)_2$ hydride is synthesized after annealing under the selected temperatures and pressures (Table 10.3).

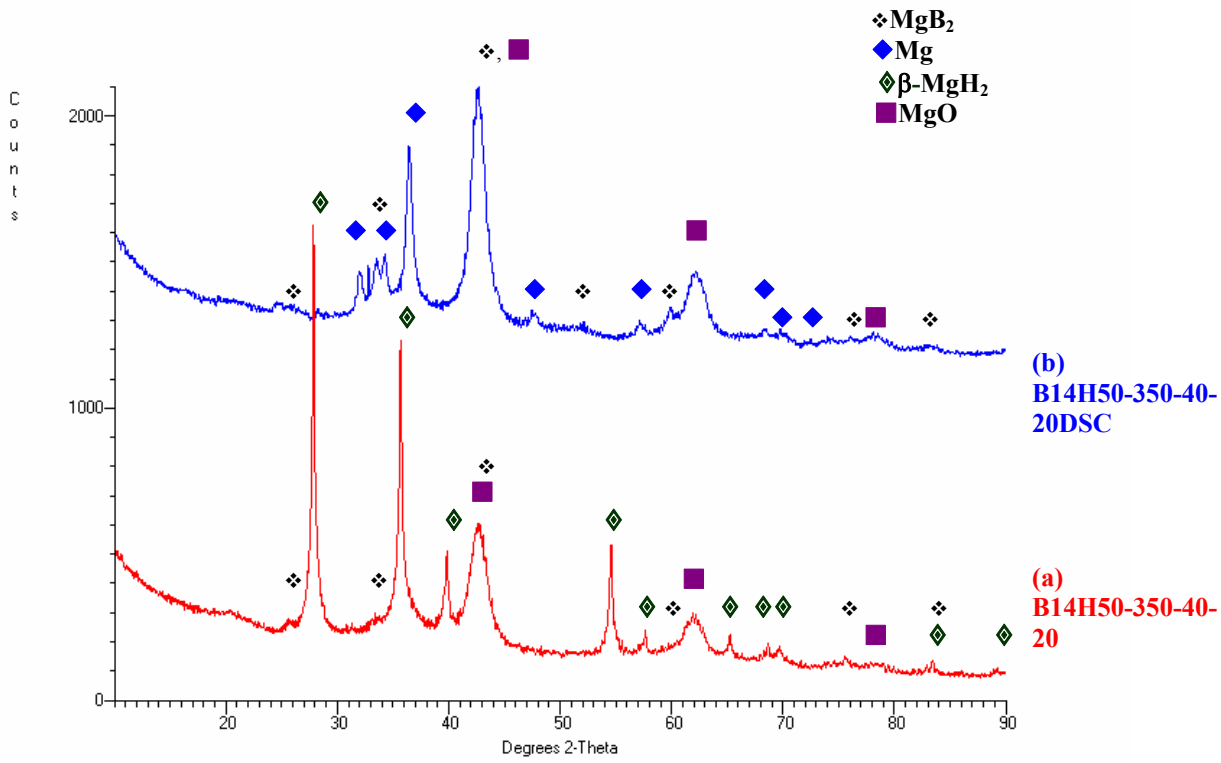

Fig.10.10 XRD patterns of (a) 50h milled B14H powder after annealing at 350°C under 4MPa of hydrogen for 20h (B14H50-350-40-20) and (b) the same annealed powder after DSC test (B14H50-350-40-20DSC).

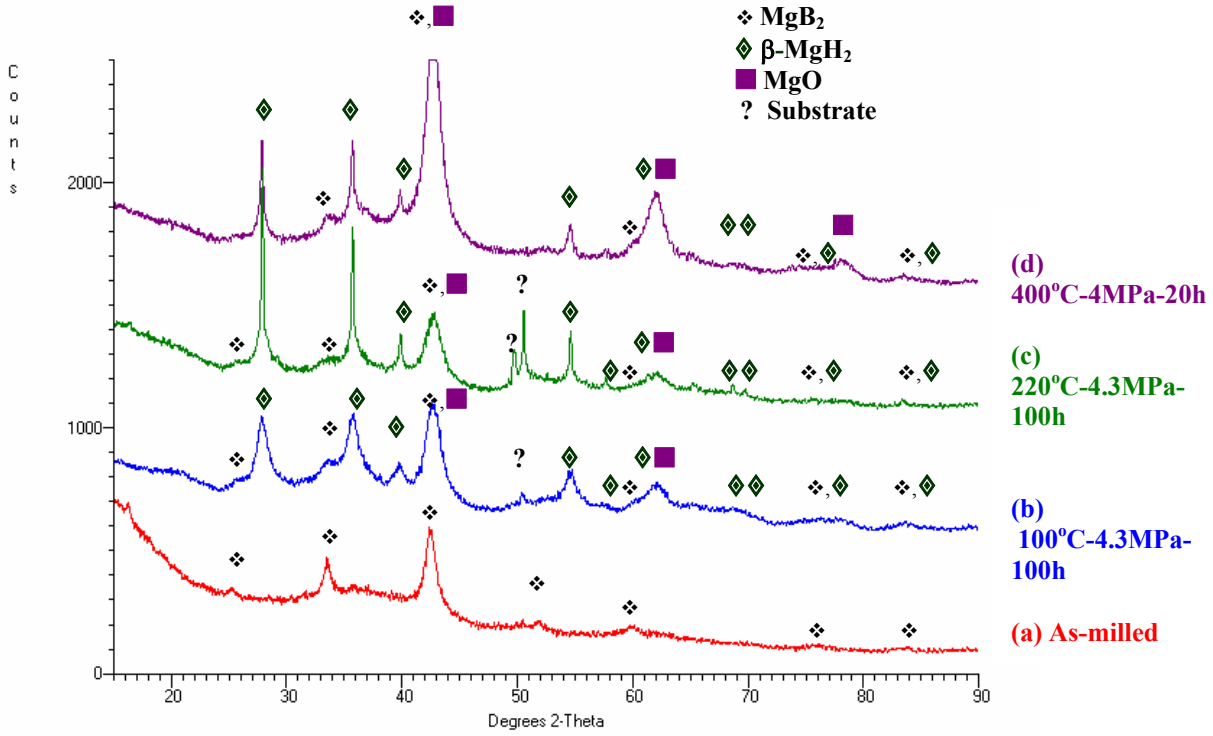

Fig.10.11 XRD pattern of as-milled and annealed B14H200 powders. (a) as-milled, (b) annealed at 100°C under 4.3MPa hydrogen for 100h (B14H200-100-43-100), (c) annealed at 220°C under 4.3MPa hydrogen for 100h (B14H200-220-43-100) and (d) annealed at 400°C under 4MPa hydrogen for 20h (B14H200-400-40-20) in a Sieverts-type apparatus.

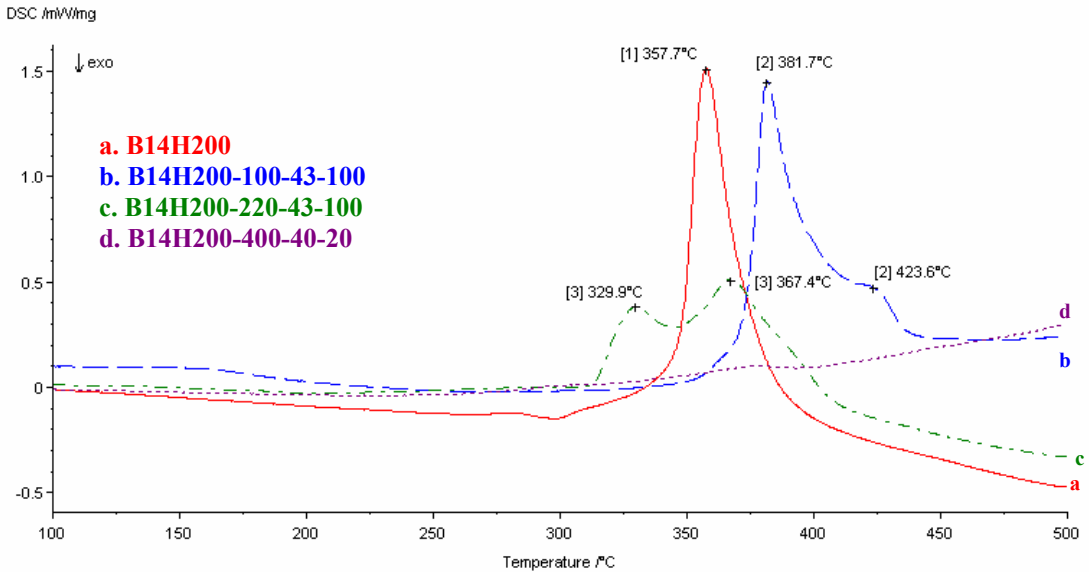

Fig.10.12 DSC curves for (a) the 200h milled Mg-2B mixture made with oxide-free amorphous boron (B14H200) and the same powder after annealing at (b) 100°C under 4.3MPa H_2 for 100h, (c) 220°C under 4.3MPa H_2 for 100h, and (d) 400°C under 4MPa H_2 for 20h.

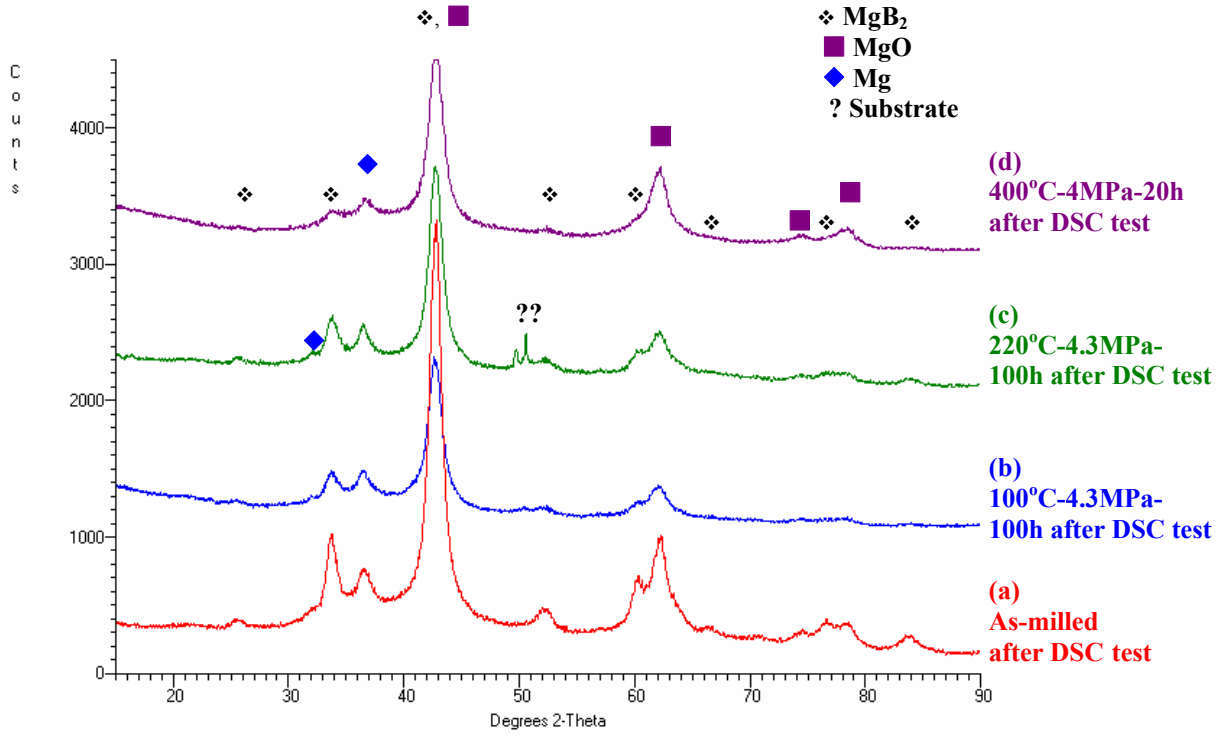

Fig.10.13 XRD pattern of B14H200 powders after DSC test up to 500°C. (a) as-milled, (b) annealed at 100°C under 4.3MPa hydrogen for 100h (B14H200-100-43-100), (c) annealed at 220°C under 4.3MPa hydrogen for 100h (B14H200-220-43-100) and (d) annealed at 400°C under 4MPa hydrogen for 20h (B14H200-400-40-20) in a Sieverts-type apparatus.

XRD patterns and corresponding DSC curves of the milled and the annealed B14H200 powders are shown in Fig.10.11 and Fig.10.12, respectively. The phase transformations after DSC analysis are shown in Fig.10.13. Annealing as-milled B14H200 sample under 4-4.3MPa of hydrogen at 100-400°C for 20-100h results in the formation of crystalline β-MgH_2 (Fig.10.11). This might indicate the transformation of the amorphous phase MgH_x into β-MgH_2. The decomposition of the amorphous phase is also supported by a transformation of a single peak in the DSC curve of the as-milled powder (Fig.10.12a) to peak doublets in DSC curves of powders annealed at 100°C or 200°C under 4.3MPa for 100h (Fig.10.12b and c), indicating a coexistence of an amorphous MgH_x phase and a crystalline β-MgH_2 phase. The presence of Mg in the annealed B14H200 powders after

DSC tests might indicate a full desorption of hydrogen after heating to 500^{o}C (Fig.10.13). A transformation of a single peak to a peak doublet in DSC curves might be also due to a difference particle size distribution [82,83]. However, a similar particle/aggregate size distribution in the B14H200 powder (1.78±1.09μm) and the annealed (B14H200-220-43-100) powder (1.26±0.76μm) rules out this possibility.

The hydrogen capacities of annealed B14H200 powders were estimated by desorption in a Sieverts-type apparatus (Fig. G.24). The amounts of desorbed hydrogen in the as-milled and the annealed B14H200 powders are less than 2 wt.% (Table 10.2).

10.3 Nanohydride formation by milling MgB_2 powder under hydrogen

In the previous section, the Mg-2B powder mixture of elemental magnesium and non-oxidized amorphous boron powder was used as starting materials to synthesize nanohydrides in the Mg-B-H system. Alternatively, in B11H powders, the as-received MgB_2 powder was used as a starting material and milled under hydrogen (Table 7.3). The representative morphology of MgB_2 powders milled under hydrogen is shown in Fig.10.14. A high tendency to form aggregates is observed after a prolonged milling time (>100h). Fig.10.15 and Fig.10.16 show the evolution of XRD pattern and DSC curve of the milled MgB_2 powders as a function of milling time. Nanograin size of phases present in the milled powders and the summary of DSC tests after various milling time are given in Table F.13 and Table G.9, respectively.

Only a nanometric MgB_2 phase (~10nm) is present in the powder after a prolonged milling of MgB_2 powders under hydrogen (Fig.10.15). No evidence is found with respect to the formation of $Mg(BH_4)_2$ hydride (Fig.10.15). Using the flat trace of as-received MgB_2 powder as a baseline, a very weak endothermic peak can be observed in both 50h and 200h-milled B11H powders (as-received MgB_2 powder milled under hydrogen) (Fig.10.16).

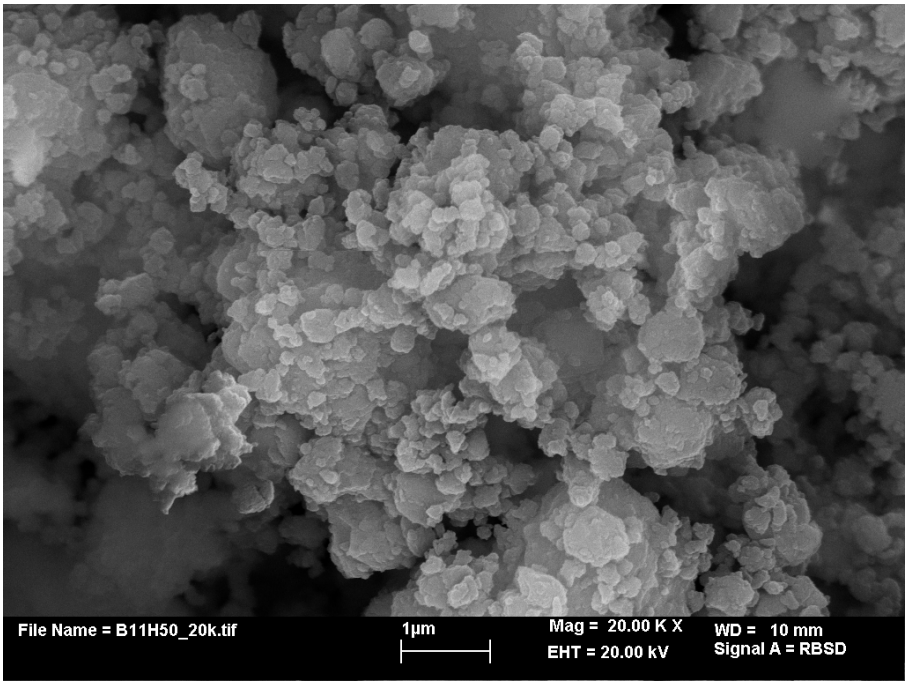

Fig.10.14 BSE micrograph showing the representative morphology of MgB_2 powders milled under IMP710 mode in the hydrogen atmosphere (B11H powders).

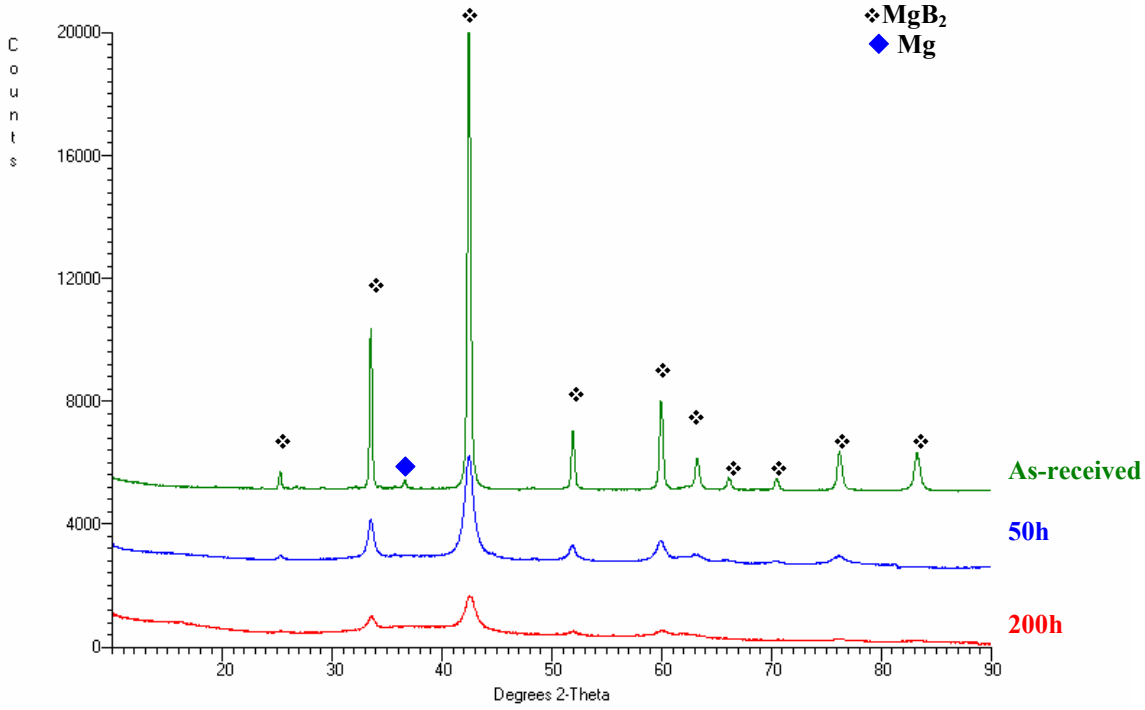

Fig.10.15 XRD patterns of the MgB_2 powders milled under IMP710 mode in the hydrogen atmosphere (B11H powders) as a function of milling time.

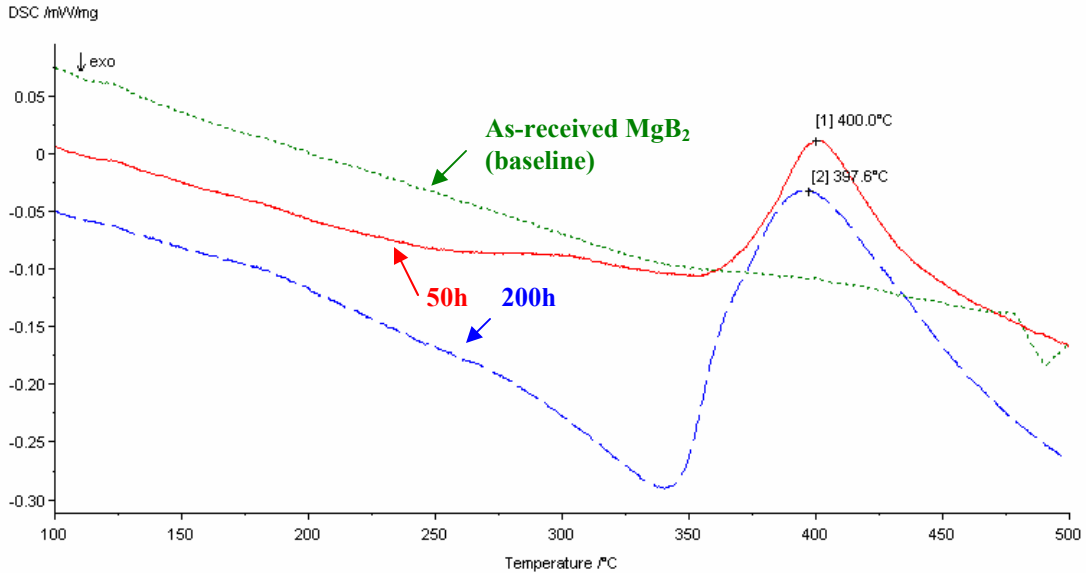

Fig.10.16 DSC curves for MgB_2 powders after milling for 50h and 200h under IMP710 mode in the hydrogen atmosphere (B11H powders). DSC curve for as-received MgB_2 powder is also plotted as baseline.

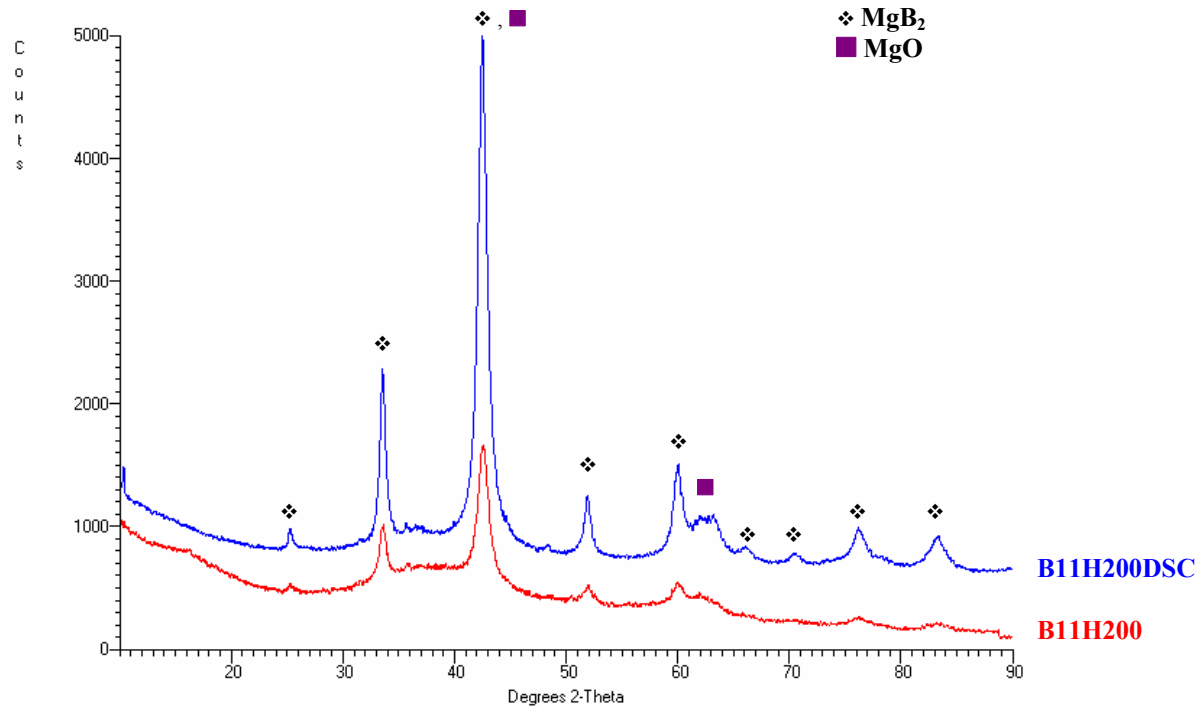

Fig.10.17 XRD pattern of the 200h milled MgB_2 powder after DSC test (B11H200DSC). The XRD pattern of 200h milled MgB_2 powder (B11H200) is replotted from Fig.10.15 for comparison.

Ternary $Mg(BH_4)_2$ hydride has not been synthesized after annealing the 200h-milled MgB_2 powder at 220°C under 4.3MPa of hydrogen for 100h in a Sieverts-type apparatus (B11H200-220-43-100) (Fig.10.18b). A very weak endothermic peak is observed in the DSC curve of the annealed powder (B11H200-220-43-100) (Fig. G.25).

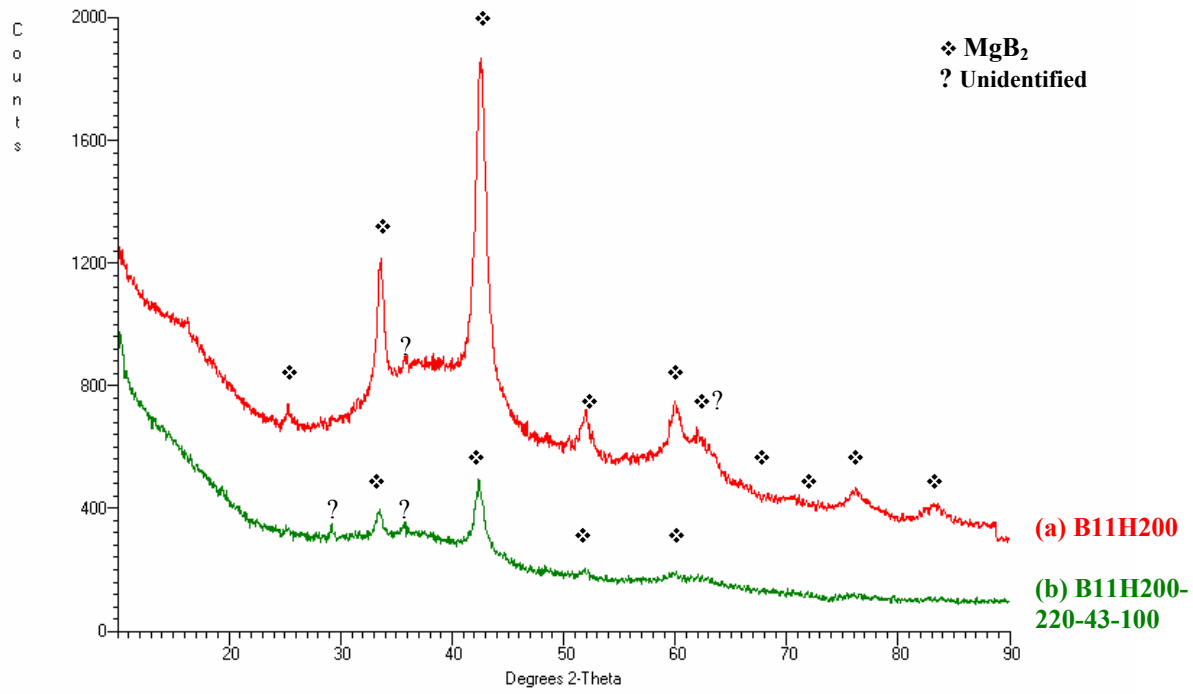

Fig.10.18 XRD patterns of the 200h milled MgB_2 powder after annealing at 220°C under 4.3MPa of hydrogen for 100h (B11H200-220-43-100 powder). The XRD pattern of 200h milled MgB_2 powder (B11H200) is replotted from Fig.10.15 for comparison.

Hydrogen desorption kinetics curves obtained from a Sieverts-type apparatus for the as-milled and the annealed B11H powders are shown in Fig. G.26 (Appendix G.3.4). The results of desorption test indicates a small amount of hydrogen (~0.4-0.8 wt.%) released from the as-milled and annealed MgB_2 powders as also shown by the weak endothermic peak in DSC curves (Fig.10.16). Since there is no crystalline hydride phase in XRD patterns of the milled and the annealed MgB_2 powders (Fig.10.18), one can infer an amorphous phase might be formed after a prolonged milling. However, it has to be

pointed out that as-received MgB_2 powder contains a small amount of retained Mg phase (Fig.10.15). Hence, another alternative might be that retained Mg absorbs hydrogen to form a hydride which amorphizes after a prolonged milling time.

10.4 Synthesis of $Mg(BH_4)_2$ hydride by mechano-chemical activation synthesis (MCAS) of $NaBH_4$ and $MgCl_2$

10.4.1 Phase evolution as a function of milling time

Mechano-chemical activation synthesis (MCAS) of $Mg(BH_4)_2$ using Uni-Ball Mill 5 was studied. The starting materials (B17H powders in Table 7.3) were selected according to the metathesis reaction of $NaBH_4$ with $MgCl_2$ in diethyl ether [41]:

$$2NaBH_4 + MgCl_2 \rightarrow Mg(BH_4)_2 + 2NaCl \qquad (10.2)$$

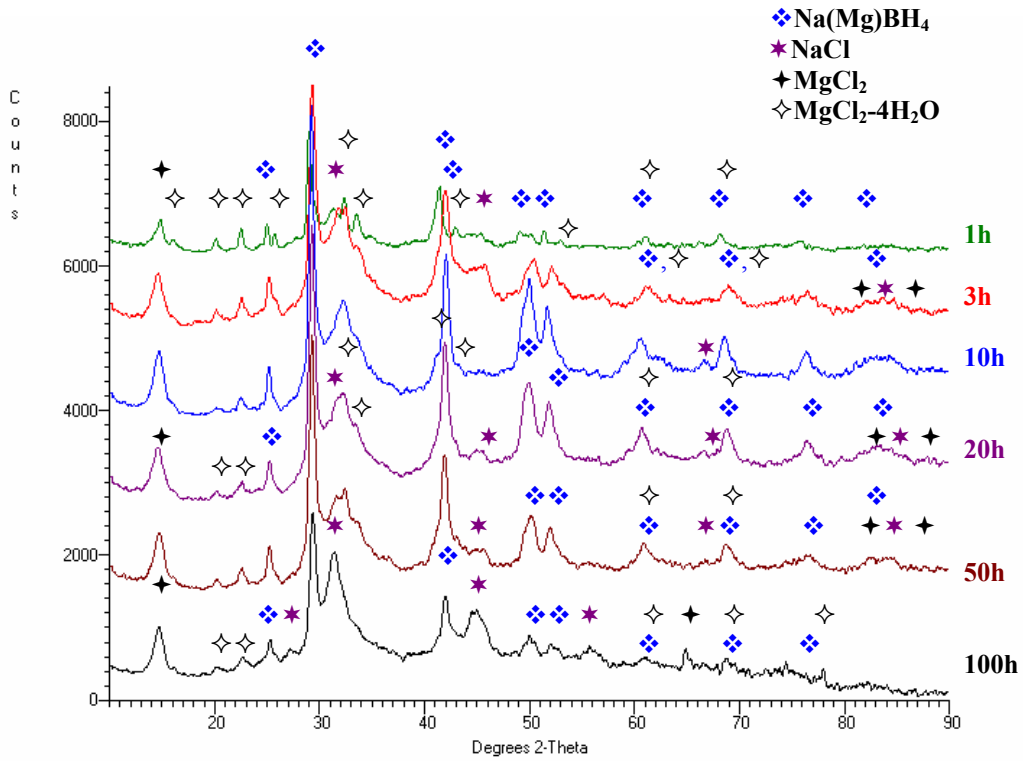

Fig.10.19 XRD patterns of powder mixtures of $2NaBH_4$ and $MgCl_2$ after milling for 1, 3, 10, 20, 50 and 100h under IMP68 mode.

Fig.10.19 shows the XRD patterns of the powder mixture of $NaBH_4$ and $MgCl_2$ in a 2 to 1 stoichiometric ratio after milling for 1, 3, 10, 20, 50 and 100h. The powders after a short milling time consist of $MgCl_2$, NaCl, $MgCl_2$-$4H_2O$ and $NaBH_4$. $MgCl_2$-$4H_2O$ is most likely formed due to the exposure of powders during XRD tests. Increasing milling time up to 100h does not change the phase content in the as-milled powder. Formation of

NaCl implies the reaction of $NaBH_4$ and $MgCl_2$ in the reaction (10.2) does occur after milling. However, peaks in the XRD patterns of milled powders do not match to those belonged to ternary α- or β-$Mg(BH_4)_2$ hydride (ICCD PDF # 26-1212 and 26-1213 [92]) or other phases containing Mg, B or H, which should be observed on the product side after the reaction. Residual $NaBH_4$ and $MgCl_2$ in the long-term milled powders indicate the reaction (10.2) is not completed.

It has to be pointed out that peaks belonged to the retained $NaBH_4$ phase in the milled powder mixtures shift to higher 2θ angles with respect to peak positions of the reference $NaBH_4$ (as-received $NaBH_4$). The shifting indicates decrease of lattice parameters and shrinkage of the unit cell volume of $NaBH_4$ as shown in Table 10.4.

Table 10.4 Lattice parameters and volume of the $NaBH_4$ phase in the milled powders.

Milling time (h)	Lattice parameters (cubic) and volume			
	a (nm)		V (nm^3) $\times 10^{-3}$	
	Average	Error[(1)]	Average	Error[(1)]
Reference $NaBH_4$	0.6163	0.0002	234.04	0.12
1	0.6140	0.0007	231.47	0.53
3	0.6110	0.0010	228.06	0.70
10	0.6122	0.0004	229.41	0.32
20	0.6111	0.0011	228.22	0.81
50	0.6106	0.0014	227.68	1.06
100	0.6061	0.0011	222.60	0.80

[(1)] Average lattice parameter, average volume and error are calculated by software TRACES™ V.6.5.1

Kumar and Cornelius [117] reported structural transitions in $NaBH_4$ under pressure. Peak positions of $NaBH_4$ shift to higher angles as pressure increases. Polymorphic structure transitions under pressure are responsible for the decrease of lattice parameter and the shrinkage of unit cell volume. During milling, enormous pressure is applied to powders due to impacts in a milling process. As a result, in the present work it is possible to have similar structure transitions in the milled $NaBH_4$. However, the structure

transition can not explain the missing of Mg on the product side after milling even though it can explain the shrinkage of unit cell volume of $NaBH_4$ as milling time increase.

Therefore, it is imperative to seek another explanation which can explain both the shrinkage of unit cell volume of $NaBH_4$ and the lack of Mg on the product side after milling. After a 100h of milling time, decrease in intensities of $NaBH_4$ peaks and visible increase in intensities of NaCl peaks are observed (Fig.10.19). This indicates the degree of reaction between $NaBH_4$ and $MgCl_2$ increases as milling time increases. Thus, as milling time increases, more free-Mg is produced. It can be postulated that aforementioned decrease of the lattice parameter (Table 10.4) is due to the formation of solid solution of Mg in $NaBH_4$.

Nakamori and Orimo [68] studied the destabilization of $LiBH_4$ and found a partial substitution of Li by Mg. Similarly, Mg might substitute Na in the $NaBH_4$ lattice and form a $Na(Mg)BH_4$ solid solution after milling. The lattice shrinkage is consistent with the magnitude of the atomic radius of Mg and Na which is 0.1604nm and 0.1858nm, respectively [103]. As milling time increases, more and more free-Mg diffuses into $NaBH_4$ lattice and substitutes Na in the lattice and causes the shrinkage in the unit cell volume.

10.4.2 Thermal behavior by DSC-TGA analysis

Thermal behavior of the milled $2NaBH_4$ and $MgCl_2$ powder was investigated by DSC and TGA. Fig.10.20 shows DSC-TGA curves of the 10h, 20h and 50h milled powders upon heating to 420^{o}C as well as the curve of the 100h milled powder upon heating to 500^{o}C. The results of DSC and TGA analysis are summarized in Table 10.5 and Table 10.6, respectively. One endothermic event at a 200-250^{o}C range, one endothermic event at 250-320^{o}C range and one endothermic event at a 320-400^{o}C range are observed in DSC curves of the milled powders after milling 10, 50 and 100h. In the DSC curve of 20h milled powder, thermal events at a 320-400^{o}C range is not observed. For the 100h milled powder, which is heated to 500^{o}C, an endothermic peak at ~412^{o}C is observed (Fig.10.20d). The DSC samples transforms from a loose powder into a layer coated on the crucible wall after cooling down from ~295-299^{o}C in DSC-TGA tests. This might indicate melting of the milled powder at ~295-299^{o}C.

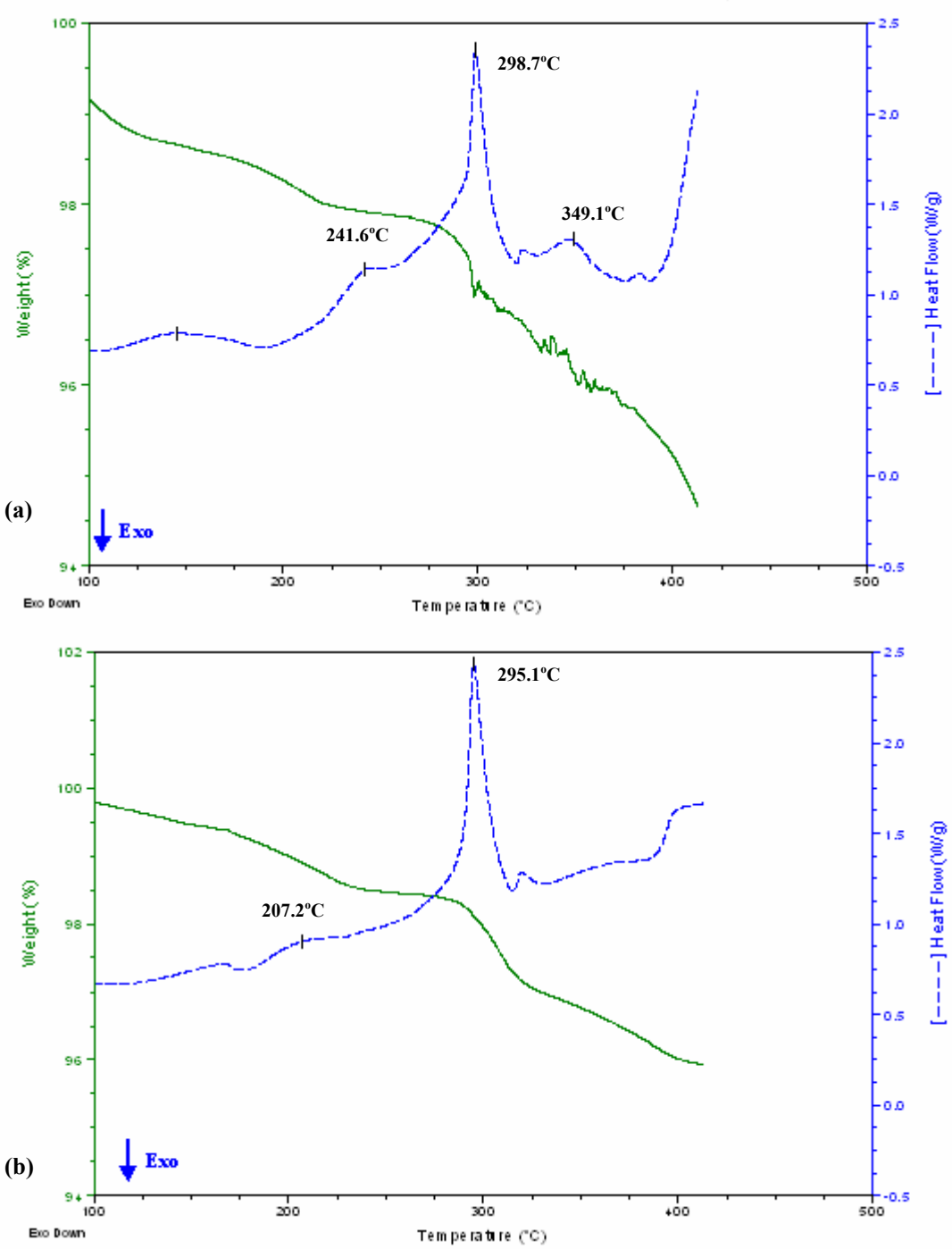

Fig.10.20 DSC-TGA curves of powder mixtures of $2NaBH_4$ and $MgCl_2$ after milling for (a) 10h, (b) 20h, and (c) 50h upon heating to 420°C and (d) 100h upon heating to 500°C.

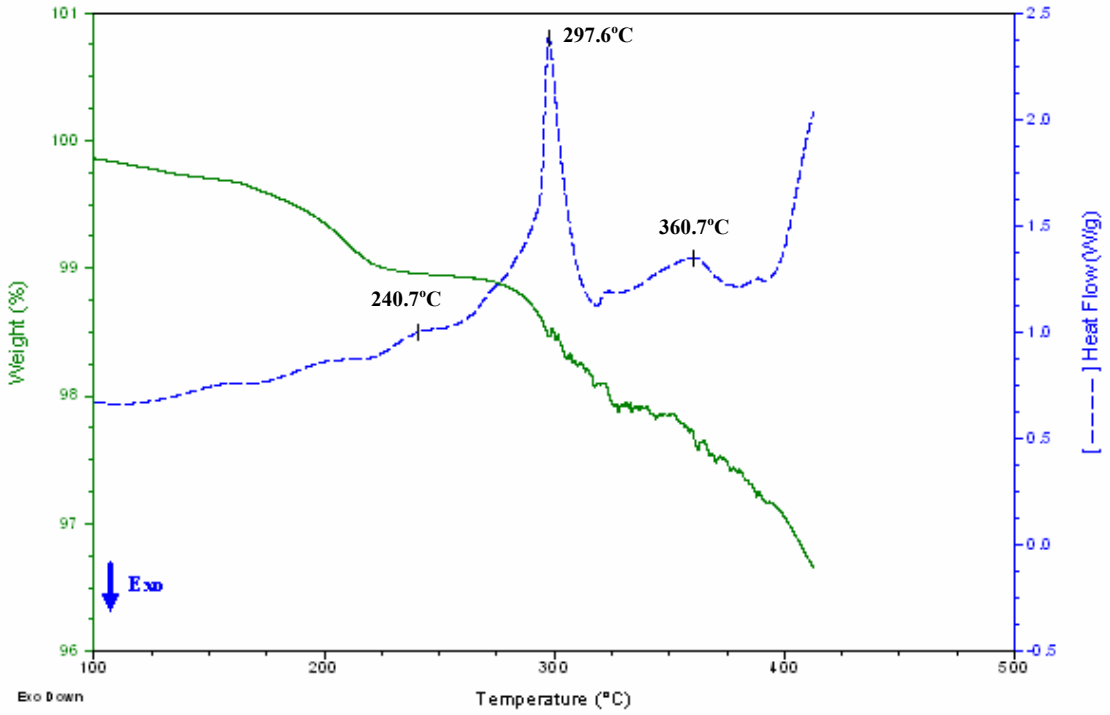

(c)

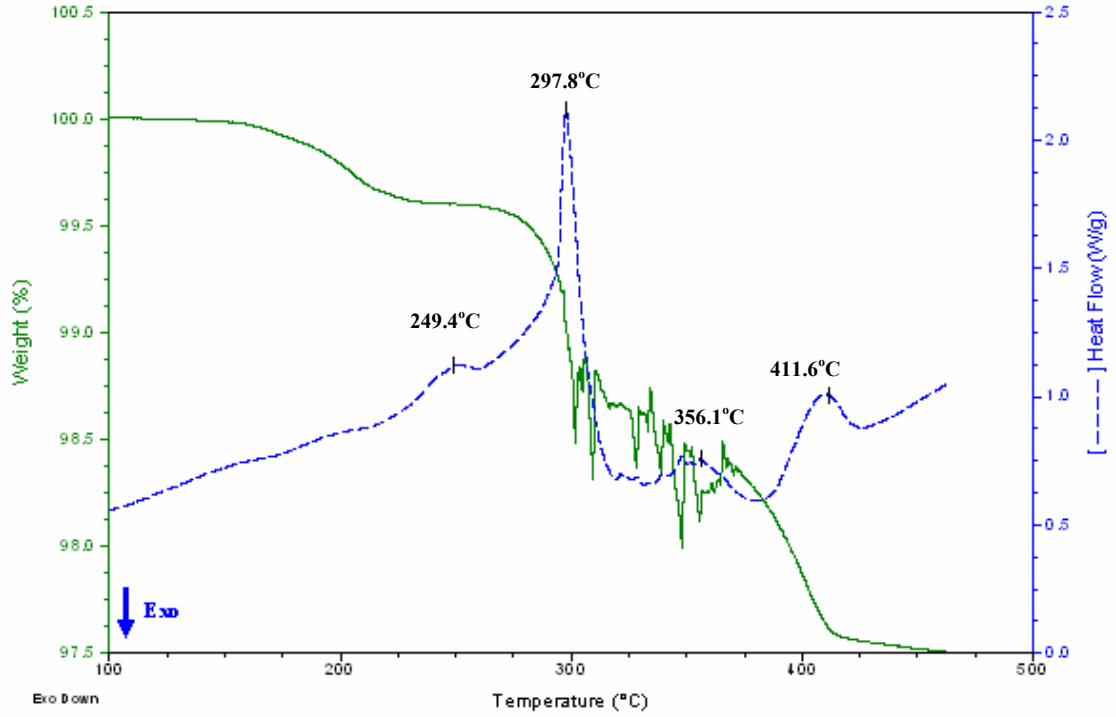

(d)

Fig.10.20 cont'd

Table 10.5 Summary of DSC results for powder mixtures of $2NaBH_4$ and $MgCl_2$ after milling for 10, 20, 50 and 100h.

Milling time (h)	10			20		
Temperature range (^oC)	T_{on} (^oC)	T_{peak} (^oC)	ΔH (J/g)	T_{on} (^oC)	T_{peak} (^oC)	ΔH (J/g)
200-250	220.7	241.6	12.5	197.2	207.2	7.3
250-320	293.4	298.7	108.6	290.1	295.1	100.8
320-400	341.9	349.1	15.6	-	-	-

Milling time (h)	50			100		
Temperature range (^oC)	T_{on} (^oC)	T_{peak} (^oC)	ΔH (J/g)	T_{on} (^oC)	T_{peak} (^oC)	ΔH (J/g)
200-250	224.8	240.7	3.5	230.0	249.4	7.5
250-320	293.7	297.6	110.7	293.6	297.8	119.8
320-400	332.6	360.7	19.5	346.6	356.1	17.2
400-450	-	-	-	387.6	411.6	31.8

Table 10.6 Weight loss measured by TGA analysis for milled powder mixtures of $2NaBH_4$ and $MgCl_2$.

	Weight loss (wt.%)			
Temperature range (^oC)	10h milled	20h milled	50h milled	100h milled
100-250	1.3	1.3	0.9	0.4
275-335	1.4	1.5	1.0	1.2
335-420	1.8	1.0	1.2	0.9

In order to analyze the nature of thermal events in the milled powder, small samples of the 100h-milled powder were heated to 250, 315 and 425^{o}C under 20kPa of argon for 0.5h in a Sieverts-type apparatus. The XRD patterns corresponding to the powders heated to the selected temperatures are shown in Fig.10.21. An estimate of the lattice parameter shows that Na(Mg)BH_4 solid solution still exists in the annealed powders(0.6116nm at 250^{o}C and 0.6076nm at 315^{o}C). After annealing at 250^{o}C (Fig.10.21b), $MgCl_2$ does not

exist and the powder contains $Na(Mg)BH_4$, NaCl, $MgCl_2$-$4H_2O$ and $MgBO_2(OH)/MgB_2O(OH)_6$ phases. $Na(Mg)BH_4$, NaCl and $MgBO_2(OH)/MgB_2O(OH)_6$ are still observed after annealing at 315^oC (Fig.10.21c). The most interesting observation in the powder annealed at 315^oC is the formation of β-MgH_2 phase (Fig.10.21c). After annealing at 425^oC, β-MgH_2 and $Na(Mg)BH_4$ phases disappear and the annealed powder only contains Mg, NaCl and $MgBO_2(OH)/MgB_2O(OH)_6$ phases. The increase of the intensity of NaCl with increasing annealing temperature implies that the degree of reaction of $MgCl_2$ and $Na(Mg)BH_4$ increases. However, peaks belonged to ternary $Mg(BH_4)_2$ hydrides are still not observed in the annealed powder.

A qualative EDS analysis shows that all of the annealed samples (250^oC, 315^oC, and 425^oC) contain elements such as Na, Cl, Mg and B. This indicates the annealed powders must have phases with a combination of these elements and supports the XRD analysis that the $MgBO_2(OH)/ MgB_2O(OH)_6$ phases exist in the annealed powders.

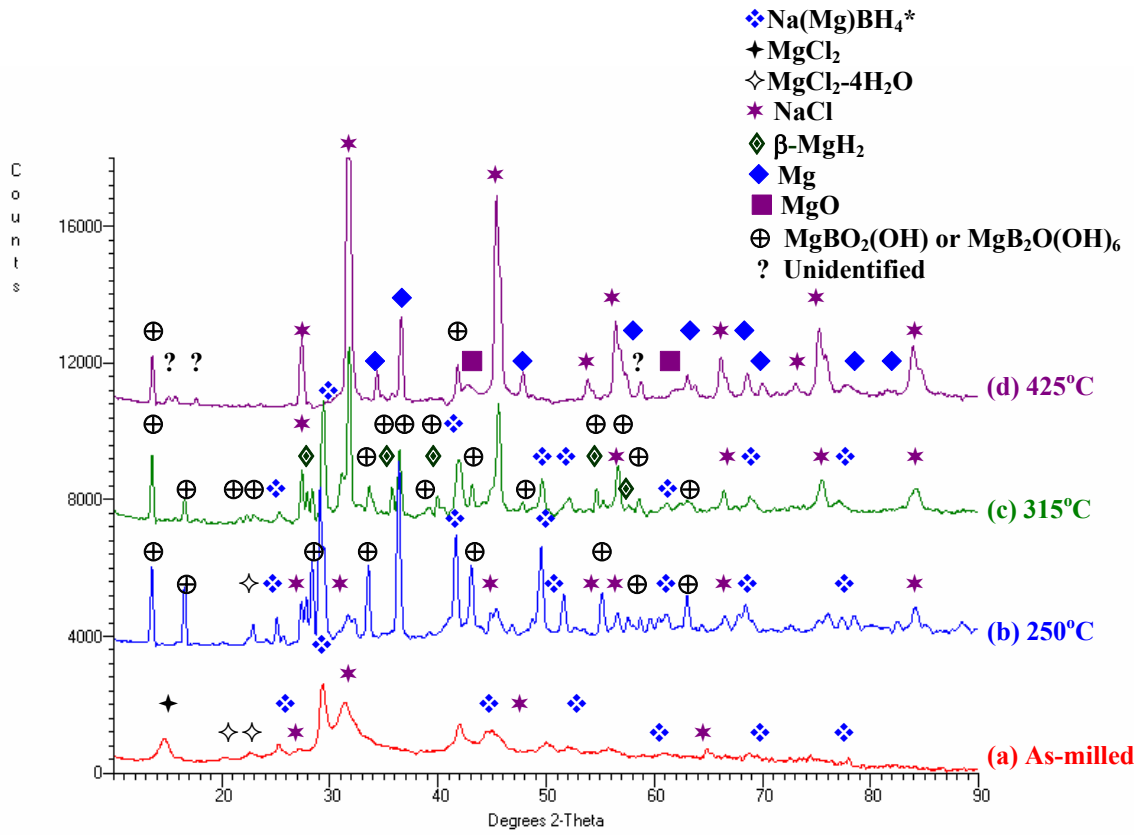

Fig.10.21 XRD pattern of (a) 100h-milled powder mixture of $2NaBH_4$ and $MgCl_2$ and the same powder after annealing at (b) 250°C, (c) 315°C and (d) 425°C under 20kPa of argon pressure for 0.5h in a Sieverts-type apparatus.

Fig.10.22 shows the XRD pattern of unmilled powder mixture of $NaBH_4$ and $MgCl_2$ in a 2 to 1 stoichiometric ratio after annealing at 315°C under 20kPa of argon for 0.5h. The powder mixture contains $MgCl_2$ and $NaBH_4$ (Fig.10.22). Annealing of the unmilled powder mixture at 315°C does not result in melting at ~295-299°C. Therefore, the melting observed at ~295-299°C in annealing of the milled powders is due to the effect of milling.

Unfortunately, the evolution of XRD patterns of the milled powders as a function of temperature does not reveal which phase melts at ~295-299°C.

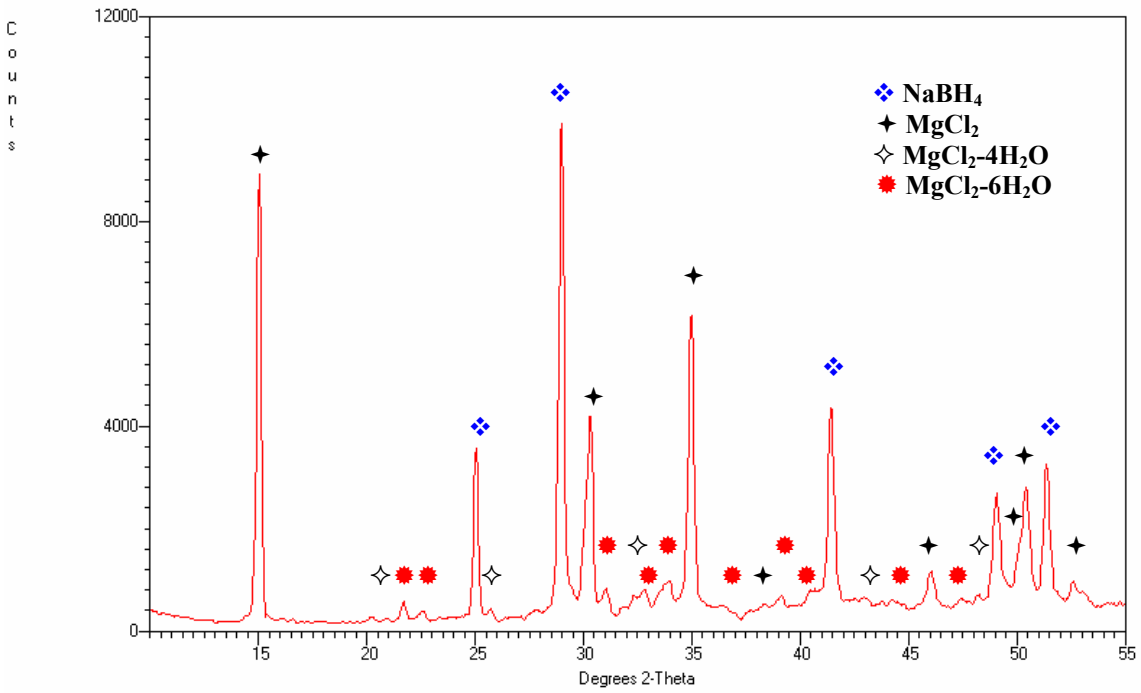

Fig.10.22 XRD pattern of unmilled powder mixture of $NaBH_4$ and $MgCl_2$ in a 2 to 1 stoichiometric ratio after annealing at 315°C under 20kPa of argon pressure for 0.5h in a Sieverts-type apparatus.

In general, TGA curves of milled powders show a three-stage weigh loss at temperature ranges of ~100-250°C, ~275-335°C and ~335-420°C. The first weight loss does not match to any heat events in the DSC curves of milled powders while the second one correlates well to the endothermic peak at ~295-299°C. The third one matches to the endothermic peak at ~349-361°C (and ~412°C for the 100h milled powder) in DSC curves.

$MgCl_2$, NaCl and $NaBH_4$ decompose at a temperature higher than the maximum test temperature in the DSC-TGA tests [118]. However, magnesium chloride hydrate ($MgCl_2$-xH_2O) starts to decompose at 95-115°C [119]. The weight loss at ~100-250°C is most likely due to the release of water absorbed by residual $MgCl_2$ in the milled powders during loading powders into the DSC-TGA apparatus. As mentioned earlier, the

morphology of the milled samples transforms from a loose powder into a layer welded on the crucible at ~295-299^{o}C in DSC-TGA test, which is a sign of melting. As a result, the second weight loss (~275-335^{o}C) can be attributed to the melting and possibly the simultaneous decomposition of an unknown hydride phase in the powder, which gives an endothermic peak at ~295-299^{o}C in the DSC curves. However, it is still needed to clarify which unknown hydride phase in the milled powders melts and decomposes at this temperature range. A zigzag shape of TGA curves from ~300 to 400^{o}C might be due to the melting and simultaneous decomposition (Fig.10.20).

The thermal behavior of 100h-milled powder studied by DSC is similar to the thermogram for $Mg(BH_4)_2$ reported by Konoplev and Bakulina [41], except for the peak related to the polymorphic transformation. The authors reported that the thermal effect at 304-314^{o}C was due to the melting with simultaneous decomposition of $Mg(BH_4)_2$ and the formation of magnesium hydride. The peak at 402-406^{o}C was due to the decomposition of magnesium hydride. The nature of the thermal effect at 375^{o}C was not clear. Endothermic peaks at ~295-299^{o}C, ~349-361^{o}C and ~412^{o}C in the DSC curve of 100h-milled powder (Fig.10.20) match to the peaks at 304-314^{o}C, 375^{o}C and 402-406^{o}C in the thermogram of $Mg(BH_4)_2$ in reference [41]. From this point of view, the peak at ~295-299^{o}C observed in the milled powders synthesized in the present work might be the melting and simultaneous decomposition of $Mg(BH_4)_2$, and the formation of magnesium hydride. The peak at ~412^{o}C might be due to the decomposition of magnesium hydride. The nature of thermal effect at ~349-361^{o}C is not clear. However, peaks in the XRD patterns of milled powders do not match to those belonged to ternary α- or β-$Mg(BH_4)_2$ hydride (PDF # 26-1212 and 26-1213).

Nakamori et al. [120] synthesized metal boronhydrides $M(BH_4)_n$ (M= Mg, Sc, Zr, Ti and Zn; n=2-4) by mechano-chemical activation synthesis (MCAS). The mixture of MCl_n and $nLiBH_4$ was milled under argon (0.1MPa) for 5h. The reaction during milling was proposed as following:

$$MCl_n + nLiBH_4 \rightarrow M(BH_4)_n + nLiCl \quad (10.3)$$

There are no XRD peaks of starting materials of MCl_n and $nLiBH_4$ after milling for 5h, which is in contrast to the result that starting materials ($NaBH_4$ and $MgCl_2$) are still observed after a 100h of milling time in the present work. All of the XRD peaks after MCAS belonged to LiCl. No XRD peaks of $M(BH_4)_n$ were observed after milling, which according to the authors was due to disordering of the crystal structure. As a result, the atomistic vibrations were investigated to confirm the existence of $M(BH_4)_n$. The Raman spectra of the as-milled samples gave peak positions agreed with vibrating modes of $M(BH_4)_n$ but not the same as those of $LiBH_4$. This confirmed the presence of $M(BH_4)_n$ after MCAS.

Thermal desorption analysis of milled powders showed desorption peaks of $M(BH_4)_n$, which are not the same as that of $LiBH_4$. Endothermic peaks at ~292 and ~427^oC were observed in the thermal desorption profile of $Mg(BH_4)_2$, which correlate well with two of four endothermic peak position of the DSC curve of milled powders in the present work (~298 and ~412^oC), and two of the three peaks in the thermalgram of $Mg(BH_4)_2$ reported by Konoplev and Bakulina (~304-314 and ~402-406^oC) [41].

10.5 Discussion

10.5.1 Synthesis of amorphous hydride by CRMA of Mg and amorphous boron powders

If one compares the synthesized phases in the 200h milled powders made with oxidized (B15H) and oxide-free boron (B14H) (Fig.10.5a and Fig.10.7b), it can be found that MgB_2 is not synthesized in the 200h-milled powder in which oxidized amorphous boron is used for milling (B15H). Boron oxide prevents reaction of boron with Mg during milling. Wang et al. [112] and Orimo et al. [113] report a preheating of amorphous boron below 1×10^{-4} Pa before milling boron under hydrogen, and synthesizing MgB_2 by annealing elemental powders under hydrogen pressure. The pretreatment of amorphous boron is necessary to remove absorbed impurity gases, most likely oxygen, in amorphous boron powders. It is most likely that in B15H powders, in which oxidized amorphous boron is used, boron particles are covered by oxide layers and even with a prolonged milling time (200h) it is not cracked.

Varin et al. [83,106-108] studied the feasibility of synthesis of MgH_2, Mg_2FeH_6, and $Mg(AlH_4)_2$ by CRMA of elemental Mg, Fe and Al under hydrogen. Only crystalline hydrides are synthesized and no amorphous hydride exists in the as-milled powders. As a result, in the present work, in which Mg and amorphous boron powders are milled under hydrogen (200h milled B14H powder), it is most likely that oxide-free amorphous boron acts as a catalyst to an amorphous transformation of MgH_2 to an amorphous phase containing hydrogen during a milling process. The possibility that the aforementioned amorphous phase is $Mg(BH_4)_2$ can not be excluded. In future work, the Raman spectra of the 200h milled B14H powder can be applied to confirm the presence of $Mg(BH_4)_2$ [120].

While synthesizing a binary A_xB_y compound by mechanical alloying from the elemental powders, i.e., the state of zero enthalpy, gaining enthalpy by mechanical milling lowers the enthalpy of the system and in the enthalpy diagram one is going from zero downward. Since the formation enthalpy of MgB_2 is -92 kJ/mol [114] versus -74 kJ/mol for the MgH_2, the latter will have a tendency to form first in the Mg-B-H mixture during mechanical milling from the elemental powders.

The tendency to form amorphous phase can be discussed using an empirical model by Egami and Waseda for producing amorphous alloys by rapid quenching of metallic glasses (a non-equilibrium processing) [115]. The value of product of (a) the atomic volume mismatch factor ($\Delta V_{AB}/V_A$), and (b) the (empirical) minimum concentration of the solute element required to form amorphous (C_B^{min}), oscillates around the constant value 0.1:

$$|\Delta V_{AB}/V_A|(C_B^{min}) \approx 0.1 \quad (10.4a)$$

$$\Delta V_{AB}/V_A = (V_A\text{-}V_B)/V_A = (r_B^3 - r_A^3)/r_A^3 \quad (10.4b)$$

It is assumed that a relationship similar to that observed by Egami and Waseda should hold for the formation of amorphous hydrides in mechanical alloying mills, as long as the thermodynamic driving forces are overruled by kinetic factors during nonequilibrium processing in ball mills under high-energy milling mode [116]. Table 10.7 summarizes the selected examples of C_B^{min}, which are calculated from Eq. 10.4a. One can find that little Mg (1.3 at% or 0.6 wt.%) is needed to form amorphous phase in B-rich Mg-B system and 10 at.% or 0.5 wt.% of hydrogen is required to produce amorphous phase in Mg-H system. Therefore, above this low limit, 0.5-0.6 wt.% of either B or H, or both, the Mg-H or Mg-B-H system should have a high tendency to amorphization under a high

energy milling mode. In the previous study of Mg-2Al system milling under hydrogen, no amorphous phases were formed after milling. It is calculated that a minimum 25 at.% of Mg is needed to amorphize Al-rich Mg-Al system. These calculations indicate the driving force towards the formation of amorphous phase would not be great.

Table 10.7 The atomic volume mismatch and the calculated minimum solute concentrations for selected alloys and metal hydrides.

A-B or A-H	r_A	r_B	r_H	$\Delta V_{AB}/V_A$	$\Delta V_{AH}/V_A$	C_B^{min}(%)	C_H^{min}(%)
Mg-H	1.60	-	0.32*	-	-0.992	-	10
Mg-H	1.60	-	0.80	-	-0.875	-	11
B-Mg	0.78	1.60	-	7.632	-	1.3	-
Al-Mg	1.43	1.60	-	0.401	-	25	-

Note: The most of atomic radii in this table were taken from Egami and Waseda [115]. Either atomic or a covalent* radius was used for hydrogen but one can note this does not affect much the calculations.

10.5.2 Synthesis of $Mg(BH_4)_2$ by MCS and MCAS in Uni-Ball Mill 5

A crystalline $Mg(BH_4)_2$ is not synthesized in the present work by MCS/MCAS using elemental Mg and amorphous boron powder as well as commercial MgB_2 powders. Fitchner et al. [121] synthesized $Mg(BH_4)_2$ by ball milling of MgB_2 under hydrogen pressures around 10 MPa. Goerrig [62] synthesized $M(BH_4)_n$ boron hydrides (M=Na, K, Mg or Ba; n = 1 or 2) by treating the metal boron mixture at a temperature of ~350 to 1000^{o}C under a hydrogen pressure of ~3 to 50MPa. $Mg(BH_4)_2$ was synthesized by annealing a tablet of Mg-2B (800kg/cm^2) at 620^{o}C under ~15MPa of hydrogen for 5h. However, even under such a high temperature and a high pressure, the formation rate of $Mg(BH_4)_2$ was only 37.6%.

As a result, it seems that the energy input and the pressure during milling as well as the pressure during annealing might not be sufficient to synthesize the $Mg(BH_4)_2$ hydride in

the present work. Stronger milling force (controlled by magnet field) and a newly designed chamber which can allow a higher pressure in a Sieverts-type apparatus should be considered in future work.

In the MCAS process, a small amount of $Mg(BH_4)_2$ (in an amorphous form) might have been synthesized but the formation of $Na(Mg)BH_4$ solid solution might prevent the synthesis of a large amount of $Mg(BH_4)_2$ hydride.

In contrast to the successful mechanochemical activation synthesis (MCAS) reaction of $NaAlH_4$ and $MgCl_2$ in which $Mg(AlH_4)_2$ is synthesized in 5h of milling time, no XRD peaks belonged to $Mg(BH_4)_2$ hydride are observed after MCAS of $2NaBH_4$ and $MgCl_2$ in the present work. However, the following indirect evidences indicate that a small amount of $Mg(BH_4)_2$ might have been form in an amorphous state after MCAS:

(1) Although the starting materials of $MgCl_2$ and $NaBH_4$ still retain after milling, the formation of NaCl indicate that certain transformation does occur after milling of $MgCl_2$ and $NaBH_4$.

(2) As mentioned earlier, thermal analysis of the milled powder mixture in the present work shows similar results to those of $Mg(BH_4)_2$ reported earlier by Nakamori et al. [120], and Konoplev and Bakulina [41].

(3) Jeon and Cho [72] synthesized $Zn(BH_4)_2$ by mechano-chemical activation synthesis (MCAS) of $NaBH_4$ and $ZnCl_2$. The XRD peaks after excluding NaCl peaks were assigned to $Zn(BH_4)_2$ phase in the milled powder. The presence of $Zn(BH_4)_2$ was confirmed by the FT-IR spectra. On the other hand, Nakamori et al. [120] reported the MCAS of $MgCl_n$ and $LiBH_4$, in which the formation of $M(BH_4)_n$ (M= Mg, Zn, Sc, Zr and Hf) was confirmed by the Raman spectra because synthesized $M(BH_4)_n$

had an disordered crystal structure (i.e., showed no XRD peaks). The differences in starting materials and milling parameters affect on the structure of the synthesized phase. The synthesized phase after milling might not be necessary to be a crystalline phase.

As a result, a small amount of an amorphous $Mg(BH_4)_2$ might exist in the milled powder mixture of $2NaBH_4$ and $MgCl_2$.

An important discovery is the formation of $Na(Mg)BH_4$ solid solution in the milled powder mixture of $2NaBH_4$ and $MgCl_2$ (Table 10.4). The solutionizing effect increases as milling time increases. In due course of MCAS of the $Mg(AlH_4)_2$, no formation of solid solutions have been observed. Therefore, it is hypothesized here that the presence of $Na(Mg)BH_4$ solid solution in the MCAS process might inhibit the fully transformation in reaction (10.2). Once solid solution is formed, the amount of Mg will not be sufficient to form a large amount of $Mg(BH_4)_2$ hydride.

If one compares enthalpy of formation of $NaBH_4$ and $NaAlH_4$, it can be found that enthalpy of formation of $NaBH_4$ (-191.84kJ/mol) is larger than that of $NaAlH_4$ (-15.5kJ/mol). As a result, MCAS of $NaBH_4$ and NaCl might be more difficult than that of $NaAlH_4$ and NaCl. The decomposition of $Zn(BH_4)_2$ starts at ~85^oC and completes at ~140^oC [72]. Furthermore, it was also found that $Zn(BH_4)_2$ decomposes after storing under a protective atmosphere for a week. This indicates that $Zn(BH_4)_2$ is unstable even at room temperature. Nakamori et al. [120] studied the thermal stability of metal boronhydrides $M(BH_4)_n$ (M= Li, Na, K, Mg, Sc, Zr, Zn and Ti) and reported that $Zn(BH_4)_2$ has the lowest thermal stability. As a result, it seems that $Zn(BH_4)_2$ is more

unstable than $Mg(BH_4)_2$, which might imply that it is easier for $Zn(BH_4)_2$ to be formed during MCAS.

$Mg(BH_4)_2$ synthesized in the present work might decompose in a two-step reaction, which can be hypothesized as following:

$$Mg(BH_4)_2 \rightarrow MgH_2 + 2B + 3H_2 \qquad \sim 295\text{-}299^oC \text{ (after melting of } Mg(BH_4)_2) \qquad (10.5a)$$

$$MgH_2 \rightarrow Mg + H_2 \qquad \sim 412^oC \qquad (10.5b)$$

After melting at ~295-299^{o}C, $Mg(BH_4)_2$ decomposes into MgH_2 directly. No intermediate ternary hydride or intermetallic phase is formed. The first reaction correlates well with the first-step reaction in the multi-step reaction proposed by Nakamori et al. [120] for borohydrides $M(BH_4)_n$ (M=Mg, Sc and Zr) except for $Zn(BH_4)_2$. The rest of steps were not proposed. The desorbed gas form $M(BH_4)_n$ (M = Li, Na, K, Mg, Sc and Zr) contained only hydrogen [120]. The purity of supplied hydrogen gas for fuel cell is very crucial. Impurities in ppm level might poison the fuel cell and decrease the power output.

Reversibility might be the other problem for the $Mg(BH_4)_2$ hydride. Synthesis of $Mg(BH_4)_2$ by MCS of elemental powders has not reported. Although $Mg(BH_4)_2$ can be synthesized by heating Mg-2B mixture under hydrogen, high pressure of hydrogen and high temperature are required [62]. Hydrogen desorption temperature of $Mg(BH_4)_2$ is still too high for PEM fuel cell, but might be suitable for fuel cells which allow higher working temperature.

11. Summary and conclusions

A study of the mechano-chemical synthesis (MCS) and the mechano-chemical activation synthesis (MCAS) of nanostructured hydrides in the Mg-H, Mg-Al-H and Mg-B-H systems by controlled reactive mechanical alloying (CRMA) or controlled mechanical milling (CMM) in the magneto-mill Uni-Ball-Mill 5 has been carried out in the present work. The effect of milling parameters on the properties of milled powders was investigated. The properties of milled powders have been studied, including refinement of particle size, grain (crystallite) size of phases existing in the milled powders, formation of nanostructured hydrides and their thermal behavior. The following conclusions can be drawn from the present study.

11.1 Mg-H system

1. Both β-MgH_2 and metastable γ-MgH_2 hydrides are synthesized by MCS of elemental Mg powder under hydrogen in the magneto-mill Uni-Ball-Mill.
2. Using the yield of MgH_2 and the milling time as rough estimation of the efficiency of milling modes in Uni Ball Mill 5, the weakest to the strongest mode applied in the present work is: HES < IMP2 < IMP710 < IMP68.
3. Increasing the number of balls increases the yield of β-MgH_2. This might be the result of increased numbers of contacts between balls and powders when the number of balls increases. Energy applied to powder particles increases as the number of collisions (contacts) increases. Four balls are required to produce sufficient numbers of contacts between balls and powders in Uni-Ball Mill which results in a very efficient milling.

4. When the number of balls is fixed, the milling time is a function of the ball-to-powder ratio and milling mode, while the latter has the stronger effect.
5. The β-MgH_2 phase in the milled Mg-H powders undergoes a very fine nanostructuring and becomes saturated (crystallite size ~6-9nm) after ~30-50h of milling time with a very small associated lattice strain or without it. Further refinement proceeds slowly, and the nanograin size finally reaches a steady-state value.
6. The appearance of peak doublet in the DSC curves of Mg-H powders in the present work can be explained by the combination results of the coexistence of both γ-and β-MgH_2 phase and possibly the inhomogeneous particle size distribution of MgH_2. The fraction of the finer particles could be preferentially occupied by γ-MgH_2 which might have a lower desorption temperature than β-MgH_2.

11.2 Mg-Al-H system

11.2.1 Mechano-chemical synthesis (MCS) of nanohydrides

1. The ternary magnesium alanate $Mg(AlH_4)_2$ has not been synthesized in the present work by mechano-chemical synthesis using CRMA of four stoichiometric Mg-2Al batches: (a) elemental Mg and Al powders, (b) elemental Al powder and AZ91 alloy, (c) powder of as-cast Mg-2Al alloy and (d) commercial MgH_2 powder and Al powder.
2. There is a strong competition between the formation of Al(Mg) solid solution and the β-MgH_2 hydride occurring to a various extent up to ~10h of CRMA in three stoichiometric Mg-2Al batches (a)-(c).
3. It is hypothesized that the presence of Al(Mg) solid solution in the initial stage of the synthesis (up to 10h) inhibits the reaction of β-MgH_2, Al(Mg) and H_2 to form

$Mg(AlH_4)_2$. Moreover, even as Al(Mg) decomposes into free Al(s) (from solid solution), as the reactive milling duration increases beyond the initial 10h, the Al(s) phase is already "poisoned", i.e. still retains its physico-chemical characteristics from the previous solid solution which strongly inhibits the reaction to form $Mg(AlH_4)_2$.

4. Although there is no solid solution before 100h of milling time in batch (d), ternary $Mg(AlH_4)_2$ is not synthesized. This can be explained by a low energy input during milling. After 100h, energy input might be sufficient but the Al(Mg) solid solution is already formed and impedes the formation of $Mg(AlH_4)_2$ hydride.
5. In the annealed Mg-Al-H powders which form solid solution and intermetallic phases, the reasons that $Mg(AlH_4)_2$ hydride has not been synthesized by hydrogenation of the as-milled powder are most likely due to the formation of Al(Mg) solid solution and intermetallic compounds, which deplete the amount of Al.
6. For the annealed Mg-Al-H powder which does not contains solid solution or intermetallics, the lack of $Mg(AlH_4)_2$ might be the reason that secondary Al still holds its properties as that in a Al(Mg) solid solution and cannot react with MgH_2 to form $Mg(AlH_4)_2$ hydride.
7. In addition to the formation of solid solution and intermetallics which deplete Al required for reaction, the hydrogen pressure used in the annealing might also be insufficient for the formation of $Mg(AlH_4)_2$.

11.2.2 Mechano-chemical activation synthesis (MCAS) of nanohydrides

1. $Mg(AlH_4)_2$ has been synthesized in the present work by mechano-chemical activation synthesis (MCAS) of the mixture of $2NaAlH_4+MgCl_2$ after a short milling time (5h). Increasing milling time to just 10h seems to result in a partial decomposition of the initially formed $Mg(AlH_4)_2$ into nanocrystalline β-MgH_2, elemental Al (grain size ~26nm) and hydrogen gas.
2. Decomposition of $Mg(AlH_4)_2$ into β-$MgH_2+2Al+3H_2(+2NaCl)$ starts at ~125°C (at the scan rate of 4°C/min). However, the nature of this transformation being either endothermic or exothermic can not be unambiguously established because a number of samples tested in DSC at the scan rate of 4 and 20°C/min showed both types of transformation, most likely, owing to a very small enthalpy of decomposition of $Mg(AlH_4)_2$ which is cited in the literature as being equal to ~1.7 kJ/molH [19].
3. From the XRD and DSC analysis in the present work, $Mg(AlH_4)_2$ decomposes into a binary MgH_2 directly. No intermediate ternary hydride is observed as those in the decomposition of $NaAlH_4$ and $LiAlH_4$.[37,73]
4. The decomposition temperature of β-MgH_2 occurring in the 250-340^oC range is much lower than ~380^oC range for the MgH_2 reactively synthesized using elemental Mg powder under the same milling condition. This might be due to a catalytic effect of a special active Al which is produced after decomposition of $Mg(AlH_4)_2$ but the nature of this mechanism is not clear at the present moment.
5. The major problem in the MCAS technology is the formation of a large amount of waste by product NaCl. The separation of $Mg(AlH_4)_2$ from NaCl needs several days

to be completed and then the product requires some additional long-time annealing in vacuum. Such a long production time is definitely not suited for industrial environment. In addition to the long production time, the extracted $Mg(AlH_4)_2$ is usually contaminated with the solvent adduct.

6. If ball milling is to be used than the most suitable method of synthesizing a relatively pure $Mg(AlH_4)_2$ is still a direct reactive synthesis from the elemental metals under hydrogen. In this case, however, an effective catalyst must be found which would accelerate the reaction between MgH_2 and Al. Such a catalyst is still unknown.
7. The enthalpy of decomposition for the first step decomposition of $Mg(AlH_4)_2$ into MgH_2, Al and H_2 indicates that $Mg(AlH_4)_2$ might not be suitable for the application for PEM fuel cell. Although the first-step decomposition temperature is relatively low (~125^oC), the second-step decomposition starts at ~225^oC, which is still higher than the working temperature for PEM fuel cell.
8. Besides the working temperature and pressure, the reversibility of $Mg(AlH_4)_2$ hydride has to be taken into account. The second-step decomposition of $Mg(AlH_4)_2$ is reversible either by milling or by hydrogenation under hydrogen pressure which is very sluggish. However, the first-step decomposition (i.e., synthesis of $Mg(AlH_4)_2$ from a mixture of Mg + Al or MgH_2 + Al either by milling or hydrogenation under hydrogen pressure) has still not been reported to be reversible. The aforementioned problems have to be solved before $Mg(AlH_4)_2$ can be used as a hydrogen storage material for PEM fuel cell.

11.3 Mg-B-H system

11.3.1 Mechano-chemical synthesis (MCS) of nanohydrides

1. The ternary $Mg(BH_4)_2$ has not been synthesized in the present work by mechano-chemical synthesis using CRMA of four stoichiometric Mg-2B batches: (a) elemental Mg and crystalline boron powder, (b) elemental Mg powder and oxidized amorphous boron powder, and (c) commercial MgB_2 powder. There might be a chance that an amorphous $Mg(BH_4)_2$ phase has been synthesized using Mg-2B batch made with oxide-free amorphous boron.
2. Regardless of the starting materials, the morphology of four Mg-2B batches after a prolonged milling time (>100h) can be characterized by a dramatic particle size refinement and a high tendency to agglomerate.
3. The synthesized phases in the batch (a) (milled under HES and IMP2 mode) and the batch (b) (milled under HES, IMP2 and IMP710 mode) are solely β-MgH_2 or coexisting γ- and β- MgH_2.
4. When the Mg-2B mixture is made with the oxidized amorphous boron containing B_2O_3 then after a prolonged milling time under IMP710 mode only nanometric γ-and β-MgH_2 hydrides are formed. In contrast, oxide-free boron in the original Mg-2B mixture prompts the formation of a resulting mixture of nanometric MgB_2 and an amorphous phase containing hydrogen. The amorphous phase might be an amorphous $Mg(BH_4)_2$ phase. The nature of bondings in the amorphous phase is needed to be analyzed (e.g., by Raman spectra) to confirm the presence of the $Mg(BH_4)_2$ phase.
5. Oxide-free amorphous boron might act as a catalyst to an amorphous transformation of MgH_2 into an amorphous phase during a milling process because the

amorphization phenomenon is not observed in milling elemental Mg as well as milling elemental Mg with Fe or Al under hydrogen.

6. Further annealing of the milled Mg-2B batches at ~100-400^{o}C under ~4-4.3 MPa of hydrogen for 20-100h results in the decomposition of amorphous phase rather than the formation of ternary $Mg(BH_4)_2$. The decomposition can be seen by a transformation of a single peak in the DSC curve of the as-milled powder to peak doublets in DSC curves of the annealed powders, indicating a coexistence of an amorphous phase and a crystalline β-MgH_2 phase in the annealed powder.
7. Ternary $Mg(BH_4)_2$ phase has not been synthesized after milling MgB_2 powder for 200h under hydrogen or after subsequent annealing the same powder at 220^{o}C under 4.3MPa of hydrogen for 100h.
8. A small amount of hydrogen (0.4-0.8 wt.%) dissolves in the as-milled and annealed MgB_2 powders. From XRD (no crystalline hydride phase) and DSC analysis (a weak endothermic peak), one can infer an amorphous phase might be formed after a prolonged milling. However, it has to be pointed out that as-received MgB_2 powder contains a retained Mg phase. Hence, another alternative is that the retained Mg absorbs hydrogen to form a hydride which amorphizes after a prolonged milling time.
9. The energy input and the pressure during milling as well as the pressure during annealing might not be sufficient to form the complex hydride in the present work. Stronger milling force (controlled by magnet field) and a newly designed chamber which can allow a higher pressure in a Sieverts-type apparatus should be considered in future work.

11.3.2 Mechano-chemical activation synthesis (MCAS) of nanohydrides

1. A small amount of amorphous $Mg(BH_4)_2$ might have been synthesized after MCAS of a mixture of $2NaBH_4$ and $MgCl_2$ but the formation of $Na(Mg)BH_4$ solid solution might prevent the synthesis of a large amount of $Mg(BH_4)_2$ hydride.
2. Although the result of XRD analysis in the present work does not indicate the presence of a crystalline $Mg(BH_4)_2$ hydride, the similarity of thermal events in the DSC curve in the milled powder mixtures to those of $Mg(BH_4)_2$ reported by Nakamori et al. [120], and Konoplev and Bakulina [41] might indicate the possibility of presence of a small amount of an amorphous $Mg(BH_4)_2$ in the in the milled powder mixture of $2NaBH_4$ and $MgCl_2$. The nature of bondings in the amorphous phase is needed to be analyzed (e.g., by Raman spectra) to confirm the presence of the $Mg(BH_4)_2$ phase.
3. An important discovery is the formation of $Na(Mg)BH_4$ solid solution in the milled powder mixture of $2NaBH_4$ and $MgCl_2$. The solutionizing effect increases as milling time increases.
4. It is hypothesized that the presence of $Na(Mg)BH_4$ solid solution in the MCAS process inhibits the formation of $Mg(BH_4)_2$. Once a solid solution is formed, the amount of Mg will not be enough to form a large amount of $Mg(BH_4)_2$ hydride.
5. Hydrogen desorption temperature of $Mg(BH_4)_2$ is still too high for PEM fuel cell, but might be suitable for fuel cells which allow higher working temperature.

References

[1] IPCC special report of working group III, Emission scenarios, Summary for policymakers, International Panel on Climate Change 2000. http://www.ipcc.ch

[2] M. Conte, A. Iacobazzi, M. Ronchetti, R. Vellone. J. Alloys Compd. 100 (2001) 171-187.

[3] A. Midilli, M. Ay, I. Dincer and M.A. Rosen. Renewable and Sustainable Energy Reviews. 9 (2005) 255-271.

[4] A.Züttel. Review: Hydrogen Storage Methods and Materials. http://www.ifres.ch/Hompage/IFRES.htm.

[5] J.A. Ritter, A.D. Ebner, J. Wang, R. Zidan. Materialstoday 6 (2003) 18-23.

[6] A. Züttel. Materialstoday 6 (2003) 24-33.

[7] I. Dincer. Renewable and Sustainable Energy Reviews. 4 (2004) 157-175.

[8] T.N. Veziroglu. Int J Hydrogen Energy. 22 (1997) 551-556.

[9] S. Dunn. Int J Hydrogen Energy. 27 (2002) 235-264.

[10] U. Wagner, B. Geiger and H. Schaefer. Int J Hydrogen Energy. 23 (1998) 1-6.

[11] M. Momirlan and T.N. Veziroglu. Renewable and Sustainable Energy Reviews. 6 (2002) 141-179.

[12] I. Dincer. Int J Hydrogen Energy. 27 (2002) 265-285.

[13] L. Schlapbach, A. Züttel. Nature 414 (2001) 353-358.

[14] L. Schlapbach. MRS Bulletin. 27 (2002) 675-676.

[15] Li Zhou. Renewable and Sustainable Energy Reviews. 9 (2005) 395-408.

[16] A.M. Seayad and D.M. Antonelli. Advanced Materials. 16 (2004) 765-777.

[17] M. Conte, P.P. Prosini and S. Passerini. Materials Science and Engineering B108 (2004) 4-8.

[18] Advanced Materials and Processes 163 (1) (2005) 99.

[19] G. Sandrock, J. Reilly, J. Graetz, W.-M. Zhou, J. Johnson, and J. Wegrzyn. Appl. Phys.A 80 (2005) 687-690.

[20] G. Sandrock. J. Alloys Compd. 293-295 (1999) 877-888.

[21] J.I. Kroschwitz, ed. Encyclopedia of Chemical Technology, 4th ed., vol. 13,John Wiley & Sons, Inc., New York, 1991.

[22] R.A.Varin, S. Li, Ch. Chiu, L. Guo, O. Morozova, T. Khomenko and Z. Wronski. J. Alloys Compd. 404-406 (2005) 494-498.

[23] G. Sandrock in Y. Yurum (Ed.), Hydrogen Energy System- Production and Utilization of Hydrogen and Future Aspects, Kluwer Academics, Dordrecht, 1995, p135-166.

[24] Fuel cell basics in Hydrogen, Fuel Cells and Infrastructure Technology Program. USDOE. http://www.eere.energy.gov/hydrogenandfuelcells/fuelcells/basics.html.

[25] G. Sandrock in W. Vielstich, H.A, Gasteiger and A. Lamm (Eds.), Handbook of Fuel Cells- Fundamentals, Technology and Applications, John Wiley and Sons, 2003, p101-112.

[26] Targets for On-board Hydrogen storage systems in Hydrogen, Fuel Cells and Infrastructure Technology Program. USDOE. http://www.eere.energy.gov/hydrogenandfuelcells/storage/current_technology.html.

[27] T.A. Doyle, Technological status of hydrogen road vehicles, IEA Report, 1997.

[28] Nedo, WE-NET Advancement Report, 2001.

[29] Hydride Information Center. http://hydpark.ca.sandia.gov.

[30] A. Zaluska, L. Zaluski, J.O. Strőm-Olsen. J. Alloys Compd. 288 (1999) 217-225.

[31] R. Janot, F. Cuevas, M. Latroche and A. Percheron-Guégan. Intermetallics 14 (2006) 163.

[32] A. Zaluska, L. Zaluski, J.O. Strőm-Olsen. Appl. Phys. A72 (2001) 157-165.

[33] A.M. Seayad and D.M. Antonelli. Adv. Mater. 16 (2004) 765-777.

[34] T. Czujko, R.A. Varin, Ch. Chiu and Z. Wronski. J. Alloys Compd. 424 (2006)356-364.

[35] T. Czujko, R.A. Varin, Ch. Chiu and Z. Wronski. J. Alloys Compd. 414 (2006) 240-247.

[36] D. Chandra, J. J. Reilly and R. Chellappa. JOM. February (2006) 26-32.

[37] B. Bogdanović and G. Sandrock. MRS Bulletin. 27 (2002) 712-716.

[38] Z.S. Wronski. International Materials Reviews. 46 (2001) 1-49.

[39] B. Bogdanović and M. Schwickardi. J. Alloys Compd. 253-254 (1997) 1-9.

[40] CRC Handbook of Chemistry and Physics, 85th Ed. http://www.hbcpnetbase.com.

[41] V.N. Konoplev, V.M. Bakulina. Izv. Akademii Nauk SSSR, 1 (1971) 136-138

[42] R.A. Varin, L. Guo, S. Li, Ch. Chiu, A. Calka. Nanostructured and Nanocomposite Light Metal-Based Compounds for Hydrogen Storage in NATO Advanced Research Workshop "Metallic Materials with High Structural Efficiency", Kiyv, Ukraine, Kluwer Academic Publishers, 2004, pp. 67-78.

[43] D. Blanchard, H.W. Brinks, B.C Hauback and P. Norby. Materials Science and Engineering B108 (2004) 54-59.

[44] P. Claudy, B. Bonnetot, J.M. Letoffe. Journal of Thermal Analysis. 15 (1979) 119-128.

[45] A. Fossdal, H.W. Brinks, M. Fitchener and B.C. Hauback. J. Alloys Compd. 404-406 (2005) 752-756.

[46] M. Mamatha, B. Bogdanović, M. Felderhoff, A. Pommerin, W. Schmidt, F. Schütt and C. Weidenthaler. J. Alloys Compd. 407 (2006) 78-86.

[47] M. Mamatha, C. Weidenthaler, M. Felderhoff, A. Pommerin, and F. Schütt. J. Alloys Compd. 407 (2006) 78-86.

[48] Yoonyoung Kim, Eung-Kyu Lee, Jae-Hyeok Shum, Young Whan cho and Kyung Byung Yoon. J. Alloys Compd. 422 (2006) 283-287.

[49] T.N. Dymova, V.N. Konoplev, A.S. Sizareva and D.P. Aleksandrov. Russian Journal of Coordination Chemistry. Vol.25, No.5, 1999, 312-315.

[50] T.N. Dymova, N.N. Mal'tseva, V.N. Konoplev, A.I. golovanova, D.P. Aleksandrov and A.S. Sizareva. Russian Journal of Coordination Chemistry. Vol.29, No.6, 2003, 385-389.

[51] B. Bogdanović, R.A. Brand, A. Marjanović, M. Schwickardi and J. Tőlle. J. Alloys Compd. 302 (2000) 36-58.

[52] G. Sandrock, K. Gross, G. Thomas, C. Jensen, D. Meeker and S. Takara. J. Alloys Compd. 330-332 (2002) 696-701.

[53] L. Zaluski, A. Zalyska, J.O. Strőm-Olsen. J. Alloys Compd. 290 (1999) 71-78.

[54] A. Zaluska, L. Zaluski, J.O. Strőm-Olsen. J. Alloys Compd. 298 (2000) 125-134.

[55] G.M. Jensen, R. Zidan, N. Mariels, A. Hee and C. Hagen. Int J Hydrogen Energy. 24 (1999) 461-465.

[56] G.M. Jensen and K.J. Gross. Appl. Phys. A 72 (2001) 213-219.

[57] G.J. Thomas, K.J. Gross, N.Y.C. Yang and C. Jensen. J. Alloys Compd. 330-332 (2002) 702-707.

[58] K.J. Gross, G.J. Thomas and C.M. Jensen. J. Alloys Compd. 330-332 (2002) 683-690.

[59] K.J. Gross, G. Sandrock and G.J. Thomas J. Alloys Compd. 330-332 (2002) 691-695.

[60] B. Bogdanović, M. Felderhoff, M. Germann, M. Härtel, A. Pommerin, F.Schüth, C. Weidenthaler and B. Zibrowius. J. Alloys Compd. 350 (2003) 246-255.

[61] H.W. Brinks, C.M. Jensen, S.S. Srinivasan, B.C. Hauback, D. Blanchard and K. Murphy. J. Alloys Compd. 376 (2004) 215.

[62] D. Goerrig, German Patent DE1077644. Dec. 27, 1958.

[63] D.S. Stasinevich and G.A. Egorenko. Russian Journal of Inorganic Chemistry 13 (1968) 341-343.

[64] M. Murtomaa, E. Laine, J. Salonen, O. Kuusinen. Powder Handing and Processing. 11 (1999) 87-90.

[65] Z.P. Li, N. Morigazaki, B.H. Liu, S. Suda. J. Alloys Compd. 349 (2003) 232-236.

[66] A. Züttel, P. Wenger, S. Rentsch, P. Sudan. J. Power Sources 118 (2003) 1-7.

[67] A. Züttel, S. Rentsch, P. Fischer, P. Wenger, P. Sudan, Ph. Mauron, ch. Emmenegger. J. Alloys Compd. 356-357 (2003) 515-520.

[68] Y. Nakamori, S.I. Orimo. J. Alloys Compd. 370 (2004) 271-275

[69] Z.P. Li, N. Morigazaki, B.H. Liu, S. Suda. J. Alloys Compd. 349 (2003) 232-236.

[70] Y. Kojima, K. Suzuki, K. Fukumoto, M. Sasaki, T. Yamamoto, Y. Kawai, H. Hayashi. International Journal of Hydrogen Energy. 27 (2002) 1029-1034.

[71] D. Hua, Y. Hanxi, A. Xinping, C. Chuansin. International Journal of Hydrogen Energy. 28 (2003) 1095-1100.

[72] Eun Jeon and Young Whan Cho. J. Alloys Compd 422 (2006) 273-275.

[73] W. Garner, F. Haycock. Proc. Roy. Soc. A 211 (1952) 335-340.

[74] Q.A. Zhang and E. Akiba. J. Alloys Compd. 394 (2005) 308-311.

[75] E. Wiberg, R. Bauer. Z. Naturforsh. 5b (1950) 397.

[76] M. Fichtner, J. Engel, O. Fuhr, O. Kircher and O. Rubner. Materials Science and Engineering B108 (2004) 42-47.

[77] M. Fichtner, J. Engel, O. Fuhr, A. Glöss, O. Rubner and R. Ahlrichs. Inorg. Chem. 42 (2003) 7060-7066.

[78] C. Suryanarayana. International Materials Reviews. 40, 2, 1995, 41-64.

[79] K. Lu. Materials Science and Engineering. R16 (1996) 161-221.

[80] H. Gleiter. Z. Metallkd. 86 (1995) 78-83.

[81] R.W. Siegel. Nanostructured Mater. 4 (1994) 121-138.

[82] R.A.Varin, T. Czujko, Ch. Chiu and Z. Wronski. J. Alloys Compd. (In Press).

[83] R.A.Varin, T. Czujko and Z.Wronski. Nanotechnology 17 (2006) 3856-3865.

[84] C. Suryanarayana. Progress in Materials Science 46 (2001) 1-184.

[85] D.R. Maurice and T.H Courtney. Metallurgical Transactions A. 21A (1990) 289-303.

[86] L. Lü and M.O. Lai. Mechanical Alloying. Kluwer Academic Publishers, Boston, 1998.

[87] E. Avvakumov, M. Senna and N. Kosova. Soft Mechanochemical Synthesis: A Basis for New Chemical Technologies. Kluwer Academic Publishers, Boston, 2001.

[88] P. Yu. Butyagin. Sov. Sci. Rev. B. Chem. 14 (1989) 1-133.

[89] A. Calka and R.A. Varin. Processing and Fabrication of Advanced Materials IX. (2000) 263-265.

[90] Patents: WO9104810, US5383615, CA2066740, EP0494899, and AU643949.

[91] R.A. Varin and T. Czujko. Materials and Manufacturing Processes 17 (2002) 129-156.

[92] ICDD-PDF database v.1.30 1997.

[93] H.P. Klug, and L. Alexander. X-ray Diffraction Procedures for Polycrystalline and Amorphous Materlais, John Wiely & Sons, New York, 1974.

[94] B.Bogdanović, A. Reiser, K. Schlichte, B. Spliethoff and B. Tesche. J. Alloys Compd. 345 (2002) 77-89.

[95] J-L Bobet, E. Akiba and B. Darriet. Int J Hydrogen Energy. 26 (2001) 493-501.

[96] N. Handada, T. Ichikawa, S.-I. Orimo and H. Fujii. J. Alloys Compd. 366 (2004) 269-273.

[97] J. Huot, G. Liang, S. Boily, A.V. Neste and R. Schulz. J. Alloys Compd. 293-295 (1999) 495-500.

[98] F.C. Gennari, F.J. Castro and G. Urretavizcaya. J. Alloys Compd. 321 (2001) 46-53.

[99] R.A. Varin, Ch. Chiu, S. Li, A. Calka, D. Wexler. J. Alloys Compd. 370 (2004) 230-243.

[100] J. Huot, H. Hayakawa, E. Akiba. J. Alloys Compd. 248 (1997) 164-167.

[101] M. Khrussanova, E. Grigorova, D. Radev, P. Peshev. J. Alloys Compd. 327 (2001) 230-234.

[102] H.J. Fecht. Scripta Mater. 44 (2001) 1719-1723.

[103] D.R.Askeland. The Science and Engineering of Materials. PWS-KENT Publ. Co, Boston. 863-864.

[104] H.Okamoto. Desk Handbook-Phase Diagrams for Binary Alloys. ASM International, Materials Park, OH. 2000, p36.

[105] J-L. Bobet, E.Akiba and B.Darriet. International Journal of Hydrogen Energy. 26 (2001) 493-501.

[106] R.A.Varin, Ch. Chiu, T.Czujko and Z.Wronski. Nanotechnology 16 (2005) 2261-2274.

[107] S. Li, R.A.Varin, O.Morozova and T.Khomenko. J. Alloys Compd. 384 (2004) 231-248.

[108] R.A.Varin, S.Li, Z.Wronski, O.Morozova and T.Khomenko. J. Alloys Compd. 390 (2005) 282-296.

[109] R.A.Varin, S.Li, A.Calka and D. Wexler. J. Alloys Compd. 373 (2004) 270-286.

[110] F.C.Gennari, F.J.Castro and J.A.Gamboa. J. Alloys Compd. 339 (2002) 261-267.

[111] M.H. Mintz, Z.Gavra, g.Kimmel, Z.Hadari. J. Less-Common Met. 74 (1980) 263-270.

[112] P.Wang, S.Orimo, K.Tanabe and H.Fujii. J. Alloys Compd. 350 (2003) 218-221.

[113] Y.Nakamori, S.Orimo, T.Ekino and H.Fujii. J. Alloys Compd. 335 (2002) L21-L24.

[114] M.W.Chase, Jr. J.Phys.&Chem. Ref. Data-Monograph No. 9. NIST-JANAF Thermochemical Tables, 4th Ed. (1998), 268.

[115] T.Egami and Y.Waseda. Journal of Non-Crystalline Solids 64 (1984) 113-134.

[116] Z.S.Wronski, R.A.Varin, Ch.Chiu and T.Czujko. International Conference on Modern Materials & Technologies. Acireale, Sicily, Italy 2006 (In press).

[117] R.S. Kumar and A.L. Cornelius. Applied Physics Letters 87 (2005) 261916.

[118] Material Safety Data Sheet (MSDS). http://www.hvchemical.com/msds-online.htm.

[119] Sina Kashani Nejad. Presentation "Oxides in Electrolytic Production of Magnesium" in Mining, Metals and Materials Eng. Dept. McGill University. March 2004.

[120] Y.Nakamori, K.Miwa, A.Ninomiya, H.Li, N.Ohba, S. Towata, A.Züttel and S.Orimo. Physical Review B74 (2006) 045126.

[121] M. Fichtner, Ch. Frommen, and A. Züttel. "Syhthesis and properties of magnesium boranate", MH2006, International Symposium on Metal-Hydrogen Systems, Lahaina, Maui, Hawaii, October 16, 2006, Book of Abstracts p. 42.

Appendix A

A.1 Controlled milling modes by changing position of magnets in Uni-Ball Mill 5

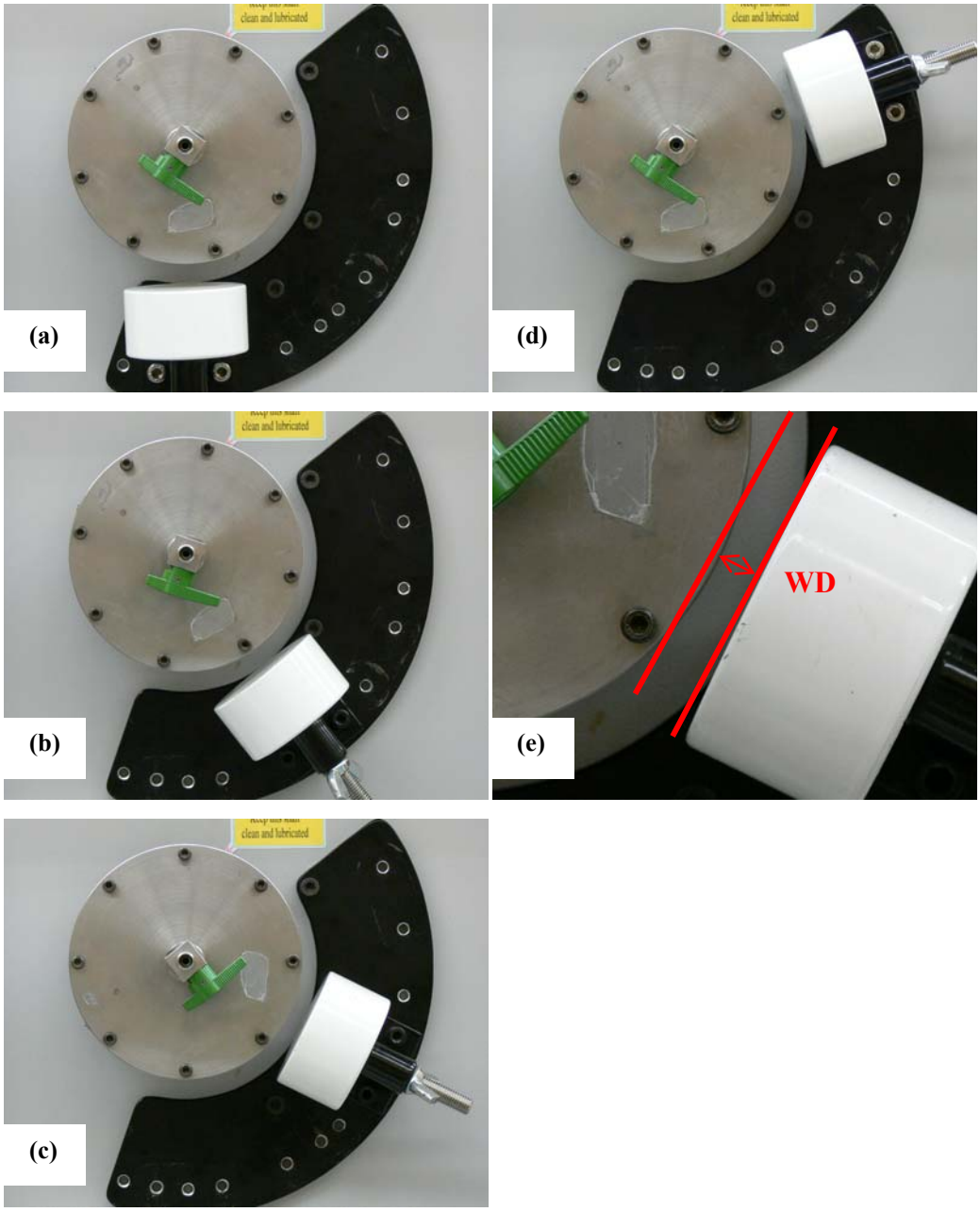

Fig. A.1 Various milling mode with one magnet by changing its position in Uni-Ball Mill 5: (a) low energy shearing (LHS) mode, (b) high energy shearing (HES) mode, (c) low energy impact (IMP1) mode, (d) high energy impact (IMP2) mode, and (e) working distance (WD) between the magnet and the milling cylinder.

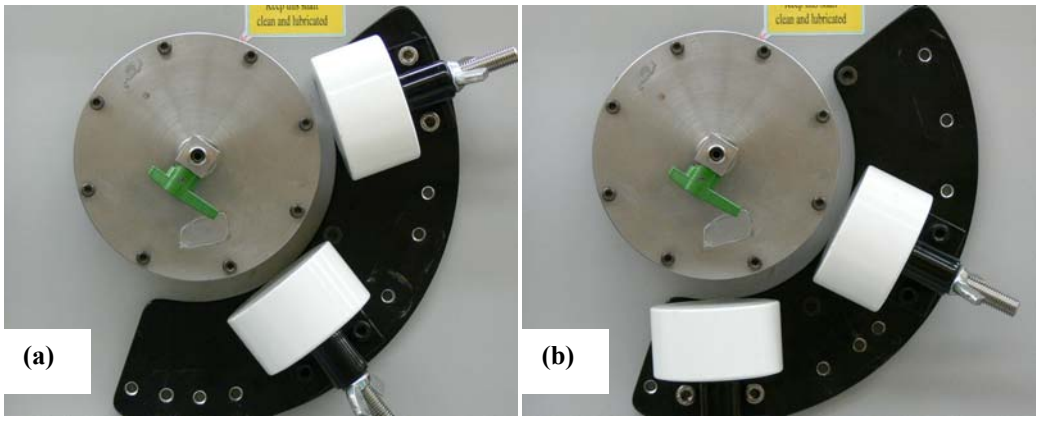

Fig. A.2 Milling modes with two magnets in Uni-Ball Mill 5: (a) milling mode with magnets at 7 and 10 o'clock positions (IMP710 mode) and (b) milling mode with magnets at 6 and 8 o'clock positions (IMP68 mode).

A.2 Procedures of loading hydrogen into milling cylinder

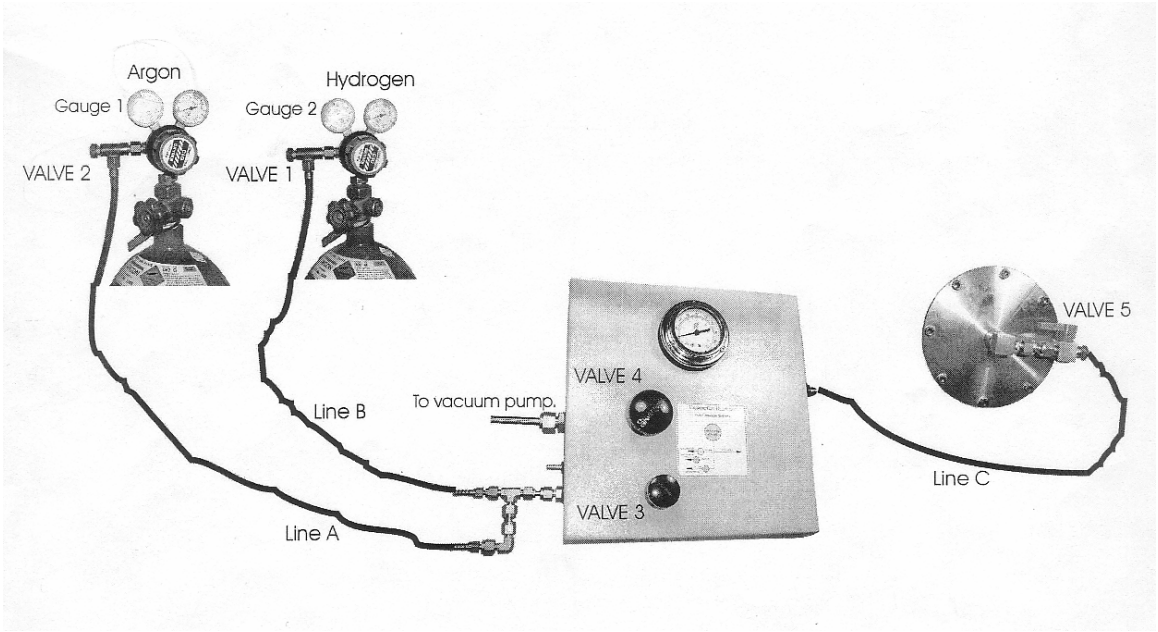

Fig. A.3 Schematic of connections between gas tanks and milling cylinders during loading hydrogen.

(1) Open up the main valves on argon and hydrogen cylinders (bottles) and set up pressure for argon and hydrogen.

(2) VALVE 1 and 2 are closed.

(3) Rubber hose line A and B connected as shown on the schematic.

(4) Rubber hose line C is DISCONNECTED from VALVE 5 which is closed.

(5) Close VALVE 4 and open up VALVE 3.

(6) Open up VALVE 2 fully. Close and open several times (i.e. 4 times) with your thumb the tip of hose line C; argon is flushing through lines A, B and C and purging lines A, B and C from air.

(7) After a while, reduce the flow rate of helium by VALVE 2 and connect rubber hose line C to VALVE 5 and open up VALVE 5 to admit argon to the milling cylinder.

(8) Close VALVE 5 and 2.

(9) Activate the rotary pump and after a while open up VALVE 4, 3 and 5. Keep VALVES 1 and 2 closed. Argon is being evacuated from lines A, B, C and the milling cylinder.

(10) Close up VALVE 4 and very slowly start opening VALVE 2 but beware that the pressure on GAUGE 1 does not drop to zero. (If it happened the air would be sucked into the cylinder!). Helium is being filled into the lines A, B, C and the milling cylinder.

(11) Close up VALVE 2 and open up VALVE 4.

   a. Evacuate helium and close up VALVE 4 and slowly open VALVE 2-fill up with helium.

   b. Evacuate helium and close up VALVE 4 and slowly open VALVE 2-fill up with helium.

   c. Evacuate helium, close up VALVE 4 and STOP the rotary pump. Remember that VALVE 1 (Hydrogen) and 2 (Helium) remain closed after final evacuation of helium.

(12) Start opening VERY SLOWLY VALVE 1 (hydrogen) but beware that the pressure

on GAUGE 2 does not drop to zero (If it happened the air would be sucked into the cylinder). Hydrogen is being filled into the lines A, B, C and the milling cylinder.

(13) After the milling cylinder has been filled up with hydrogen, close up VALVE 5 and VALVE 1.

(14) Open up VALVE 4 and start the rotary pump and remove hydrogen from the lines A, B and C.

(15) Close up VALVE 4 and open up VALVE 2; flush TWICE with helium.

(16) Close up VALVE 2 and DISCONNECT the milling cylinder.

(17) Open up VALVE 4 and shut down the rotary pump.

A.3 Effective volume of milling cylinder

(1) Volume of milling cylinder

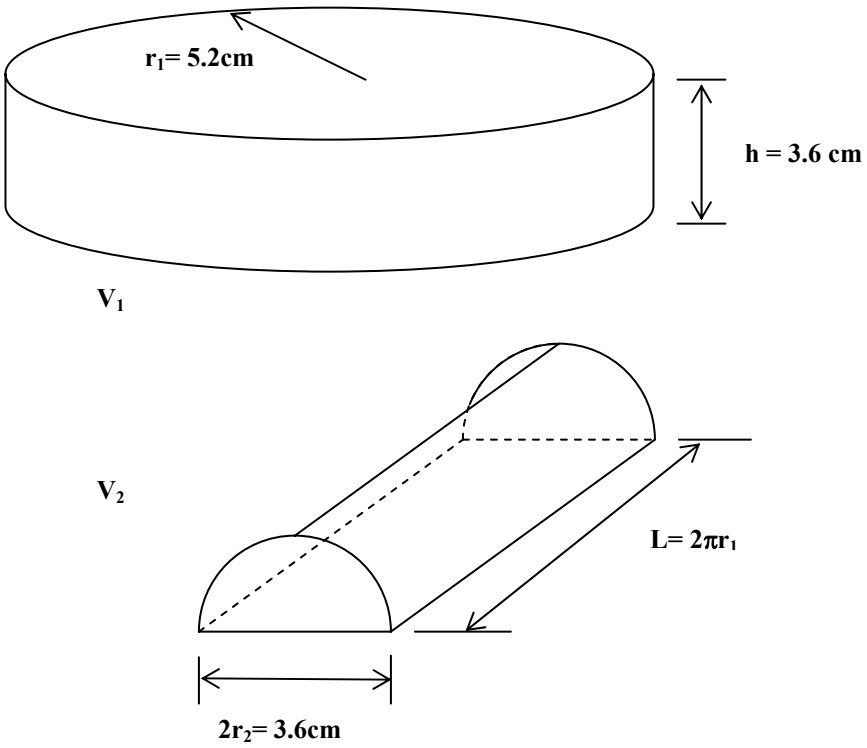

Fig. A.4 Schematic of the volume of milling cylinder.

$$V_1 = \pi r_1^2 h = \pi \times 5.2^2 \times 3.6 = 305.82 cm^3$$

$$V_2 = \frac{\pi r_2^2 L}{2} = \frac{\pi r_2^2 \times (2\pi r_1)}{2} = \frac{\pi \times 1.8^2 \times (2 \times \pi \times 5.2)}{2} = 166.28 cm^3$$

Volume of milling cylinder, $V_{cylinder}$:

$V_{cylinder} = V_1 + V_2 = 305.82 + 166.28 = 472.10\ cm^3$

(2) Volume of a ball

r = 1.25 cm

$$V_{ball} = \frac{4}{3}\pi r^3 = \frac{4}{3}\pi \times 1.25^3 = 8.18 cm^3$$

(3) Volume of starting materials

$$V_{sm} = \sum_{i=1}^{m} \frac{W_i}{\rho_i}$$

where W is the weight (g) of a starting material and ρ is the density (g/cm^3)of a starting material

(4) Effective volume during milling with n balls, V_{eff} :

$$V_{eff} = V_{cylinder} - nV_{ball} - V_{sm} = 472.10 - 8.18n - \sum_{i=1}^{m} \frac{W_i}{\rho_i}\ (cm^3) \qquad (A.1)$$

where n is the number of balls

A.4 Hydrogen storage capacity estimated by pressure drop during milling using a volumetric method

Assuming hydrogen behave as ideal gas, one can estimate the mass of absorbed hydrogen from:

$$\Delta P V_{eff} = (m/M_H)RT \qquad (A.2)$$

where ΔP is the total pressure drop of H_2 in a milling period (Pa)

V_{eff} is the effective volume of the vial (m^3)

(V_{eff} = absolute volume – volume of balls – volume of the material) (Appendix A.3)

m is weight of absorbed H_2 (g)

M_H is molar mass of H_2 (g/mol)

T is the temperature (K)

R is the gas constant (8.314J $(mol)^{-1}K^{-1}$)

and hydrogen capacity (wt % H_2) = m/M × 100% (A.3)

where M is the initial powder mass (g)

A.5 Hydrogen capacity/ weight percent of a phase in the milled powder by DSC method

In DSC measurements, the weight percent of a phase was calculated using the peak area of the DSC curve and its reported heat of formation. For example, weight percent of β-MgH_2 in a milled powder can be estimated using the peak area of the DSC curves and the reported β-MgH_2 heat of formation (-74 kJ/mol [94], which equals to -2811J/g). The DSC curve was analyzed by the NETZSCH thermal analysis software. First, the onset and end temperature of the peak were determined. Then, the peak area was calculated using the linear approach from the onset temperature to the end temperature (Fig.A.5) by the DSC software.

The weight percent of β-MgH_2 is given by:

wt% of β-MgH_2 = peak area (J/g)/ β-MgH_2 heat of decomposition (J/g) (A.4)

where heat of decomposition = -(heat of formation)

From the decomposition of β-MgH_2 ($MgH_2 \rightarrow Mg + H_2$), the weight percent of desorbed hydrogen can be calculated by:

wt% of H_2 = wt% of MgH_2 × (molecular weight of H_2 / molecular weight of MgH_2) (A.5)

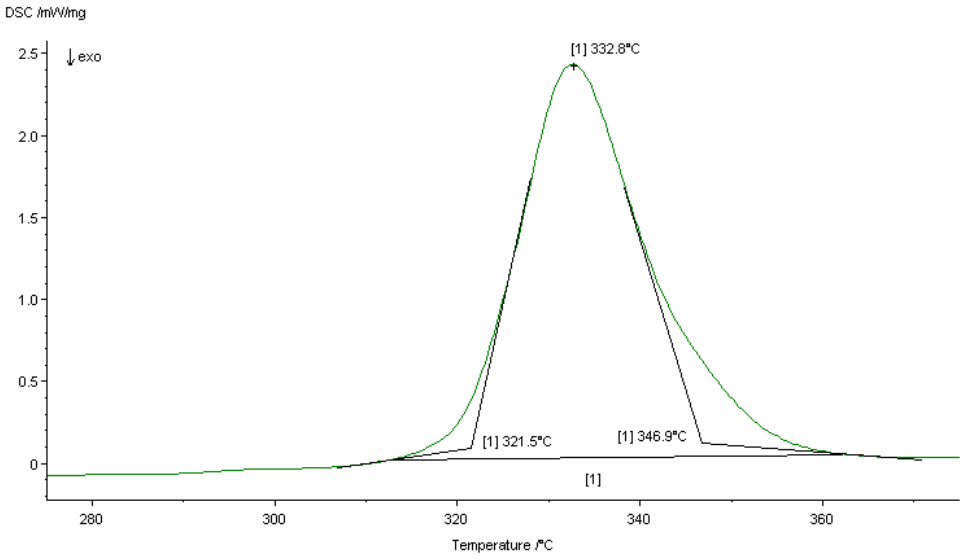

Fig. A.5 Schematic of calculating the weight percent of a phase by DSC analysis.

Appendix B ICDD-PDF files

Table B.1 List of ICDD-PDF files which are used for phase identification in the present work.

Name	PDF #	Table #
Al	04-0787	B.2
B	31-0207	B.3
Fe	06-0696	B.4
Mg	35-0821	B.5
Al_3Mg_2	29-0048	B.6
B_2O_3	06-0297	B.7
$Mg(AlH_4)_2$	47-0980	B.8
α-$Mg(BH_4)_2$	26-1212	B.9
β-$Mg(BH_4)_2$	26-1213	B.10
MgB_2	38-1369	B.11
β-MgH_2	12-0697	B.12
γ-MgH_2	35-1184	B.13
MgO	45-0946	B.14
$MgCl_2$	37-0774	B.15
$MgCl_2$-$4H_2O$	01-1210	B.16
$MgCl_2$-$6H_2O$	25-0515	B.17
$NaAlH_4$	85-0374	B.18
$NaBH_4$	09-0386	B.19
NaCl	05-0628	B.20
$MgB_2O(OH)_6$	72-2360	B.21
$MgBO_2(OH)$	33-0860	B.22

Table B.2 X-ray diffraction data for Al (PDF # 04-0787) [92].

(1/1)

4- 787 JCPDS-ICDD Copyright (c) 2000 Radiation: 1.54060 Quality: *

Al	2-theta	Int.	h k l
	38.473	100	1 1 1
Aluminum	44.740	47	2 0 0
	65.135	22	2 2 0
Aluminum, syn	78.230	24	3 1 1
	82.438	7	2 2 2
Rad: CuKa1 Lambda: 1.54056 Filter: Ni d-sp:			
Cutoff: Int: Diffractometer I/Icor: 3.62	99.081	2	4 0 0
Ref: Swanson, Tatge, Natl. Bur. Stand. (U.S.), Circ. 539, I 11 (1953)	112.046	8	3 3 1
	116.574	8	4 2 0
	137.463	8	4 2 2
Sys: Cubic S.G.: Fm-3m (225)			
a: 4.0494 b: c: A: C:			
A: B: C: Z: 4 mp:			
Ref: Ibid.			
Dx: 2.70 Dm: SS/FOM: F(9)=92.8(.0108,9)			
ea: nwB: ey: Sign: 2V:			
Ref:			
Color: Light gray metallic			
Pattern taken at 25 C. CAS no.: 7429-90-5. The material used for the NBS sample was a melting point standard sample of aluminum prepared at NBS, Gaithersburg, Maryland, USA. The chemical analysis (%): Si 0.011, Cu 0.006, Fe 0.007, Ti 0.0001, Zr 0.003, Ga 0.004, Mo 0.00002, S 0.0001, Al 99.9+ (by difference). Mineral species of doubtful validity, \ITAm. Mineral.\RG, \BF65\RG 205 (1980). \Cu\ type. Gold group, gold subgroup. PSC: cF4. See ICSD 64700 (PDF 85-1327). Mwt: 26.98. Volume[CD]: 66.40.			

Table B.3 X-ray diffraction data for boron (PDF # 31-0207) [92].

31-207 JCPDS-ICDD Copyright (c) 2000 Radiation: 1.54060 Quality: C

beta-B

Boron

Rad: CuKa Lambda: 1.54188 Filter: d-sp: Calculated
Cutoff: Int: Calculated I/Icor: 0.22
Ref: Calvert, L., National Research Council of Canada, Ottawa, Canada, ICDD
Grant-in-Aid

Sys: Rhombohedral (Hex) S.G.: R-3m (166)
a: 10.925 b: c: 23.814 A: C: 2.1798
A: B: C: Z: 314 mp:
Ref: Callmer, B., Acta Crystallogr., Sec. B, 33 1951 (1977)

Dx: 2.290 Dm: SS/FOM: F(30)=84.4(.0108,33)

ea: nwB: ey: Sign: 2V:
Ref:

Peak height intensities. PSC: hR105 for filled cell. \B\ type. PSC: hR104.67.
Plus 51 reflections to 0.9560. Mwt: 10.81. Volume[CD]: 2461.53.

2-theta	Int.	h k l
10.060	2	1 0 1
11.140	64	0 0 3
11.940	12	0 1 2
16.221	18	1 1 0
17.600	100	1 0 4
19.120	59	0 2 1
19.721	27	1 1 3
20.198	22	2 0 2
20.880	24	0 1 5
22.399	13	0 0 6
24.019	21	0 2 4
25.179	20	2 1 1
26.002	12	1 2 2
26.539	3	2 0 5
27.840	1	1 0 7
29.121	6	2 1 4
30.480	7	3 0 3
31.260	16	1 2 5
31.480	8	0 1 8
32.400	5	0 2 7
32.760	9	2 2 0
33.880	9	0 0 9
34.380	13	1 3 1
34.740	9	2 2 3
35.001	7	3 1 2
35.619	9	2 0 8
36.419	24	2 1 7
37.421	12	1 3 4
37.740	7	1 1 9
38.200	11	4 0 1
38.780	9	0 4 2
39.159	3	3 1 5
40.041	5	2 2 6
41.021	6	4 0 4
41.759	1	3 2 1
42.461	1	0 2 10
42.639	1	0 4 5
42.801	1	0 1 11
43.521	4	1 3 7
44.379	7	3 2 4
44.661	3	3 0 9
49.740	1	4 1 6
50.061	2	3 3 0
50.720	1	1 0 13
51.201	1	2 4 1
51.440	2	3 3 3
51.662	2	4 2 2
51.961	8	5 0 5
52.102	12	2 3 8

Table B.4 X-ray diffraction data for Fe (PDF # 06-0696) [92].

6- 696 JCPDS-ICDD Copyright (c) 2000 Radiation: 1.54060 Quality: *

Fe

Iron

Iron, syn

Rad: CuKa1 Lambda: 1.5405 Filter: Ni d-sp:
Cutoff: Int: Diffractometer I/Icor:
Ref: Swanson et al., Natl. Bur. Stand. (U.S.), Circ. 539, IV 3 (1955)

Sys: Cubic S.G.: Im-3m (229)
a: 2.8664 b: c: A: C:
A: B: C: Z: 2 mp:
Ref: Ibid.

Dx: 7.88 Dm: SS/FOM: F(6)=225.2(.0044,6)

ea: nwB: ey: Sign: 2V:
Ref:

Color: Gray, light gray metallic
Pattern taken at 25 C. CAS no.: 7439-89-6. The iron used was an exceptionally pure rolled sheet prepared at the NBS, Gaithersburg, Maryland, USA., [Moore, G., \ITJ. Met.\RG, \BF5\RG 1443 (1953)]. It was annealed in an \H2\ atmosphere for 3 days at 1100 C and slowly cooled in a He atmosphere. Total impurities of sample <0.0013% each metals and non-metals. gamma-Fe (fcc)=(1390 C) delta-Fe (bcc). Opaque mineral optical data on specimen from Meteorite: RR2Re= 57.7, Disp.=16, VHN=158 (mean at 100, 200, 300), Color values=.311, .316, 57.9, Ref.: IMA Commisssion on Ore Microscopy QDF. \W\ type. Iron group, iron subgroup. Also called: ferrite. PSC: cI2. See ICSD 64795 (PDF 85-1410). Mwt: 55.85. Volume[CD]: 23.55.

2-theta	Int.	h k l
44.674	100	1 1 0
65.023	20	2 0 0
82.335	30	2 1 1
98.949	10	2 2 0
116.390	12	3 1 0
137.144	6	2 2 2

Table B.5 X-ray diffraction data for Mg (PDF # 35-0821) [92].

(1/1)

35-821 JCPDS-ICDD Copyright (c) 2000 Radiation: 1.54060 Quality: *

Mg

Magnesium

Rad: CuKa1 Lambda: 1.540598 Filter: Mono. d-sp: Diff.
Cutoff: 17.7 Int: Diffractometer I/Icor:
Ref: Natl. Bur. Stand. (U.S.) Monogr. 25, 21 82 (1984)

Sys: Hexagonal S.G.: P63/mmc (194)
a: 3.20936(11) b: c: 5.2112(3) A: C: 1.6238
A: B: C: Z: 2 mp:
Ref: Ibid.

Dx: 1.736 Dm: SS/FOM: F(27)=75.6(.0123,29)

ea: nwB: ey: Sign: 2V:
Ref:

Color: Dark gray
Peak height intensities. The temperature of data collection was approximately 25.0 C. The sample was obtained from Fisher Scientific Company, Fair Lawn, New Jersey, USA. It contained a small amount of \Mg (O H)2\. CAS no.: 7439-95-4. Pyrotechnic. sigma(Iobs)=+/-0.01. \Mg\ type. Tungsten used as internal standard. PSC: hP2. To replace 4-770. Structure reference: Jevins, A. et al., Z. Phys. Chem. (B), 40 347 (1938). Mwt: 24.31. Volume[CD]: 46.48.

2-theta	Int.	h k l
32.197	25	1 0 0
34.399	36	0 0 2
36.619	100	1 0 1
47.830	15	1 0 2
57.374	12	1 1 0
63.060	16	1 0 3
67.313	2	2 0 0
68.630	13	1 1 2
69.999	8	2 0 1
72.494	2	0 0 4
77.820	2	2 0 2
81.531	2	1 0 4
90.420	3	2 0 3
94.311	1	2 1 0
96.824	4	2 1 1
99.187	3	1 1 4
104.229	2	1 0 5
104.502	2	2 1 2
108.273	<1	2 0 4
112.469	1	3 0 0
117.970	2	2 1 3
123.881	1	3 0 2
134.989	<1	2 0 5
136.653	<1	1 0 6
140.752	<1	2 1 4

Table B.6 X-ray diffraction data for Al_3Mg_2 (PDF # 29-0048) [92].

29-48 JCPDS-ICDD Copyright (c) 2000 Radiation: 1.54060 Quality: C

Al Mg
3 2

Aluminum Magnesium

Rad: CuKa1 Lambda: 1.54056 Filter: d-sp: Calculated
Cutoff: Int: Calculated I/Icor:
Ref: Smith, D., Yu, Penn State Univ., University Park, PA, USA, ICDD Grant-in-Aid, (1975)

Sys: Cubic S.G.: Fd-3m (227)
a: 28.239 b: c: A: C:
A: B: C: Z: 233.6 mp:
Ref: Samson, S., Acta Crystallogr., 19 401 (1965)

Dx: 2.232 Dm: SS/FOM: F(30)=92.4(.0031,104)

ea: nwB: ey: Sign: 2V:
Ref:

Peak height intensities. \Al3 Mg2\ type. PSC: cF1168. To replace 18-34. Mwt: 129.55. Volume[CD]: 22518.94.

2-theta	Int.	h k l
15.360	3	4 2 2
16.296	3	5 1 1
18.842	3	4 4 2
19.869	2	6 2 0
20.610	5	5 3 3
31.498	6	7 7 1
32.940	3	10 2 2
35.222	6	11 1 1
35.951	85	8 8 0
36.527	55	8 8 2
37.105	6	10 6 0
37.523	100	11 3 3
38.218	4	12 0 0
38.628	38	11 5 1
39.312	8	12 2 2
39.710	9	11 5 3
40.894	26	12 4 2
41.404	2	10 8 2
41.806	10	11 7 1
41.928	10	10 6 6
42.423	13	12 4 4
42.803	15	13 3 1
42.931	10	10 8 4
43.805	3	13 3 3
44.903	2	12 6 4
45.383	6	10 10 0
45.861	4	10 10 2
46.687	6	11 9 3
48.533	2	15 1 1
58.712	4	17 5 3
61.950	15	14 12 4
62.624	10	13 13 5
64.623	7	16 8 8
65.003	3	12 12 10
65.377	16	14 14 0
65.656	12	15 13 1
67.149	3	17 11 1
67.884	2	17 11 3
68.710	2	18 10 2
69.348	2	17 11 5
69.808	2	20 6 2
70.803	5	21 3 1
71.253	3	16 14 2
76.228	3	16 16 0
76.583	2	16 16 2
77.888	2	19 13 1
78.590	6	23 3 1
82.045	2	17 17 1
84.879	3	20 14 4
85.221	2	24 6 2
96.499	2	26 6 6
97.101	2	23 15 1
104.124	2	24 16 2
104.746	2	29 1 1

Table B.7 X-ray diffraction data for B_2O_3 (PDF # 06-0297) [92].

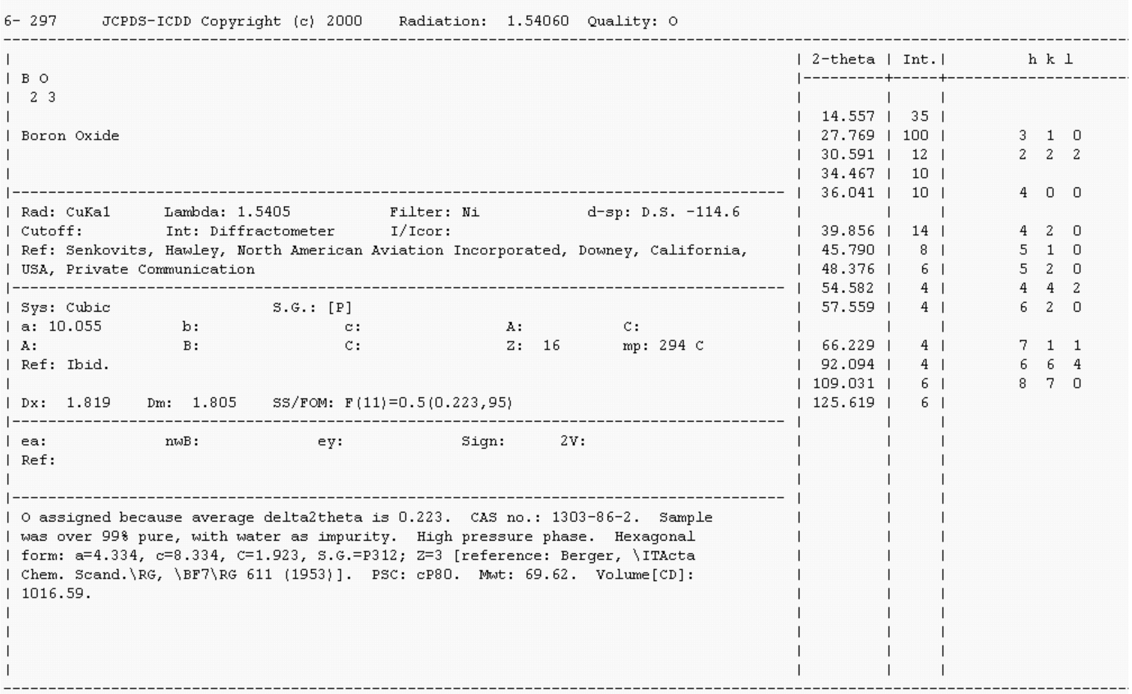

```
6- 297     JCPDS-ICDD Copyright (c) 2000    Radiation:  1.54060  Quality: O
------------------------------------------------------------------------------------------------------------------------------
|                                                                                       | 2-theta | Int.|         h k l
| B O                                                                                   |---------+-----+-------------------
|  2 3                                                                                  |         |     |
|                                                                                       |  14.557 |  35 |
| Boron Oxide                                                                           |  27.769 | 100 |        3  1  0
|                                                                                       |  30.591 |  12 |        2  2  2
|                                                                                       |  34.467 |  10 |
|-------------------------------------------------------------------------------------- |  36.041 |  10 |        4  0  0
| Rad: CuKa1      Lambda: 1.5405           Filter: Ni            d-sp: D.S. -114.6      |         |     |
| Cutoff:         Int: Diffractometer      I/Icor:                                      |  39.856 |  14 |        4  2  0
| Ref: Senkovits, Hawley, North American Aviation Incorporated, Downey, California,     |  45.790 |   8 |        5  1  0
| USA, Private Communication                                                            |  48.376 |   6 |        5  2  0
|-------------------------------------------------------------------------------------- |  54.582 |   4 |        4  4  2
| Sys: Cubic                  S.G.: [P]                                                 |  57.559 |   4 |        6  2  0
| a: 10.055         b:                c:                A:           C:                 |         |     |
| A:                B:                C:                Z:  16       mp: 294 C          |  66.229 |   4 |        7  1  1
| Ref: Ibid.                                                                            |  92.094 |   4 |        6  6  4
|                                                                                       | 109.031 |   6 |        8  7  0
| Dx:  1.819    Dm:  1.805    SS/FOM: F(11)=0.5(0.223,95)                               | 125.619 |   6 |
|-------------------------------------------------------------------------------------- |         |     |
| ea:             nwB:            ey:             Sign:      2V:                        |         |     |
| Ref:                                                                                  |         |     |
|                                                                                       |         |     |
|-------------------------------------------------------------------------------------- |         |     |
| O assigned because average delta2theta is 0.223.  CAS no.: 1303-86-2.  Sample         |         |     |
| was over 99% pure, with water as impurity.  High pressure phase.  Hexagonal           |         |     |
| form: a=4.334, c=8.334, C=1.923, S.G.=P312; Z=3 [reference: Berger, \ITActa           |         |     |
| Chem. Scand.\RG, \BF7\RG 611 (1953)].  PSC: cP80.  Mwt: 69.62.  Volume[CD]:           |         |     |
| 1016.59.                                                                              |         |     |
|                                                                                       |         |     |
|                                                                                       |         |     |
|                                                                                       |         |     |
|                                                                                       |         |     |
------------------------------------------------------------------------------------------------------------------------------
```

Table B.8 X-ray diffraction data for $Mg(AlH_4)_2$ (PDF # 47-0980) [92].

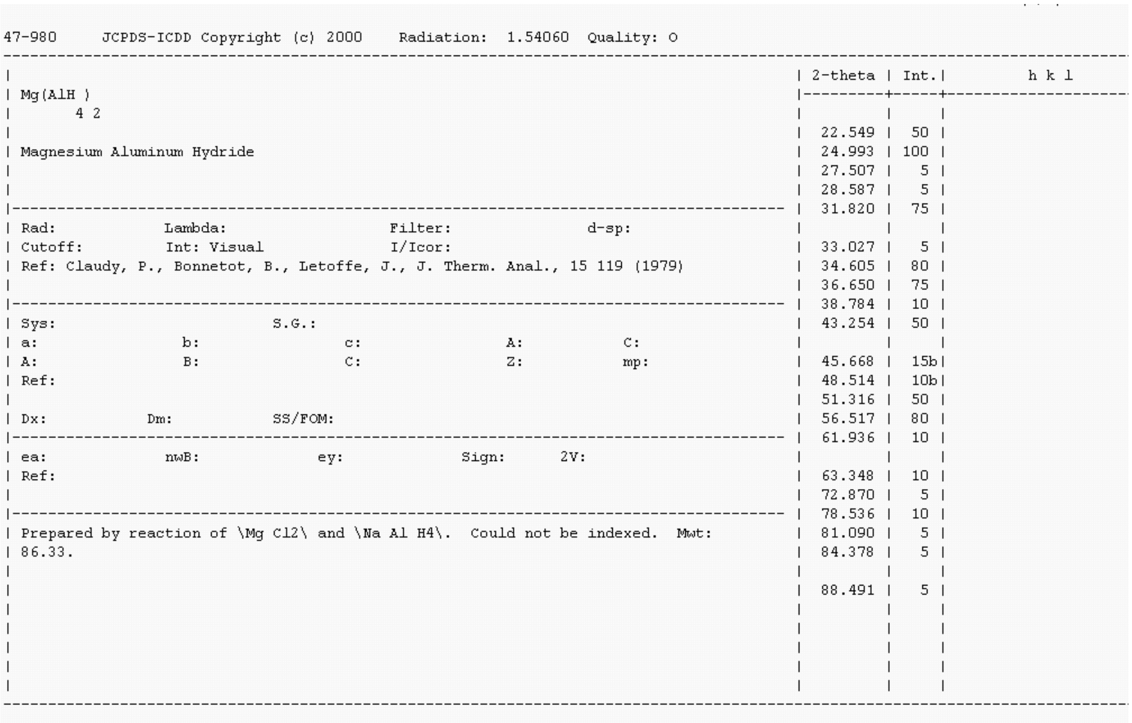

```
47-980     JCPDS-ICDD Copyright (c) 2000    Radiation:  1.54060  Quality: O
------------------------------------------------------------------------------------------------------------------------------
|                                                                                       | 2-theta | Int.|         h k l
| Mg(AlH )                                                                              |---------+-----+-------------------
|       4 2                                                                             |         |     |
|                                                                                       |  22.549 |  50 |
| Magnesium Aluminum Hydride                                                            |  24.993 | 100 |
|                                                                                       |  27.507 |   5 |
|                                                                                       |  28.587 |   5 |
|-------------------------------------------------------------------------------------- |  31.820 |  75 |
| Rad:            Lambda:                  Filter:               d-sp:                  |         |     |
| Cutoff:         Int: Visual              I/Icor:                                      |  33.027 |   5 |
| Ref: Claudy, P., Bonnetot, B., Letoffe, J., J. Therm. Anal., 15 119 (1979)            |  34.605 |  80 |
|                                                                                       |  36.650 |  75 |
|-------------------------------------------------------------------------------------- |  38.784 |  10 |
| Sys:                        S.G.:                                                     |  43.254 |  50 |
| a:                b:                c:                A:           C:                 |         |     |
| A:                B:                C:                Z:           mp:                |  45.668 |  15b|
| Ref:                                                                                  |  48.514 |  10b|
|                                                                                       |  51.316 |  50 |
| Dx:           Dm:           SS/FOM:                                                   |  56.517 |  80 |
|-------------------------------------------------------------------------------------- |  61.936 |  10 |
| ea:             nwB:            ey:             Sign:      2V:                        |         |     |
| Ref:                                                                                  |  63.348 |  10 |
|                                                                                       |  72.870 |   5 |
|-------------------------------------------------------------------------------------- |  78.536 |  10 |
| Prepared by reaction of \Mg Cl2\ and \Na Al H4\.  Could not be indexed.  Mwt:         |  81.090 |   5 |
| 86.33.                                                                                |  84.378 |   5 |
|                                                                                       |         |     |
|                                                                                       |  88.491 |   5 |
|                                                                                       |         |     |
|                                                                                       |         |     |
|                                                                                       |         |     |
|                                                                                       |         |     |
|                                                                                       |         |     |
------------------------------------------------------------------------------------------------------------------------------
```

Table B.9 X-ray diffraction data for α-$Mg(BH_4)_2$ (PDF # 26-1212) [92].

26-1212 JCPDS-ICDD Copyright (c) 2000 Radiation: 1.54060 Quality: O

alpha-MgB H
2 8

Boron Magnesium Hydride

Rad: Cu Lambda: 1.54056 Filter: Ni d-sp: D.S. -57.3
Cutoff: Int: Visual I/Icor:
Ref: Konoplev, Bakulina, Bull. Acad. Sci. (USSR), Div. Chem. Sci., 20 136 (1971)

Sys: Tetragonal S.G.: [P]
a: 13.59 b: c: 16.51 A: C: 1.2149
A: B: C: Z: 50 mp:
Ref: Ibid.

Dx: 1.470 Dm: SS/FOM: F(15)=0.6(0.071,358)

ea: nwB: ey: Sign: 2V:
Ref:

Transformation temperature: 182-186 C. Indexed by editor. Refined cell:
a=13.73, c=16.48. (Ed.)
*Poor fit to given cell. Closer fit to d=4.78.
PSC: tP550. Mwt: 53.99. Volume[CD]: 3049.20.

2-theta	Int.	h k l
16.132	50	0 0 3
18.785	100	1 1 3
21.035	20	2 0 3
23.144	20	3 1 2
30.699	10	2 1 5
34.605	20	4 3 2
37.604	50	2 2 6
42.402	10	6 2 1
44.833	50	1 1 8
46.840	50	4 0 7
51.039	10	5 4 5
53.345	10	6 4 4
56.936	20	8 2 2
59.940	10	3 1 10
62.353	10	6 2 8
66.070	10	8 2 6

Table B.10 X-ray diffraction data for β-$Mg(BH_4)_2$ (PDF # 26-1213) [92].

26-1213 JCPDS-ICDD Copyright (c) 2000 Radiation: 1.54060 Quality:

beta-MgB H
2 8

Boron Magnesium Hydride

Rad: Cu Lambda: 1.54056 Filter: Mo d-sp:
Cutoff: Int: Visual I/Icor:
Ref: Konoplev, Bakulina, Bull. Acad. Sci. (USSR), Div. Chem. Sci., 20 136 (1971)

Sys: Cubic S.G.: [P]
a: 15.5 b: c: A: C:
A: B: C: Z: 62 mp:
Ref: Ibid.

Dx: 1.493 Dm: SS/FOM: F(19)=1.8(0.116,91)

ea: nwB: ey: Sign: 2V:
Ref:

Transformation temperature: 182-186 C. PSC: cP682. Mwt: 53.99. Volume[CD]:
3723.88.

2-theta	Int.	h k l
18.826	100	3 1 1
19.891	80	2 2 2
22.962	50	4 0 0
24.993	20	3 3 1
25.652	20	4 2 0
28.401	20	4 2 2
30.485	20	
32.412	50	4 4 0
34.331	1	5 3 1
37.768	50	5 4 1
39.135	10	6 3 0
40.416	20	4 4 4
41.989	50	6 4 0
43.917	80	7 2 2
46.284	80	7 3 2
48.104	10	7 3 3
50.049	20	6 6 0
55.623	10	6 6 4
58.971	50	8 5 3
61.799	50	9 5 1

Table B.11 X-ray diffraction data for MgB_2 (PDF # 38-1369) [92].

38-1369 JCPDS-ICDD Copyright (c) 2000 Radiation: 1.54060 Quality: *

MgB
2

Boron Magnesium

Rad: CuKa1 Lambda: 1.540598 Filter: Mono. d-sp: Diff.
Cutoff: 17.7 Int: Diffractometer I/Icor:
Ref: Wong-Ng, W., McMurdie, H., Paretzkin, B., Hubbard, C., Dragoo, A., NBS (USA), ICDD Grant-in-Aid, (1987)

Sys: Hexagonal S.G.: P6/mmm (191)
a: 3.0864(2) b: c: 3.5215(2) A: C: 1.1410
A: B: C: Z: 1 mp:
Ref: Wong-Ng, W. et al., Powder Diffraction, 3 54 (1988)

Dx: 2.625 Dm: SS/FOM: F(20)=86.8(.0105,22)

ea: nwB: ey: Sign: 2V:
Ref:

Color: Dark grayish brown
Peak height intensities. Mean temperature of data collection was 23.8 C. The sample was obtained from Alfa Products/Thiokol Ventron Division, Danvers, Massachusetts, USA. It contained a very small amount of magnesium d=2.440 (I<3) and unidentified reflections at d=3.15, 1.22, 0.943, 0.861 and 0.835 with I<2. CAS no.: 12007-25-9. SEM with Energy Dispersive Spectrometer (EDS) indicated no impurity. The structure was determined by Jones and Marsh (1). \Al B2\ type. Tungsten used as internal standard. PSC: hP3. To replace 6-640. Structure reference: 1. Jones, M., Marsh, R., J. Am. Chem. Soc., 76 1434 (1954). Mwt: 45.93. Volume[CD]: 29.05.

2-theta	Int.	h k l
25.267	4	0 0 1
33.485	26	1 0 0
42.402	100	1 0 1
51.885	12	0 0 2
59.884	21	1 1 0
63.175	11	1 0 2
66.044	5	1 1 1
70.401	4	2 0 0
76.127	11	2 0 1
83.193	11	1 1 2
91.586	6	1 0 3
92.698	2	2 0 2
99.347	3	2 1 0
104.960	9	2 1 1
111.069	<1	1 1 3
119.681	3	3 0 0
121.725	2	2 0 3
122.053	2	0 0 4
123.077	2	2 1 2
134.202	<1	1 0 4

Table B.12 X-ray diffraction data for β-MgH_2 (PDF # 12-0697) [92].

12-697 JCPDS-ICDD Copyright (c) 2000 Radiation: 1.54060 Quality: i

MgH
2

Magnesium Hydride

Rad: CuKa1 Lambda: 1.5405 Filter: Ni d-sp:
Cutoff: Int: Diffractometer I/Icor:
Ref: Batt, A., Polytechnic Institute of Brooklyn, Brooklyn, New York, USA, ICDD Grant-in-Aid, (1960)

Sys: Tetragonal S.G.: P42/mnm (136)
a: 4.517 b: c: 3.0205 A: C: 0.6687
A: B: C: Z: 2 mp:
Ref: Ellinger et al., J. Am. Chem. Soc., 77 2647 (1955)

Dx: 1.418 Dm: 1.450 SS/FOM: F(27)=15.2(0.040,44)

ea: nwB: ey: Sign: 2V:
Ref:

Color: Light gray
CAS no.: 7693-27-8. Reference: Zachariasen et al., \ITActa Crystallogr.\RG, \BF16\RG 352 (1963). \O2 Ti\ type. PSC: tP6. See ICSD 26624 (PDF 74-934). Mwt: 26.32. Volume[CD]: 61.63.

2-theta	Int.	h k l
27.947	100	1 1 0
35.744	90	1 0 1
39.856	20	2 0 0
54.617	40	2 1 1
57.756	5	2 2 0
61.345	<1	0 0 2
65.341	5	3 1 0
68.768	5	1 1 2
69.761	5	3 0 1
75.727	1	2 0 2
83.483	5	3 2 1
86.045	<1	4 0 0
89.206	5	2 2 2
92.766	<1	3 3 0
95.821	5	3 1 2
96.811	1	4 1 1
99.401	<1	4 2 0
103.187	<1	1 0 3
116.882	<1	4 0 2
117.506	1	2 1 3
120.781	<1	5 1 0
124.602	<1	3 3 2
125.877	5	5 0 1
133.115	1	4 2 2
133.911	1	3 0 3

Table B.13 X-ray diffraction data for γ-MgH_2 (PDF # 35-1184) [92].

5-1184 JCPDS-ICDD Copyright (c) 2000 Radiation: 1.54060 Quality: i DELETED

gamma-MgH
2

Magnesium Hydride

Rad: CuKa Lambda: 1.54178 Filter: d-sp: D.S.
Cutoff: Int: Visual I/Icor:
Ref: Bastide, J. et al., Mater. Res. Bull., 15 1779 (1980)

Sys: Orthorhombic S.G.: Pbcn (60)
a: 4.53 b: 5.44 c: 4.93 A: C:
A: B: C: Z: 4 mp:
Ref: Ibid.

Dx: 1.439 Dm: SS/FOM: F(13)=5.1(0.068,38)

ea: nwB: ey: Sign: 2V:
Ref:

\O2 Pb\ type. C.D. Cell: a=4.930, b=5.440, c=4.530, a/b=0.9062, c/b=0.8327, S.G.=Pnab (60). PSC: oP12. Deleted by 51-621, pattern has better FN, Mayo 12/98. Mwt: 26.32. Volume[CD]: 121.49.

2-theta	Int.	h k l
25.584	50	1 1 0
31.453	100	1 1 1
32.890	20	0 2 0
37.719	60	0 2 1
44.974	20	1 1 2
47.046	10	2 1 1
49.961	5	0 2 2
52.520	5	2 2 0
56.029	40	2 2 1
67.253	30	3 1 1, 1 3 2
71.842	5	0 4 1
74.405	10	3 2 1
80.678	5	0 4 2, 1 0 4

Table B.14 X-ray diffraction data for MgO (PDF # 45-0946) [92].

45-946 JCPDS-ICDD Copyright (c) 2000 Radiation: 1.54060 Quality: *

MgO

Magnesium Oxide

Periclase, syn

Rad: CuKa1 Lambda: 1.540598 Filter: Ge Mono. d-sp: Diff.
Cutoff: Int: Diffractometer I/Icor: 1.0
Ref: Kern, A., Doetzer, R., Eysel, W., Mineralogisch-Petrographisches Inst., Univ. Heidelberg, Germany, ICDD Grant-in-Aid, (1993)

Sys: Cubic S.G.: Fm-3m (225)
a: 4.2112 b: c: A: C:
A: B: C: Z: 4 mp:
Ref: Ibid.

Dx: 3.59 Dm: 3.56 SS/FOM: F(10)=101.1(.0099,10)

ea: nwB: ey: Sign: 2V:
Ref: Winchell, Winchell, Elements of Optical Mineralogy, 57 (1964)

Color: Colorless
Integrated intensities. MgO (Heraeus, 99.99 %) annealed in open Au crucible at 800 C for 1 week. Validated by calculated pattern 43-1022. \Cl Na\ type. Halite group, periclase subgroup. Silicon used as internal standard. PSC: cF8. To replace 4-829. Structure reference: Moscow University Geology Bulletin, 47 80 (1992). Mwt: 40.30. Volume[CD]: 74.68.

2-theta	Int.	h k l
36.931	4	1 1 1
42.918	100	2 0 0
62.302	39	2 2 0
74.693	5	3 1 1
78.629	10	2 2 2
94.053	8	4 0 0
105.736	2	3 3 1
109.768	19	4 2 0
127.277	14	4 2 2
143.758	4	5 1 1

Table B.15 X-ray diffraction data for $MgCl_2$ (PDF # 37-0774) [92].

37-774 JCPDS-ICDD Copyright (c) 2000 Radiation: 1.54060 Quality: i

MgCl
2

Magnesium Chloride

Chloromagnesite, syn [NR]

Rad: CuKa1 Lambda: 1.54056 Filter: Mono. d-sp: Diff.
Cutoff: Int: Diffractometer I/Icor:
Ref: Dorrepaal, J., J. Appl. Crystallogr., 17 483 (1984)

Sys: Rhombohedral (Hex) S.G.: R-3m (166)
a: 3.640(4) b: c: 17.673(15) A: C: 4.8552
A: B: C: Z: 3 mp:
Ref: Ibid.

Dx: 2.34 Dm: SS/FOM: F(20)=20.7(0.032,30)

ea: 1.59 nwB: 1.675 ey: Sign: - 2V:
Ref: Dana's System of Mineralogy, 7th Ed., II 41 (1951)

Molybdenite group, rhombohedral subgroup. Silicon used as internal standard.
PSC: hR3. See ICSD 26157 (PDF 74-521). Structure reference: Ferrari et al.,
Acta Crystallogr., Sec. B, 16 46 (1963). Mwt: 95.21. Volume[CD]: 202.79.

2-theta	Int.	h k l
15.029	100	0 0 3
30.336	50	0 0 6
34.925	10	1 0 4
38.422	<1	0 1 5
45.986	1	1 0 7
50.049	2	1 1 0
50.405	5	0 1 8
52.585	<1	1 1 3
59.430	<1	2 0 2
59.684	<1	1 1 6
59.897	1	1 0 10
62.493	5	0 2 4
63.013	10	0 0 12
65.084	1	0 1 11
70.359	1	0 2 7
73.796	2	2 0 8
81.673	10	0 0 15
82.181	<1	0 1 14
84.116	1	2 1 4
84.560	3	1 1 12

Table B.16 X-ray diffraction data for $MgCl_2$-4H_2O (PDF # 01-1210) [92].

1- 1210 JCPDS-ICDD Copyright (c) 2000 Radiation: 1.54060 Quality:

MgCl !4H O
2 2

Magnesium Chloride Hydrate

Rad: MoKa1 Lambda: 0.70930 Filter: ZrO2 d-sp: D.S. -406.4
Cutoff: Int: I/Icor:
Ref: The Dow Chemical Company, Midland, Michigan, USA, Private Communication

Sys: S.G.:
a: b: c: A: C:
A: B: C: Z: mp:
Ref:

Dx: Dm: SS/FOM:

ea: nwB: ey: Sign: 2V:
Ref:

Mwt: 167.27.

2-theta	Int.	h k l
16.102	30	
20.165	20	
22.665	40	
24.367	2	
25.577	20	
29.555	60	
32.412	80	
33.666	40	
40.991	100	
43.038	40	
44.142	2	
45.790	4	
48.104	12	
49.786	20	
52.880	20	
56.403	2	
60.899	40	
63.204	8	
68.425	20	
72.033	2	
73.330	2	
75.374	2	
77.549	2	
79.870	2	
82.352	2	

2-theta	Int.	h k l	2-theta	Int.	h k l	2-theta	Int.	h k l
85.017	2							
88.898	4							

Table B.17 X-ray diffraction data for $MgCl_2$-6H_2O (PDF # 25-0515) [92].

25-515 JCPDS-ICDD Copyright (c) 2000 Radiation: 1.54060 Quality: *

MgCl !6H O
2 2

Magnesium Chloride Hydrate

Bischofite, syn

Rad: CuKa1 Lambda: 1.54056 Filter: Mono. d-sp: Diff.
Cutoff: Int: Diffractometer I/Icor: 0.80
Ref: Natl. Bur. Stand. (U.S.) Monogr. 25, 11 37 (1974)

Sys: Monoclinic S.G.: C2/m (12)
a: 9.871(2) b: 7.113(1) c: 6.079(1) A: 1.3877 C: 0.8546
A: B: 93.74(1) C: Z: 2 mp:
Ref: Ibid.

Dx: 1.59 Dm: SS/FOM: F(30)=92.4(.0081,40)

ea: 1.498 nwB: 1.505 ey: 1.525 Sign: + 2V: 70(15) deg.
Ref: Ibid.

Color: Colorless
Pattern taken at 25 C. The sample was somewhat hygroscopic. The sample was prepared by boiling a saturated aqueous solution of \Mg Cl2\ and filtering off the crystals. Nickelbischofite is the Ni analogue. \Br2 H12 Mg O6\ type. PSC: mC42. To replace 1-431. Mwt: 203.30. Volume[CD]: 425.91.

2-theta	Int.	h k l
15.344	17	1 1 0
20.820	20	-1 1 1
21.653	100	1 1 1
22.462	30	-2 0 1
23.980	10	2 0 1
25.021	30	0 2 0
29.082	2	0 2 1
29.435	5	0 0 2
29.951	35	3 1 0
30.994	65	2 2 0
32.655	35	-3 1 1
32.803	55	-1 1 2
33.653	8	-2 0 2
33.889	90	1 1 2
34.250	7	3 1 1
34.925	9	2 2 1
36.450	7	4 0 0
38.507	9	-4 0 1
38.993	25	0 2 2
40.378	30	4 0 1
41.148	2	-3 1 2
41.644	5	-1 3 1
42.092	8	1 3 1
42.381	3	-2 2 2
43.805	8	3 1 2
44.119	11	2 2 2
46.485	2	-4 2 1
47.254	5	-3 3 0
47.464	7	-2 0 3
48.104	6	4 2 1
49.241	35	-1 3 2
49.383	20	-5 1 1
49.786	6	2 0 3
50.315	7	3 3 1
51.347	15	0 4 0
52.006	5	0 2 3
52.972	13	-4 2 2
53.152	11	-3 1 3
54.372	4	-2 2 3
55.962	3	6 0 0
56.703	6	-2 4 1
57.701	5	3 3 2
61.399	4	1 3 3
62.381	12	-5 3 1

Table B.18 X-ray diffraction data for $NaAlH_4$ (PDF # 85-0374) [92].

85-374 JCPDS-ICDD Copyright (c) 2000 Radiation: 1.54060 Quality: C

NaAlH
4

Rad: CuKa1 Lambda: 1.54060 Filter: d-sp: Calculated
Cutoff: 17.7 Int: Calculated I/Icor: 3.46
Ref: ***misspelled or not in coden file***, (1997)

Sys: Tetragonal S.G.: I41/a (88)
a: 5.02000(20) b: c: 11.33000(30) A: C: 2.2570
A: B: C: Z: 4 mp:
Ref: Ibid.

Dx: 1.256 Dm: 1.256 SS/FOM: F(30)=420.0(.0017,41)

ea: nwB: ey: Sign: 2V:
Ref:

Peak height intensities. R-factor: 0.039. PSC: tI24. See PDF 22-1337.
Structure reference: Dougherty, D., Herley, P.J., Lauther, J.W., Acta
Crystallogr., Sec. B, 35 1454 (1979). Mwt: 54.00. Volume[CD]: 285.52.

2-theta	Int.	h k l
19.324	40	1 0 1
29.676	999	1 1 2
31.561	179	0 0 4
35.744	249	2 0 0
39.227	1	2 0 2
40.721	1	1 1 4
40.949	1	1 2 1
43.798	1	1 0 5
47.051	3	1 2 3
48.415	192	2 0 4
51.446	72	2 2 0
55.040	112	1 1 6
57.764	2	2 1 5
60.004	1	1 0 7
60.520	152	1 3 2
61.617	69	2 2 4
65.902	12	0 0 8
67.755	2	3 2 1
69.814	1	3 0 5
71.849	1	2 1 7
72.269	1	2 3 3
75.727	14	4 0 0
77.289	24	2 0 8
78.222	1	1 0 9
78.683	45	3 1 6

2-theta	Int.	h k l	2-theta	Int.	h k l	2-theta	Int.	h k l
80.982	1	3 2 5	88.189	13	2 2 8			
82.922	1	3 0 7	89.103	1	1 2 9			
83.377	18	4 1 3, 3 3 2	89.745	1	3 3 4			
84.342	17	4 0 4						
86.666	15	4 2 0						

Table B.19 X-ray diffraction data for $NaBH_4$ (PDF # 09-0386) [92].

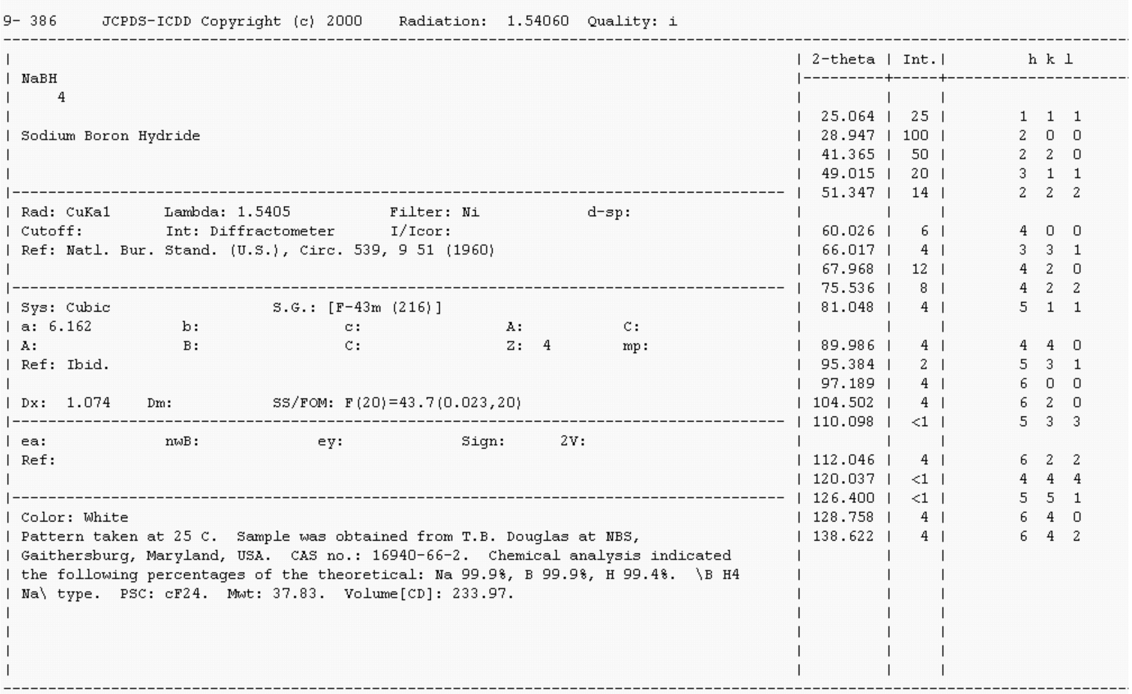

```
9- 386     JCPDS-ICDD Copyright (c) 2000    Radiation:  1.54060  Quality: i
----------------------------------------------------------------------------------------------------------------------------
|                                                                                  | 2-theta | Int.|        h k l
| NaBH                                                                             |---------+-----+--------------------
|    4                                                                             |         |     |
|                                                                                  |  25.064 |  25 |       1  1  1
| Sodium Boron Hydride                                                             |  28.947 | 100 |       2  0  0
|                                                                                  |  41.365 |  50 |       2  2  0
|                                                                                  |  49.015 |  20 |       3  1  1
|--------------------------------------------------------------------------------- |  51.347 |  14 |       2  2  2
| Rad: CuKa1      Lambda: 1.5405          Filter: Ni           d-sp:               |         |     |
| Cutoff:         Int: Diffractometer      I/Icor:                                  |  60.026 |   6 |       4  0  0
| Ref: Natl. Bur. Stand. (U.S.), Circ. 539, 9 51 (1960)                            |  66.017 |   4 |       3  3  1
|                                                                                  |  67.968 |  12 |       4  2  0
|--------------------------------------------------------------------------------- |  75.536 |   8 |       4  2  2
| Sys: Cubic                 S.G.: [F-43m (216)]                                   |  81.048 |   4 |       5  1  1
| a: 6.162         b:                c:                A:           C:             |         |     |
| A:               B:                C:                Z:  4        mp:            |  89.986 |   4 |       4  4  0
| Ref: Ibid.                                                                       |  95.384 |   2 |       5  3  1
|                                                                                  |  97.189 |   4 |       6  0  0
| Dx:  1.074    Dm:            SS/FOM: F(20)=43.7(0.023,20)                        | 104.502 |   4 |       6  2  0
|--------------------------------------------------------------------------------- | 110.098 |  <1 |       5  3  3
| ea:             nwB:             ey:             Sign:      2V:                  |         |     |
| Ref:                                                                             | 112.046 |   4 |       6  2  2
|                                                                                  | 120.037 |  <1 |       4  4  4
|--------------------------------------------------------------------------------- | 126.400 |  <1 |       5  5  1
| Color: White                                                                     | 128.758 |   4 |       6  4  0
| Pattern taken at 25 C.  Sample was obtained from T.B. Douglas at NBS,            | 138.622 |   4 |       6  4  2
| Gaithersburg, Maryland, USA.  CAS no.: 16940-66-2.  Chemical analysis indicated  |         |     |
| the following percentages of the theoretical: Na 99.9%, B 99.9%, H 99.4%.  \B H4 |         |     |
| Na\ type.  PSC: cF24.  Mwt: 37.83.  Volume[CD]: 233.97.                          |         |     |
|                                                                                  |         |     |
|                                                                                  |         |     |
|                                                                                  |         |     |
|                                                                                  |         |     |
----------------------------------------------------------------------------------------------------------------------------
```

Table B.20 X-ray diffraction data for NaCl (PDF # 05-0628) [92].

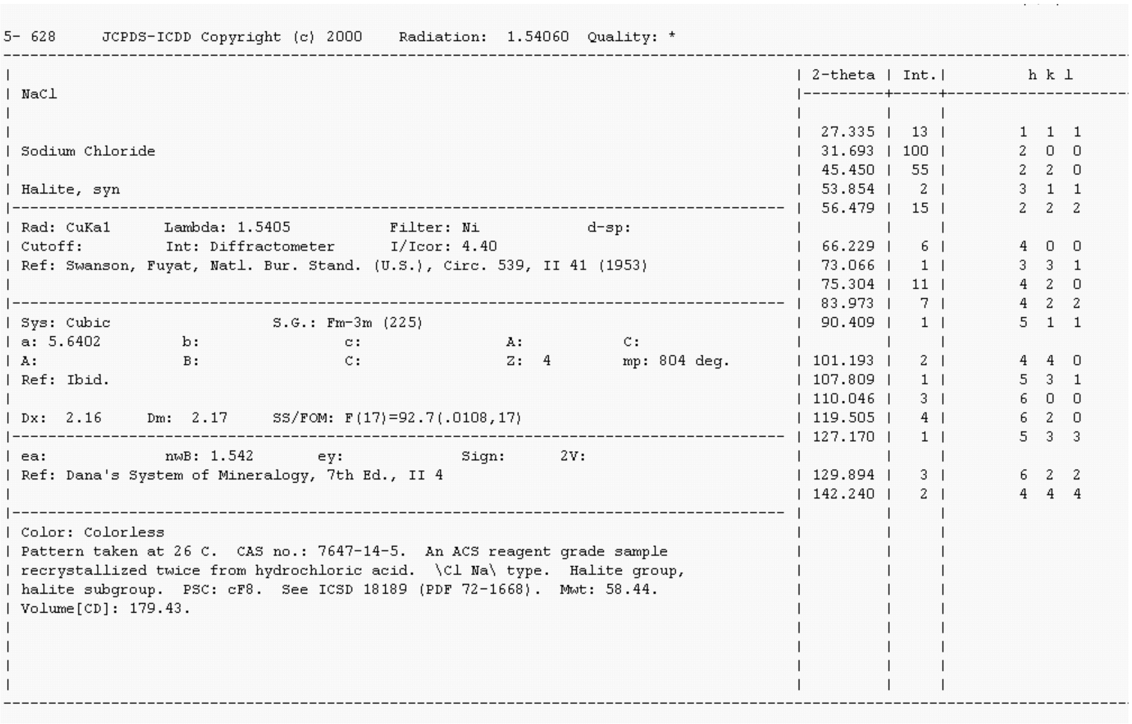

```
5- 628     JCPDS-ICDD Copyright (c) 2000    Radiation:  1.54060  Quality: *
----------------------------------------------------------------------------------------------------------------------------
|                                                                                  | 2-theta | Int.|        h k l
| NaCl                                                                             |---------+-----+--------------------
|                                                                                  |         |     |
|                                                                                  |  27.335 |  13 |       1  1  1
| Sodium Chloride                                                                  |  31.693 | 100 |       2  0  0
|                                                                                  |  45.450 |  55 |       2  2  0
| Halite, syn                                                                      |  53.854 |   2 |       3  1  1
|--------------------------------------------------------------------------------- |  56.479 |  15 |       2  2  2
| Rad: CuKa1      Lambda: 1.5405          Filter: Ni           d-sp:               |         |     |
| Cutoff:         Int: Diffractometer      I/Icor: 4.40                             |  66.229 |   6 |       4  0  0
| Ref: Swanson, Fuyat, Natl. Bur. Stand. (U.S.), Circ. 539, II 41 (1953)           |  73.066 |   1 |       3  3  1
|                                                                                  |  75.304 |  11 |       4  2  0
|--------------------------------------------------------------------------------- |  83.973 |   7 |       4  2  2
| Sys: Cubic                 S.G.: Fm-3m (225)                                     |  90.409 |   1 |       5  1  1
| a: 5.6402        b:                c:                A:           C:             |         |     |
| A:               B:                C:                Z:  4        mp: 804 deg.   | 101.193 |   2 |       4  4  0
| Ref: Ibid.                                                                       | 107.809 |   1 |       5  3  1
|                                                                                  | 110.046 |   3 |       6  0  0
| Dx:  2.16     Dm:  2.17     SS/FOM: F(17)=92.7(.0108,17)                         | 119.505 |   4 |       6  2  0
|--------------------------------------------------------------------------------- | 127.170 |   1 |       5  3  3
| ea:             nwB: 1.542       ey:             Sign:      2V:                  |         |     |
| Ref: Dana's System of Mineralogy, 7th Ed., II 4                                  | 129.894 |   3 |       6  2  2
|                                                                                  | 142.240 |   2 |       4  4  4
|--------------------------------------------------------------------------------- |         |     |
| Color: Colorless                                                                 |         |     |
| Pattern taken at 26 C.  CAS no.: 7647-14-5.  An ACS reagent grade sample         |         |     |
| recrystallized twice from hydrochloric acid.  \Cl Na\ type.  Halite group,       |         |     |
| halite subgroup.  PSC: cF8.  See ICSD 18189 (PDF 72-1668).  Mwt: 58.44.          |         |     |
| Volume[CD]: 179.43.                                                              |         |     |
|                                                                                  |         |     |
|                                                                                  |         |     |
|                                                                                  |         |     |
|                                                                                  |         |     |
----------------------------------------------------------------------------------------------------------------------------
```

Table B.21 X-ray diffraction data for $MgB_2O(OH)_6$ (PDF # 72-2360) [92].

72-2360 JCPDS-ICDD Copyright (c) 2000 Radiation: 1.54060 Quality: C

Mg(B O(OH))
2 6

Pinnoite

Rad: CuKa1 Lambda: 1.54060 Filter: d-sp: Calculated
Cutoff: 17.7 Int: Calculated I/Icor: 0.71
Ref: ***misspelled or not in coden file***, (1997)

Sys: Tetragonal S.G.: P42 (77)
a: 7.61400(13) b: c: 8.18980(80) A: C: 1.0756
A: B: C: Z: 4 mp:
Ref: Ibid.

Dx: 2.29 Dm: SS/FOM: F(30)=450.4(.0019,35)

ea: nwB: ey: Sign: 2V:
Ref:

Peak height intensities. R-factor: 0.033. PSC: tP64. See PDF 73-2357.
Structure reference: Genkina, E.A., Malinovskii, Y.A., Kristallografiya, 28 803
(1983). Mwt: 163.97. Volume[CD]: 474.79.

2-theta	Int.	h k l
11.613	1	1 0 0
15.880	11	1 0 1
16.452	999	1 1 0
19.718	156	1 1 1
21.685	113	0 0 2
23.347	288	2 0 0
24.666	449	1 0 2
25.786	5	2 0 1
26.149	2	1 2 0
27.341	38	1 1 2
28.363	406	1 2 1
32.076	57	2 0 2
33.255	1	2 2 0
34.220	58	1 2 2
34.885	179	1 0 3
36.887	111	1 1 3
37.053	129	3 0 1
37.316	51	1 3 0
38.958	610	1 3 1
40.052	272	2 2 2
40.634	103	2 0 3
41.842	22	3 0 2
42.404	106	1 2 3
43.570	122	1 3 2
44.199	183	0 0 4, 3 2
45.858	1	1 0 4
47.471	21	1 1 4
47.742	207	4 0 0
48.461	9	2 3 2
48.964	7	3 0 3
49.096	10	4 0 1
50.500	86	1 3 3
50.578	88	2 0 4, 1 4 1
52.134	84	1 2 4, 3 3 1
53.009	84	4 0 2
53.802	16	4 2 0
54.463	3	4 1 2
54.926	13	2 3 3
55.047	9	2 4 1
55.892	25	3 3 2
56.418	61	2 2 4
57.816	4	3 0 4
58.679	146	4 2 2
58.888	93	1 1 5
59.187	37	1 3 4
60.476	32	1 4 3
61.589	52	2 0 5
61.817	56	3 3 3
61.932	33	5 0 1
62.112	26	5 1 0
62.913	1	1 2 5
63.252	23	2 3 4, 1 5 1
64.448	8	2 4 3
65.325	28	3 4 2
66.023	1	5 2 0
66.607	27	1 5 2
66.801	15	2 2 5
67.083	70	4 0 4, 5 2 1
68.074	6	3 0 5
68.351	7	4 1 4
68.710	1	0 0 6
69.331	27	1 3 5
69.820	41	4 4 0
69.969	20	1 0 6
70.389	6	5 2 2
70.791	15	5 0 3
71.210	1	1 1 6
72.026	11	1 5 3, 4 2 4
72.301	18	3 5 0
73.046	26	3 2 5
73.363	25	5 3 1
74.085	26	4 4 2
74.748	1	6 0 0
74.886	2	2 1 6
75.692	7	5 2 3
75.962	4	1 6 0
76.510	9	3 5 2
76.692	5	4 0 5
77.000	2	1 6 1
77.895	1	4 1 5
78.161	2	3 4 4
78.505	1	2 2 6
78.915	8	6 0 2
79.095	10	3 3 5
79.354	30	5 1 4
79.559	15	2 6 0
80.102	3	1 6 2
80.588	2	2 6 1
80.892	11	3 1 6
81.472	24	2 4 5
81.673	30	5 3 3
82.922	6	2 5 4
83.661	1	6 2 2
84.035	1	6 0 3
84.432	1	3 2 6
84.843	6	4 5 2
85.221	5	6 1 3
85.481	2	3 6 0
86.493	5	3 6 1
87.063	14	2 0 7
87.366	9	5 0 5
87.969	1	4 0 6
88.239	2	2 1 7
88.542	9	1 5 5
88.745	9	6 2 3, 5 3 4
89.134	4	1 4 6
89.537	1	6 3 2
89.913	7	5 4 3

Table B.22 X-ray diffraction data for $MgBO_2(OH)$ (PDF # 33-0860) [92].

33-860 JCPDS-ICDD Copyright (c) 2000 Radiation: 1.54060 Quality: C

MgBO (OH)
2

Magnesium Borate Hydroxide

Szaibelyite-\ITO\RG

Rad: Lambda: Filter: d-sp: Calculated
Cutoff: Int: Calculated I/Icor:
Ref: Takeuchi, Y., Yamanaka, Mineralogical Institute, University of Tokyo, Tokyo, Japan, ICDD Grant-in-Aid, (1979)

Sys: Orthorhombic S.G.: P212121 (19)
a: 12.511 b: 10.393 c: 3.139 A: C:
A: B: C: Z: [8] mp:
Ref: Takeuchi, Y., Kudoh, Am. Mineral., 60 273 (1975)

Dx: 2.74 Dm: SS/FOM: F(30)=999.9(.0005,47)

ea: nωB: εγ: Sign: 2V:
Ref:

Sussexite is the Mn analogue. Also called: szaibelyite-\ITO\RG. C.D. Cell: a=10.393, b=12.511, c=3.139, a/b=0.8307, c/b=0.2509. PSC: oP48. Plus 13 additional reflections to 1.0410. Mwt: 84.12. Volume[CD]: 408.15.

2-theta	Int.	h k l
11.059	5	1 1 0
14.147	93	2 0 0
17.049	29	0 2 0
22.960	11	3 1 0
26.679	10	1 3 0
27.399	36	3 2 0
29.311	15	1 0 1
29.449	28	2 3 0
29.707	45	0 1 1
30.572	7	1 1 1
33.045	53	2 1 1
33.604	31	3 3 0
34.104	100	1 2 1
35.775	12	3 0 1
36.361	99	2 2 1
36.839	20	3 1 1
36.920	43	5 1 0
37.450	5	2 4 0
38.678	46	0 3 1
39.368	30	1 3 1
39.880	26	3 2 1
40.888	58	3 4 0
41.646	8	4 1 1
43.359	54	6 0 0
44.414	22	4 2 1
44.568	24	3 3 1
44.637	8	5 3 0
45.270	15	0 4 1
45.340	19	4 4 0
45.878	17	1 4 1
45.971	7	2 5 0
46.369	5	5 0 1
46.912	7	6 2 0
47.233	14	5 1 1
48.749	6	4 3 1
51.866	9	7 1 0
52.778	19	0 5 1
53.322	28	1 5 1
53.443	29	6 1 1
53.761	19	5 3 1
54.375	5	4 4 1
54.929	23	2 5 1
57.602	7	5 5 0
59.054	21	5 4 1
59.292	49	1 0 2
59.485	33	6 3 1
60.194	5	7 1 1
61.544	13	1 6 1
62.348	7	7 2 1

Appendix C

C.1 Reference FWHM for calculation of nanograin size and strain

Table C.1 FWHM for LaB_6 phase obtained from Rigaku Rotaflex D/Max B powder diffractometer.

2θ (deg)	FWHM (deg)
21.2096	0.1218
30.2462	0.1201
37.3108	0.1068
43.3815	0.1023
48.8393	0.1045
53.8731	0.1065
63.1106	0.1081
67.4431	0.1071
71.6428	0.1046
75.7425	0.1086
79.7728	0.1036
83.7515	0.1078
87.7014	0.1102

Table C.2 Reference FWHM for Al phase used in XRD analysis of data from Rigaku Rotaflex D/Max B powder diffractometer.

2θ (deg)	FWHM (deg)
38.472	0.1068
44.738	0.1023
65.133	0.1071
78.227	0.1036
82.435	0.1078

Table C.3 Reference FWHM for Mg phase used in XRD analysis of data from Rigaku Rotaflex D/Max B powder diffractometer.

2θ (deg)	FWHM (deg)
32.1958	0.1201
34.4100	0.1068
36.6362	0.1068
47.8454	0.1045
57.4037	0.1065
63.0930	0.1081
67.3487	0.1071
68.6602	0.1071
70.0346	0.1046
72.5208	0.1046
77.8543	0.1036
81.5491	0.1078

Table C.4 Reference FWHM for MgH_2 phase used in XRD analysis of data from Rigaku Rotaflex D/Max B powder diffractometer.

2θ (deg)	FWHM (deg)
27.9970	0.1201
35.8110	0.1068
39.9715	0.1023
54.6887	0.1065
57.7515	0.1065
61.4097	0.1081
65.3521	0.1071
68.7521	0.1071
69.7990	0.1046
75.7547	0.1086
83.5337	0.1078
86.0697	0.1102
89.2333	0.1102

Table C.5 Reference FWHM for MgB_2 phase used in XRD analysis of data from Rigaku Rotaflex D/Max B powder diffractometer.

2θ (deg)	FWHM (deg)
25.265	0.1218
33.482	0.1201
42.411	0.1023
51.884	0.1045
59.884	0.1065
63.171	0.1081
66.043	0.1071
70.401	0.1046
76.123	0.1086
83.189	0.1078

Table C.6 FWHM for LaB_6 phase obtained from Bruker D8 powder diffractometer.

2θ (deg)	FWHM (deg)
21.2096	0.1695
30.2462	0.1656
37.3108	0.1656
43.3815	0.1673
48.8393	0.1673
53.8731	0.1534
63.1106	0.1662
67.4431	0.1662
71.6428	0.1621
75.7425	0.1604
79.7728	0.1715
83.7515	0.1711
87.7014	0.1711

Table C.7 Reference FWHM for Al phase used in XRD analysis of data from Bruker D8 powder diffractometer.

2θ (deg)	FWHM (deg)
38.472	0.1656
44.738	0.1733
65.133	0.1534
78.227	0.1604
82.435	0.1715

Table C.8 Reference FWHM for MgH_2 phase used in XRD analysis of data from Bruker D8 powder diffractometer.

2θ (deg)	FWHM (deg)
27.9970	0.1695
35.8110	0.1656
39.9715	0.1656
54.6887	0.1673
57.7515	0.1673
61.4097	0.1534
65.3521	0.1662
68.7521	0.1662
69.7990	0.1621
75.7547	0.1604
83.5337	0.1715
86.0697	0.1711
89.2333	0.1711

Table C.9 Reference FWHM for $Mg(AlH_4)_2$ phase used in XRD analysis of data from Bruker D8 powder diffractometer.

2θ (deg)	FWHM (deg)
24.9975	0.1218
34.5772	0.1201
36.6795	0.1068
43.1249	0.1023
51.2871	0.1045
59.2843	0.1065
61.9145	0.1081
63.3356	0.1081
72.8556	0.1046
78.3069	0.1036
80.8397	0.1036

C.2 Calculation of nanograin size and strain

Using MgH_2 phase as an example, crystallite size (L) and strain (e) are calculated as the following steps by Eq. 6.1:

1) Covert values B, b and θ (Table C.7) from degree to radian.

2) Use Eq. C1 to calculate δ(2θ) value.

$$\delta(2\theta) = B\left(1 - \frac{b^2}{B^2}\right) \tag{C.1}$$

3) Calculate $\frac{\delta^2(2\theta)}{\tan^2\theta}$ and $\frac{\delta(2\theta)}{\tan\theta\sin\theta}$ (Eq. 7.1) for each plane/peak (Table C.7).

4) Perform a least square fit (linear regression) to $\frac{\delta^2(2\theta)}{\tan^2\theta}$ plotted against $\frac{\delta(2\theta)}{\tan\theta\sin\theta}$ for all of the planes/peaks of a sample measured at a certain milling time (Fig. C.1).

5) From the slope $\frac{\lambda}{L}$ and the intercept $16e^2$, the values L and e can be determined.

6) From Fig. C.1, $\frac{\lambda}{L} = 0.002$ and $16e^2 = 5\times10^{-6}$. As a result, nanograin size and strain for MgH_2 phase are 77 (nm) and 5.6×10^{-4}, respectively.

Table C.10 List of values B, b, θ, δ(2θ), $\delta^2(2\theta)/\tan^2(\theta_0)$ and $\delta(2\theta)/\tan(\theta_0)\sin(\theta_0)$ for the MgH_2 phase in the milled powder.

2θ (deg)	B(deg)	b(deg)	θ (deg)	θ(rad)	B(rad)	b(rad)	δ(2θ)	$\delta^2(2\theta)/\tan^2(\theta)$	$\delta(2\theta)/\tan(\theta)\sin(\theta)$
27.913	0.1888	0.1201	13.9565	0.243587	0.003295	0.002096	0.001962	6.23E-05	0.032729
35.7335	0.1937	0.1068	17.86675	0.311834	0.003381	0.001864	0.002353	5.33E-05	0.023792
39.8963	0.1987	0.1023	19.94815	0.348161	0.003468	0.001785	0.002549	4.93E-05	0.020583
54.6339	0.2015	0.1065	27.31695	0.476771	0.003517	0.001859	0.002534	2.41E-05	0.010692
57.6958	0.19	0.1065	28.8479	0.503491	0.003316	0.001859	0.002274	1.7E-05	0.008557
61.3555	0.2276	0.1081	30.67775	0.535428	0.003972	0.001887	0.003076	2.69E-05	0.010164
65.3219	0.12	0.1071	32.66095	0.570041	0.002094	0.001869	0.000426	4.42E-07	0.001232
68.7059	0.2426	0.1071	34.35295	0.599572	0.004234	0.001869	0.003409	2.49E-05	0.008838
69.7561	0.2593	0.1046	34.87805	0.608737	0.004526	0.001826	0.003789	2.96E-05	0.009507
75.7243	0.2498	0.1086	37.86215	0.660819	0.00436	0.001895	0.003536	2.07E-05	0.00741
83.4965	0.2373	0.1078	41.74825	0.728644	0.004142	0.001881	0.003287	1.36E-05	0.005531

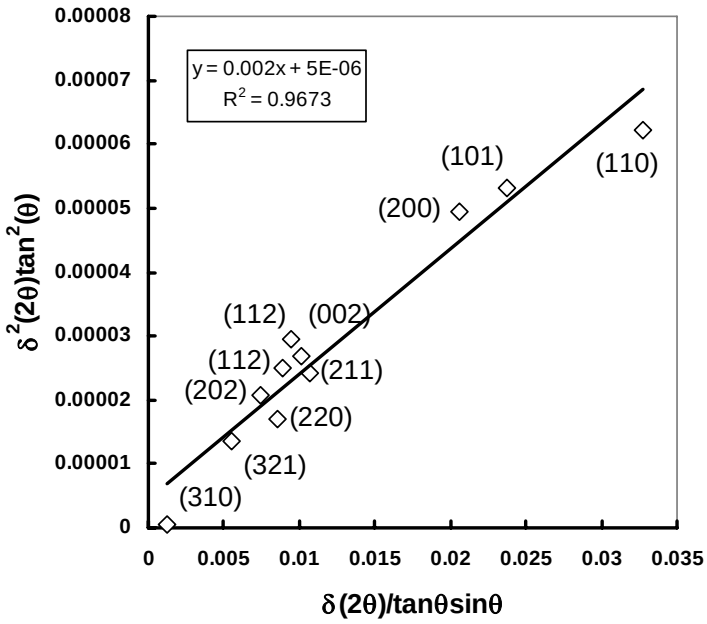

Fig. C.1 Nanograin size/strain separation according to the Gaussian/Cauchy approximation (Eq. 6.1) for the MgH_2 phase.

Appendix D SEM/BSE micrographs

D.1 As-received materials

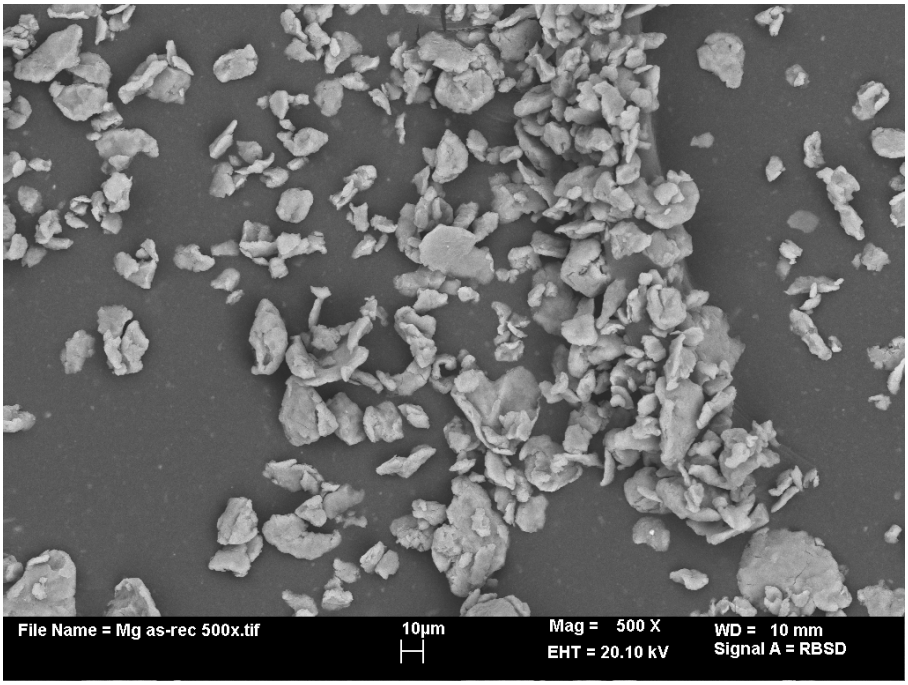

Fig. D.1 BSE micrograph of the elemental Mg powder.

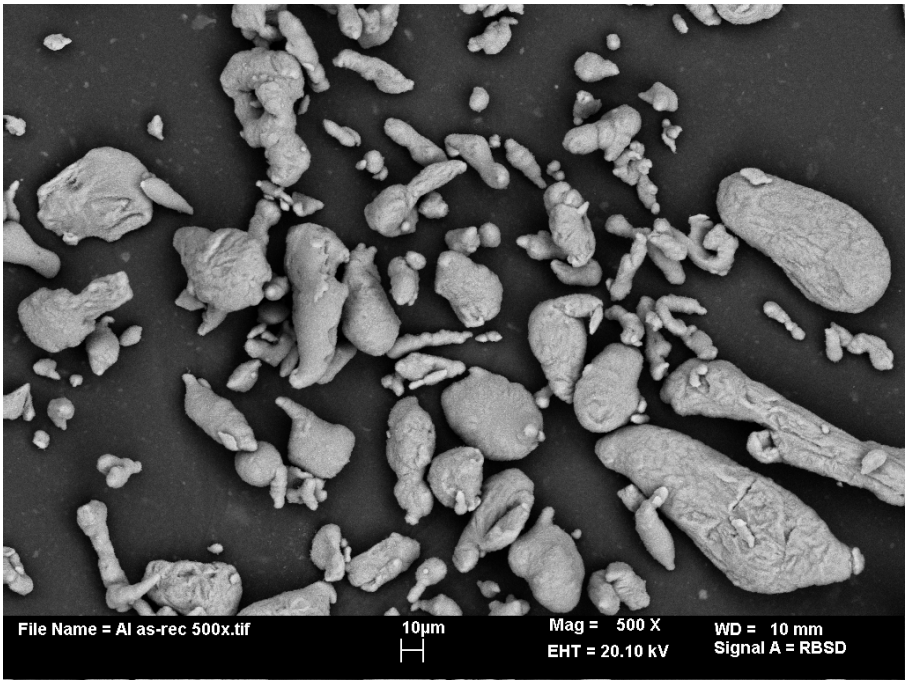

Fig. D.2 BSE micrograph of the elemental Al powder.

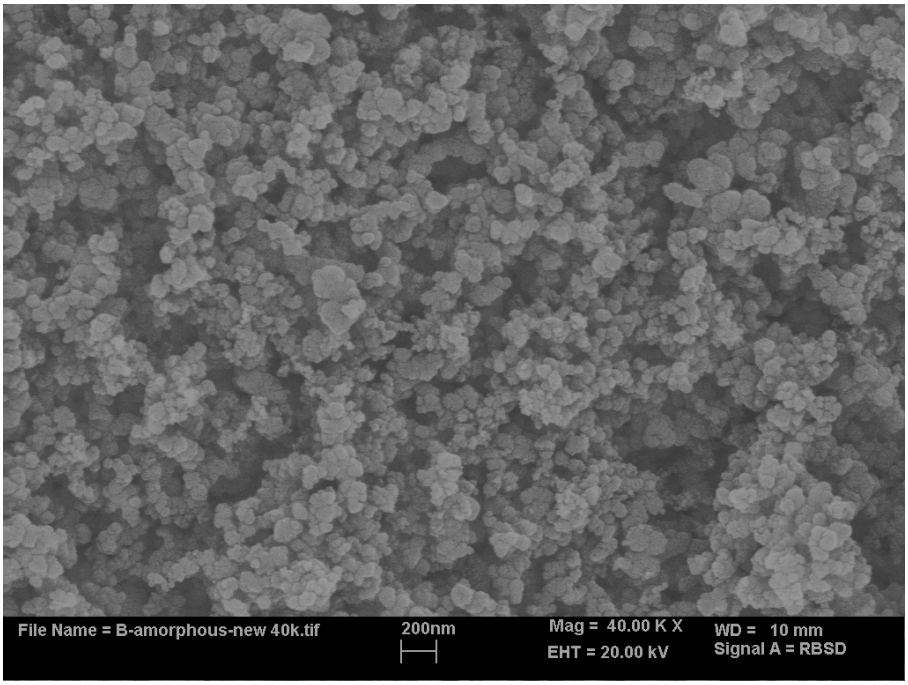

Fig. D.3 BSE micrograph of the amorphous boron powder.

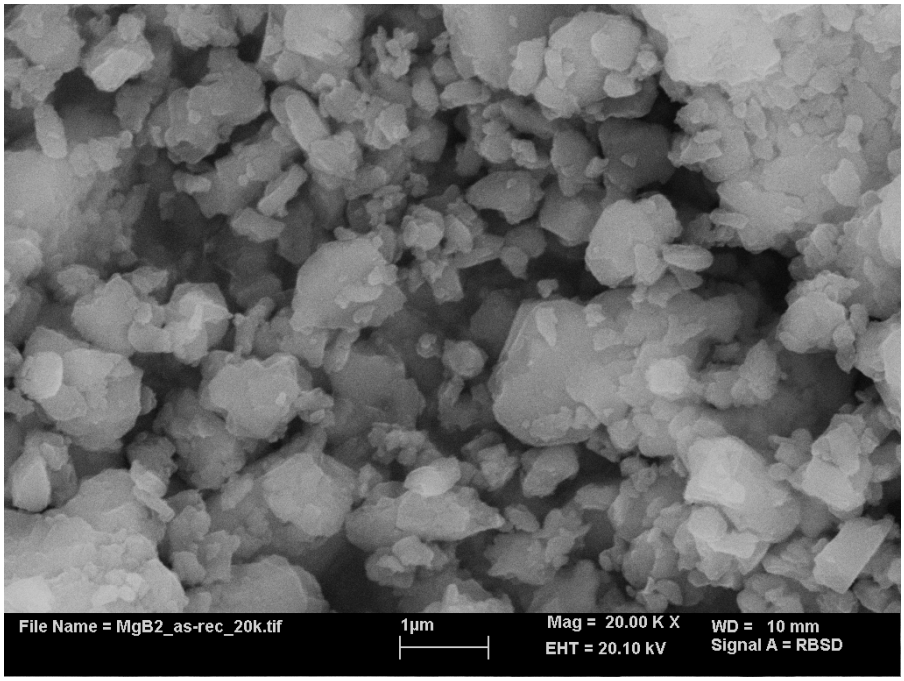

Fig. D.4 BSE micrograph of the as-received MgB_2 powder.

D.2 Mg7H powders

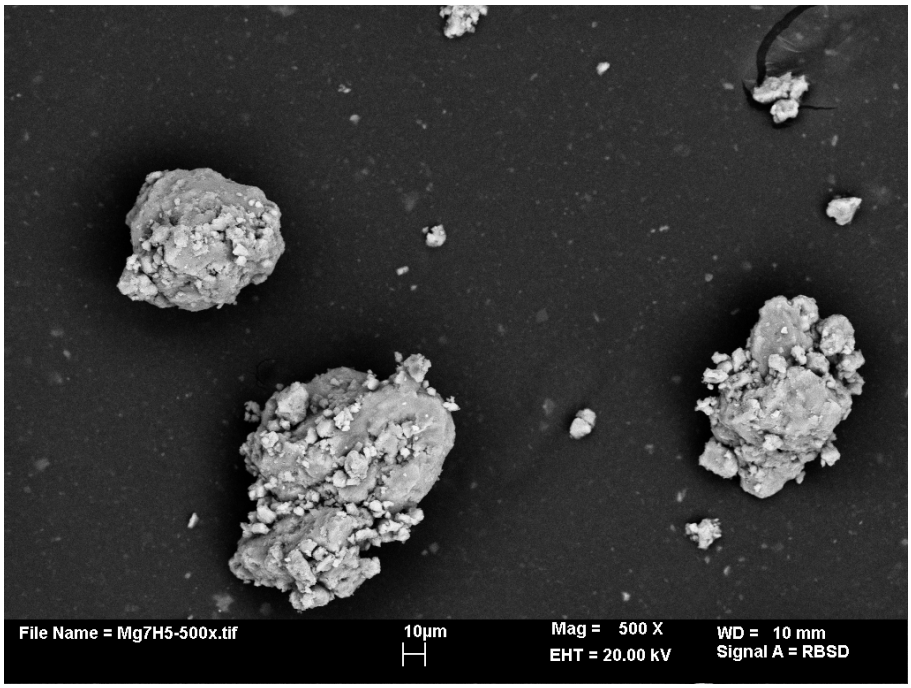

(a) 5h

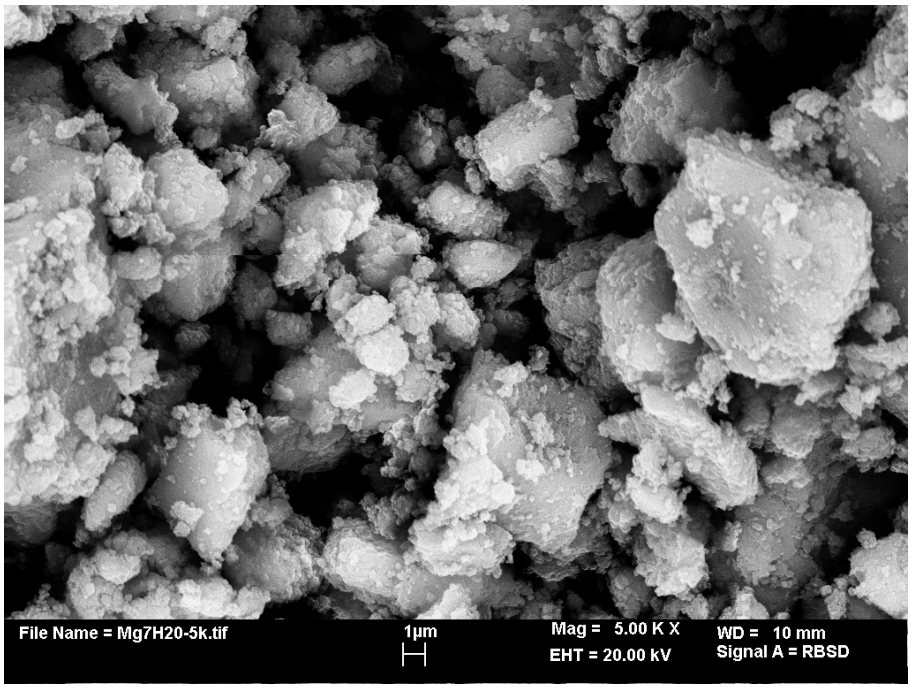

(b) 20h

Fig. D.5 BSE micrographs of Mg7H powder after milling for (a) 5h, (b) 20h, (c) 50h, and (d) 100h under HES mode.

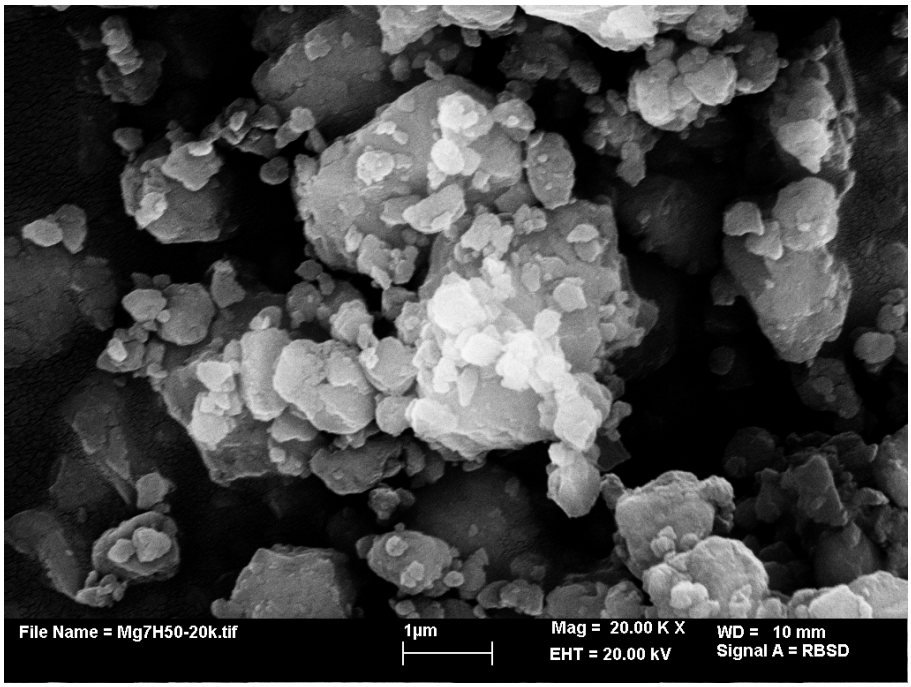

(c) 50h

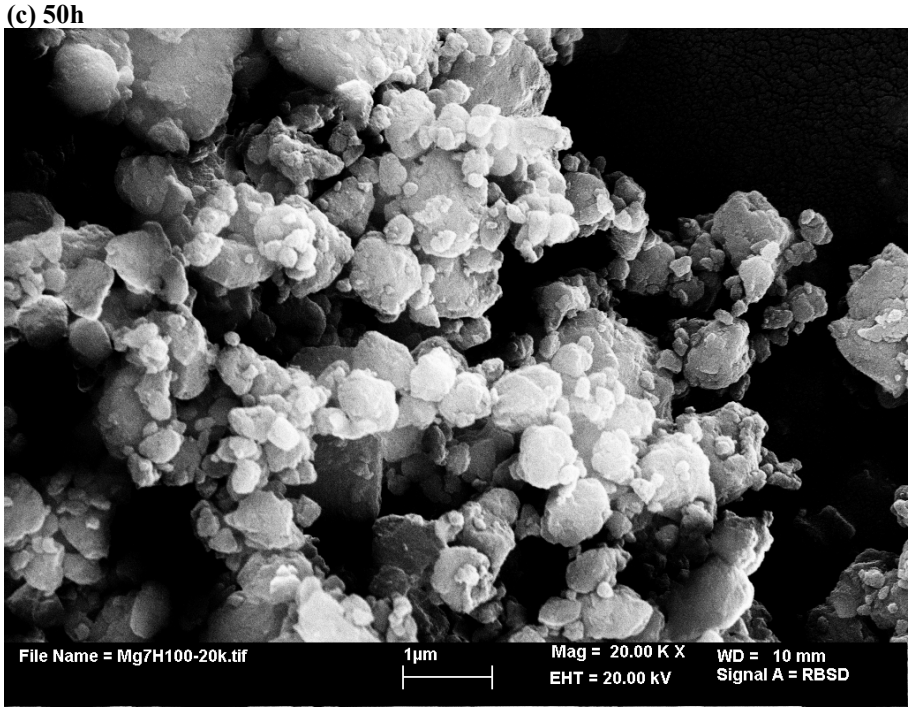

(d) 100h

Fig. D.5 cont'd

Appendix E Amount of absorbed hydrogen during milling process

Table E.1 Amount of hydrogen in Mg-H powder calculated from pressure drop during milling and from DSC analysis

Powder	Milling time (h)	wt% H_2 (calculated from pressure drop)	wt% H_2 (estimated by DSC)
Mg1H	5	0.5	0.4
	20	3.4	2.7
Mg4H	150	5.7	6.2
Mg5H	150	6.7	5.7
Mg6H2	150	5.0	6.0
Mg7H	5	0.9	0.8
Mg7H	20	3.2	3.7
Mg7H	50	4.9	5.1
Mg7H	100	5.3	5.6
Mg7H	150	5.3	5.7
Mg9H2	60	5.6	5.7
Mg10H1	60	5.7	5.5
Mg11H	100	5.6	5.4
Mg12H	30	6.7	6.5
Mg13H	30	6.0	6.6
Mg14H	30	6.5	6.8

Table E.2 Absorbed hydrogen in Mg-Al-H powders calculated from pressure drop during milling and from DSC analysis.

Powder	Milling time (h)	wt% H_2 (calculated from pressure drop)	wt% H_2 (estimated by DSC)
A1H	1	0.2	0
	10	1.5	1.2
A2H	10	0.4	0.5
	50	1.7	2.0
	100	1.9	2.5
	200	1.9	1.9
A3H	10	0	0.1
	50	1.8	2.4
	100	2.8	2.6
	200	2.8	2.5
A5H	50	1.8	1.1
A10H	30	2.1	1.4

Table E.3 weight percent of hydrogen in B6H and B7H/LES powders calculated from pressure drop, DSC analysis and desorption test.

Alloy description	Milling time (h)	wt% H_2 (calculated from pressure drop)	wt% H_2 (estimated by DSC)	wt% H_2 (estimated by desorption test)
B15H	200	3.2	2.7	2.6
B14H	50	2.5	2.7	2.9
	200	2.6	-	1.4

Appendix F Summary of XRD analysis results

F.1 Mg-H system

Table F.1 Nanograin size and strain of β-MgH_2 in the milled Mg-H powders.

Powder	Nanograin size, L and strain, e of β-MgH_2				
	Milling time (h)	L (nm)	e	R^2	No of XRD peaks
Mg1H	5	39	0	0.763	4
	20	13	0	0.909	5
	50	9	0	0.991	6
	100	7	0	0.988	6
	150	6	0	0.99	6
Mg7H	5	42	3.5×10^{-4}	0.949	7
	20	15	1.4×10^{-3}	0.961	6
	50	9	0	0.991	7
	100	8	0	0.993	7
	150	7	0	0.981	7
Mg6H	150	8	0	0.979	9
Mg2H	100	8	0	0.979	4
	200	8	0	0.978	4
Mg4H	150	8	0	0.989	5
Mg5H	150	8	0	0.990	5
Mg9H	60	8	0	0.968	5
Mg10H	60	7	0	0.990	5
Mg11H	100	8	0	0.983	8
Mg12H	30	9	0	0.994	10
Mg13H	30	9	0	0.988	10
Mg14H	30	9	0	0.986	9

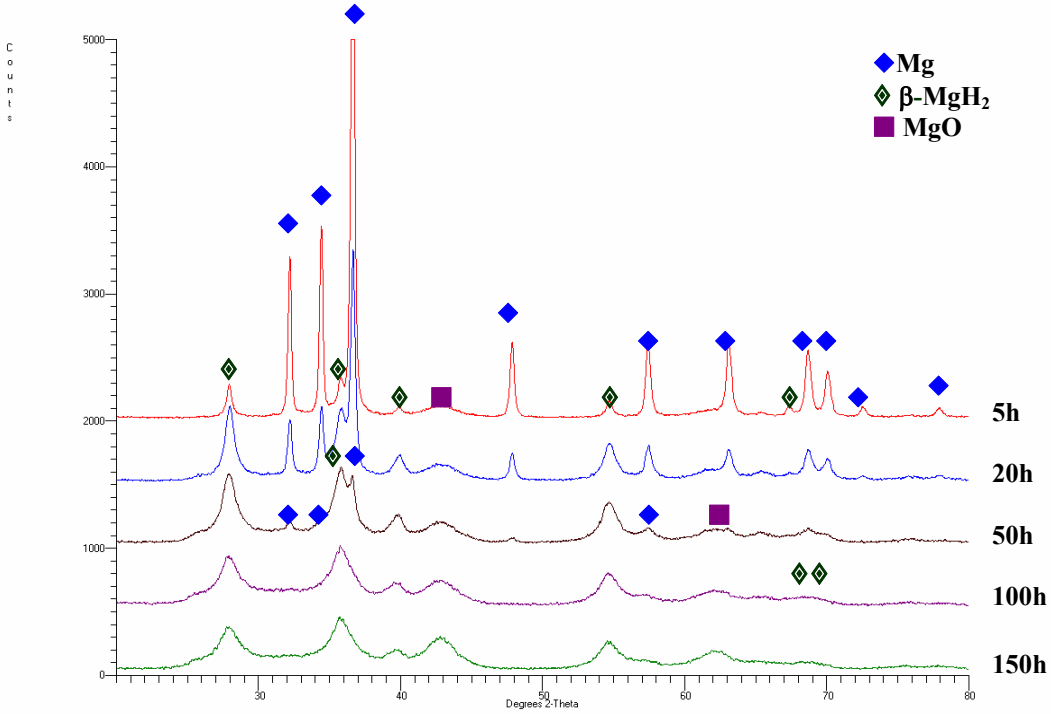

Fig. F.1 XRD pattern evolution of the Mg1H powders milled under HES mode.

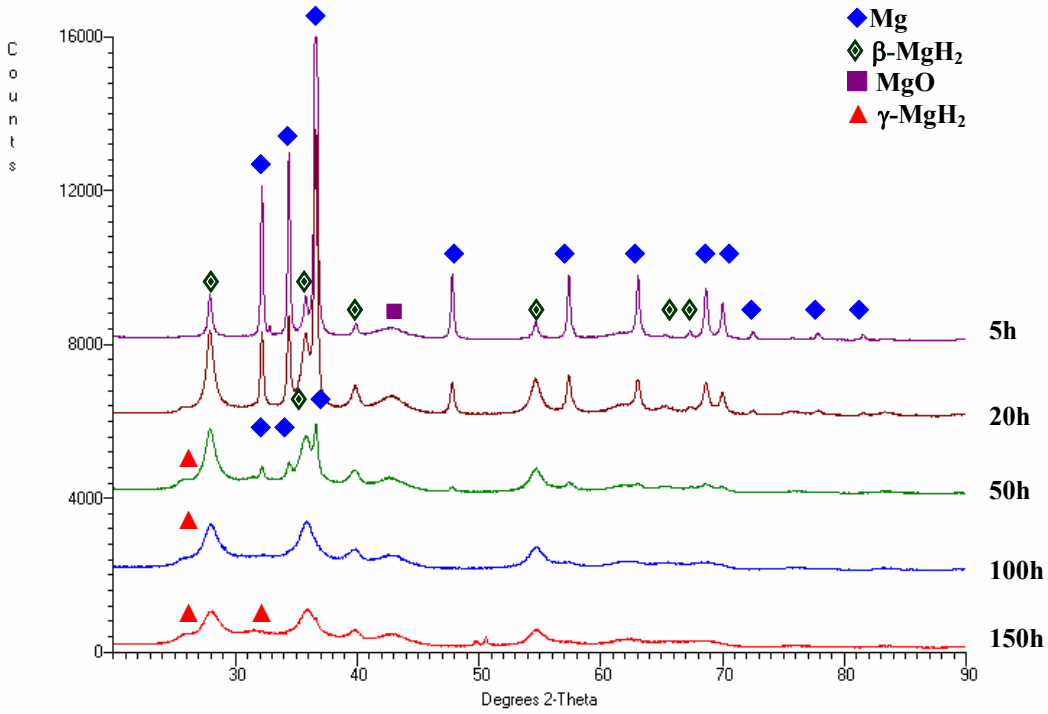

Fig. F.2 XRD pattern evolution of the Mg7H powders milled under HES mode.

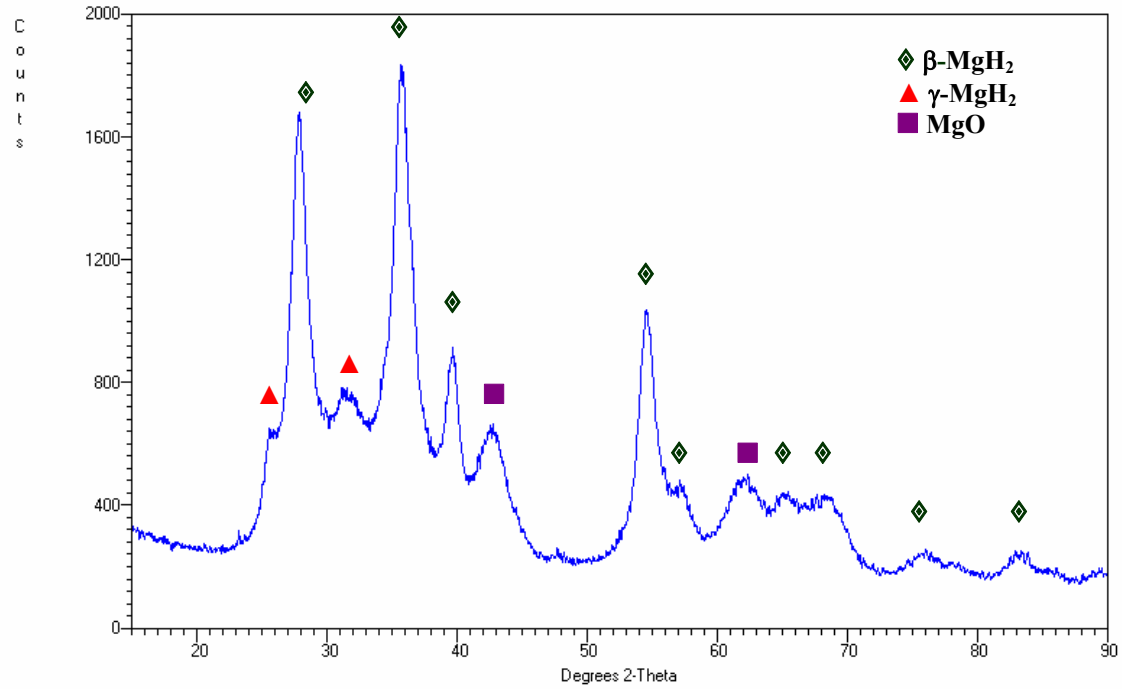

Fig. F.3 XRD pattern of the Mg6H powder after milling for 150h under HES mode.

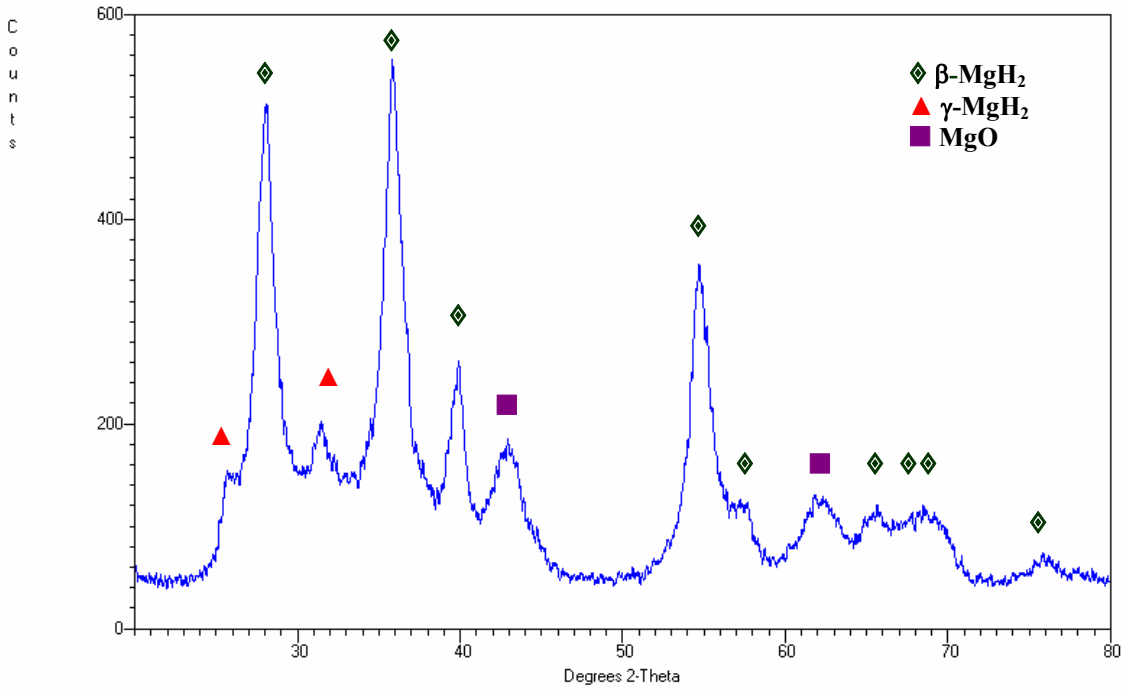

Fig. F.4 XRD pattern of the Mg2H powder after milling for 100h under IMP2 mode.

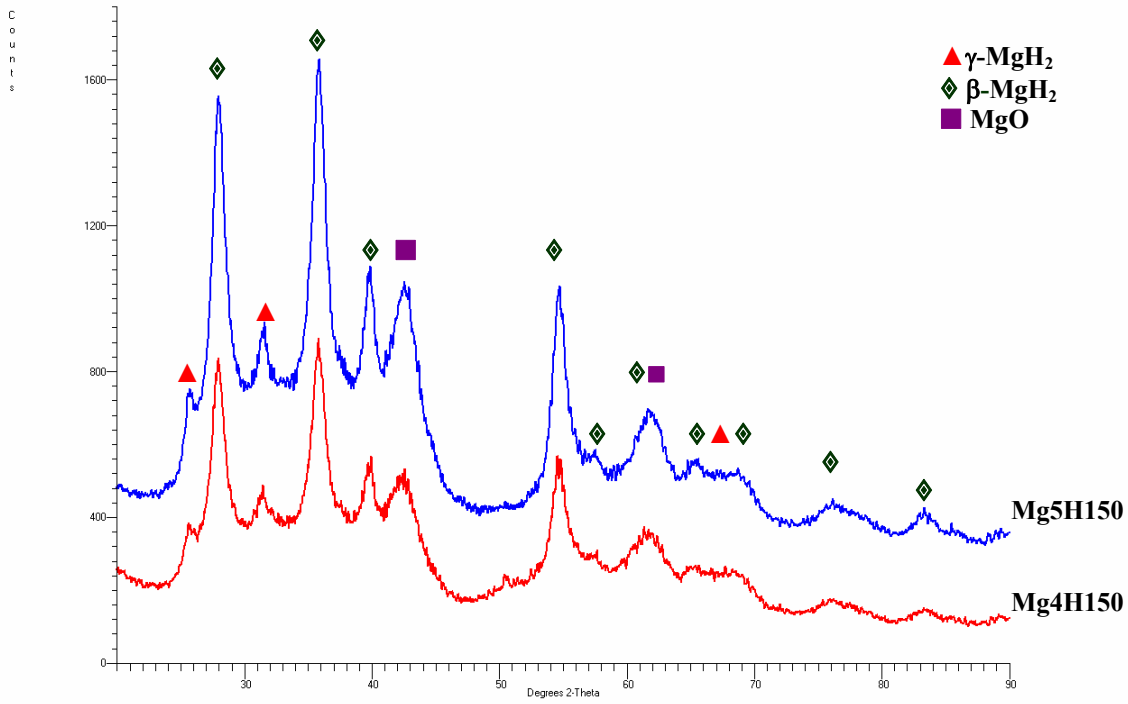

Fig. F.5 XRD patterns of the Mg4H and Mg5H powders after milling for 150h under IMP2 mode.

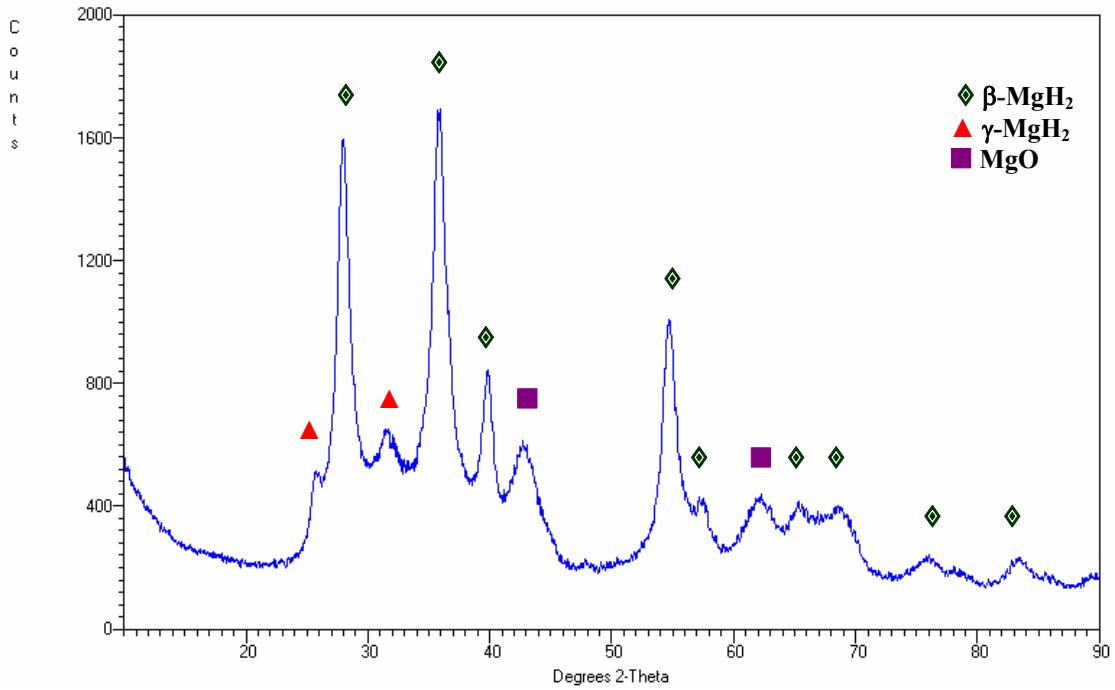

Fig. F.6 XRD pattern of the Mg9H powder after milling for 60h under IMP710 mode.

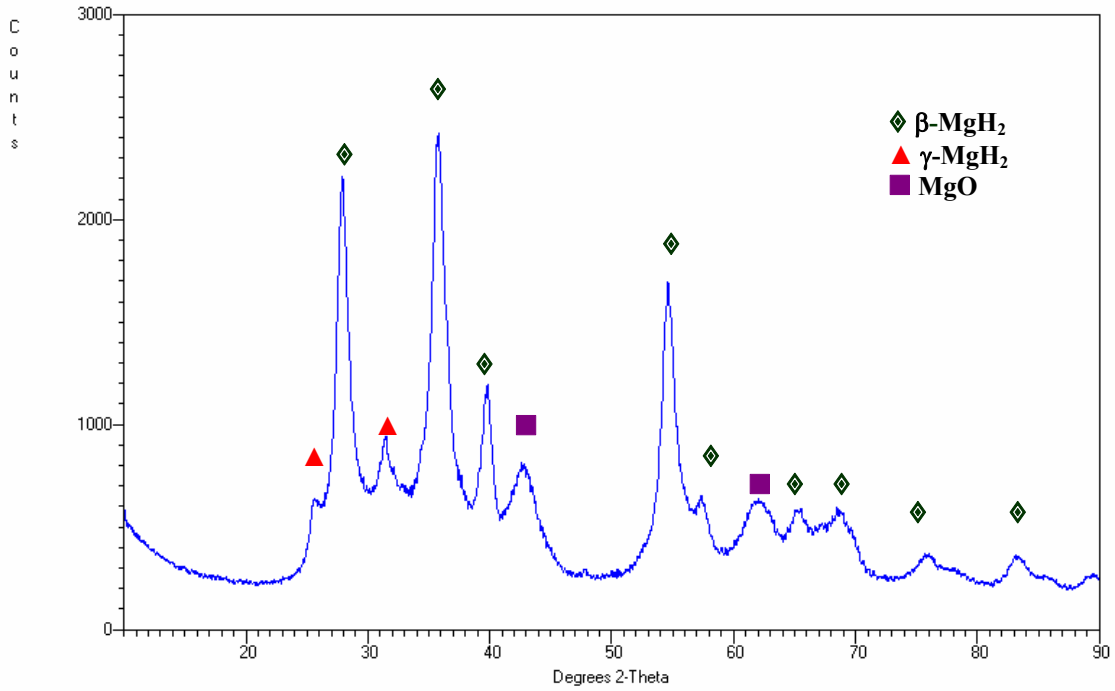

Fig. F.7 XRD pattern of the Mg10H powder after milling for 60h under IMP710 mode.

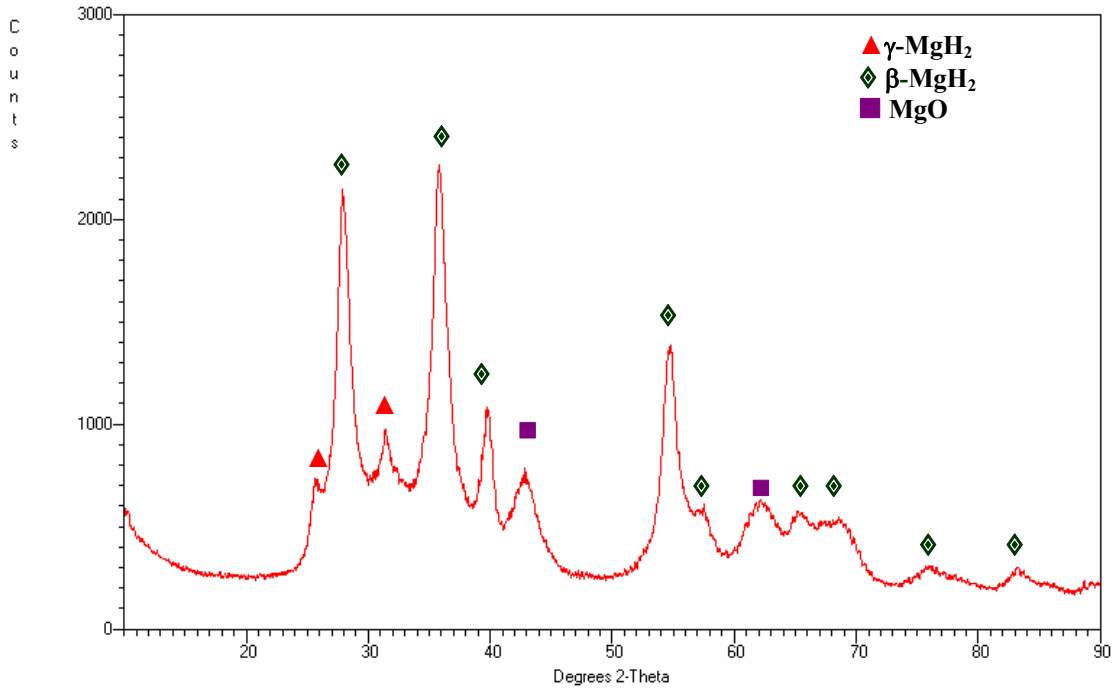

Fig. F.8 XRD pattern of the Mg11H powder after milling for 100h under IMP710 mode.

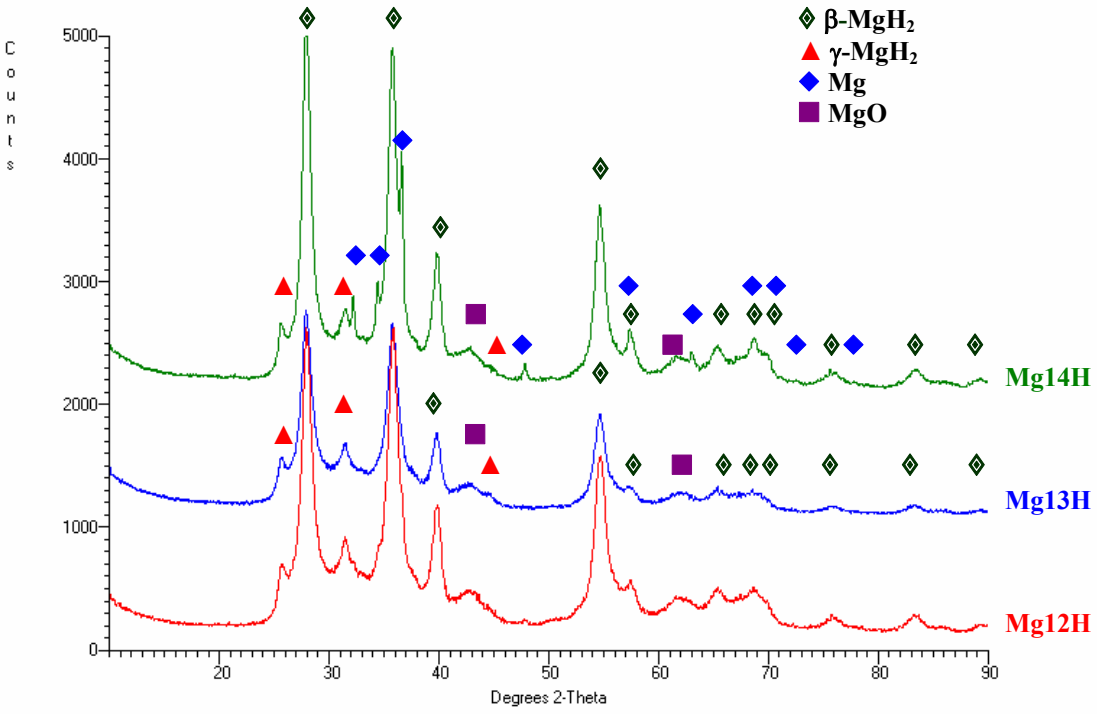

Fig. F.9 XRD patterns of the Mg12H-Mg14H powders after milling for 30h under IMP68 mode.

F.2 Mg-Al-H system

F.2.1 Annealed A1H powders

Table F. 2 Lattice parameter of Al and Al(Mg) solid solution present in the annealed A1H powders.

Powder	Lattice parameter (nm) (FCC)
A1H1-350-40-20	0.4069±0.0014*
A1H5-350-40-20	0.4070±0.0013*
A1H1-100-40-100	0.4035±0.0014
A1H5-100-40-100	0.4043±0.0015*
A1H270-100-45-100	0.4034±0.0015

***Al(Mg) solid solution**

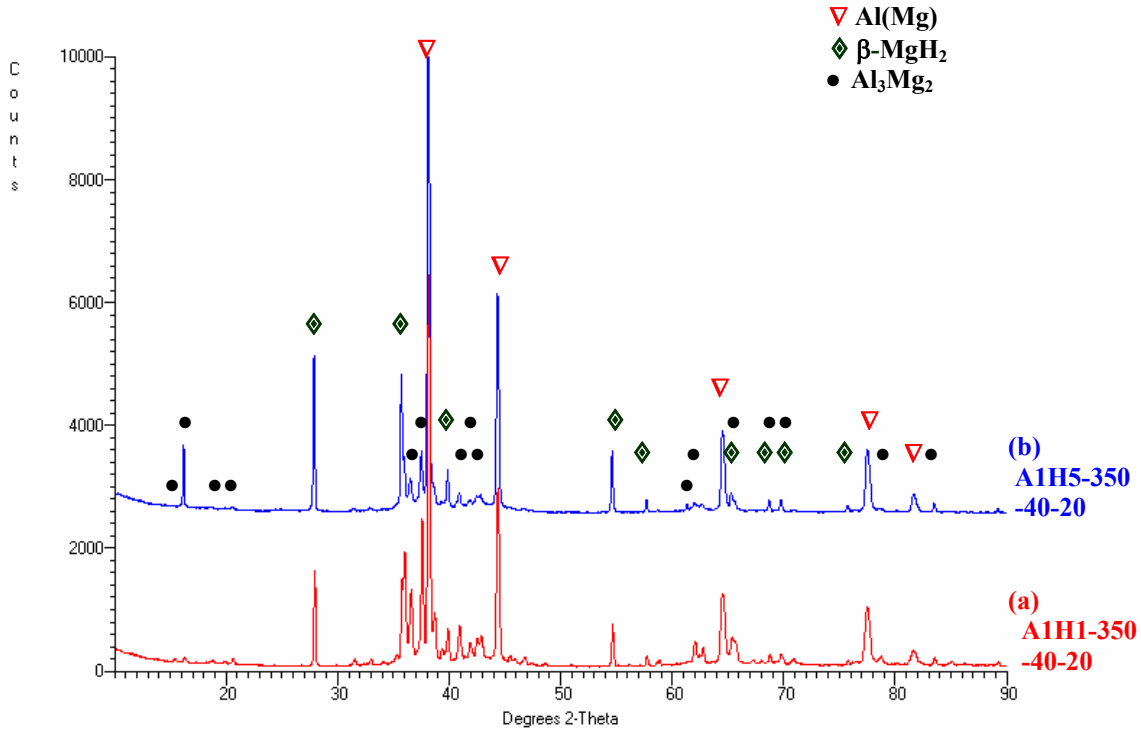

Fig. F. 10 XRD patterns of A1H powders under different annealing conditions: (a) 1h milled powder after annealing at 350°C under 4.0 MPa of H_2 for 20h, (b) 5h milled powder after annealing at 350°C under 4.0 MPa of H_2 for 20h, (c) 1h milled powder after annealing at 100°C under 4.0 MPa of H_2 for 100h, (d) 5h milled powder annealing at 100°C under 4.0 MPa of H_2 for 100h, and (e) 270h milled powder after annealing at 100°C under 4.5 MPa of H_2 for 100h.

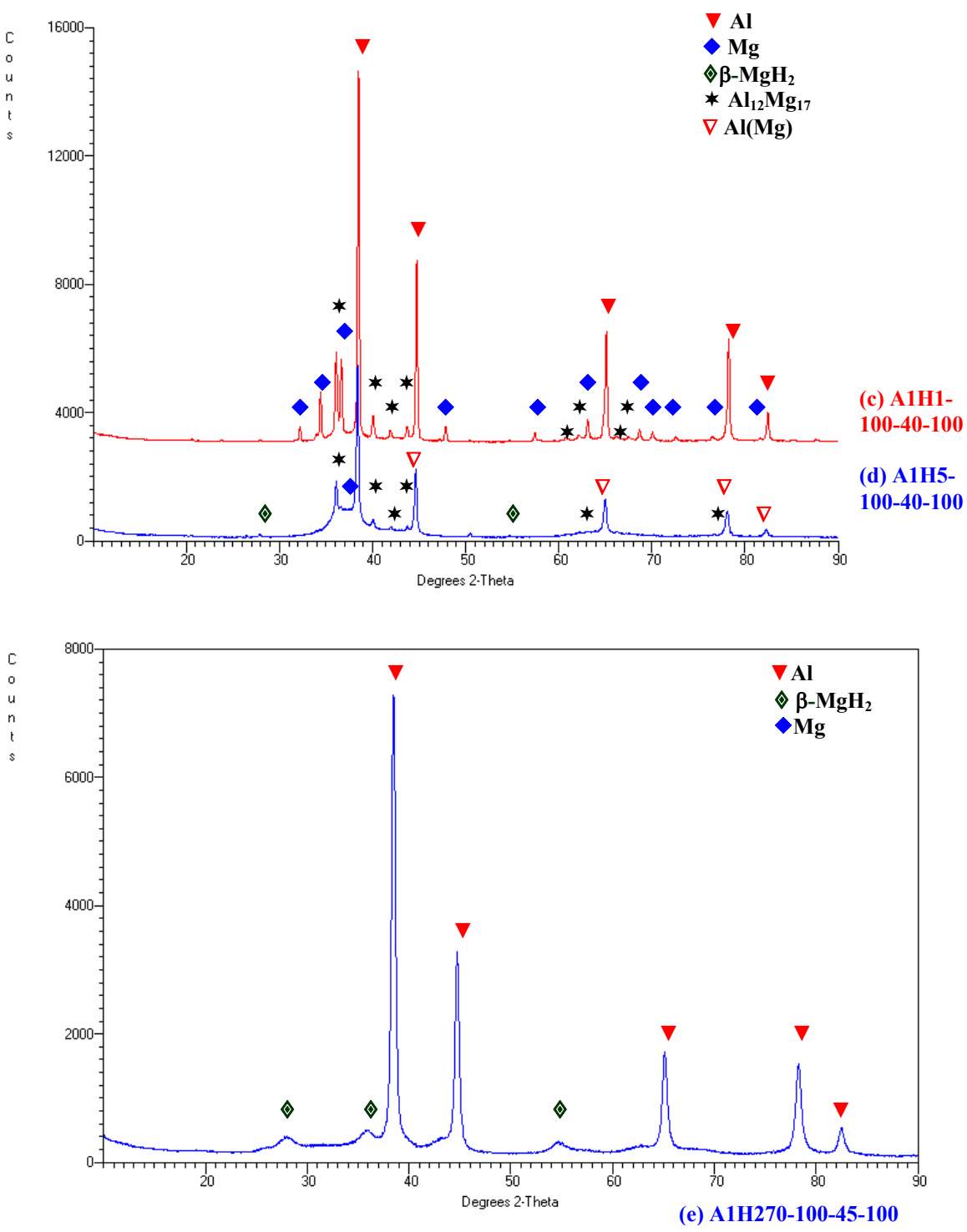

Fig. F. 10 cont'd

F.2.2 A5H and A10H powders

Table F. 3 Lattice parameter of Al in the as-milled and the annealed A10H and A5H powders.

Powder	Milling time (h)	Lattice parameter (nm) (FCC)
A5H50	50	0.4038±0.0014
A10H30	30	0.4039±0.0015
A5H50-260-43-144	-	0.4032±0.0018
A10H-350-40-20	-	0.4039±0.0015

Table F. 4 Lattice parameter of β-MgH_2 in the as-milled and the annealed A10H and A5H powders.

Powder	Milling time (h)	Lattice parameter (nm) (Tetragonal)	
		a	c
A5H50	50	0.4520±0.0119	0.3032±0.0033
A5H50-260-43-144	-	0.4520±0.0134	0.3034±0.0036
A10H30	30	0.4533±0.0019	0.3013±0.0011
A10H-350-40-20	-	0.4522±0.0017	0.3023±0.0007

Table F. 5 Nanograin size of Al in the as-milled and the annealed A10H and A5H powders.

Powder	Al nanograin size, L and strain, e				
	Milling time (h)	L (nm)	e	R^2	No. of XRD peaks
A5H50	50	20	0	0.848	5
A10H30	30	30	2.5×10^{-3}	0.971	5
A5H50-260-43-144	-	28	0	0.878	5
A10H-350-40-20	-	50	0	0.994	3

Table F. 6 Nanograin size of β-MgH_2 in the as-milled and the annealed A10H and A5H powders.

Powder	β-MgH_2 Nanograin size, L and strain, e				
	Milling time (h)	L (nm)	e	R^2	No. of XRD peaks
A5H	50	8	0	0.999	3
A10H	30	12	0	0.988	8
A5H50-260-43-144	-	23	1.9×10^{-3}	0.982	4
A10H-350-40-20	-	77	5.6×10^{-4}	0.945	10

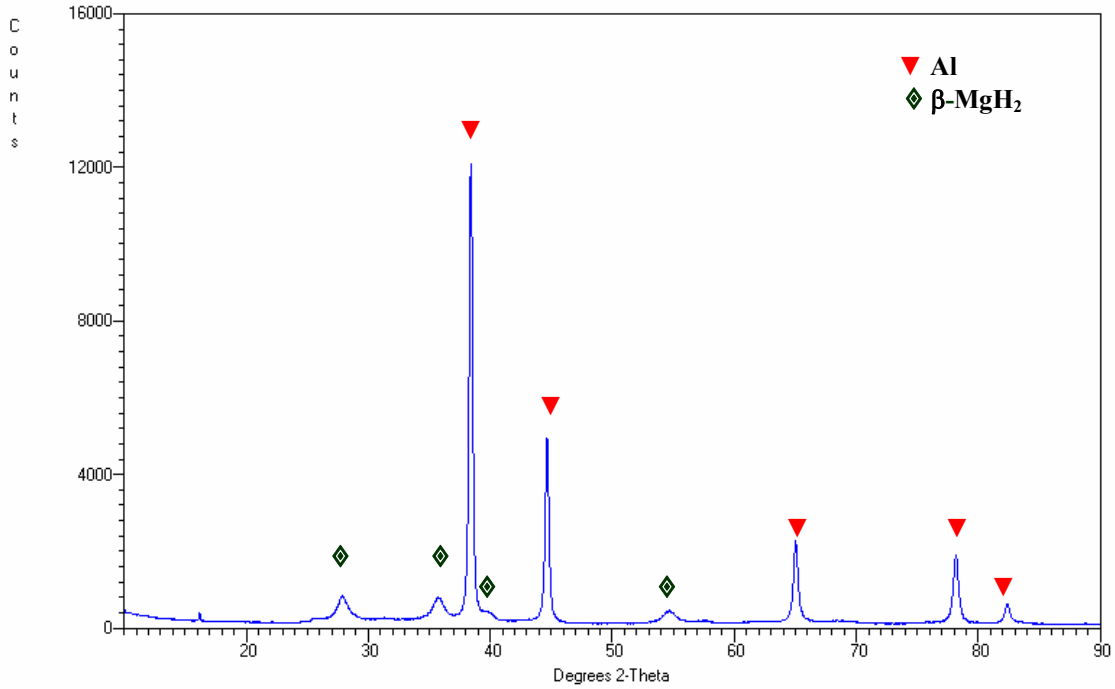

Fig. F. 11 XRD pattern of A10H30 powder milled using elemental Mg and Al as starting materials under higher impact mode (IMP68) with two magnets.

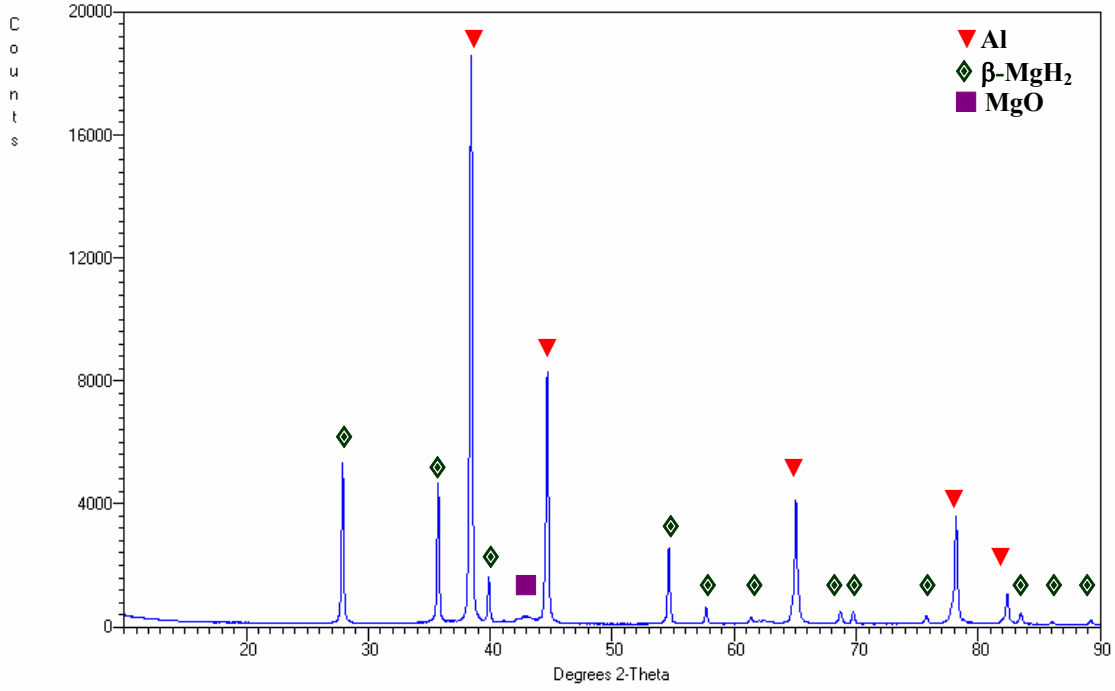

Fig. F. 12 XRD pattern of A10H30 powder after annealing at 350°C under 4MPa of hydrogen for 20h.

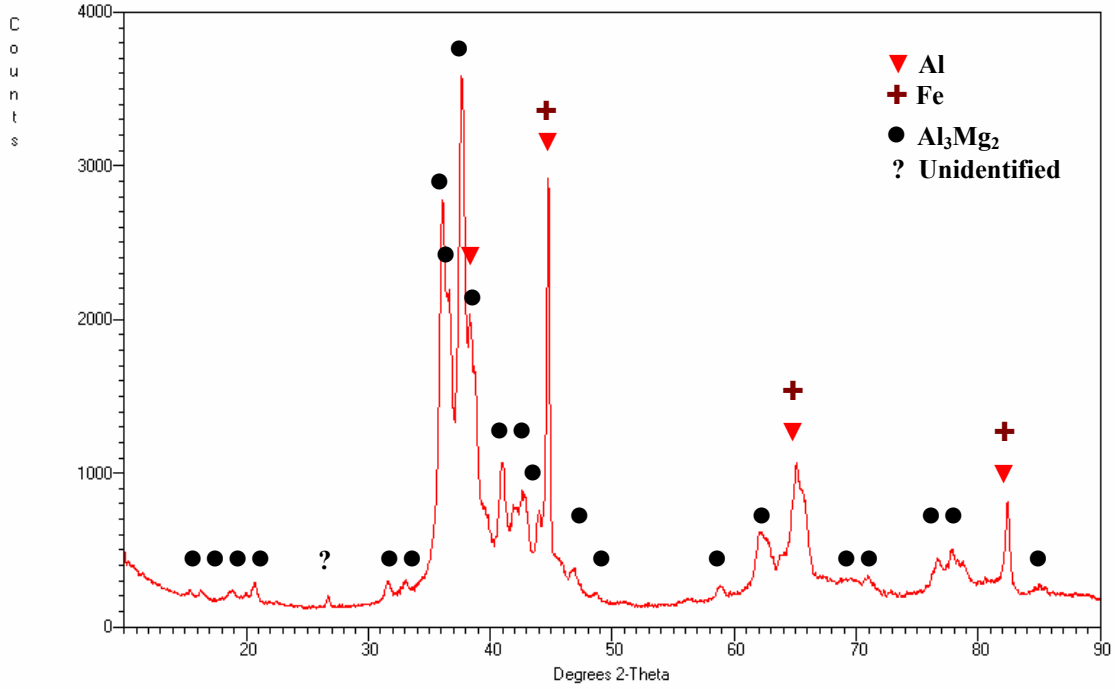

Fig. F.13 XRD pattern of the starting material used in A5H powders, which is a powder mixture of Mg-2Al cast ingot plus 10wt.%Fe after milling for 10h under argon in a SPEX ball mill.

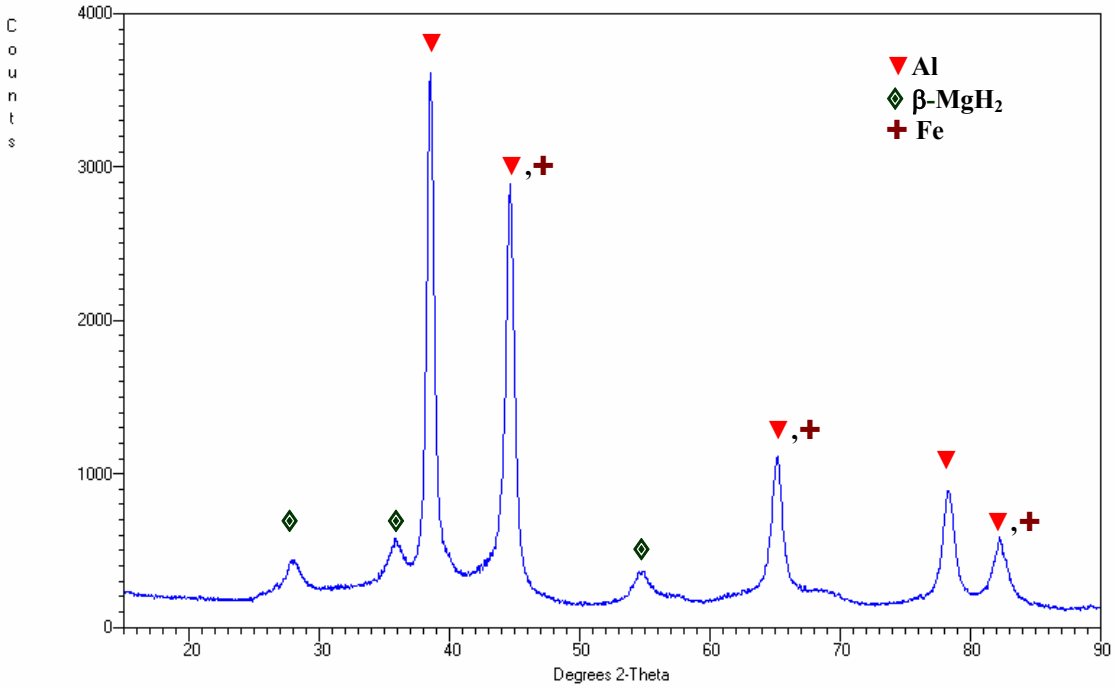

Fig. F.14 XRD pattern of A5H powders milled using Mg-2Al cast ingot +10wt.%Fe as starting material after milling for 50h.

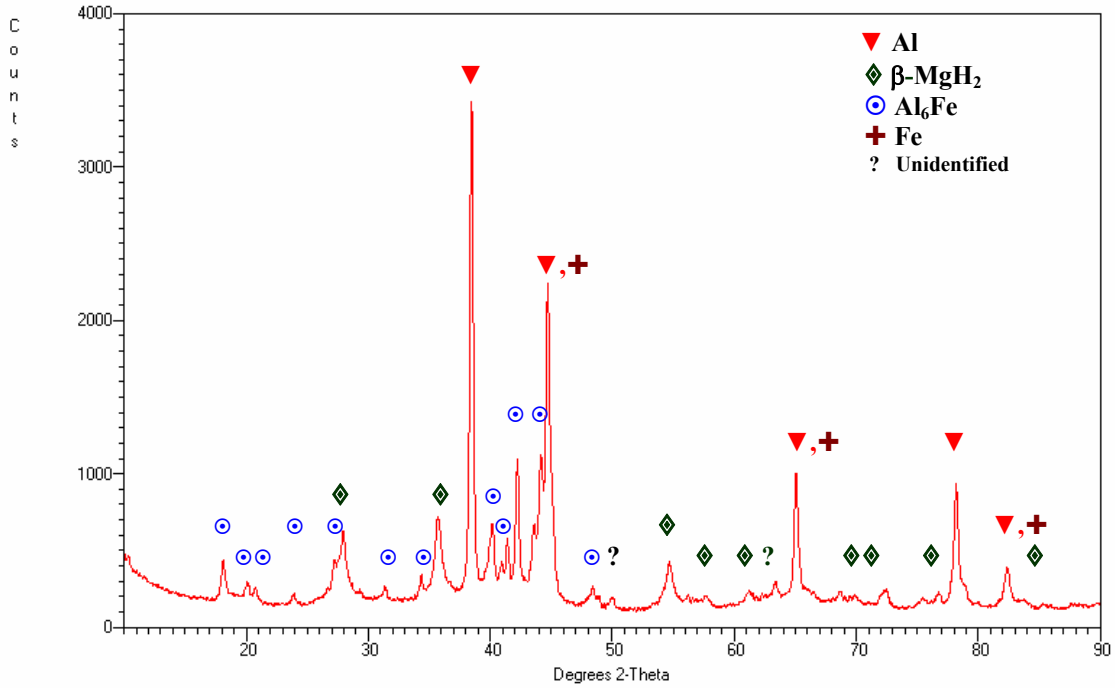

Fig. F.15 XRD patterns of A5H50 powder (milled 50h) after annealing at 260°C under 4.3MPa of hydrogen for 144h.

F.3 Mg-B-H system

F.3.1 B6H and B8H powders

Table F.7 Nanograin size and strain of β-MgH_2 phase in B6H and B8H powders.

Powder	β-MgH_2 Nanograin size, D and strain, e				
	Milling time (h)	D (nm)	e	R^2	No of XRD peaks
B6H	100	5	0	0.979	6
	200	5	0	0.989	6
B8H	100	9	$5x10^{-4}$	0.893	5

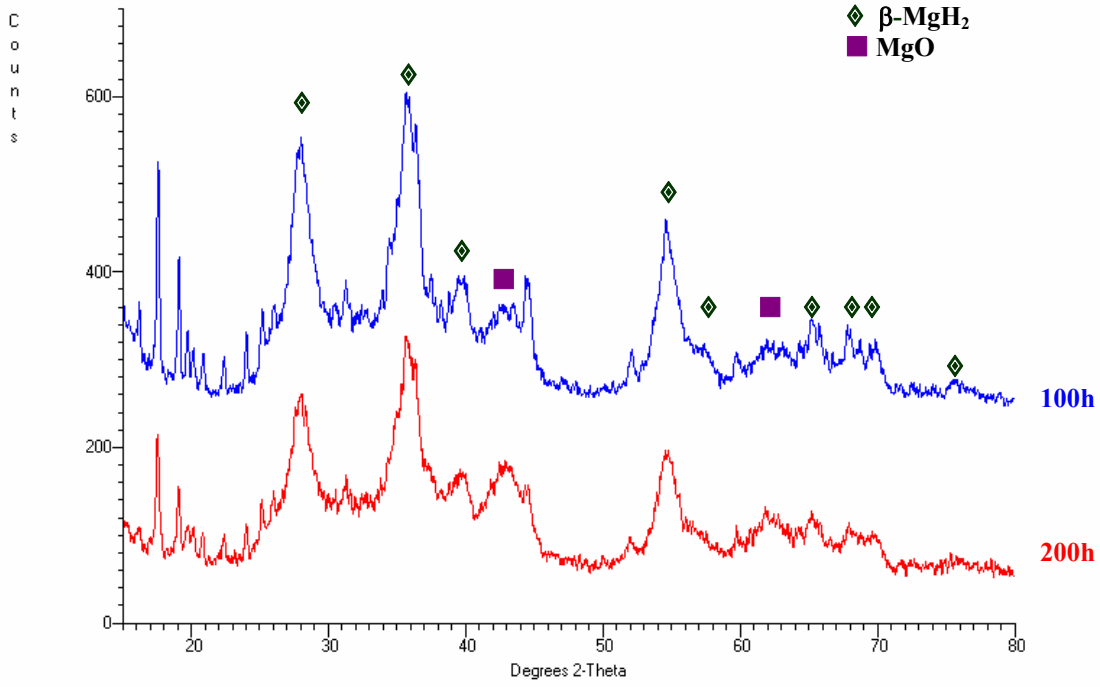

Fig. F.16 XRD patterns of B6H powders after milling for 100 and 200h under LES mode. Unmarked peaks belong to crystalline boron phase.

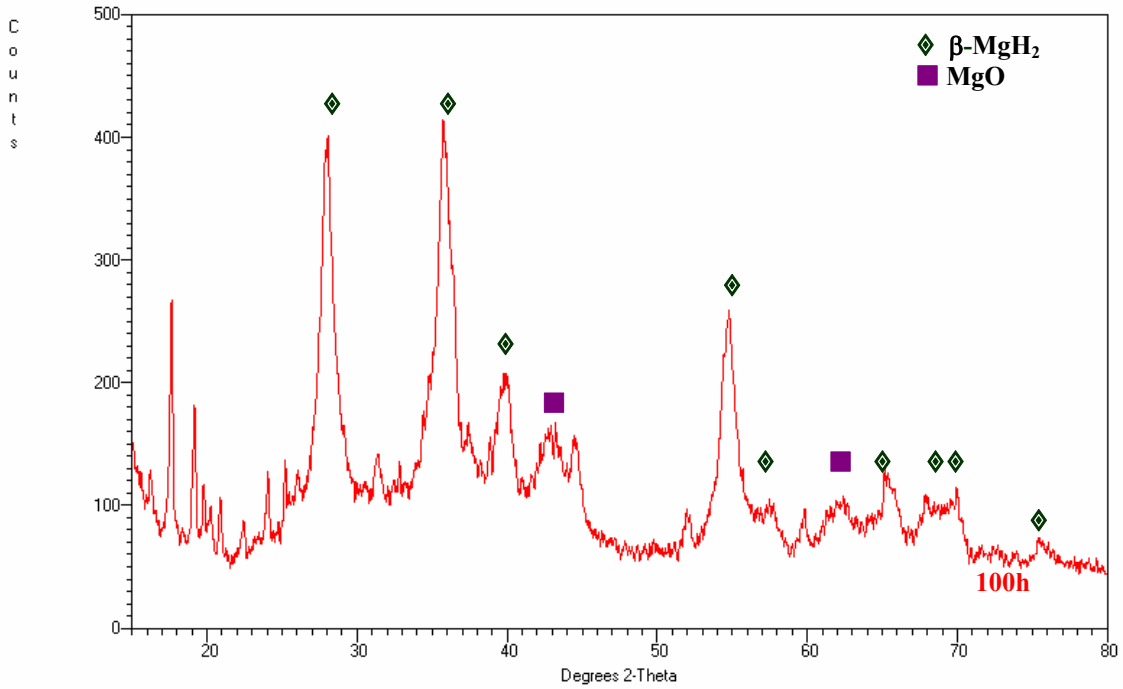

Fig. F.17 XRD pattern of B8H powders after milling for 100h under IMP2 mode. Unmarked peaks belong to crystalline boron phase.

F.3.2 B7H, B9H and B10H powders

Table F.8 Nanograin size and strain of β-MgH_2 phase in B7H, B9H and B10H powders.

Powder	β-MgH_2 Nanograin size, D and strain, e				
	Milling time (h)	D (nm)	e	R^2	No of XRD peaks
B7H	100	8	0	0.979	5
	200	5	0	0.982	4
B9H	100	8	0	0.984	5
B10H	200	7	0	0.901	9
	300	8	0	0.883	7
B10H300-126-46-24	-	7	0	0.956	8
B10H300-212-46-24	-	7	0	0.932	8

Table F.9 Nanograin size and strain of Mg phase in B7H and B9H powders.

Powder	Mg Nanograin size, D and strain, e				
	Milling time (h)	D (nm)	e	R^2	No of XRD peaks
B7H	100	25	$2.5x10^{-3}$	0.706	7
	200	4	0	0.963	4
B9H	100	18	$7x10^{-4}$	0.979	5

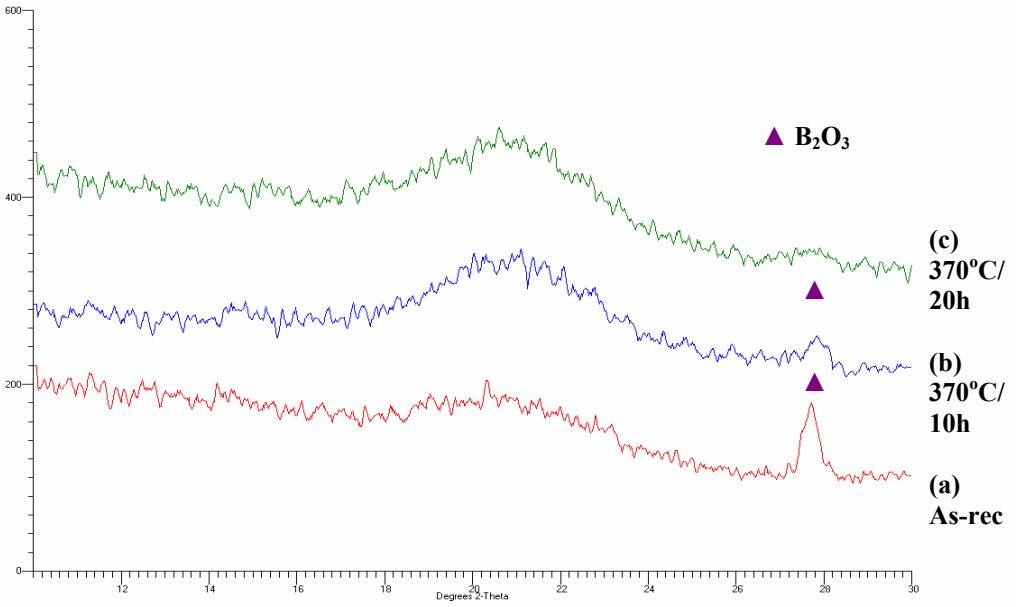

Fig. F.18 XRD pattern of (a) as-received amorphous boron powder and the same powder after annealing at 370°C for (b) 10h and (c) 20h.

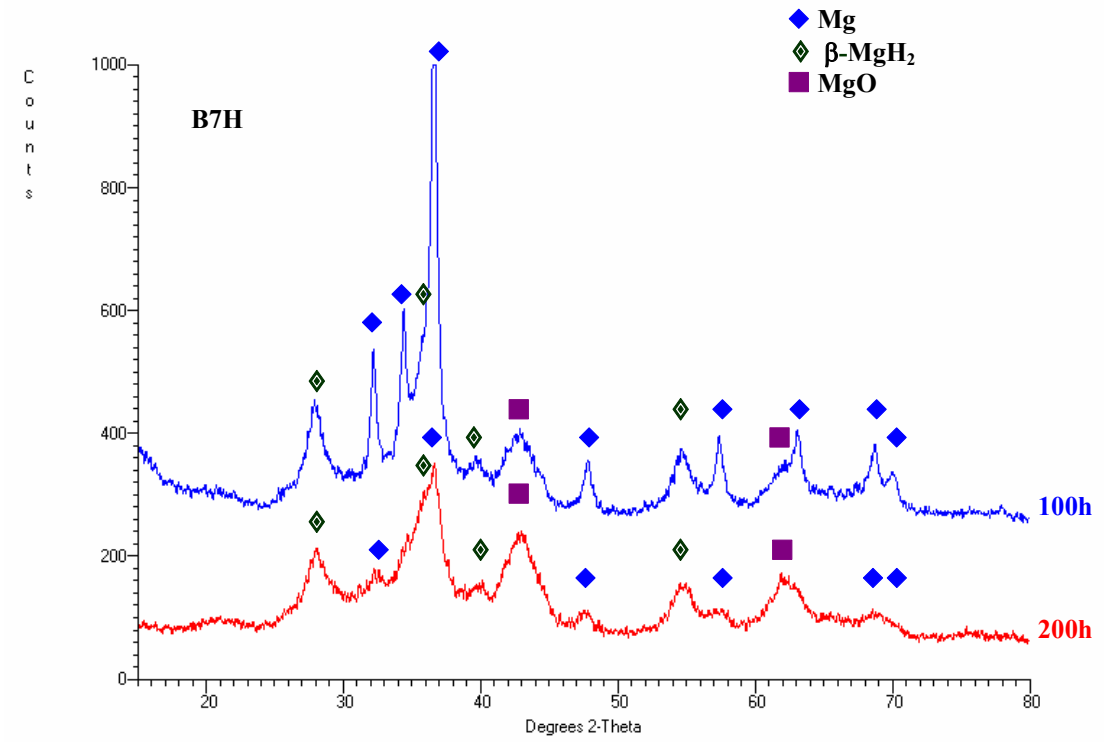

(a)

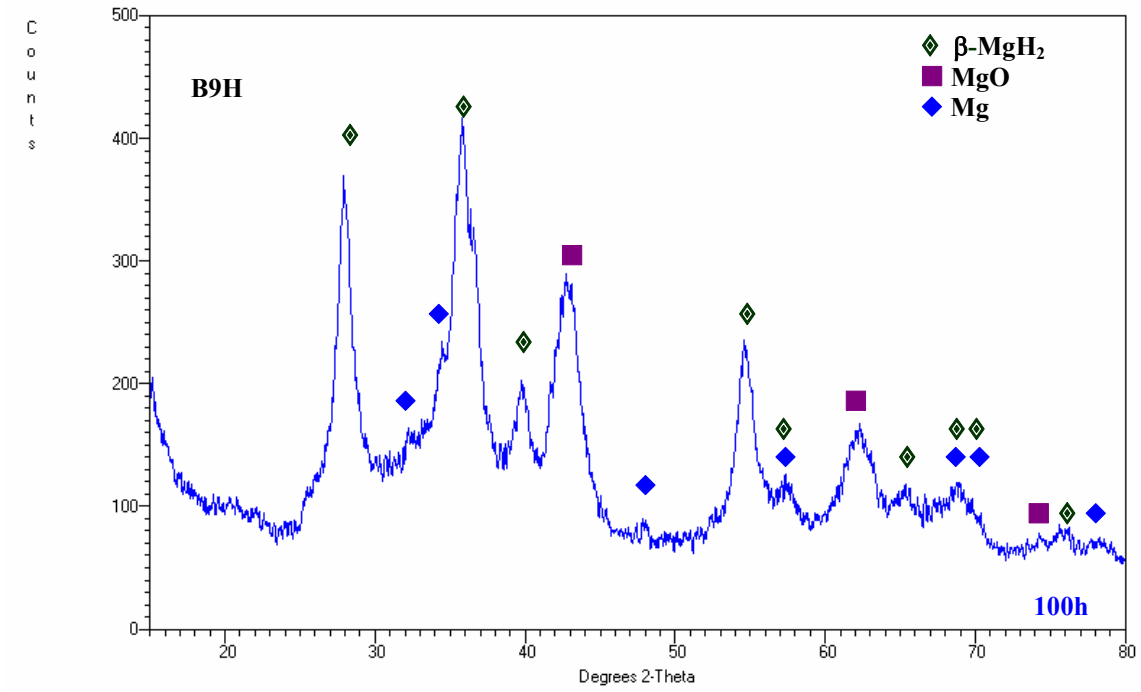

(b)

Fig. F.19 XRD patterns of (a) B7H powders after milling for 100 and 200h under LES mode, and (b) B9H powder after milling for 100h under IMP2 mode.

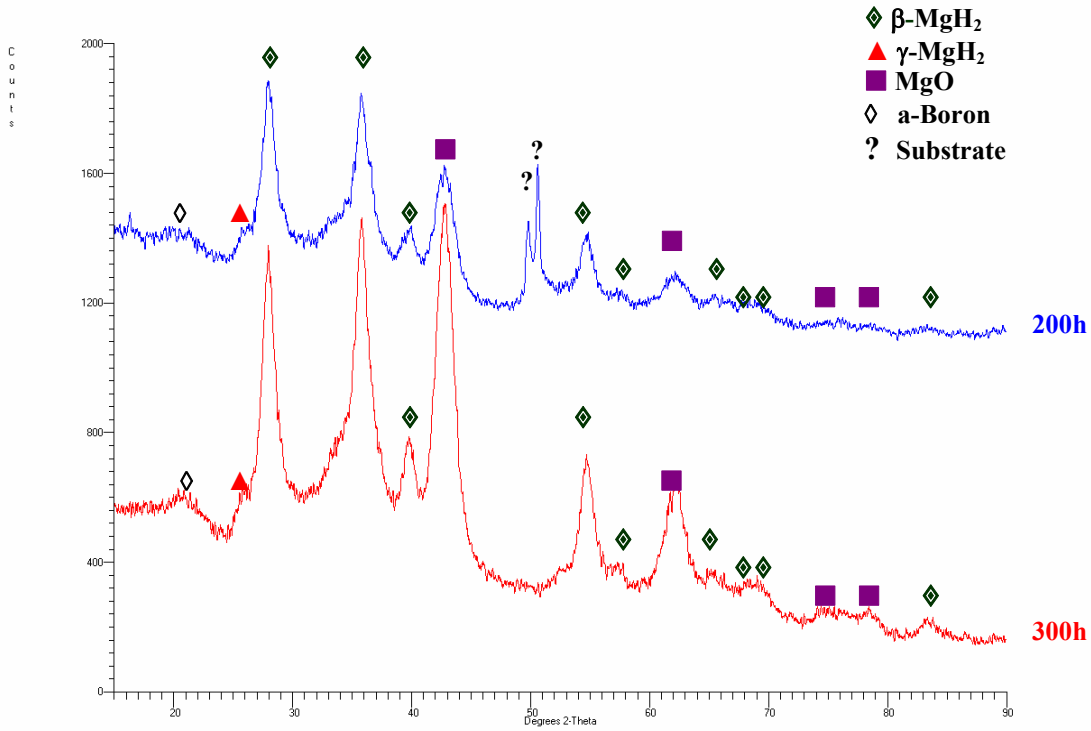

Fig. F.20 XRD patterns of the powder mixture of a stoichiometric Mg-2B powder mixture (B10H powders) with oxide-free amorphous boron after milling for 200 and 300h under IMP2 mode.

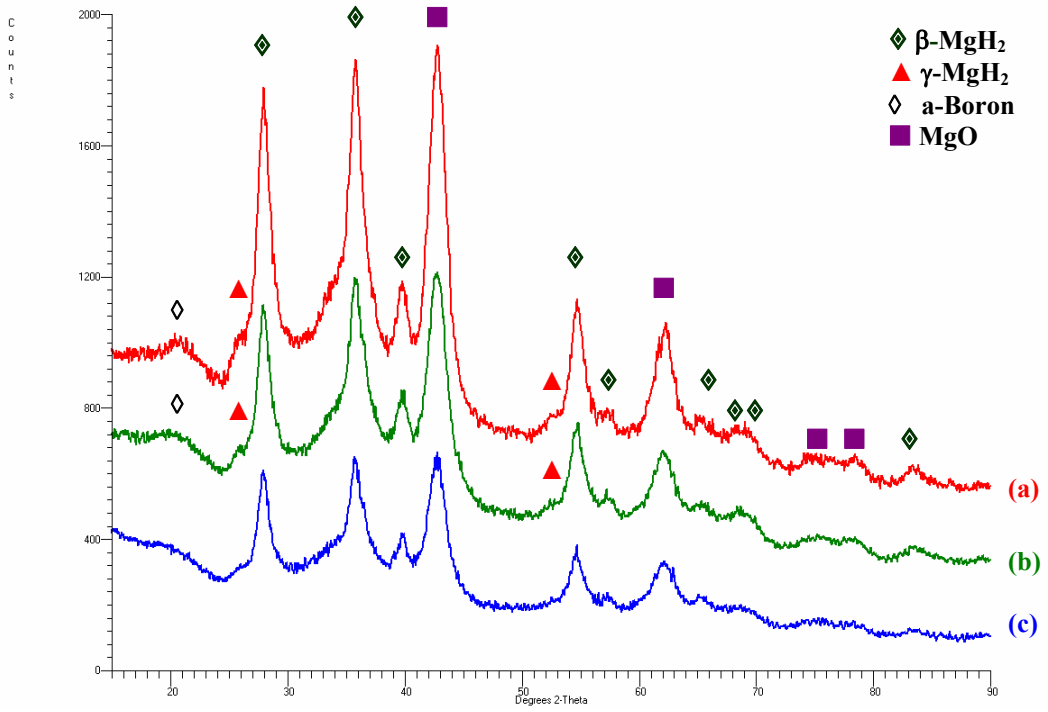

Fig. F.21 XRD patterns of B10H300 powder. (a) as-milled, (b) annealed at 126°C under 4.6 MPa H_2 for 24h and (c) annealed at 212°C under 4.6 MPa H_2 for 24h.

F.3.3 B14H and B15H powders

Table F.10 Nanograin size D, strain e, numbers of XRD peaks used for calculation and linear regression coefficient R^2 from equation 6.1 of β-MgH_2 phase in B14H and B15H powders.

Powder	β-MgH_2 Nanograin size, D and strain, e				
	Milling time (h)	D (nm)	e	R^2	No of XRD peaks
B14H50	50	6	0	0.939	8
B14H50-350-40-20	-	35	0	0.961	10
B14H200-100-43-100	-	8	0	0.982	7
B14H200-220-43-100	-	11	0	0.993	3
B14H200-400-40-20	-	43	$1.1x10^{-3}$	0.689	6
B14H200s350	-	11	0	0.949	4
B14H200-100-43-100s350	-	14	0	0.981	5
B14H200-220-43-100s350	-	38	0	0.929	4
B14H200-400-40-20s350	-	57	0	0.991	7
B15H200	200	6	0	0.972	6

Table F.11 Nanograin size D, strain e, numbers of XRD peaks used for calculation and linear regression coefficient R^2 from equation 6.1 of MgB_2 phase in B14H and B15H powders.

Powder	MgB_2 Nanograin size, D and strain, e				
	Milling time (h)	D (nm)	e	R^2	No of XRD peaks
B14H50DSC	-	14	0	0.916	5
B14H50-350-40-20DSC	-	16	0	0.955	8
B14H200	200	8	0	0.985	5
B14H200-100-43-100	-	8	0	0.990	9
B14H200-220-43-100	-	7	0	0.983	5
B14H200-400-40-20	-	11	0	0.967	9
B14H200DSC	-	9	0	0.975	9
B14H200-100-43-100DSC	-	9	0	0.904	7
B14H200-220-43-100DSC	-	14	0	0.990	6
B14H200-400-40-20DSC	-	8	0	0.983	10
B15H200DSC	-	13	0	0.920	8

Table F.12 Nanograin size D, strain e, numbers of XRD peaks used for calculation and linear regression coefficient R^2 from equation 6.1 of Mg phase in B14H and B15H powders.

Powder	Mg Nanograin size, D and strain, e				
	Milling time (h)	D (nm)	e	R^2	No of XRD peaks
B14H50DSC	-	12	0	0.815	5
B14H50-350-40-20DSC	-	18	0	0.925	8
B14H200DSC	-	8	0	0.981	8
B14H200-100-43-100DSC	-	9	0	0.946	7
B14H200-220-43-100DSC	-	12	0	0.965	8
B14H200-400-40-20DSC	-	14	0	0.979	7
B14H200s350	-	21	0	0.922	8
B14H200-100-43-100s350	-	22	0	0.832	6
B14H200-220-43-100s350	-	27	0	0.912	6
B14H200-400-40-20s350	-	36	0	0.848	6
B15H200DSC	-	11	0	0.930	7

F.3.4 B11H powder

Table F.13 Nanograin size and strain of MgB_2 phase in B11H powders.

Powder	MgB_2 Nanograin size, D and strain, e				
	Milling time (h)	D (nm)	e	R^2	No of XRD peaks
B11H50	50	13	$2.2x10^{-3}$	0.865	9
B11H200	200	10	0	0.836	5
B11H50DSC	-	19	$5.0x10^{-4}$	0.945	5
B11H200DSC	-	16	0	0.957	7
B11H200-220-43-100	-	13	0	0.956	7
B11H200-220-43-100DSC	-	12	0	0.991	8

Table F.14 Lattice parameters of MgB_2 phase in B11H powders.

Powder	Milling time (h)	Lattice parameter (nm) (Hexagonal)			
		a		c	
		Average	Error[(1)]	Average	Error[(1)]
MgB_2	-	0.3085	0.0008	0.3521	0.0024
B11H50	50	0.3085	0.0007	0.3518	0.0024
B11H50DSC	-	0.3082	0.0069	0.3520	0.0024
B11H200	200	0.3082	0.0007	0.3522	0.0026
B11H200DSC	-	0.3081	0.0007	0.3520	0.0023
B11H200-220-43-100	-	0.3082	0.0007	0.3520	0.0023
B11H200-220-43-100DSC	-	0.3082	0.0007	0.3520	0.0023

[(1)] Average lattice parameter and error are calculated by software TRACES™ V.6.5.1

Appendix G Summary of data for DSC analysis and desorption kinetics

G.1 Mg-H system

Table G.1 Summary of DSC data for Mg-H powders upon heating to 500°C.

Powder	Milling time (h)	T_{on} (°C)	T_{peak} (°C)	T_{end} (°C)	ΔH (J/g)	Yield of MgH_2 (wt.%)	Desorbed Hydrogen from MgH_2 (wt.%)	Mg reaction rate (MgH_2) (%)
Commercial MgH_2 (Tego Magnan®)	-	399.0	410.1	426.1	2251	95.0	7.3	95.0
Mg1H	5	311.8	375.7	398.5	134	4.7	0.4	5.8
Mg1H	20	372.1	380.8/406.8	421.3	813	28.5	2.7	35.3
Mg1H	50	361.2	369.5/408.4	420.5	1223	42.9	4.1	53.2
Mg1H	100	341.1	352.8/392.4	409.3	1262	44.3	4.2	54.9
Mg1H	150	339.5	354.2/382.1	393.3	1288	45.2	4.3	56.0
Mg7H	5	398.8	410.5	418.9	224	7.9	0.8	9.8
Mg7H	20	375.3	387.3/398.1	412.8	1114	39.1	3.7	48.5
Mg7H	50	350.8	372.9/389.3	404.8	1541	54.1	5.1	67.1
Mg7H	100	349.0	365.5/397.7	409.7	1677	58.9	5.6	73.0
Mg7H	150	351.8	370.5/392.7	404.6	1716	60.2	5.7	74.6
Mg6H	150	351.7	371.3/391.3	405.6	1794	63.0	6.0	78.1
Mg2H	100	335.4	349.7/376.3	391.5	1926	68.0	6.5	84.3
Mg4H	150	347.0	361.6/380.3	398.0	1842	65.5	6.2	81.2
Mg5H	150	326.0	348.3/369.0	383.0	1698	60.4	5.7	74.9
Mg9H	60	351.8	348.3/394.6	409.1	1724	60.5	5.7	75.0
Mg10H	60	351.0	367.8/388.6	406.4	1640	57.6	5.5	71.4
Mg11H	100	350.5	365.5/392.0	407.7	1610	56.5	5.4	70.1
Mg12H	30	346.2	365.9/392.1	409.9	1919	84.7	6.5	84.7
Mg13H	30	348.7	367.5/379.7	397.5	1949	86	6.6	86.0
Mg14H	30	347.9	363.8/383.8	403.4	2002	88.3	6.8	88.3

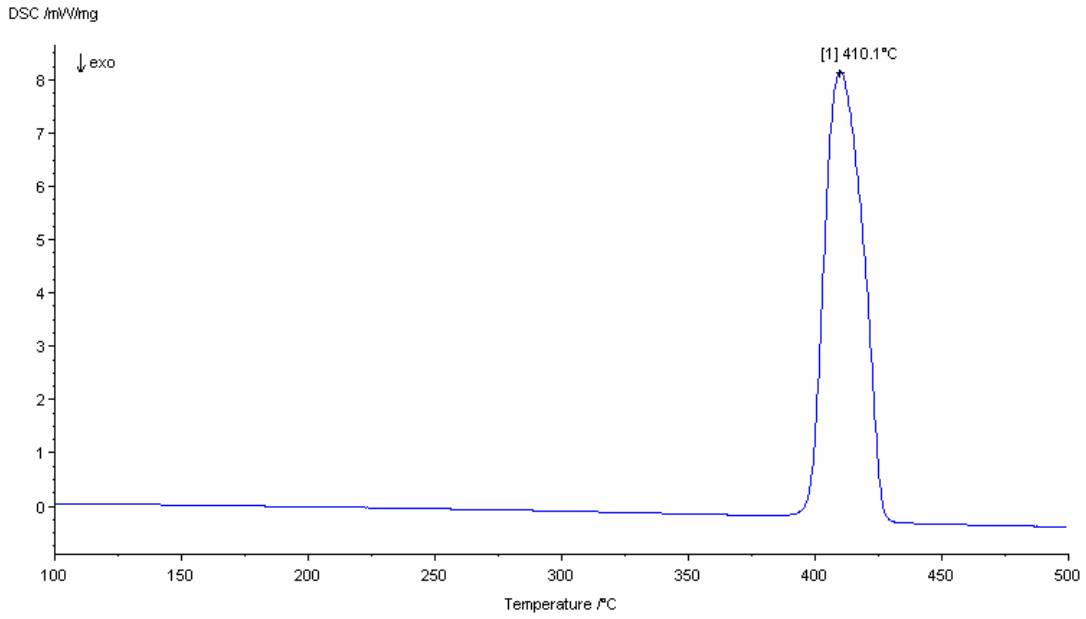

Fig. G.1 DSC curves of commercial MgH_2 powder (Tego Magnan®).

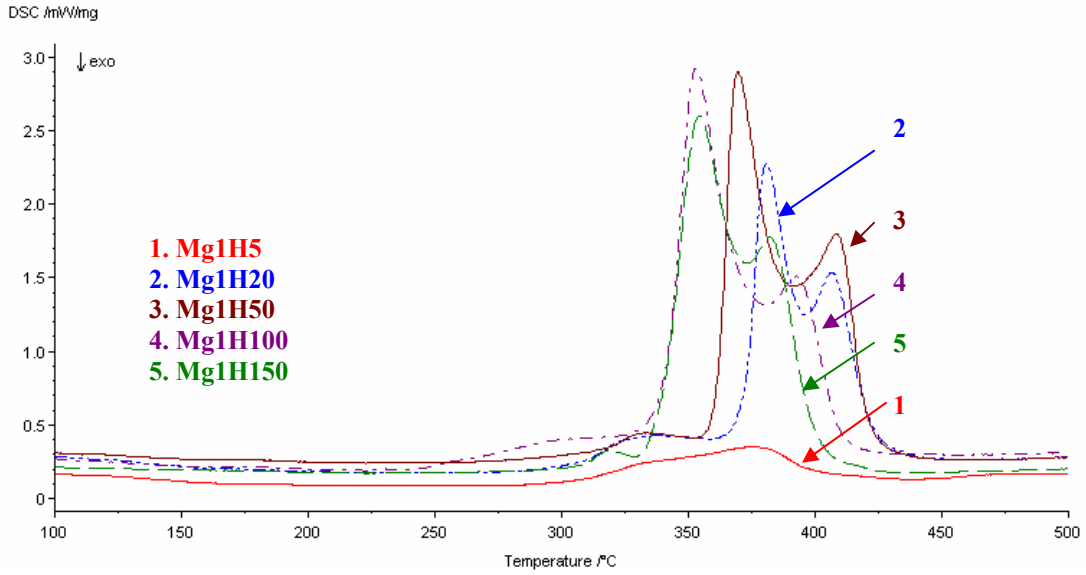

Fig. G.2 DSC curves of Mg1H powders as a function of milling time.

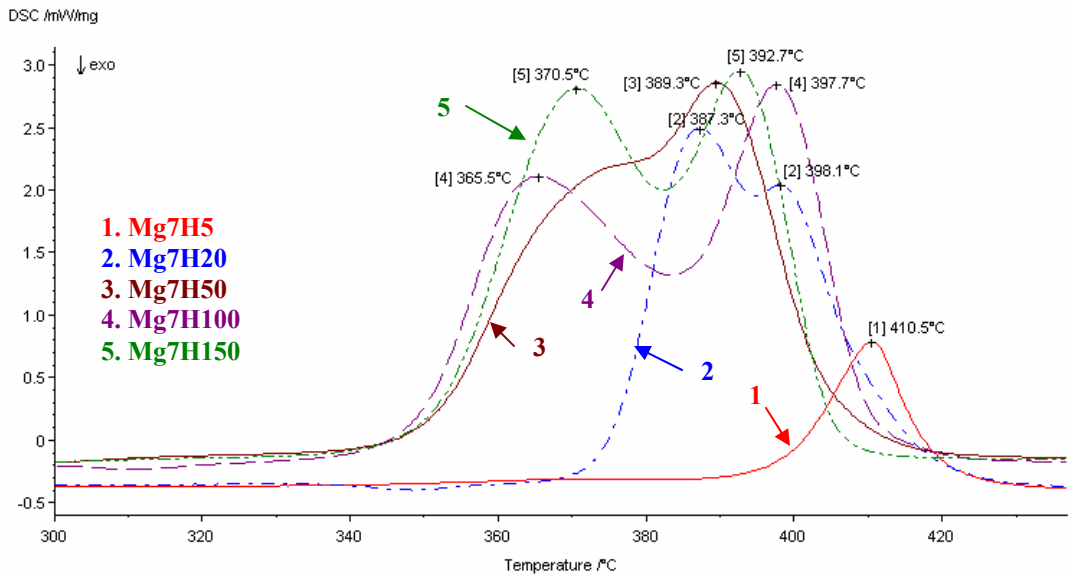

Fig. G.3 DSC curves of Mg7H powders as a function of milling time.

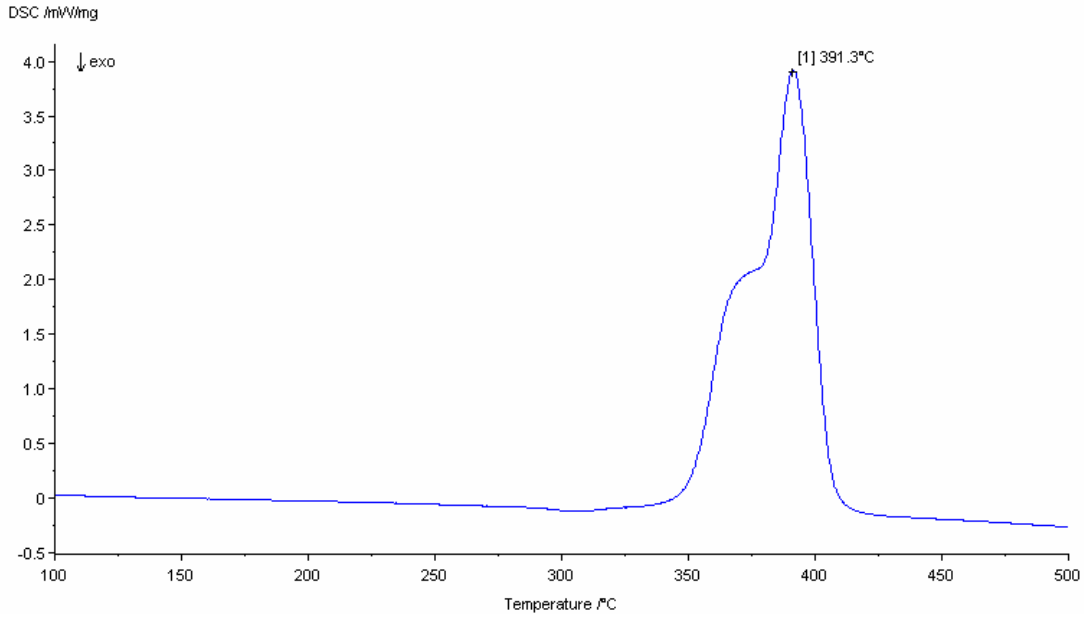

Fig. G.4 DSC curve of Mg6H powder after milling for 150h under HES mode.

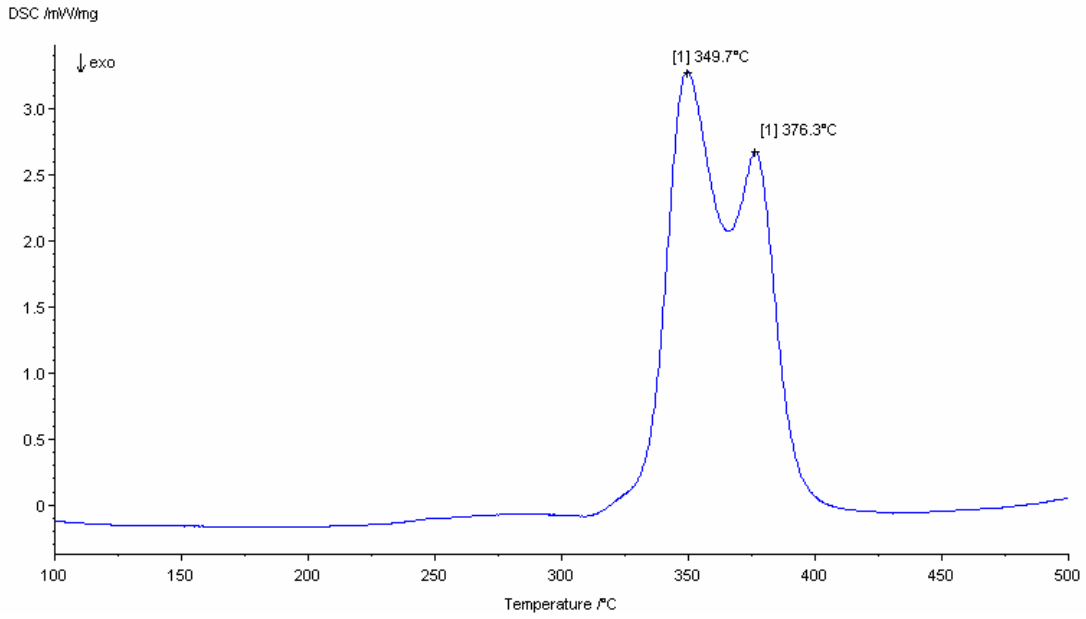

Fig. G.5 DSC curve of Mg2H powder after milling for 100h under IMP2 mode.

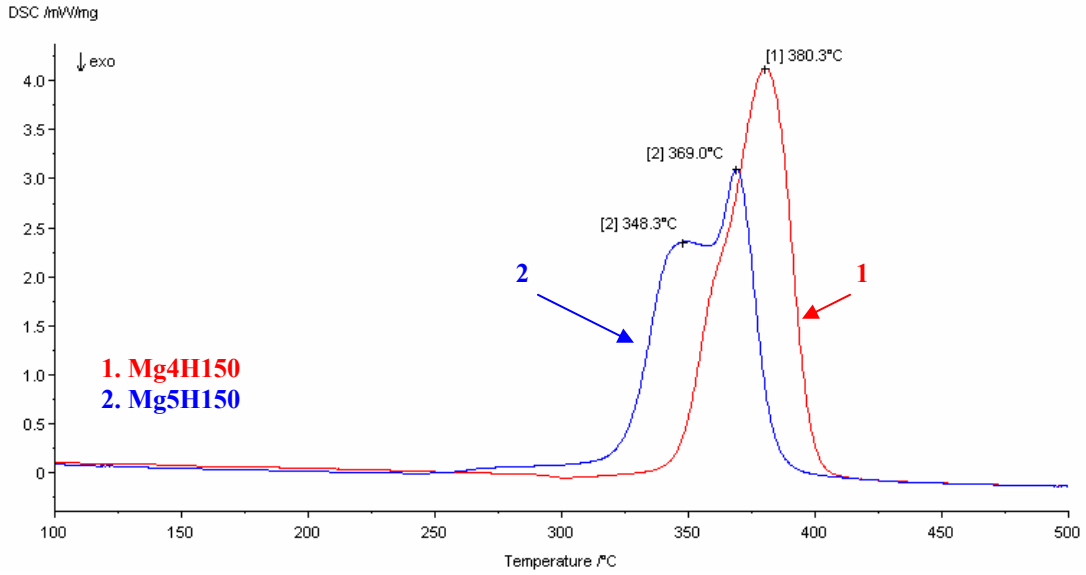

Fig. G.6 DSC curves of Mg4H and Mg5H powders after milling for 150h under IMP2 mode.

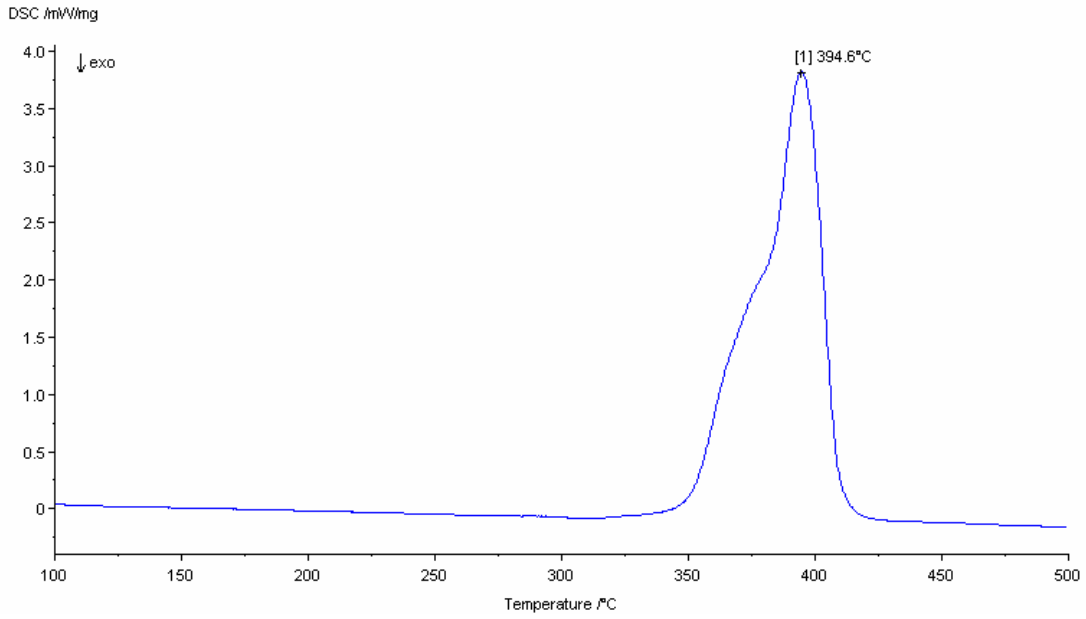

Fig. G.7 DSC curve of Mg9H powder after milling for 60h under IMP710 mode.

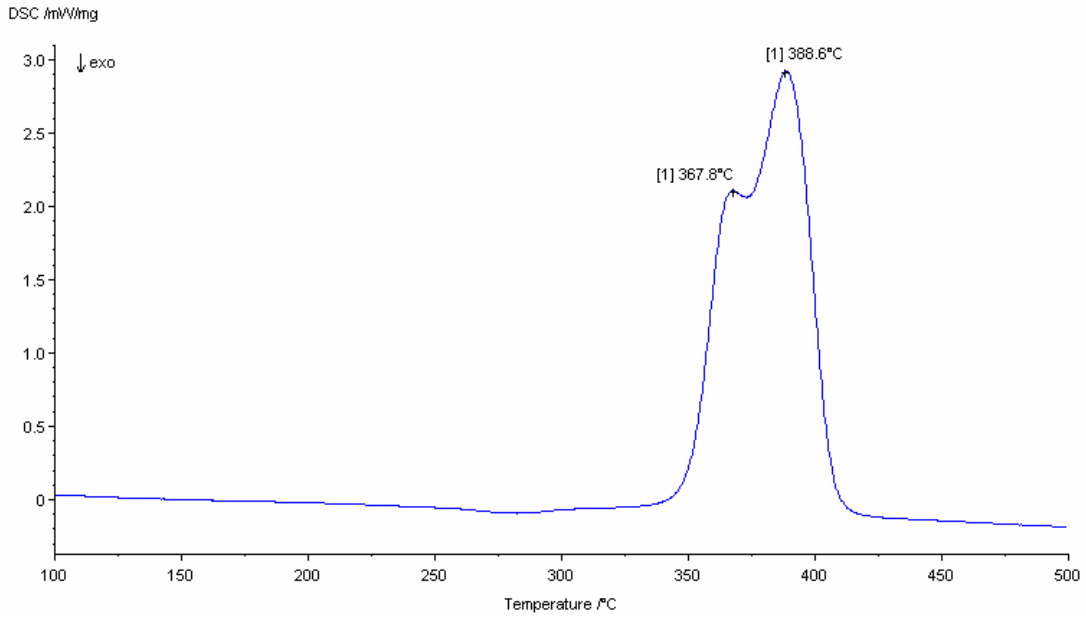

Fig. G.8 DSC curve of Mg10H powder after milling for 60h under IMP710 mode.

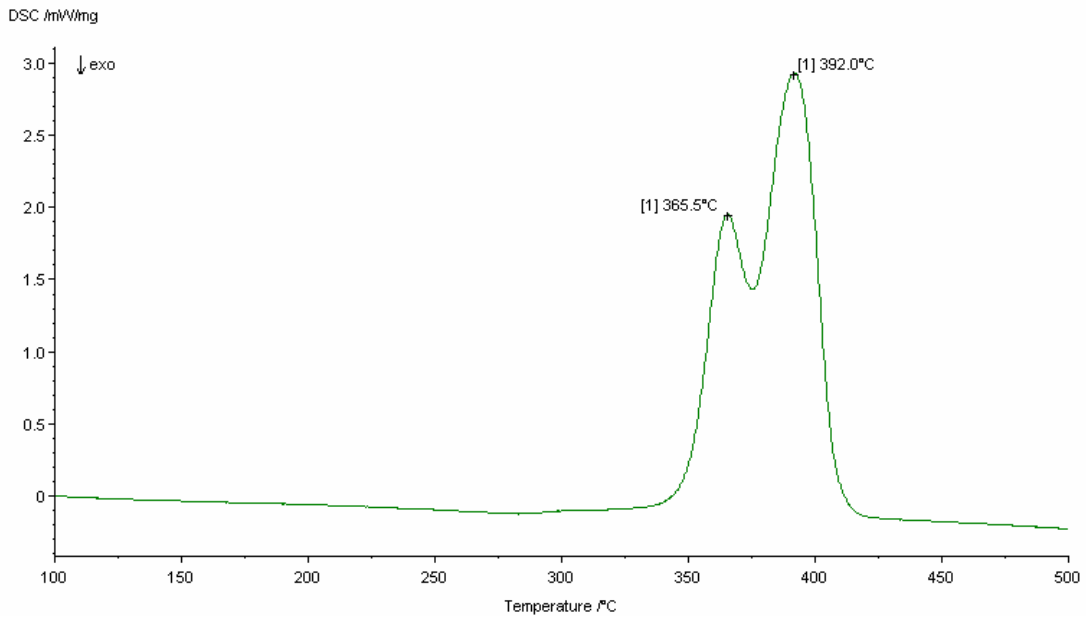

Fig. G.9 DSC curve of Mg11H powder after milling for 100h under IMP710 mode.

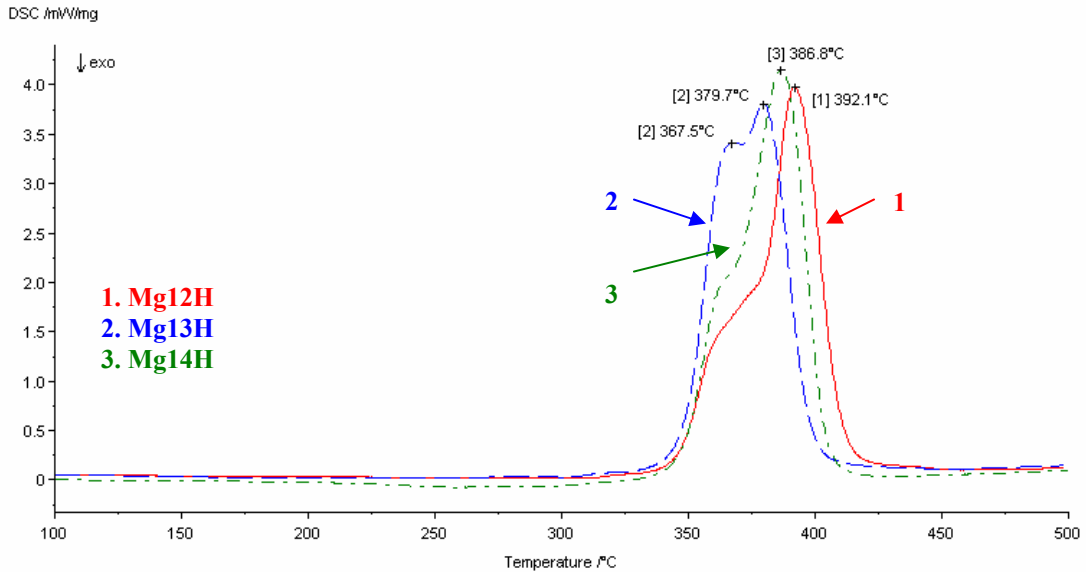

Fig. G.10 DSC curve of Mg12H, Mg13H and Mg14H powders after milling for 60h under IMP68 mode.

G.2 Mg-Al-H system

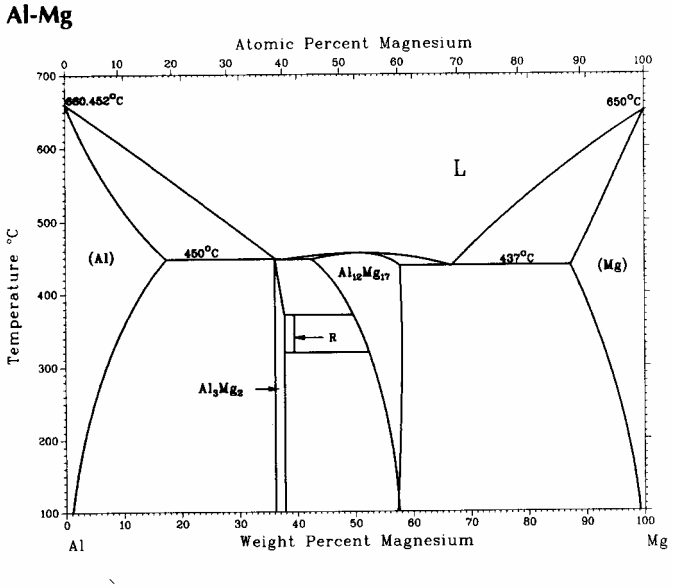

Fig. G. 11 Binary Al-Mg phase diagram [104].

G.2.1 Annealed A1H powders

Table G. 2 Summary of DSC data for the annealed A1H powders obtained upon heating to 500°C.

Powder	Endothermic-Peak #1 (LT)				Endothermic-Peak #2 (HT)						
	T_{on} (°C)	T_{peak} (°C)	T_{end} (°C)	ΔH (J/g)	T_{on} (°C)	T_{peak} (°C)	T_{end} (°C)	ΔH^{melt} (J/g)	Yield of MgH_2 (wt.%)	Desorbed Hydrogen from MgH_2 (wt.%)	Mg reaction rate (%)
A1H1-350-40-20	385.3	409.7	424.8	341	448.3	455.4	462.8	219	12.0	0.9	35.6
A1H5-350-40-20	401.6	408.9	421.5	463	448.0	455.3	463.3	208	16.2	1.2	48.3
A1H1-100-40-100	-	-	-	-	447.6	451.4	460.8	228	-	-	-
A1H5-100-40-100	404.7	418.7	433.3	21	444.7	455.6	474.0	221	0.7	0.1	2.2
A1H270-100-45-100	346.0	354.1	365.3	553	438.2	443.5	448.6	40	19.5	1.5	57.7

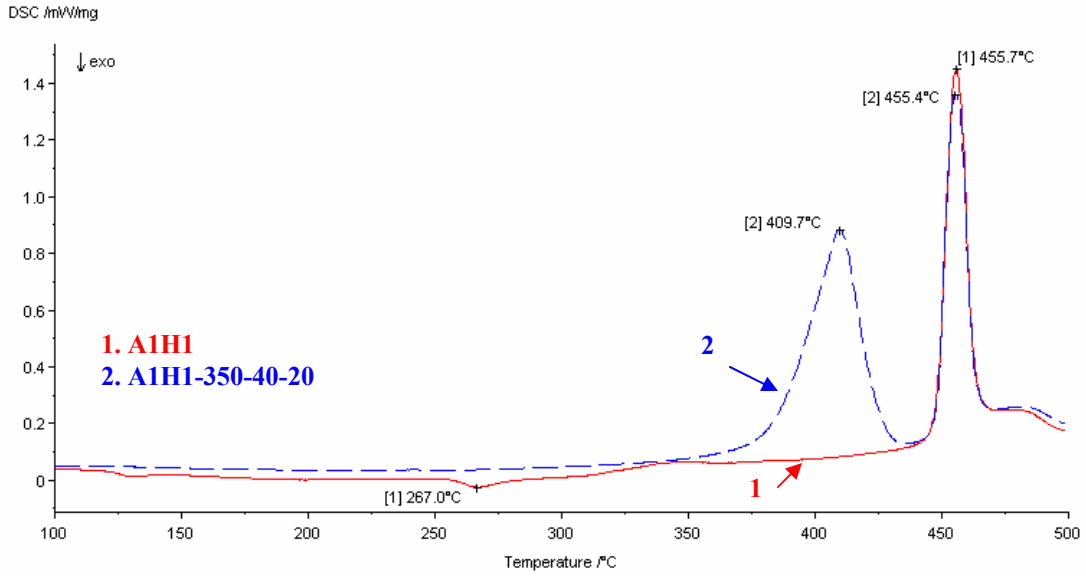

(a)

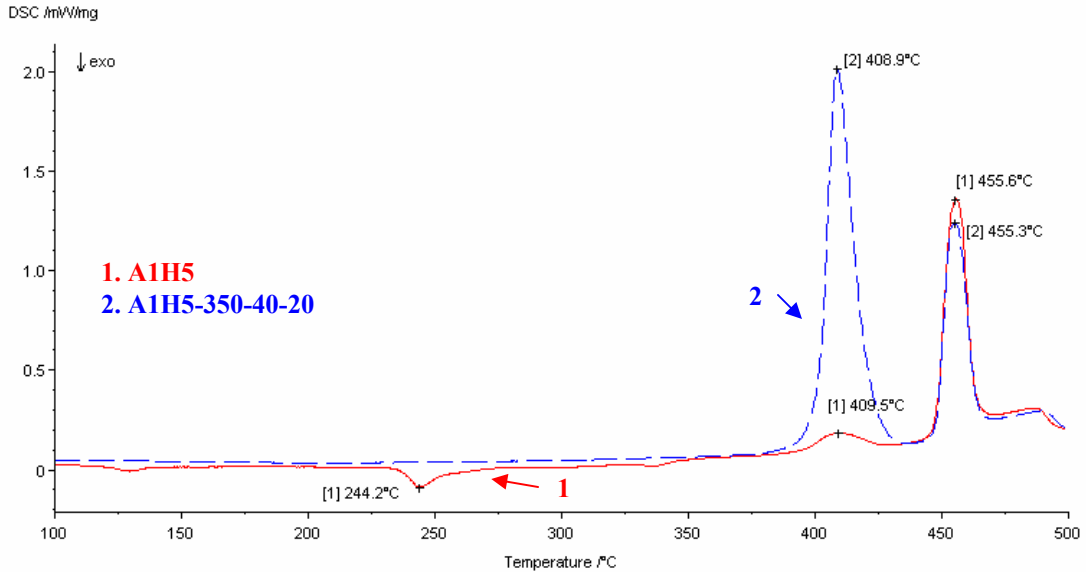

(b)

Fig. G. 12 DSC curves of the annealed A1H powders obtained upon heating. (a) 1h milled powder after annealing at 350°C under 4.0 MPa of H_2 for 20h (A1H1-350-40-20), (b) 5h milled powder after annealing at 350°C under 4.0 MPa of H_2 for 20h (A1H5-350-40-20), (c) 1h milled powder after annealing at 100°C under 4.0 MPa of H_2 for 100h (A1H1-100-40-100), (d) 5h milled powder after annealing at 100°C under 4.0 MPa of H_2 for 100h (A1H5-100-40-100), and (e) 270h milled powder after annealing at 100°C under 4.5 MPa of H_2 for 100h (A1H270-100-45-100). The DSC curves upon heating of as-milled counterparts are replotted for comparison.

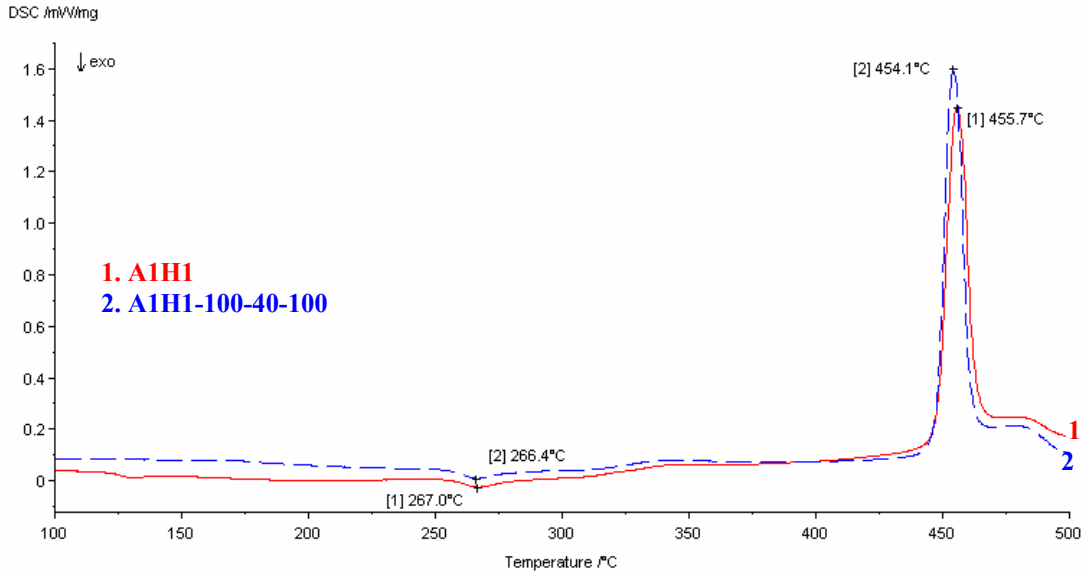

(c)

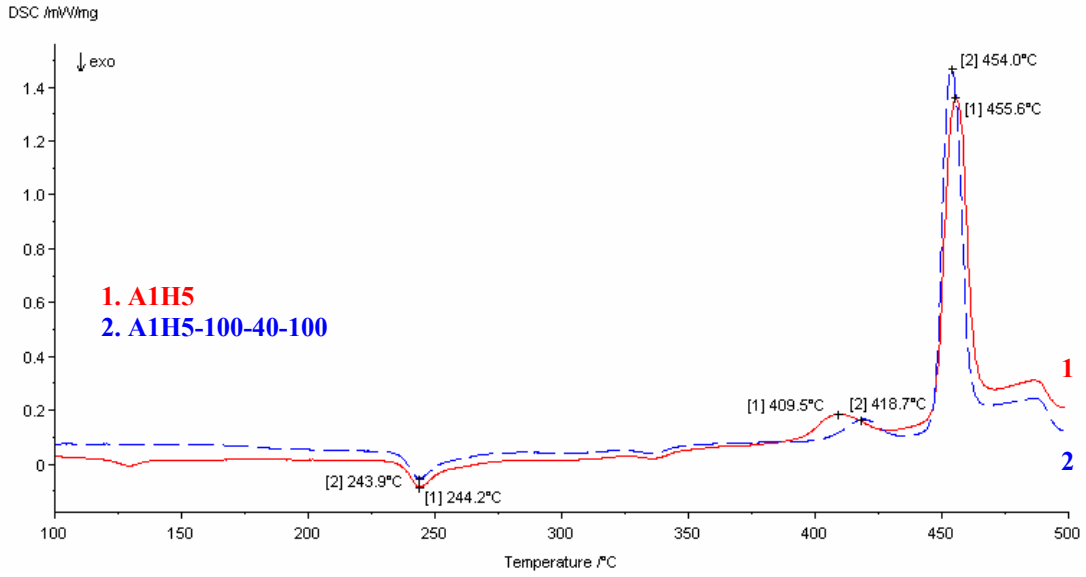

(d)

Fig. G. 12 cont'd

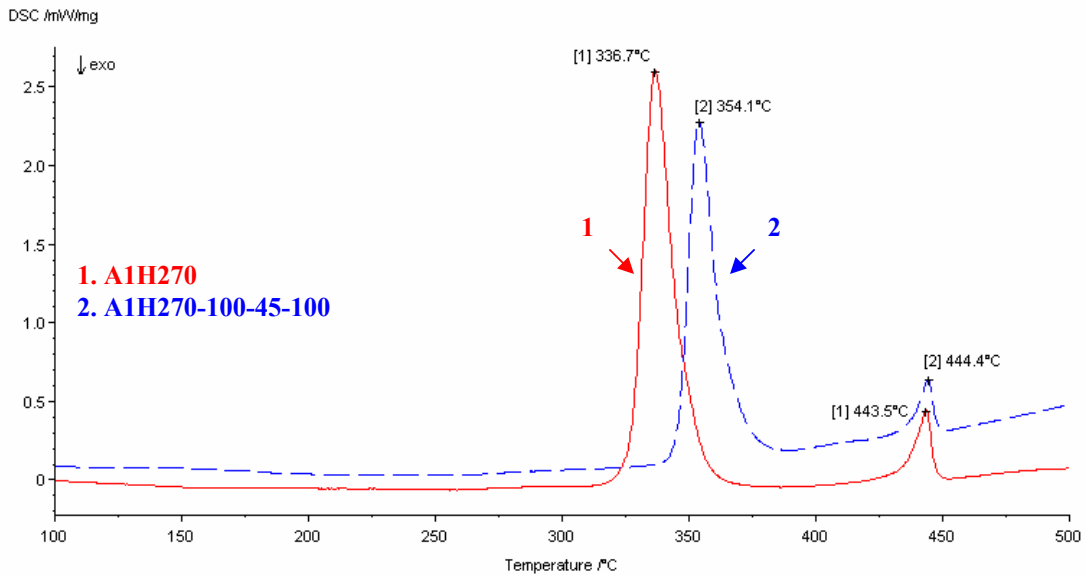

(e)

Fig. G. 12 cont'd

Table G. 3 Summary of DSC data for the annealed powders upon cooling from 500°C.

Powder	Exothermic peak			
	T_{on} (°C)	T_{peak}(°C)	T_{end}(°C)	ΔH (J/g)
A1H1-350-40-20	439.7	428.8	415.7	-193
A1H5-350-40-20	438.7	428.2	411.5	-172
A1H1-100-40-100	438.9	430.6	417.9	-197
A1H5-100-40-100	433.8	429.9	414.3	-182
A1H270-100-45-100	435.6	428.7	417.9	-43

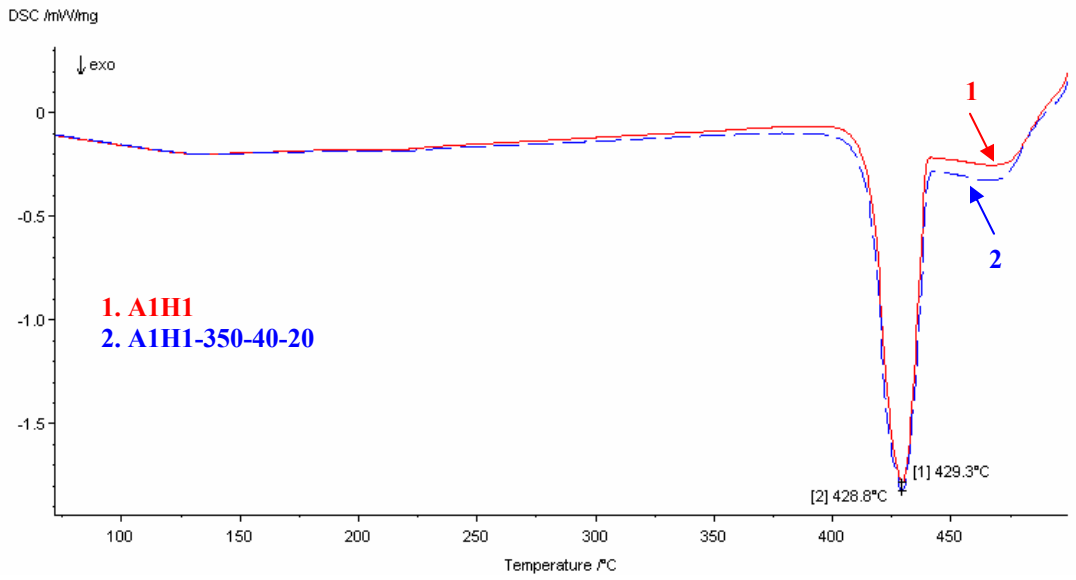

(a)

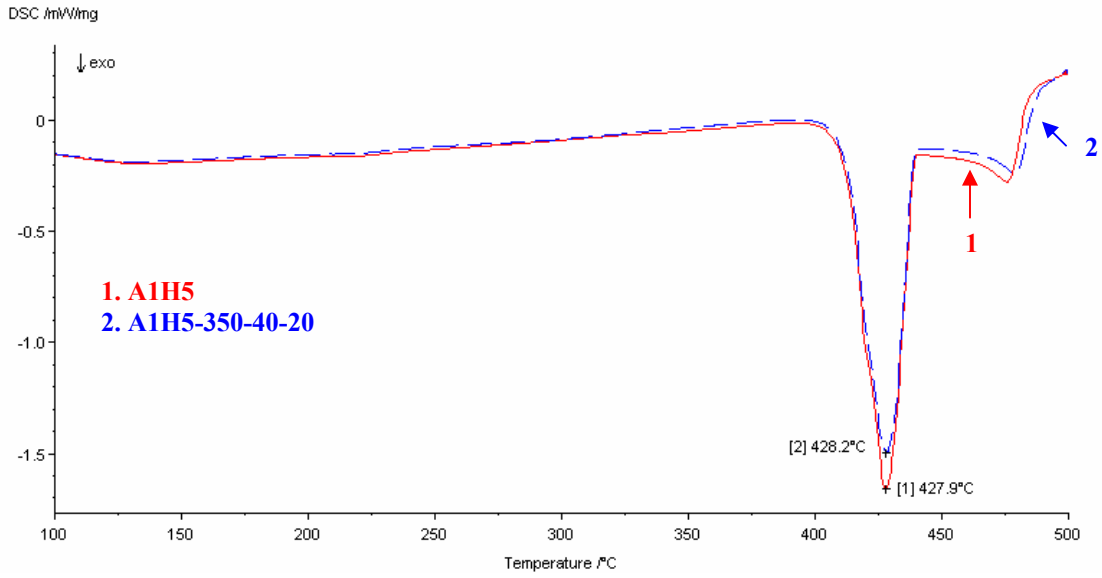

(b)

Fig. G. 13 DSC curves of the annealed A1H powders obtained upon cooling from 500°C. (a) 1h milled powder after annealing at 350°C under 4.0 MPa of H_2 for 20h (A1H1-350-40-20), (b) 5h milled powder after annealing at 350°C under 4.0 MPa of H_2 for 20h (A1H5-350-40-20), (c) 1h milled powder after annealing at 100°C under 4.0 MPa of H_2 for 100h (A1H1-100-40-100), (d) 5h milled powder after annealing at 100°C under 4.0 MPa of H_2 for 100h (A1H5-100-40-100), and (e) 270h milled powder after annealing at 100°C under 4.5 MPa of H_2 for 100h. The DSC curves upon cooling of as-milled counterparts are replotted for comparison (A1H270-100-45-100).

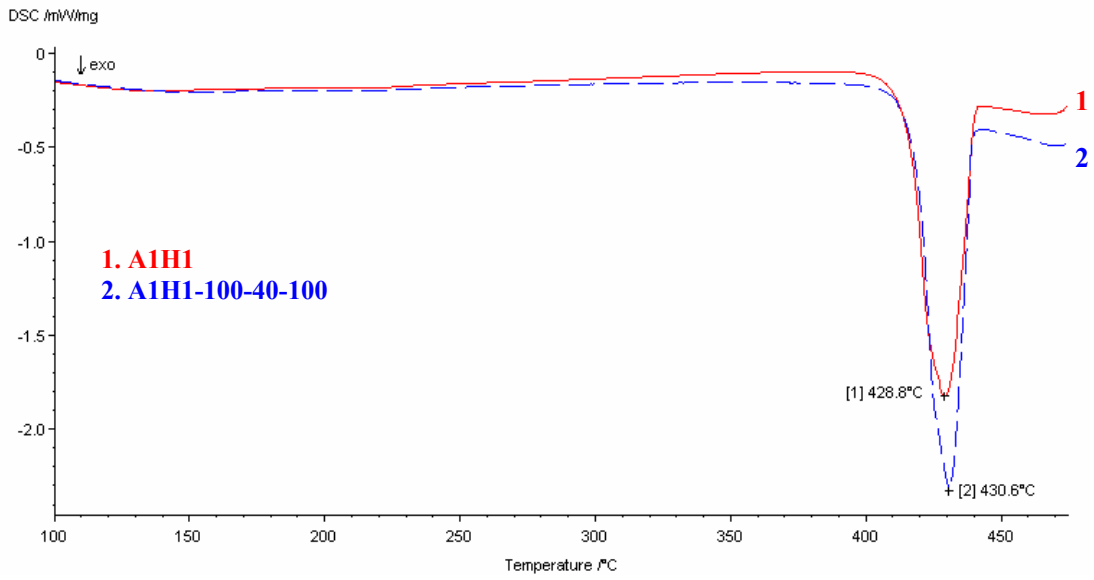

(c)

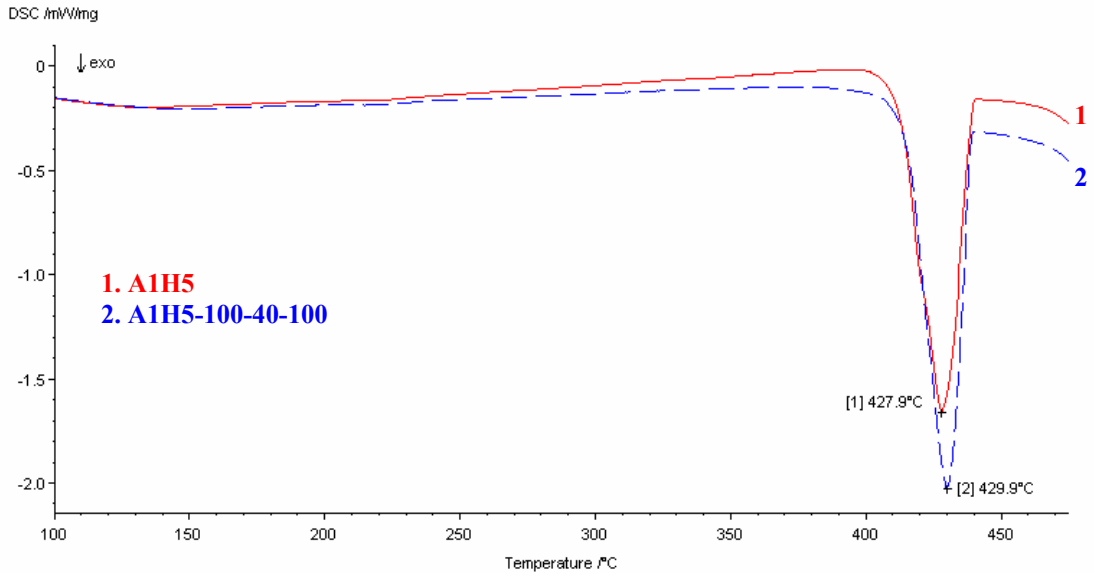

(d)

Fig. G. 13 cont'd

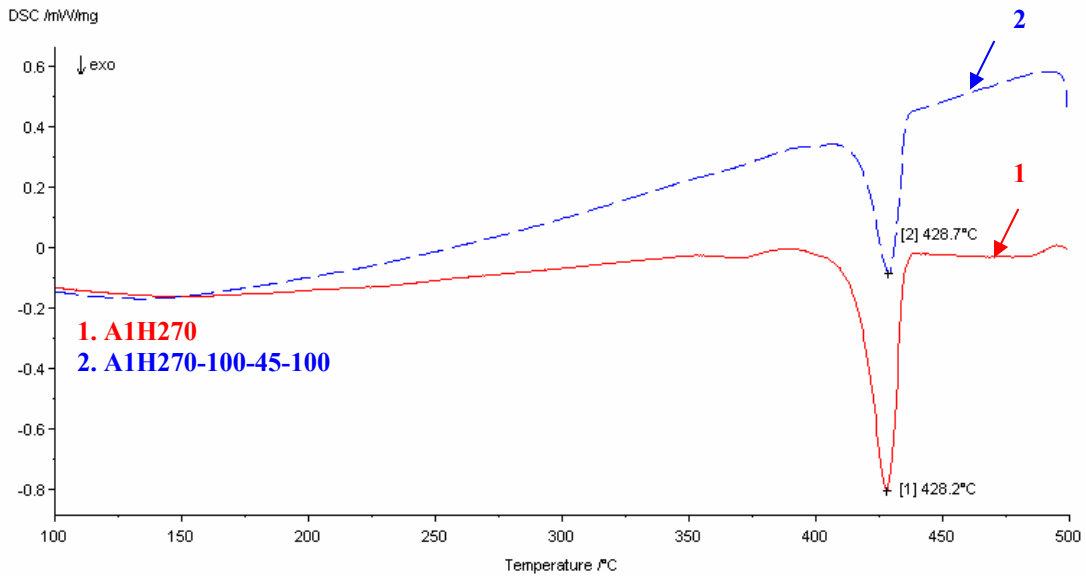

(e)

Fig. G. 13 cont'd

G.2.2 A5H and A10H powders

Table G.4 Summary of DSC data for the as-milled and annealed A5H and A10H powders upon heating.

Powder	Endothermic-Peak #1 (LT)				Endothermic-Peak #2 (HT)						
	T_{on} (^oC)	T_{peak} (^oC)	T_{end} (^oC)	ΔH (J/g)	T_{on} (^oC)	T_{peak} (^oC)	T_{end} (^oC)	ΔH^{melt} (J/g)	Yield of MgH_2 (wt.%)	Desorbed Hydrogen from MgH_2 (wt.%)	Mg reaction rate (%)
A5H50	322.6	339.0	355.6	490	439.1	448.4	455.7	170	17.2	1.4	56.8
A5H50-260-43-144	337.8	361.1	392.2	662	439.0	447.0	453.8	149	23.2	1.7	76.8
A10H30	340.3	351.2	372.8	750	444.7	452.5	458.3	149	26.3	2.0	78.3
A10H30-350-40-20	348.9	367.0	419.1	781	446.6	453.9	461.0	149	27.4	2.1	81.5

Table G.5 Summary of DSC data for the as-milled and annealed A5H and A10H powders upon cooling.

Powder	Exothermic peak			
	T_{on} (^oC)	T_{peak}(^oC)	T_{end}(^oC)	ΔH (J/g)
A5H50	407.8	422.3	437.1	-187
A5H50-260-43-144	436.3	423.3	412.0	-161
A10H30	439.3	428.5	417.0	-135
A10H30-350-40-20	439.6	426.8	406.7	-128

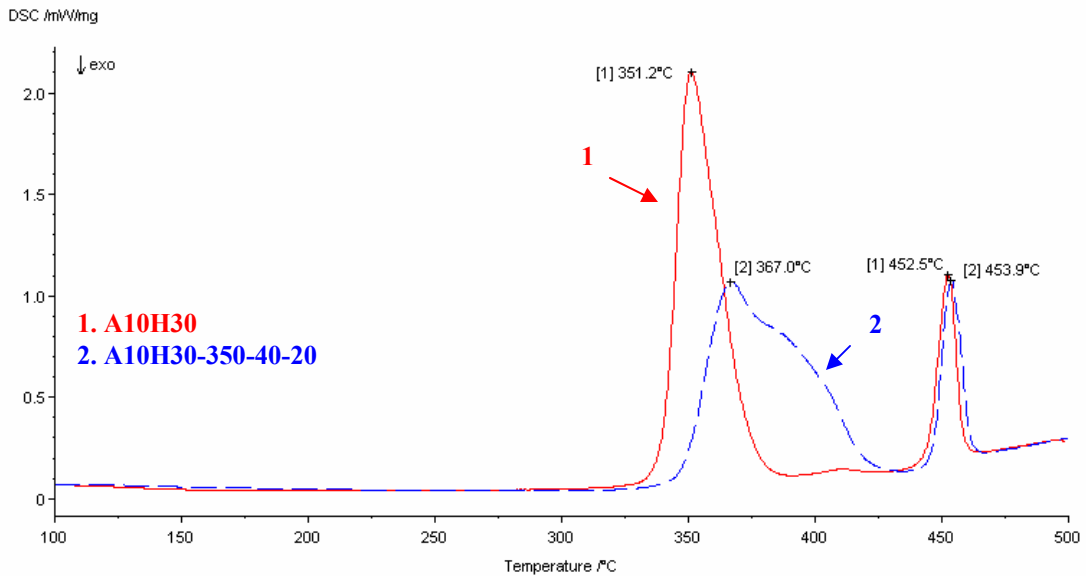

(a)

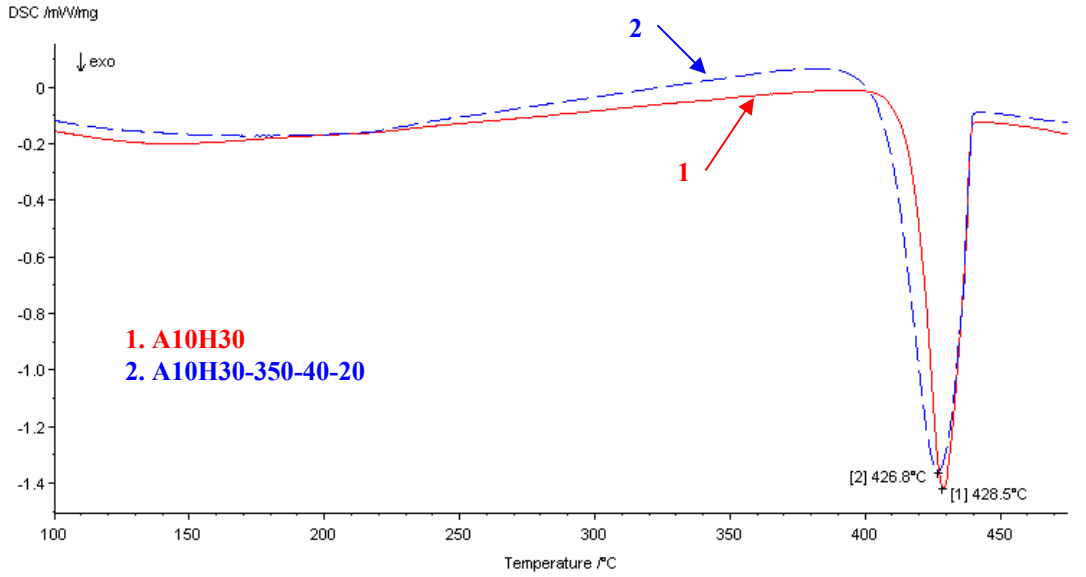

(b)

Fig. G.14 DSC curves obtained upon (a) heating to 500°C and (b) cooling from 500°C for the 30h milled A10H powder after annealing at 350°C under 4.0MPa of hydrogen for 20h (A10H30-350-40-20). DSC curves for the 30h milled powder (A10H30) are also plotted for comparison.

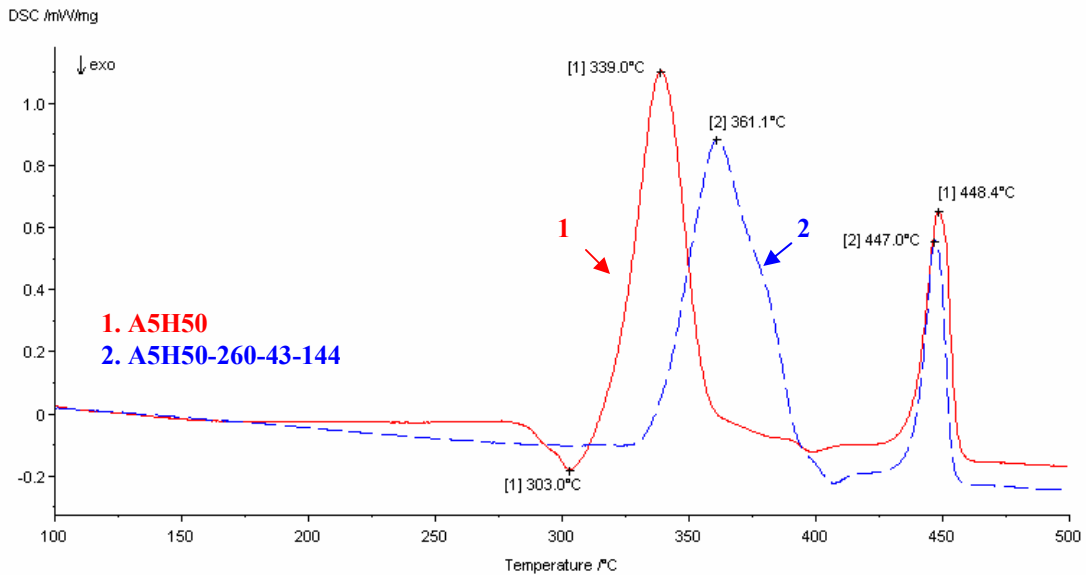

Fig. G.15 DSC curves for A5H50 powder (milled for 50h) and the same powder after annealing at 260°C under 4.3MPa of hydrogen for 144h (A5H50-260-43-144).

G.3 Mg-B-H system

G.3.1 B6H and B8H powders

Table G.6 Summary of DSC data for B6H and B8H powders upon heating to 500°C.

Powder	Milling time (h)	Peak						
		T_{on} (°C)	T_{peak} (°C)	T_{end} (°C)	ΔH (J/g)	Yield of MgH_2 (wt.%)	Desorbed Hydrogen from MgH_2 (wt.%)	Mg reaction rate (%)
B6H	100	325.7	338.5	366.8	1009	36.0	2.7	64.6
B6H	200	363.6	374.1	407.3	1090	38.8	3.0	69.8
B8H	100	352.4	365.7	379.5	972	34.6	2.6	65.3

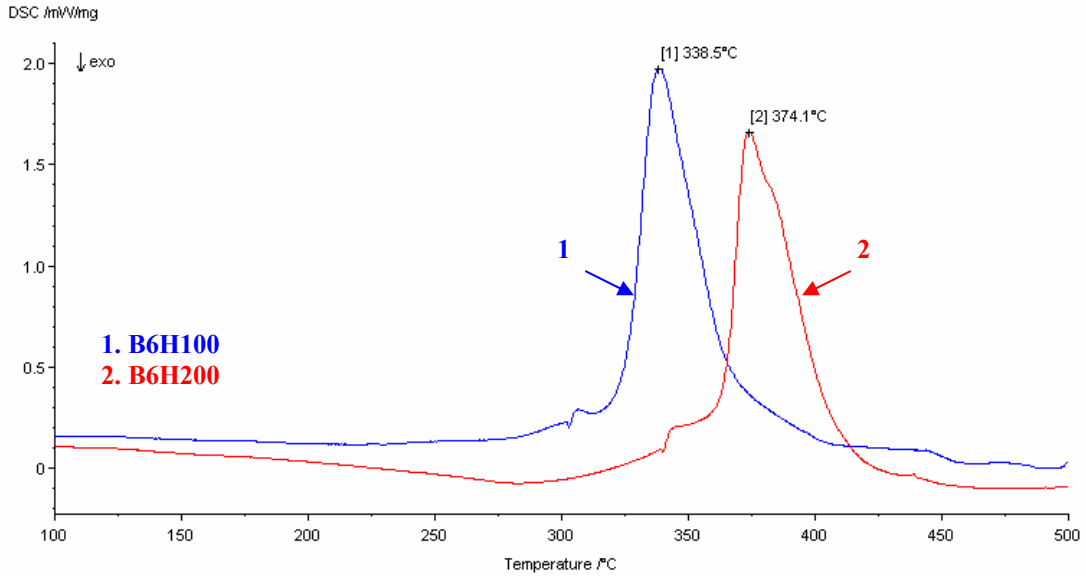

Fig. G.16 DSC curves for B6H powders after milling for 100h and 200h under LES mode.

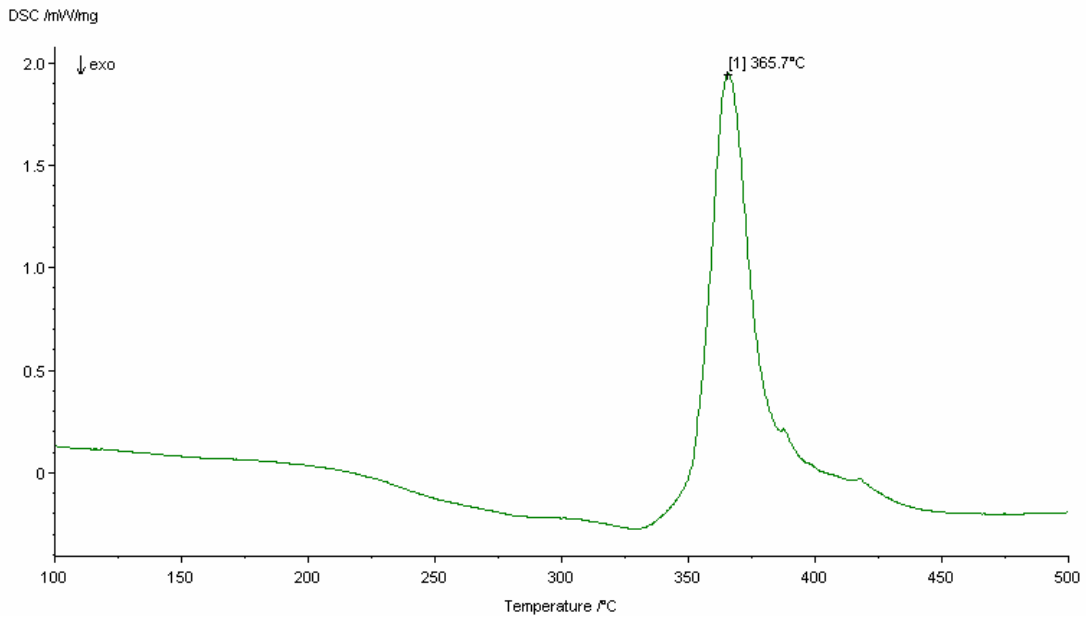

Fig. G.17 DSC curves for B8H powder after milling for 100h under IMP2 mode.

G.3.2 B7H, B9H and B10H powders

Table G.7 Summary of DSC data for B7H, B9H and B10H powders upon heating to 500°C.

Powder	Milling time (h)	Peak						
		T_{on} (°C)	T_{peak} (°C)	T_{end} (°C)	ΔH (J/g)	Yield of MgH_2 (wt.%)	Desorbed Hydrogen from MgH_2 (wt.%)	Mg reaction rate (MgH_2) (%)
B7H	100	385.6	392.6/402.0	425.3	822	29.3	2.2	51.2
B7H	200	381.7	392.9	424.4	770	27.4	2.1	48.0
B9H	100	386.7	391.1	416.4	929	33.0	2.5	62.4
B10H	200	375.1	386.1	397.4	1019	36.2	2.7	67.3
B10H	300	380.0	388.4	399.9	872	31.0	2.4	57.5

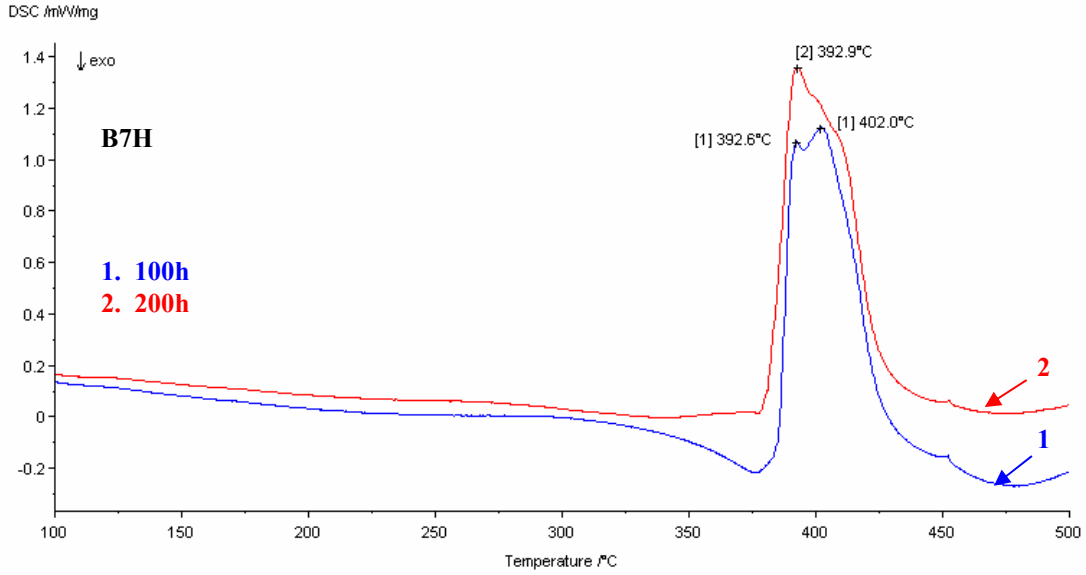

(a)

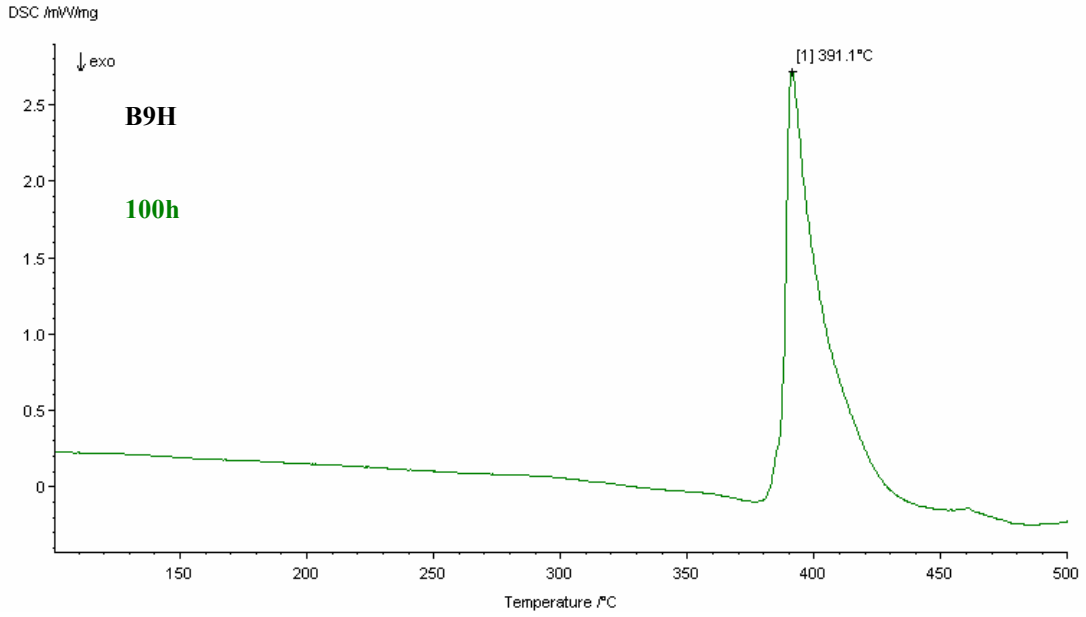

(b)

Fig. G. 18 DSC curves of (a) 100h- and 200h-milled B7H powders and (b) 100h-milled B9H powder upon heating to 500°C.

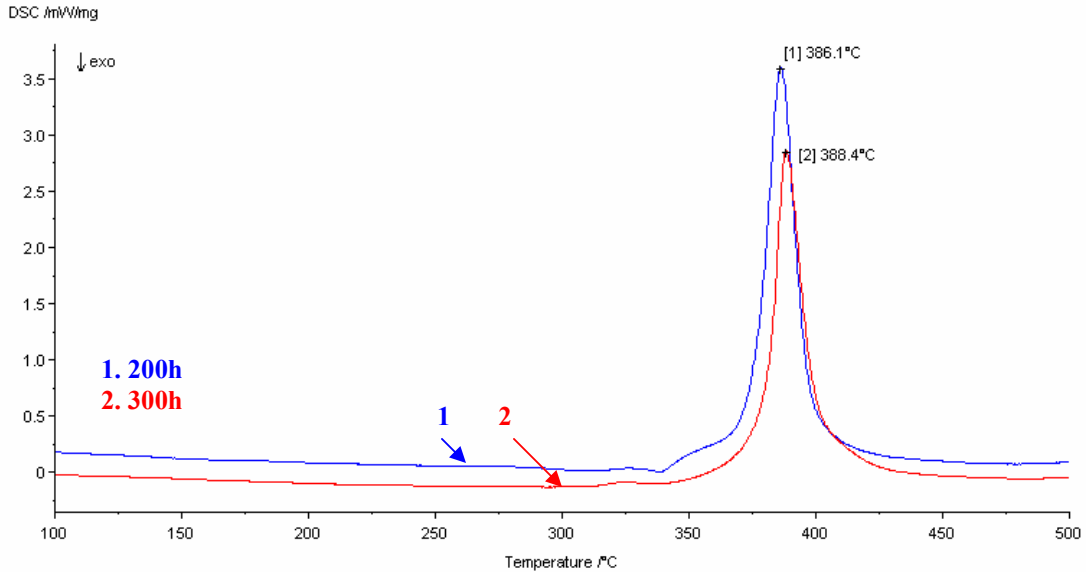

Fig. G.19 DSC curves for the powder mixture of Mg and oxide-free amorphous boron in a stoichiometric ratio Mg-2B (B10H powders) after milling for 200 and 300h under IMP2 mode.

G.3.3 B14H and B15H powders

G.3.3.1 Data of DSC analysis

Table G.8 Summary of DSC data for B15H200 powders upon heating to 500°C.

Powder	Milling time (h)	Peak						
		T_{on} (°C)	T_{peak} (°C)	T_{end} (°C)	ΔH (J/g)	Yield of MgH_2 (wt.%)	Desorbed Hydrogen from MgH_2 (wt.%)	Mg reaction rate (MgH_2) (%)
B15H	200	373.9	385.5/397.4	410.2	1027	36.1	2.7	68.9

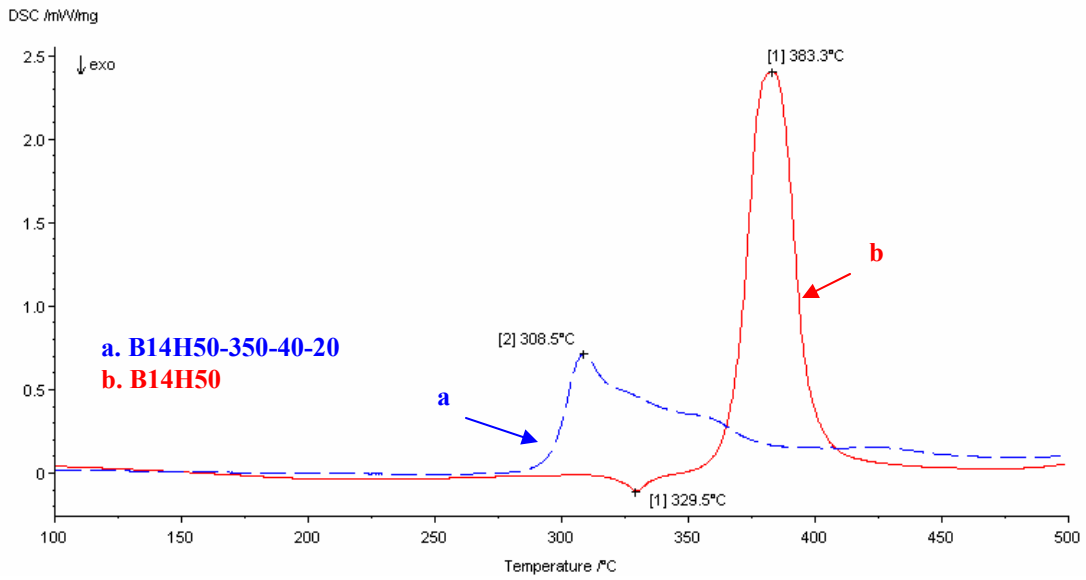

Fig. G.20 DSC curves of (a) 50h milled B14H powder (B14H50-350-40-20) after annealing at 350°C under 4MPa of hydrogen for 20h and (b) 50h milled B14H powder (B14H50) is replotted for comparison.

G.3.3.2 Hydrogen desorption kinetics measured in a Sieverts-type apparatus

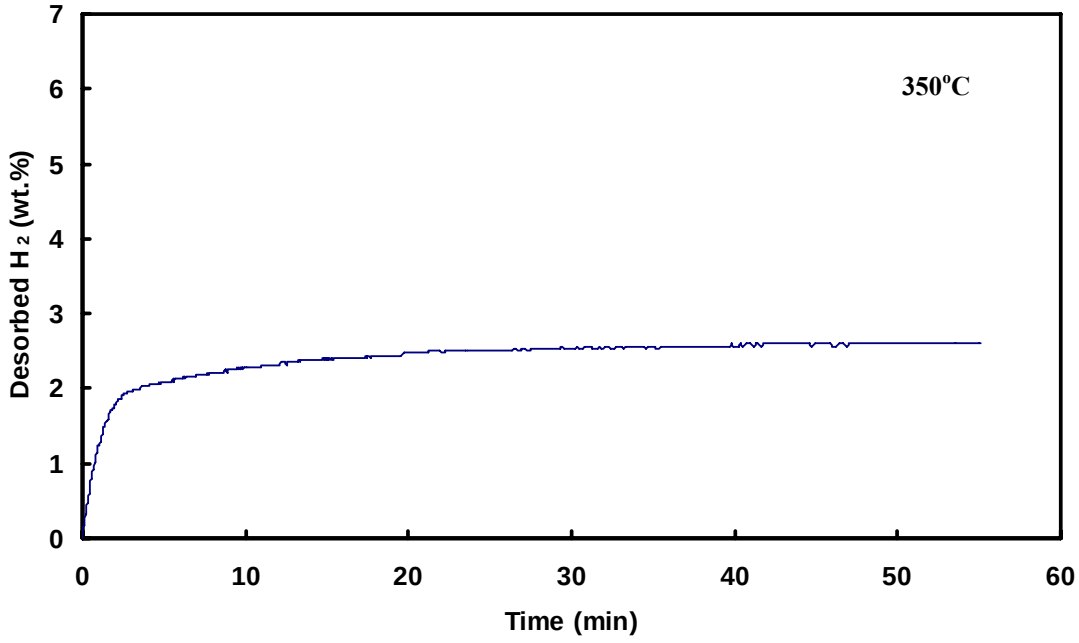

Fig. G.21 Hydrogen desorption kinetics at 350°C for the 200h-milled B15H powder.

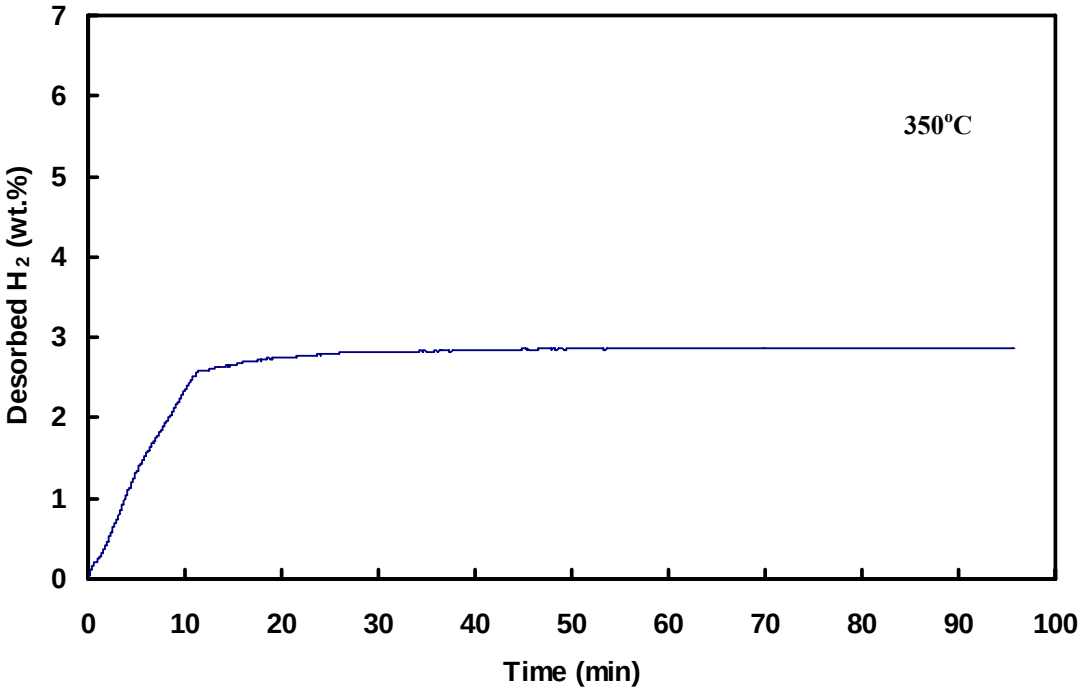

Fig. G.22 Hydrogen Desorption kinetics at 350°C for the 50h-milled B14H powder.

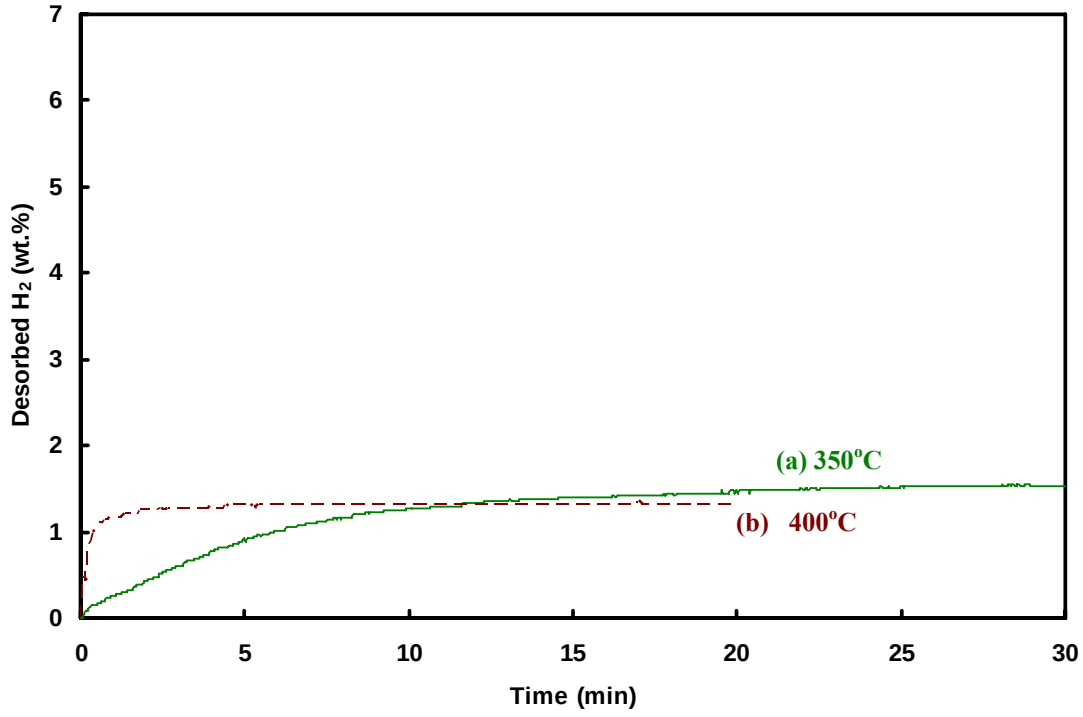

Fig. G.23 Hydrogen Desorption kinetics at (a) 350°C and (b) 400°C for the 200h-milled B14H powder.

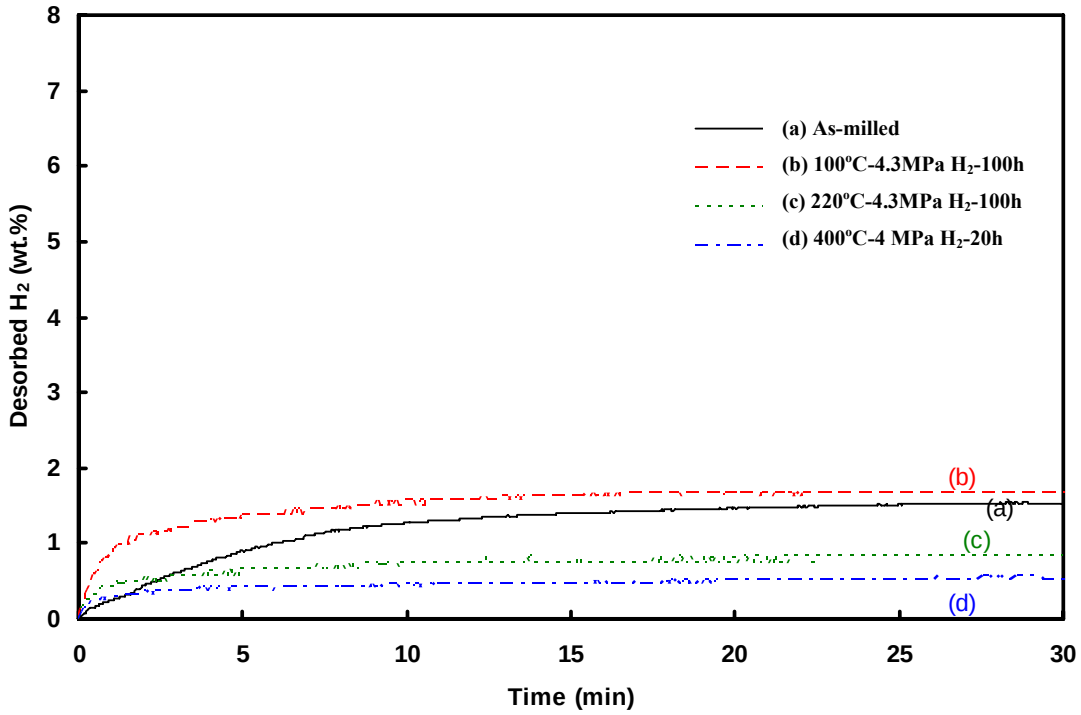

Fig. G.24 Hydrogen Desorption kinetics at 350°C for the milled and the annealed B14H200 powders.

G.3.4 B11H powders

Table G.9 Summary of DSC results as well as hydrogen capacity (wt.%) of as-milled and annealed B11H powders measured in a desorption test using a Sieverts-type apparatus.

Powder	DSC Peak				Desorption test*
	T_{on} (^oC)	T_{peak} (^oC)	T_{end} (^oC)	ΔH (J/g)	Hydrogen capacity (wt.%)
B11H50	375.0	400.0	437.8	113	0.4
B11H200	349.2	397.6	458.5	325	0.8
B11H200-220-43-100	273.1	303.2	359.8	92	0.5

***Using a Sieverts-type apparatus at 350^{o}C**

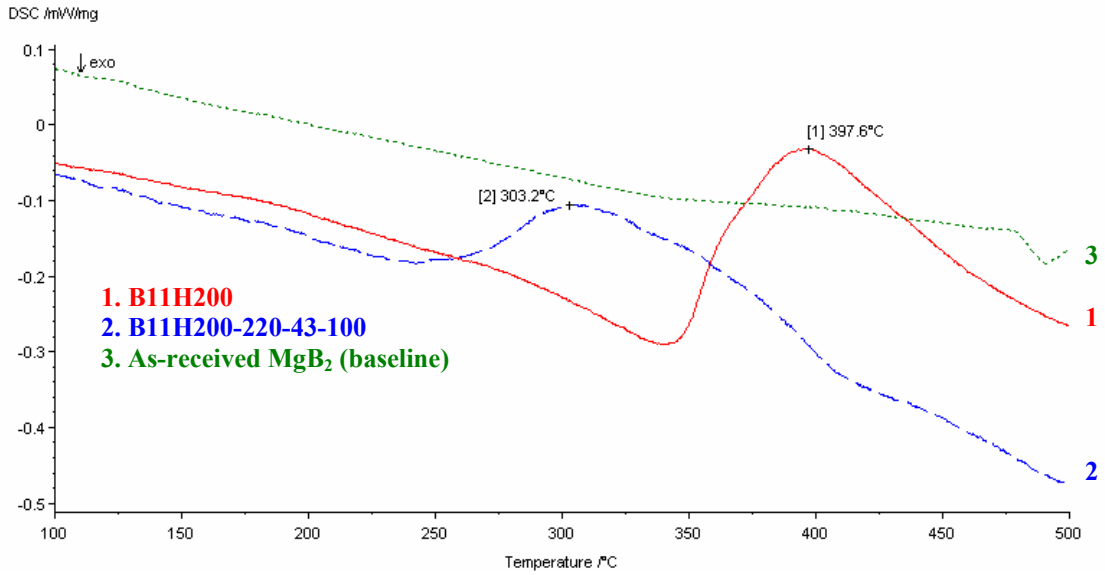

Fig. G.25 DSC curves for B11H powders after (1) milling for 200h under IMP710 mode and (2) after annealing at 220^{o}C under 4.3MPa of hydrogen for 100h in Sieverts apparatus (B11H200-220-43-100) as well as (3) DSC curve for as-received MgB_2 powder.

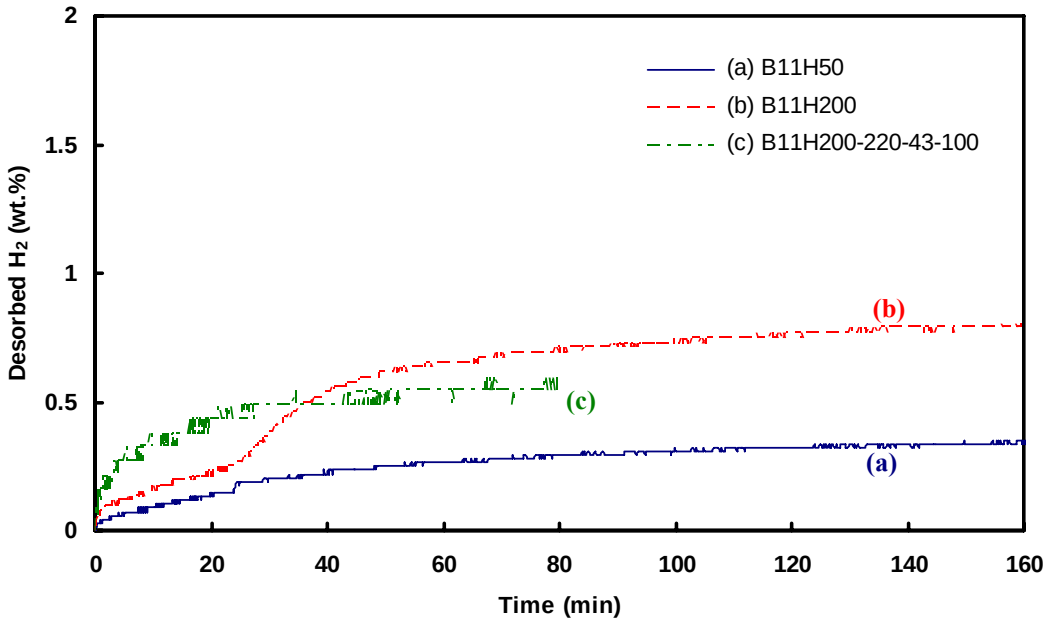

Fig. G.26 Hydrogen Desorption kinetics at 350°C for the (a) 50h-milled (B11H50), (b) 200h-milled powder (B11H200) and (c) 200h-milled powder after annealing at 220°C under 4.3Mpa of hydrogen for 100h (B11H200-220-43-100).